

Multi-scale Modelling of Hot Rolled Dual-phase Steels for Process Design

Von der Fakultät für Georessourcen und Materialtechnik
der Rheinisch-Westfälischen Technischen Hochschule Aachen

zur Erlangung des akademischen Grades eines
Doktors der Ingenieurwissenschaften

genehmigte Dissertation

vorgelegt von **Master of Metallurgy**
(MMet)

Piyada Suwanpinij

aus Bangkok

Berichter: Univ.Prof. Dr.-Ing. Wolfgang Bleck
Univ.Prof. Dr.-Ing. Gerhard Hirt
Emer.Prof.Dr.Takateru Umeda

Tag der mündlichen Prüfung: 12. November 2012

Diese Dissertation ist auf den Internetseiten der Hochschulbibliothek online verfügbar

The complexity of '*modelling*' depends on what '*modelling*' means to you.

Piyada Suwanpinij, Aachen, 2012

To everyone who I owe.

Acknowledgement

I have a great opportunity to carry out the project '*Simulation, Optimisation and Control of Microstructure Evolution and Mechanical Properties during Hot Rolling of Multiphase Steels*' during the whole period I am in Aachen. It brings me the focus on the hot rolling of the dual phase steels as we worked with this steel group in the first four years of the project. It is a member project under the frame project SPP1204 or '*Algorithms for fast, material specific process-chain design and -analysis in metal forming*' under the support from Deutsche Forschungsgemeinschaft (DFG). The macroscopic kinetics model is therefore the main result as it is expected to be transferable to the online application in the industry. My second project '*Design of Bainite in Steels from Homogeneous and Inhomogeneous Microstructures using Physical Approaches*' or for short '*Bainite Design*' should be also mentioned. It was funded by Research Fund for Coal and Steel (RFCS). It gave me a chance to have closer contact to the industry people who are professional in the multiphase steels and modelling.

I am grateful to my advisor, Univ.Prof. Dr.-Ing Wolfgang Bleck, for the opportunity for the doctoral study. Thanks Univ.Prof. Dr.-Ing Gerhard Hirt for kindly being my second examiner. Special thanks to Emer.Prof. Dr.Takateru Umeda for his interest in my topic and for a long time spent on the intercontinental flight from Thailand to my defence.

The first colleague I have to mention is Dr.Krishnendu Mukherjee who helped me since before he started his job at this department until after he left. He also went through my thesis and gave several fruitful comments. Dr.Monideepa Mukherjee supported me very much about the recrystallisation analysis. Mr. Hans Henning Dickert is so far the best supporter and gives always good ideas to me. Mr.Dingshun Yan and Mr.Xiaoxiao Li are my student co-workers who help me the most with programming with MATLAB program. Ms. Daniela Niespodziany worked with me the longest and helped with the whole literature database which eased my thesis work very much. Thanks also all other student co-workers who I do not mention.

I also appreciate the discussion with Mr. Christoph Keul every time I needed help with the dilatometer experiments. Mr. Klaus Herrmann is a professional technician at the dilatometry and is always helpful and patient with tons of questions. Mr. Marcel Graf kindly managed all the pilot rolling experiments at IMF, TU Bergakademie Freiberg. Dr. Silvia Richter and Mr. Philippe Pinard at GFE, RWTH Aachen University brought me the best results of FEG EPMA. Dr. Alexander Schwedt kindly gave lots of advice about the EBSD. Big thanks to Dr. Bernd Böttger at Access, RWTH Aachen University, for the fruitful discussion about the phase field modelling with MICRESS™. I appreciate the help from Dr. Suzana

Fries, ICAMS, Ruhr-University Bochum for all kind of questions related to ThermoCalc™ as well as the help with the script from Dr. Beng Hallstedt, Materials Chemistry, RWTH Aachen University. I am impressed also in the private communication with Prof. Ernst Kozeschnik for the criterion for modelling classification and quick response by email. Thanks to Mr. Wislaw Tupiec for his readiness to help with all the SEM measurement. Ms. Kirsten Dyrda and her team at our library saved me lots of time for searching the literature and ordering some articles. Thanks Ms. Christina Beumers for all the appointment arrangement. Thanks also to the community of hot rolling and austenite decomposition for the discussion and exchange of ideas. Big thanks to the office colleagues: Ms.Linda Mosecker and Ms.Wenwen Song for the nice atmosphere during writing.

Finally, I have to say thank you to my family and friends for all kind of support, love, friendship and patience. Thanks all kinds of constraints which make me become tougher.

Thank you all so much

Piyada Suntamphij

Abstract

This thesis investigates and models the austenite to ferrite transformation in the hot rolling of two different dual phase steels. The investigation has been carried out in a deformation dilatometer as well as a 4-stand pilot rolling mill. Three different modelling approaches were employed to give different aspects of information and for different applications. Macroscopic kinetics model based on JMAK rate form gives simple overall kinetics information and indicates the appropriate process window as a function of temperature on the Run Out Table and the degree of deformation in the non-recrystallisation region. Thermodynamics model show the effect of chemical composition on critical temperatures and therefore on the processing temperature window. Phase field yields the microstructure evolution in details, namely, ferrite grain size distribution and phase fraction as well as the diffusion profile in the remaining austenite. It supports the information for the finding of significant amount of retained austenite and the strong carbon gradient found by field emission electron microprobe.

Zusammenfassung

Im Rahmen dieser Arbeit wurde die Phasenumwandlungen des unterkühlten Austenits nach dem Warmwalzen am Beispiel zweier Dualphasenstähle untersucht und modelliert. Die experimentellen Untersuchungen wurden mit Hilfe eines Umform-Dilatometers sowie einer 4-gerüstigen Pilotwalzstraße durchgeführt. Drei unterschiedliche Modellierungsansätze wurden genutzt, um die verschiedenen Aspekte der simulierten Phasenumwandlungen abzubilden und Informationen für verschiedene Anwendungen zu generieren. Ein auf dem JMAK-Ansatz basierendes makroskopisches Kinetikmodell beschreibt die Gesamtkinetik der Phasenumwandlung und gibt geeignete Prozessfenster als Funktion der Temperatur auf dem Auslaufrollgang und dem Umformgrad beim Fertigwalzen im nicht-rekristallisierendem Temperaturbereich an. Das thermodynamische Modell zeigt den Einfluss der chemischen Zusammensetzung auf kritische Temperaturen und damit auf das für den Prozess nutzbare Temperaturfenster. Das Phasenfeldmodell beschreibt im Detail die Mikrostrukturentwicklung, wie die Ferritkorngrößenverteilung, die Phasenanteile sowie das Diffusionsprofil im verbleibenden Austenit. Die aus dem Modell gewonnenen Informationen stützen die experimentell gefundenen hohen Restaustenitgehalte sowie den starken Kohlenstoffgradienten innerhalb des Restaustenits, welcher mittels Feldemission-Elektronenmikroskopie nachgewiesen wurde.

Table of Content

1	INTRODUCTION AND OVERVIEW	8
2	THEORETICAL BACKGROUND	10
2.1	<i>The hot rolled multiphase steels</i>	10
2.2	<i>Phenomena relating to hot rolling</i>	14
2.3	<i>Classification of modelling related to the hot rolled DP steel</i>	16
2.4	<i>Modelling of austenite recrystallisation</i>	19
2.5	<i>Modelling of austenite to ferrite transformation</i>	23
2.5.1	Structure-properties model	23
2.5.2	Semi-empirical kinetic model	23
2.5.3	Nucleation and growth model	29
2.5.4	Spatially mesoscopic model	32
2.5.5	Thermodynamic modelling	35
2.6	<i>Martensite transformation</i>	40
2.7	<i>Bainite transformation</i>	41
2.7.1	Thermodynamics modelling for the non-equilibrium phases	44
3	LABORATORY PROCESS SIMULATION	50
3.1	<i>Material selection, melt production and sample preparation</i>	50
3.2	<i>Process simulation in deformation dilatometer</i>	52
3.2.1	Austenite grain size determination	56
3.2.2	Determination of the recrystallised fraction and the grain size after recrystallisation	58
3.2.3	The flow curve for the calculation of the stored energy in austenite	60
3.2.4	Ferrite formation kinetics	60
3.2.5	The hardenability of austenite after the carbon partitioning	60
3.3	<i>Process simulation in 4-stand rolling line</i>	62
3.4	<i>Plane strain compression at hot deformation simulator</i>	66
3.5	<i>Microstructure analysis</i>	67
3.5.1	Austenite grain size determination	67
3.5.2	Ferrite fraction, morphology, grain size, grain size distribution and nucleation density	67
3.5.3	Identification of bainite, martensite and retained austenite constituents	68
3.6	<i>Mechanical properties of the hot rolled sheets</i>	71
3.6.1	Tensile testing	71

3.6.2	Hardness mapping.....	71
4	RESULTS FROM LABORATORY PROCESS SIMULATION.....	72
4.1	<i>Process simulation in deformation dilatometer</i>	<i>72</i>
4.1.1	Austenite grain size by quenching and etching	72
4.1.2	Austenite grain size by ferrite decoration	75
4.1.3	Austenite grain size by oxidation method.....	77
4.1.4	Fraction recrystallised between rolling passes.....	78
4.1.5	The flow curve for stored energy of austenite	80
4.1.6	Ferrite formation kinetics.....	81
4.1.7	Plane strain compression at hot deformation dilatometer	93
4.1.8	Ferrite grain size and the ferrite nucleation density	94
4.1.9	The hardenability of austenite after carbon partitioning.....	94
4.2	<i>The rolling experiment and the hot rolled DP steel sheets</i>	<i>111</i>
5	MODELLING WORK	117
5.1	<i>Alloying and process window speculation by CALPHAD</i>	<i>117</i>
5.1.1	Calculation of the isopleths	117
5.1.2	Calculation of the critical temperatures.....	117
5.1.3	Calculation of the maximum phase fraction	122
5.2	<i>Austenite recrystallisation between rolling passes</i>	<i>123</i>
5.3	<i>Modelling of the effect of austenite grain size and retained strain</i>	<i>125</i>
5.4	<i>Modelling of the macroscopic ferrite transformation kinetics</i>	<i>125</i>
5.4.1	Modelling of the carbon partitioning after ferrite transformation	127
5.5	<i>Modelling of the macroscopic martensite transformation kinetics.....</i>	<i>128</i>
5.6	<i>Modelling of the mesoscopic ferrite transformation with phase field modelling....</i>	<i>129</i>
5.6.1	The simulation of the pancaked austenite	134
6	MODELLING RESULTS.....	136
6.1	<i>Alloying and process window design by CALPHAD.....</i>	<i>136</i>
6.1.1	Calculation of the isoplethal phase diagrams.....	136
6.1.2	Calculation of the critical temperatures.....	138
6.1.3	Calculation of the maximum phase fraction	142
6.2	<i>Modelling of the evolution of austenite grain size during recrystallisation.....</i>	<i>145</i>
6.3	<i>Modelling of the effect of austenite grain size and retained strain</i>	<i>148</i>
6.4	<i>Modelling of the macroscopic ferrite transformation kinetics</i>	<i>149</i>
6.5	<i>Modelling of the macroscopic martensite transformation kinetics.....</i>	<i>153</i>

6.6	<i>Modelling of the mesoscopic ferrite transformation with phase field modelling..</i>	155
7	DISCUSSION	164
7.1	<i>Comments on the experimental process simulation</i>	164
7.2	<i>Comments on the macroscopic kinetics modelling</i>	167
7.3	<i>Comments on the phase field modelling</i>	168
7.4	<i>Comments on the thermodynamic modelling</i>	169
8	CONCLUSIONS	171
9	Bibliography.....	173
10	Cirriculum vitae	187

List of Abbreviations

ANNs	Artificial neural networks
CA	Cellular Automata
CALPHAD	Calculation of Phase Diagrams
CCT	Continuous Cooling Transformation
DP steel	Dual phase steel
EBSD	Electron BackScatter Diffraction
EQAD	Equivalent Area Diameter
FEG EPMA	Field Emission Electron Microprobe
GES	Gibbs Energy System
JMAK	Johnson-Mehl-Avrami-Kolmogorov
LOM	Light Optical Microscope
MC-P	Monte Carlo-Potts
NPLE	Negligible Partitioning Local Equilibrium
PAG	Prior Austenite Grain boundary
PF	Phase Field
ROT	Run-Out Table
SEM	Scanning Electron Microscope
TMCP	Thermo-Mechanical Controlled Process
UTS	Ultimate tensile strength
XRD	X-Ray Diffraction
YS	Yield strength

List of Nomenclatures

A_{e3}	Temperature, below which ferrite starts to form in hypoeutectoid alloys
A_{e3_para}	Same as A_{e3} but calculated with paraequilibrium constrains
A_{e3_NPLE}	Same as A_{e1} but calculated with NPLE constrains
A_{e3d}	Same as A_{e3} but consider the effect of deformation
A_{e3d_para}	Same as A_{e3d} but calculated with paraequilibrium constrains
A_{e3d_NPLE}	Same as A_{e3d} but calculated with NPLE constrains
A_{r3}	Temperature, below which ferrite starts to form in non-equilibrium condition i.e. during cooling
A_{e1}	The temperature of the austenite-to-pearlite eutectoid transformation or the temperature below which austenite completely transform into ferrite in the lower carbon range
A_{e1_para}	Same as A_{e1} but calculated with paraequilibrium constrains
b	Burgers vector
b_{max}	Maximum bainitic ferrite fraction
B_s	Bainite start temperature
B_{s_para}	Same as B_s but calculated with paraequilibrium constrains
C_{KM}	Constant in Koistinen-Marburger equation
C_γ	Average carbon content in the remaining austenite
$C_{nominal}$	Nominal carbon content of the respective steel
C_α	Carbon content in ferrite
$C^{\gamma\alpha}$	Carbon content at the interface between α and γ on the γ side
$C^{\alpha\gamma}$	Carbon content at the interface between α and γ on the α side
D	Diffusion coefficient
D_γ	Austenite grain diameter
D_γ^{eff}	Effective austenite grain diameter
D_0	Original austenite grain diameter (before recrystallisation)
D_{rex}	Recrystallised austenite grain diameter.
D_c^γ	Diffusion coefficient of carbon in austenite
e_u	Uniform elongation
e_f	Total elongation
E	Total energy of dislocation per unit length
f	Ferrite fraction
\dot{f}	Time derivative of ferrite fraction

f_{eq}	Equilibrium ferrite fraction
F_x	Recrystallised fraction
F_s	Softening fraction
g_{Cool}	Function representing the effect of cooling profile
g_{S_v}	Function representing the effect of austenite conditioning, S_v
g_{Temp}	Function representing the effect of temperature
G	Growth rate or free energy
G_N	Universal nucleation function
ΔG_v	Free energy difference per unit volume
ΔG_m	Free energy difference per mole
$\Delta G^{i\Phi}$	Activation energy for the formation of a critical nucleus for an i -type nucleation site
h	Planck's constant
H	Enthalpy
k	Boltzmann's constant
\dot{m}	Time derivative of martensite fraction
m_{KM}	Volume fraction of martensite according to Koistinen-Marburger
M	Interface mobility
M_0	Pre-exponential component of interface mobility
M_s	Martensite start temperature
M_f	Martensite finish temperature
n	Strain hardening exponent
N_n^i	Number of i -type nucleation sites per austenite grain
N_v	Nucleation rate or number of nuclei
Q_D	Activation energy for grain boundary diffusion
$r^{i\Phi}$	Critical size of a nucleus
S	Half-thickness of the ferrite allotriomorph.
S_v	Grain boundary surface area of austenite in a unit volume
t	Time
$t_{0.5}$	Time for 50% recrystallisation
T	Temperature
T_0	Locus of chemical composition and temperature for a diffusionless transformation
T_{nr}	Non-recrystallisation temperature
u	Ratio of mole fraction of a substitutional atom component to the

	sum of base alloy and all substitutional atoms
V_m^γ	Molar volume of austenite
W_s	Widmanstätten ferrite start temperature
$W_{s,para}$	Same as W_s but calculated with paraequilibrium constrains
X	Composition or mole fraction
Z_1^i, Z_2^i, Z_3^i	Nucleation parameters
ε	Logarithm strain
$\dot{\varepsilon}$	Logarithm strain rate
ε_{thick}	Logarithm strain in the thickness direction
ε_{eq}	Equivalent strain
$\dot{\varepsilon}_{eq}$	Equivalent strain rate
ε_p	Peak strain for dynamic recrystallisation
μ	Chemical potential or shear modulus of austenite
η	Width of the transition boundary
ρ	Dislocation density
σ	Flow stress
λ	Scaling factor
$\gamma_{\alpha\gamma}$	Surface energy of γ - α interface
$\gamma_{\gamma\gamma}$	Surface energy of γ - γ interface
$\gamma_{\alpha\alpha}$	Surface energy of α - α interface
α_1	Parabolic growth rate constant of allotriomorph ferrite
ϕ	Phase field parameter value
$v(T)$	Transformation interface velocity, as a function of temperature

1 INTRODUCTION AND OVERVIEW

This thesis deals with different modelling approaches in hot strip rolling of dual phase (DP) steel. Its focus is the austenite to ferrite transformation on the run out table (ROT) in a hot strip mill. The models couple the acceleration effect from the retained strain from the last finishing stand(s) as it is the heart of Thermo-Mechanical Controlled Processes (TMCPs).

DP steels generally contain carbon, manganese, chromium and other alloying elements. The variation of the composition depends on the following processes and applications. The work deals with 2 different alloying concepts of DP steels. The first one contains molybdenum and is selected as it shows slower ferrite transformation kinetics while the other contains silicon and chromium and results in rapid transformation kinetics which can be barely observed by experiments. The through process simulation by means of deformation dilatometer experiment was carried out. It starts from austenite grain growth during reheating and austenite recrystallisation and grain refinement during rolling. It includes also the martensite and/or bainite transformation after the phase transformation on the ROT. A selected processing route was selected and transferred to a pilot rolling mill, from which hot rolled DP strips were produced and investigated for their mechanical properties. The entire process simulation and its results are allocated in Chapters 3 and 4.

Chapters 5 and 6 describe the three different groups of modelling of the phase transformation. They are intentionally allocated behind the experimental part as some results from the experiments are necessary for the modelling. The modelling includes thermodynamics modelling, semi-empirical modelling with rate form equation and equations for the critical temperatures from the literature and mesoscopic modelling by means of phase field model. The thermodynamics model illustrates the first rough process window, which is later mapped more accurately by a semi-empirical model for the phase transformation. The semi-empirical model employs a simple algorithm and can be transferred to an industrial context. The phase field modelling helps to analyse the carbon partitioning during the phase transformation to support the findings in the microstructure.

This thesis therefore illustrates how different modelling approaches can be used to identify the process window of hot rolled DP steel by taking into account the acceleration effect of the TMCPs on the phase transformation. It analyses also their contribution to the industrial usage especially in terms of computational time and cost. The intensive material

characterisation as well as the phase field modelling provides a deeper understanding in the carbon partitioning during austenite to ferrite transformation.

2 THEORETICAL BACKGROUND

2.1 The hot rolled multiphase steels

One of the best well-known and most important multiphase steels is the DP steel. Fig. 1 shows greater urgency and importance of DP steels estimated from year 2003. DP steels are very low-carbon steels and can be either non-micro-alloyed or micro-alloyed. Their microstructure is composed of ferritic multiphase matrix containing 10-30 volume% of martensite island and also less than 7 volume% of retained austenite [Ble04]. The dispersed martensite on the soft matrix of ferrite in DP steels results in superior cold formability due to the continuous yielding behaviour, the low proof stress to tensile strength ratio as well as the high uniform and total elongation values.

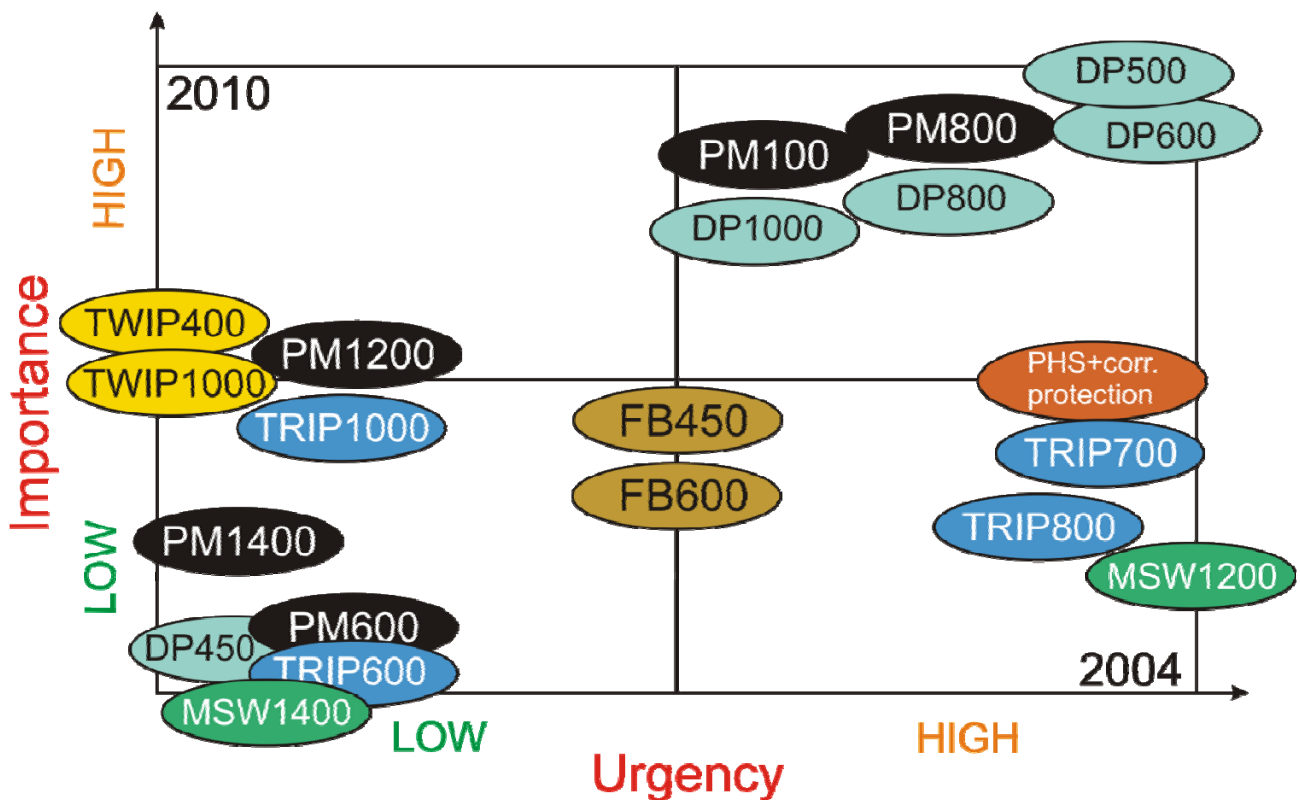


Fig. 1 The importance and urgency of multiphase steels according to German Iron and Steel Institute (VDEh) [Ste03].

There are two different processing routes for DP steels, as compared in Fig. 2

1) Cold rolling route

The starting material is thin cold-rolled sheets with ferrite-pearlite microstructure. The martensite is induced through the intercritical annealing for

ferrite-austenite microstructure and the subsequent fast cooling. It is either quenched to room temperature or the quenching is interrupted to galvanise the sheet in hot dip galvanising lines.

2) Hot rolling route

The ferrite and martensite are created directly after the steel is hot rolled. Namely, the ferrite is formed on the ROT and the martensite is formed during coiling.

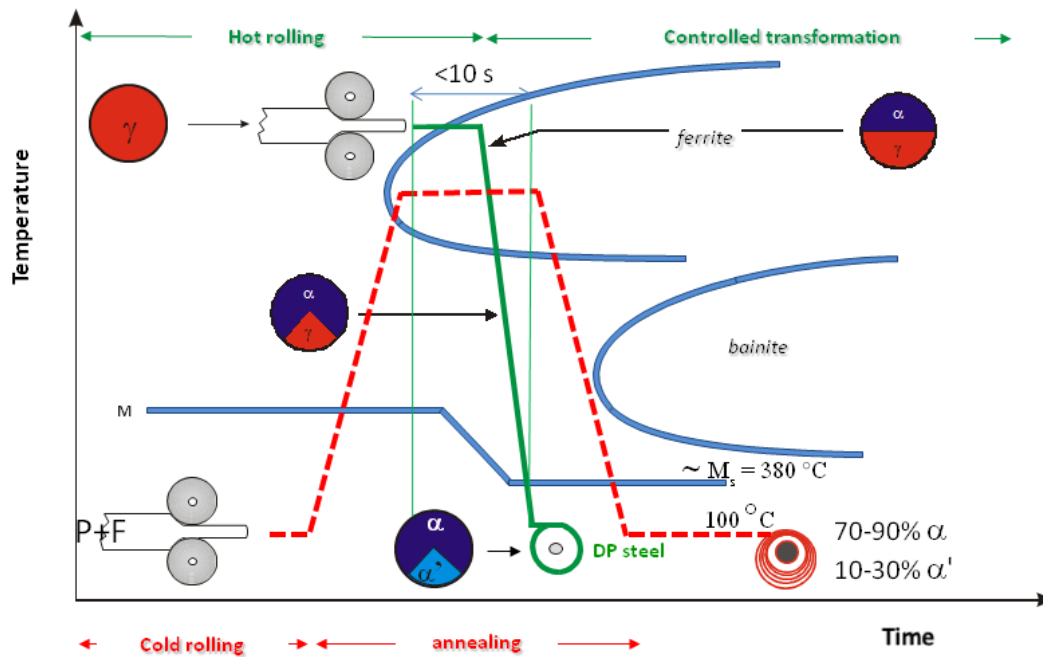


Fig. 2 The cold rolling and hot rolling processing routes for the production of DP steels. The solid line shows the hot rolling process and the dash line shows the cold rolling process.

Producing DP steels through the cold rolling process deals only with austenite formation in the intercritical region and its transformation into martensite during quenching. The phase fraction depends therefore mainly on the intercritical temperature and the production encounters less problems with bainite formation. On the other hand, hot rolled sheets are much more sensitive to the processing. The issues of too little ferrite fraction and some bainite are unavoidable in some cases. Its advantage comes from the economic point of view, as it produced DP steels in a single-step process.

The applications of the hot-rolled grades are, for example, wheel disks, wheel webs, B-pillar and longitudinal members such as beams and chassis in automobiles [Hof10, Arc1] as shown in Fig.3. Its market share is, however, much smaller than the cold-rolled grades.

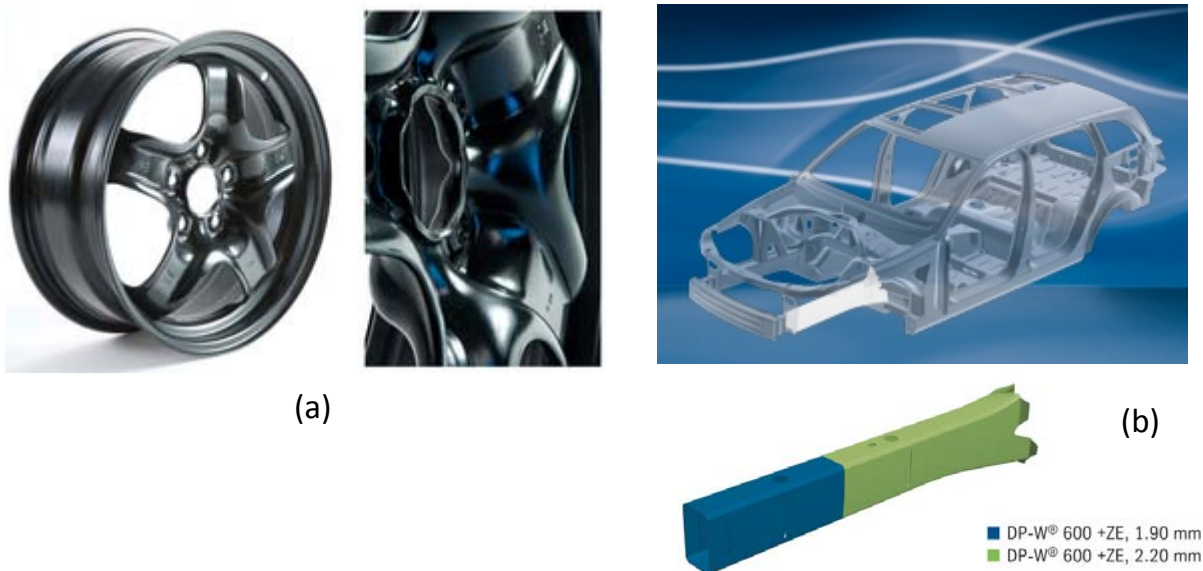


Fig. 3 (a) wheel webs in car wheels [Arc1] fabricated by Hayes Lemmerz International, Inc. [62] (b) the longitudinal members in car bodies [Hof10]. Both are produced from hot rolled DP steel grade 600.

The alloying design for the hot rolled grades should be considered for the workability in the austenite state as well as the influence on the ferrite formation kinetics. The microstructure obtained afterwards depends strongly on the processing and its chemical composition. On the other hand, the cold rolling alloys should be designed that soft material with not too high strain hardening is guaranteed. It should result also on fine and homogeneous ferrite-pearlite microstructure at the end of the hot rolling step so that good carbon distribution for good re-austenitisation can be achieved.

The chemical compositions of DP steels are generally similar to those of low carbon steels except the higher content of manganese. It is the main solid solution strengthener, which contrarily results in the retardation of ferrite nucleation [Kop01] and growth [Bra81, Gup93]. Silicon and chromium are added generally by the fact that the coiling temperature can be raised to the temperatures higher than 150°C, which is the normal coiling temperature in C-Mn steels [Mil04]. Moreover, they accelerate the ferrite transformation kinetics as they are ferrite formers. [Lee07 and Ble02]. Industrial melts, however, contain low amount of silicon such as 0.06 mass% to improve the weldability take chromium as the ferrite former.

It is not common to add molybdenum in the hot rolled grades but some research work selected the molybdenum-containing grades for hot working conditions [Muk09]. For cold rolling, the industrial constraints (e.g. insufficient cooling rates in the processing line or the interrupted cooling to the zinc bath, which is approximately 460°C in hot dip galvanizing

lines) require the addition of some alloying elements e.g. molybdenum to avoid or minimise the austenite transformation to ferrite and/or bainite during holding and/or cooling [Muk09, Moh10]. Molybdenum will retard ferrite by forming from the fully austenitic structure in the hot rolling, which can result in insufficient fraction of ferrite and some bainite formation during the consecutive quenching. However, this can be avoided by refining the austenite grain by recrystallisation and deformation under the T_{nr} temperature. Molybdenum, on the other hand, cannot result into the insufficient fraction of ferrite in case of the cold rolling. This is because the ferrite-pearlite structure with large amount of ferrite is induced after hot rolling as longer transformation time is available than in the case of hot rolling of the DP steels.

The term multiphase steels in this thesis is strictly reserved for those produced to improve the mechanical properties. Some modelling scientists [Lus03, Wol07] use this term differently by calling the existence of different transformation products, i.e., ferrite, pearlite, bainite and martensite, as multiphase.

2.2 Phenomena relating to hot rolling

The hot rolling is a hot working in long or flat products at high temperatures which allows dynamic restoration processes, namely, dynamic recovery [Die88] and dynamic recrystallisation [Hum04]. Therefore, the process benefits from the lower rolling load. This is in contrast with the cold working, in which only static recovery and static recrystallisation after the deformation step are feasible.

Most steels as well as in copper and nickel alloys and other metals with low stacking fault energy, have relatively low dynamic recovery at the hot working temperatures. As soon as they reach the critical dislocation density, the dynamic recrystallisation occurs [Tam88]. The static recovery, which occurs between the rolling passes, contributes to softening together with static recrystallisation. The softening can be measured by applying a second deformation after some delay period of time, which corresponds to the term '*static*'. The recovery fraction is generally taken to be 0.2-0.25 of the total softening fraction [Mav88, Sel90]

For a single rolling stand, if the strain does not reach the critical strain for the dynamic recrystallisation, the static recrystallisation might take place afterwards. If it is not the case, the retained strain in this rolling stand will be accumulated with the next rolling stand and as soon as the sum reaches the critical strain, the dynamic recrystallisation will be activated. The first rolling passes, which may take place at 1250 °C, has commonly the strain less than 15%, Gladman [Gla97] claimed that dynamic recrystallisation does not take place in the first rolling passes. As the temperature falls in the following passes, the critical strain for dynamic recrystallisation even increases and the possibility to have dynamic recrystallisation in a single pass also decreases. If no complete static recrystallisation takes place between passes, the dynamic recrystallisation can occur only through the strain accumulation after a few passes [Gla97]. A much more number of literature focus on the modelling of austenite microstructure during rolling under static recrystallisation [Don96, Sic99, Ane92] while only very few describe the dynamic recrystallisation kinetics, which is faster [Hod93].

The concept of Thermo-Mechanical Controlled Process (TMCP) has been introduced since late 19th centuries and it deals with both shaping and controlling the microstructure so that the required properties can be yielded, especially by rolling in non-recrystallisation region so that the austenite grains are deformed.

In sum, the hot rolling of DP steels encounters the following phenomena:

1. *Austenite formation and grain growth* during slab reheating.
2. *Dynamic recrystallisation*, directly during being rolled at high temperatures
3. *Static recovery and recrystallisation*, between rolling passes at lower temperatures
4. *Deformed austenite*, in the non-recrystallisation region

2.3 Classification of modelling related to the hot rolled DP steel

Different types of modelling can be classified by using different criteria such as

1. **scale** : macro to microscopic models
2. **predicted properties** : phase fraction or mechanical properties
3. **degree of insight** : black to white box models
4. **degree of predictiveness** : phenomenological to fully predictive models

The names of the first and second criteria explain their meanings well. Note that the criterion scale includes time and distance scale. The thermodynamics modelling is the only approach which has no dimension scale neither time scale. Newer generations contribute to 2D or 3D models where an area or volume of the microstructure is simulated. This group are generally termed mesoscopic which falls on a scale between microscopic and macroscopic. More interest should be paid to the classification according to the degree of insight and predictiveness. According to the degree of insight, the type of modelling varies from black box models such as regression analysis and artificial neural networks (ANNs) to grey box models such as empirical or half-empirical equations, like those summarised by Kwon [Kwo92] and to white box. The majority of the modelling nowadays still falls in grey box category. According to Beynon [Bey05], in the context of austenite recrystallisation, the models which can be defined to be '*white box*' must satisfy the microstructure in the dislocation scale as well as the effect of changing strain component and strain path such as a constitutive model. In spite of its highest insight, the accuracy is considered the lowest. An alternative approach is to create a better model is to combine the black and white box models and yields the name '*hybrid model*' and gains both highest insight and accuracy. The relation of insight and accuracy for each model type is shown in Fig. 4.

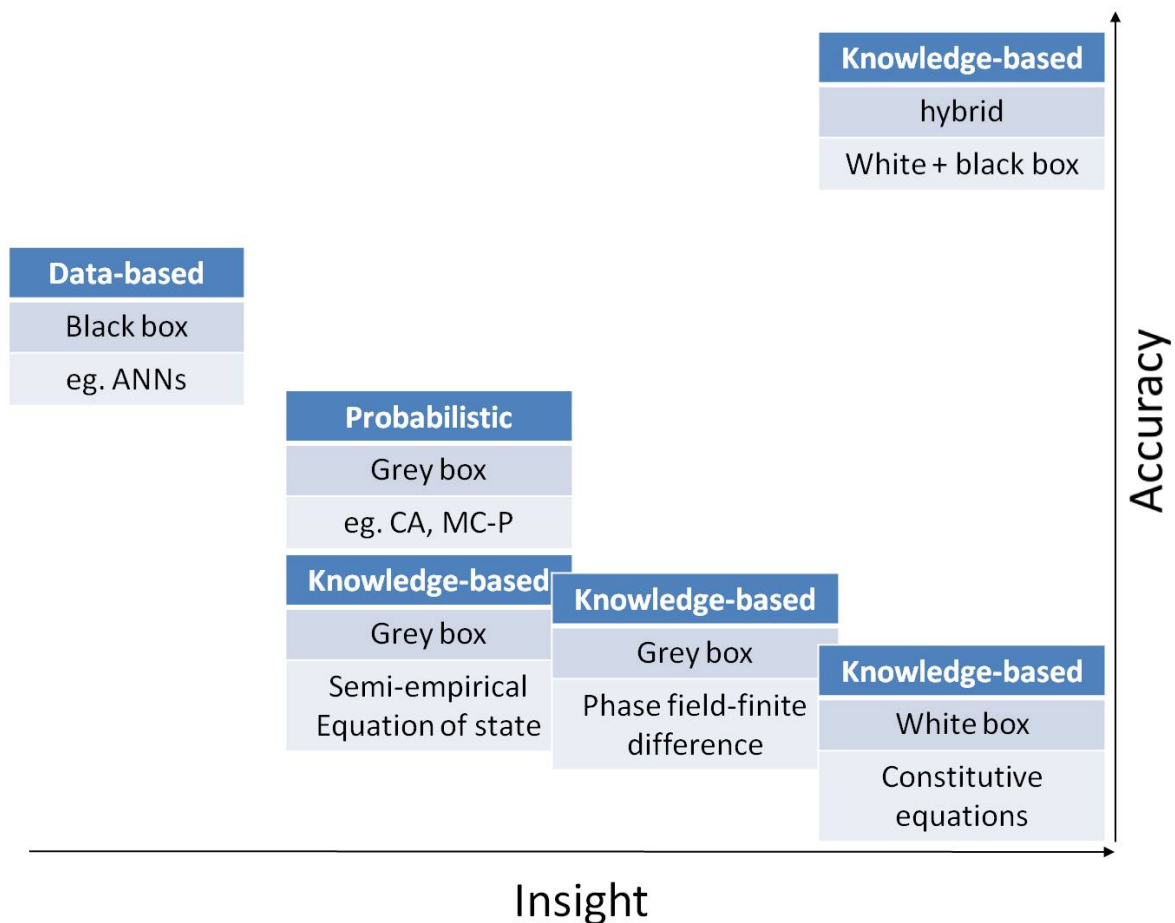


Fig. 4 Classification of modelling work according to the degree of insight, modified from [Bey05].

Classifying by the degree of predictiveness corresponds to the modelling in this work better. The models which mimic some phenomena without paying detailed attention to their fundamental significance are called phenomenological approaches such as the JMAK-based transformation model and statistical methods such as ANNs. The class which is fully predictive is absolutely fundamental and very time consuming such as the molecular dynamics/statics, Monte Carlo and cluster expansion as it requires no fitting parameter [Koz11] and can be also considered to be white box models. In between lie the semi-predictive/semi-phenomenological approaches which are more commonly used in practice in the today's materials science. They can be considered as lighter grey box models compared with the phenomenological JMAK model. This group includes the thermo-kinetics model describing the nucleation and growth under either diffusion controlled, interface controlled or mixed mode controlled growth in the microscopic to mesoscopic scale and employ the popular modelling techniques such as phase field approach, which frequently run in MICRESS™ software. DICTRA™ is so far the most well-known simulation software for the purely diffusion-controlled model. The equilibrium thermodynamic

databases under CALPHAD approach is widely utilised by employing softwares such as ThermoCalc™, MatCalc™, Prisma™. The classification according to the predictivity is represented in Fig. 5.

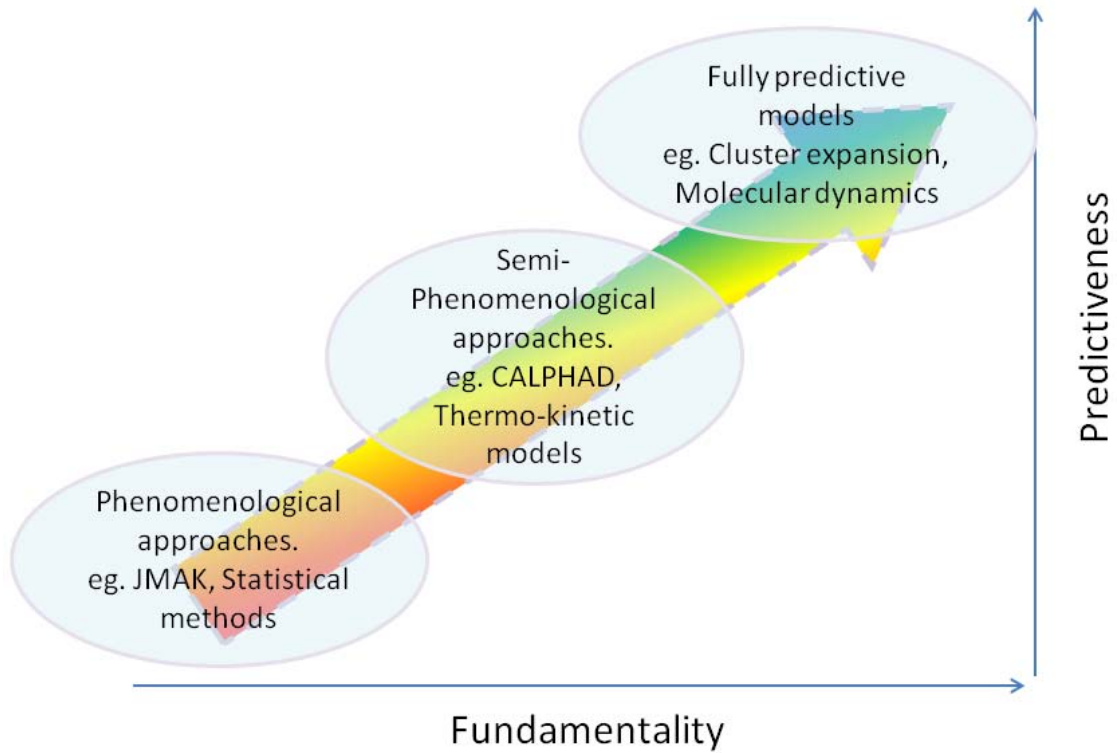


Fig. 5 Classification of modelling work according to the degree of predictiveness and computational cost/time [Koz11]

2.4 Modelling of austenite recrystallisation

At higher temperatures in former rolling passes, it is important to model the austenite recrystallisation so that the austenite conditioning at the last rolling pass can be properly modelled. The first step to analyse the recrystallisation in austenite roughly is to predict the temperature, below which the recrystallisation is not possible or very sluggish. Such the temperature is termed non-recrystallisation temperature (T_{nr}). The deformation done below this temperature is predicted to result in a retained strain, which accelerates the transformation kinetics. Only few equations are available in the literature. The most often cited equation is from Boratto [Bor88]

$$T_{nr} = 887 + 464C + (6645Nb - 644\sqrt{Nb}) + (732V - 230\sqrt{V}) + 890Ti + 363Al - 357Si$$

Eq.1

All the elements are in mass%. It was derived by regression analysis on the experiments from a number of microalloyed steels including a non-microalloyed steel.

The descriptions of both static and dynamic recrystallisations have similar forms and are summarised in Table 2.1 and Table 2.2. The Avrami type rate equations for recrystallisation originated by Sellars in the 80s are the most well-known. Much fewer equations contribute to the dynamic recrystallisation especially in terms of the predicted dynamically recrystallised austenite grain size. The statically recrystallised austenite grain size is known to depend mainly on the strain and depend on the strain rate to a minor extent [Sic00]. The most effective way of austenite grain refinement is resulted at lower deformation temperatures with a high strain.

The research group in Canada led by Jonas assume the recovery fraction between 0.2 to 0.25 [Mav88]. Another group led by Millitzer claims that a previous work by Sellars [Sel90] shows that the recovery contributes to the initial 0.15-0.20 from the total softening fraction. The fraction of 0.25 was proven to work well at 950-1050 °C in a Nb steel and a boron containing Nb steel [Mav88]. However, Sun [Sun98], his former colleague at McGill University, continued the recrystallisation analysis with the recovery fraction of 0.2, which was further taken for DP and TRIP steels in the last few years by Liu [Liu07, Liu07a]. Sun reported also an empirical equation for the prediction of recrystallised austenite grain size in plain carbon steel, which was also employed by Liu [Liu07] for DP steels. It will be described in details in section 5.2.

Table 2.1 Static and dynamic recrystallisation kinetics

		Static Recrystallisation			Dynamic Recrystallisation		
Author	Steel	Ref.	Equation	No.	Ref.		No.
Hodgson	C-Mn	Hod92, Hod95, Sel90a	$X = 1 - \exp\left(-0.693\left(\frac{t}{t_{0.5}}\right)\right)$ $t_{0.5} = 2.3 \cdot 10^{-15} \cdot \varepsilon^{-2.5} D_0^2 \cdot \exp\left(\frac{230000}{RT}\right)$	Eq.2	Hod92, Hod95, Sel90a	$X = 1 - \exp\left(-0.693\left(\frac{t}{t_{0.5}}\right)^{1.5}\right)$ $t_{0.5} = 1.1 \cdot Z^{-0.8} \exp\left(\frac{230000}{RT}\right)$	Eq.3
Hodgson	Nb	Hod92, Hod95	$X = 1 - \exp\left(-0.693\left(\frac{t}{t_{0.5}}\right)\right)$ $t_{0.5} = (-5.24 + 550[Nb]) \times$ $10^{-18} \varepsilon^{(-4+77[Nb])} D_0^2 \exp\left(\frac{330000}{RT}\right)$	Eq.4	-	-	-
Roberts	C-Mn	Rob83	$X = 1 - \exp\left(-0.693\left(\frac{t}{t_{0.5}}\right)^{1.7}\right)$ $t_{0.5} = 5.1 \cdot 10^{-21} \cdot \varepsilon^{-4} D_0^2 \cdot \exp\left(\frac{330000}{RT}\right)$	Eq.5	-	-	-
Sellars	C-Mn, Nb	Sel90a	$X = 1 - \exp\left(-0.693\left(\frac{t}{t_{0.5}}\right)^2\right)$ $t_{0.5} = 2.5 \cdot 10^{-19} \cdot \varepsilon^{-4} D_0^2 \cdot \exp\left(\frac{300000}{RT}\right)$ <p>For $\varepsilon \leq 0.8 \cdot \varepsilon_p$,</p> $\varepsilon_p = 4.9 \times 10^{-4} \cdot D_0^{0.5} \cdot Z^{0.15}$ $Z = \dot{\varepsilon} \cdot \exp\left(\frac{312000}{RT}\right)$	Eq.6	Sel90a, Sel90b	$X = 1 - \exp\left(-0.693\left(\frac{t}{t_{0.5}}\right)^2\right)$ $t_{0.5} = 1.06 \cdot 10^{-5} \cdot Z^{-0.6} \cdot$ $\exp\left(\frac{300000}{RT}\right)$ <p>For $\varepsilon \geq 0.8 \cdot \varepsilon_p$,</p> $\varepsilon_p = 4.9 \times 10^{-4} \cdot D_0^{0.5} \cdot Z^{0.15}$ $Z = \dot{\varepsilon} \cdot \exp\left(\frac{312000}{RT}\right)$	Eq.7

		Static Recrystallisation			Dynamic Recrystallisation		
Author	Steel	Ref.	Equation	No.	Ref.		No.
Yada and Senuma	C-Mn	Sen86, Yad88	$X = 1 - \exp\left(-0.693\left(\frac{t}{t_{0.5}}\right)^2\right)$ $t_{0.5} = 2.2 \cdot 10^{-12} \cdot \varepsilon^{-2} \cdot \dot{\varepsilon}^{-0.2} \cdot S_v^{-0.5} \cdot \exp\left(\frac{30000}{RT}\right)$ $S_v = \frac{24}{\pi \cdot D_0} [0.491 \cdot \exp(\varepsilon) + 0.155 \cdot \exp(-\varepsilon + 0.1433 \cdot \exp(-3 \cdot \varepsilon))]$	Eq.8	Yad88	$X = 1 - \exp\left(-0.693\left(\frac{\varepsilon - \varepsilon_c}{\varepsilon_{0.5}}\right)^2\right)$ $\varepsilon_c = 4.76 \times 10^{-4} \exp\left(\frac{8000}{T}\right)$ $\varepsilon_{0.5} = 1.144 \times 10^{-5} \cdot D_0^{0.28} \dot{\varepsilon}^{0.05} \exp\left(\frac{6420}{T}\right)$	Eq.9

Table 2.2 The recrystallised grain size after static recrystallisation

Author	Steel	Ref.	Equation	No.
Anelli	Low C-Mn (ES 17)	Ane92	$D_{rex} = 1150 \cdot \dot{\epsilon}^{-0.1} \cdot \epsilon^{-0.3} \cdot D_0^{0.39} \cdot \exp\left(\frac{-6.5 \times 10^3}{T}\right)$	Eq.10
	Medium C-Mn (QC 29B)		$D_{rex} = 84 \cdot \dot{\epsilon}^{-0.1} \cdot \epsilon^{-0.6} \cdot D_0^{0.33} \cdot \exp\left(\frac{-3.5 \times 10^3}{T}\right)$	Eq.11
	Eutectoid (FP 69 and FF 82)		$D_{rex} = 95.5 \cdot \dot{\epsilon}^{-0.1} \cdot \epsilon^{-0.5} \cdot D_0^{0.39} \cdot \exp\left(\frac{-3.5 \times 10^3}{T}\right)$	Eq.12
Choquet	C-Mn	Cho90	$D_{rex} = 45 \cdot \exp\left(\frac{-24980}{RT}\right) \cdot \epsilon^{-0.6} \cdot D_0^{0.374} \cdot \dot{\epsilon}^{0.1}$	Eq.13
	Nb		$D_{rex} = 472 \cdot \exp\left(\frac{-48597}{RT}\right) \cdot \epsilon^{-0.7} \cdot D_0^{0.277} \cdot \dot{\epsilon}^{0.1}$	Eq.14
Leduc	C	Led80	$D_{rex} = 0.743 \cdot D_0^{0.67} \cdot \epsilon^{-1}$	Eq.15
Sun and Liu	C	Sun98, Liu07	$D_{rex} = 100 \cdot D_0^{1/3} \epsilon^{-0.37} \exp\left(-\frac{28000}{RT}\right)$	Eq.16
Yada	C-Mn	Yad88, Sen86	$D_{rex} = \frac{5}{(S_v \cdot \epsilon)^{0.6}}, S_v$ see Eq.8	Eq.17
Yoshie	Nb	Yos92	$D_{rex} = \frac{5}{(S_v \cdot \epsilon)^{0.7}}, S_v$ see Eq.8	Eq.18

2.5 Modelling of austenite to ferrite transformation

2.5.1 Structure-properties model

In this category, the product properties or microstructure and product properties or state variable and product properties are correlated by regression method as those developed in the late 80s to 90s [Pic78, Cho84, Kwo88]. They are therefore categorised to be macroscopic property black box phenomenological models.

Nowadays the ANNs come to play the most important role in this category. This approach works sufficiently in case of huge database such as in the industry. However, they lose their function outside the range of database.

2.5.2 Semi-empirical transformation kinetics model

It is the class with the most industrial application nowadays and can be categorised as macroscopic kinetics knowledge-based greybox phenomenological approach. The most well-known model is the JMAK based model [Avr39, Avr40, Wei97, Kol37, Joh39, Avr41, Fan98], which was originally established in 1939. Here, the transformation kinetics S curve of a single product phase is represented in exponential form for an isothermal temperature. It applies to all diffusion controlled transformations as well as the semi-diffusion controlled transformations such as for bainite, as will be shown in section 2.7.

It has been developed since 1937 and is still in use for the sake of its simplicity and short time calculation [Mur06, Liu07, Don96] and still among the intensive reviews and discussion [Fan98]. The JMAK equation which is in use nowadays is described as follows.

$$f = 1 - e^{-kt^n} \quad \text{Eq.19}$$

The coefficients k is a temperature dependant growth constant and n is the avrami exponent, which lies usually between 1 to 4 [Por92, Tam88, Cah56a]. It was derived from the original form

$$f = 1 - \exp \left[-\frac{\pi}{3} N_v G^3 t^4 \right], \quad \text{Eq.20}$$

where N_v is the nucleation rate in nuclei/(volume×time), G is the growth rate in distance/time, t is time. Therefore, n in Eq.19 is independent of temperature and k depends on the nucleation and growth rates and very sensitive to temperature as N_v and G are very temperature sensitive.

The JMAK model works under several assumptions, i.e., random nucleation and growth and constant nucleation rate [Por92] as well as that the nucleation rate is proportional to the growth rate [Fac05]. In other words, it works only for isokinetic reactions.

As in the mathematical sense, that the non-isothermal transformation models are not well established in metallurgists' community [Bro96], the history of developing the models for continuous cooling is rather long. The first attempt to model a continuous cooling came was from Scheil in 1935 [Sch35], which was even earlier than the time the JMAK model was established for isothermal transformations. He did it originally to predict the phase evolution during the incubation period, i.e. the initial state of phase transformation. Avrami [Avr40] and Cahn [Cah56] later extended this approach into the so-called '*additive rule*' and proved that it is valid for some phase transformations. This concept says

$$\int_0^t \frac{dt}{\tau(f,T)} = 1. \quad \text{Eq.21}$$

The function $\tau(f,T)$ is the isothermal time at which the transformation process has reached a fraction of f at temperature, T . Therefore, it strictly says that the additive rule only works for the case where the transformation can reach 100% such as the case of eutectoid steel, where austenite can transform into pearlite completely. However, it was proved to give satisfactory results for general transformations [Den92, Bok98]. Fachinotti [Fac05] proved that this classical way of using the additive rule is accurate enough and more accurate than the rate form although it is not a correct comparison as the rate form is the derivation of the JMAK model [Höm11].

It is also often in engineering works that the JMAK model is applied with discretisation during continuous cooling or at most proposed some modifications [Han01, Ven01, Mur06]. Donnay [Don96] and Murugaiyan [Mur06] suggested that the constant k in the JMAK equation (Eq.19) has the form of modified Gaussian function which is a function of the prior austenite grain size and the A_{e3} temperature with other constants to fit the cooling

profile. For austenite to ferrite transformation, Donnay [Don96] and Murugaiyan [Mur06] considered the n value to be 1.5.

Apart from using the additivity rule and the discretisation for continuous cooling, some other scientists employ the factorised JMAK rate form as an isokinetic model [Chr75]. The factorised rate form separates each controlling factor: the temperature and the transformed fraction, as

$$\dot{f} = g(T) \cdot h(f). \quad \text{Eq.22}$$

It has been proven for its additivity [Lus97] and has been utilised by a number of scientists [Lus03, Lus97, Ser04] also in case of a large number of internal state variables. Lusk [Lus03] identified 59 kinetics fitting parameters for all the phase transformation in the system.

The next possibility is to write the rate law in a more general form, namely, the influence of each controlling factor: temperature and the transformed fraction, is not separate

$$\dot{f} = g(T \cdot f) \quad \text{Eq.23}$$

However, it can be easily proven that both the factorised and general rate forms are of limited applicability [Leb84, Leb85]. Leblond therefore [Leb84, Leb85] derived a more general rate form coupled with the physical quantity '*equilibrium fraction*' and the remaining austenite fraction which yields

$$\dot{f} = \frac{f_{eq}(T) - f}{\tau(T)} \quad \text{Eq.24}$$

He suggested also that the influence of austenite grain size be coupled. The equilibrium fraction of the transformation product at each isothermal temperature, f_{eq} , is readable from the respective phase diagram or obtained from dilatometry in case of extremely low heating rate and long holding time. The usage of such the equilibrium fraction in the transformation model can be seen in several works [Leb84, Leb85, Haw85, Lus03, Mur06]. τ is a positive time constant.

The rate forms allow the coupling with heat and mechanic equations and require less computational resources [Ble10a, Höm11, Lus03]. Therefore, they are of use in SYSWELD™ code and the simulation tools in ANSYS™. Moreover, it can be employed together with the Koistinen-Marburger model for the martensite transformation.

2.5.2.1 Macroscopic modelling of the effect of austenite grain size and retained strain

Under deformation, the austenite is flattened and contains some irregularities at the grain boundaries and deformation bands inside the grains. This feature accelerates the phase transformation as the irregularities and deformation bands can act as additional nucleation sites. Consequently, it results in faster transformation kinetics as if the austenite grain size becomes smaller. Umemoto [Ume83] models a deformed austenite grain as an ellipsoid. Its surface area as shown in Fig. 6 follows

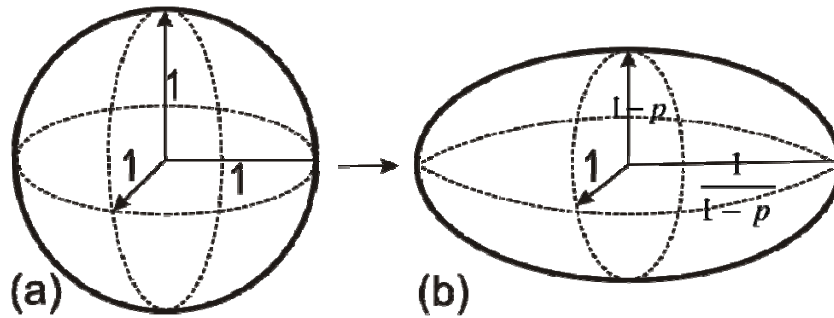


Fig. 6 The shape of an austenite grain under deformation with a degree of reduction p [Ume83]. a) The original grain b) the deformed grain

$$S_{gb}^d = \int_{-1/(1-p)}^{1/(1-p)} \left(\left\{ 4x \int_0^{\pi/2} \sqrt{1 - (2p - p^2) \sin^2 \theta} d\theta \right\} * \sqrt{\frac{x^2(1-p)^6}{1-x^2(1-p)^2} + 1} \right) dx. \quad \text{Eq.25}$$

A rough estimation of the equivalent austenite grain size from such the deformed austenite was proposed by Donnay [Don96].

$$D_{\gamma}^{eff} = \frac{D_{\gamma}}{1+5\varepsilon} \quad \text{Eq.26}$$

D_{γ} stands for the original austenite grain size. ε represents the logarithm strain from the deformation.

A simpler alternative was proposed by Anelli [Ane86], which was also taken by Kern [Ker92].

$$D_{\gamma}^{eff} = C \cdot D_{\gamma} \exp(-\varepsilon)$$

Lacroix [Lac03] take the coefficient C as 1 and it was followed by Militzer [Mil08].

Another representative of the austenite grain size and the flattening effect of austenite grains, is the S_v value, which indicates the grain boundary surface area of austenite in a unit volume. The equation proposed by Kvačakaj [Kva98] was adopted and shown in Eq.27.

$$S_v = 429 \frac{1}{D_{\gamma} e^{\varepsilon}} + 1571 \frac{e^{\varepsilon}}{D_{\gamma}} + [157.2(1 - e^{-\varepsilon}) - 59.47]_+ \quad \text{Eq.28}$$

The plus sign indicates that it is always a positive quantity. The quantity in the bracket comes from the deformation bands, which are taken into account by Kvačakaj only when the retained strain, ε , exceeds 0.475. Another form comes from Senuma [Sen84].

$$S_v = \frac{24}{\pi \cdot D_{\gamma}} \cdot [0.491 \cdot \exp(\varepsilon) + 0.155 \cdot \exp(-\varepsilon)] + 0.1433 \cdot \exp(-3\varepsilon) \quad \text{Eq.29}$$

Cahn [Cah56] defined it simpler as

$$S_v = \frac{3.35}{D_{\gamma}} \cdot \quad \text{Eq.30}$$

The most widely accepted austenite grain form is actually tetrakaidecahedron [Gla97, Lee01, Tam88, Sin98]. It has 14 faces with 8 hexagons and 6 squares as shown in Fig. 7. If the tetrakaidecahedral grains are assumed, the number of nuclei will follow [Bey92]

$$N_v = 0.43 D_{\gamma}^{-3}. \quad \text{Eq.31}$$

Provided that recrystallisation arises during multiple deformation steps, the portion of the retained strain, ε , must be specified and subtracted from the total strain. In this case, the austenite grain size, D_{γ} , in Eq.25 to Eq.30 means the grain size after the recrystallisations.

2.5.2.2 Empirical equations for the ferrite transformation start temperature

In practice, the ferrite transformation does not start at the equilibrium A_{e3} temperature during cooling but at A_{r3} temperature. There are several empirical equations for the A_{r3} temperatures in the literature and tabulated in Table 2.3.

Table 2.3 The empirical A_{r3} equations from the literature.

Author	Steel	Ref.	Equations	No.
Blás	Very Low C (0.024-0.068 mass% C)	Blã89	$A_{r3} = 903 - 328 C - 102 Mn + 116 Nb - 0.909 v$ <p>v - cooling rate in °C/s (valid from 1.0-35°C/s)</p>	Eq.32
Choquet	C-Mn, C-Mn-Nb	Cho85	$A_{r3} = 902 - 527 C - 62 Mn + 60 Si$	Eq.33
Ouchi	173 steels of C-Mn, C-Mn-Nb	Ouc79	$A_{r3} = 910 - 310 C - 80 Mn - 20 Cu - 15Cr - 55 Ni - 80 Mo$ <p>Derived from case of 8 mm thick plate</p>	Eq.34
Shiga	Linepipe	Shi81	$A_{r3} = 910 - 273 C - 74 Mn - 56 Ni - 16 Cr - 9 Mo - 5 Cu$	Eq.35
Pickering	Plain carbon steels	Pic86	$A_{r3} = 910 - 230 C - 21 Mn - 15 Ni + 45 Si + 32 Mo + 13 W + 104 V$	Eq.36

2.5.3 Nucleation and growth model

A common method in modelling the macroscopic austenite to ferrite transformation physically is to model with nucleation and growth mechanism. Ferrite nucleation sites in tetracaidecahedrons are divided in three dimensions into grain corner, grain edge and grain boundary. In two dimensions, the nucleation at grain boundaries and edges will be observed without any difference and the nucleation sites are assigned as triple junction, boundary and bulk.

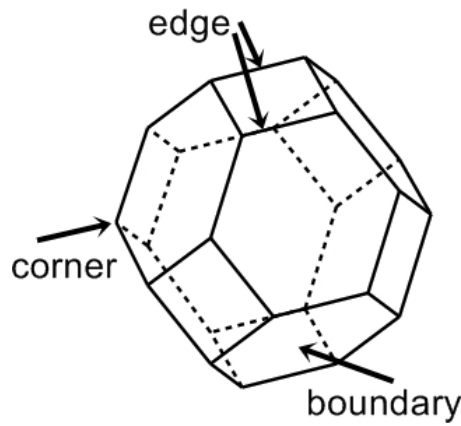


Fig. 7 The shape of a tetrakaidecahedron

The nucleation rate of ferrite has been well established by the time-dependent classical nucleation theory [Rus70, Rus80]. By integrating all types of nucleation sites, a nucleation rate was derived [Lee01] as

$$\frac{dN}{dt} = \sum_i N_n^i \frac{kT}{h} \exp\left(\frac{-\Delta G^{i\phi} \lambda}{kT}\right) \exp\left(\frac{-Q_D}{kT}\right). \quad \text{Eq.37}$$

N_n^i represents the number of i -type nucleation sites per austenite grain and will be listed in Table 2.4. h is the Planck's constant, which is $6.626068 \times 10^{-34} \text{ m}^2 \text{ kg/s}$. k means the Boltzmann's constant, which is $1.3806503 \times 10^{-23} \text{ m}^2 \text{ kg s}^{-2} \text{ K}^{-1}$. Q_D stands for the activation energy for grain boundary diffusion for iron atoms, which amounts to $4 \times 10^{-19} \text{ J}$. λ represents a scaling factor of 10^{-4} [Lee01] due to the inhomogeneity in solid. $\Delta G^{i\phi}$ is the activation energy for the formation of a critical nucleus for an i -type nucleation site.

Each type of nucleation site has a specific activation energy for the formation of a critical nucleus as shown in Eq.38 [Cle55]

$$\Delta G^{i\phi} = \left(\frac{4}{27}\right) \frac{(Z_1^i \gamma_{\alpha\gamma} - Z_2^i \gamma_{\gamma\gamma})^3}{Z_3^i \Delta G_v^2}. \quad \text{Eq.38}$$

The nucleation parameters for each nucleation site, Z_1^i , Z_2^i and Z_3^i , are described in Table 2.4.

Table 2.4 The nucleation parameters for each nucleation site for the calculation in Eq.37

	Z_1^i	Z_2^i	Z_3^i	N_n^i
Homogeneous	13	0	4.2	$\frac{3}{64\pi} \left(\frac{D_\gamma}{r^\phi}\right)^3$
Boundary (face)	3.7	1.6	0.48	$\frac{6+16\sqrt{3}}{32\pi} \left(\frac{D_\gamma}{r^\phi}\right)^2$
Edge	1.3	0.72	0.096	$\frac{9\sqrt{2}}{2} \left(\frac{D_\gamma}{r^\phi}\right)$
Corner	0.51	0.18	0.16	24

The critical nucleation size is determined by

$$r^{i\phi} = \frac{2(Z_1^i \gamma_{\alpha\gamma} - Z_2^i \gamma_{\gamma\gamma})}{3Z_3^i \Delta G_v} \quad \text{Eq.39}$$

$\gamma_{\alpha\gamma}$ stands for the surface energy of γ - α interface 0.6 J/m² [Cle55]. $\gamma_{\gamma\gamma}$ is the surface energy of an austenite grain boundary 0.85 J/m² [Cle55]. ΔG_v means the free energy difference between austenite and ferrite per unit volume. D_γ represents the austenite grain diameter.

The ferrite growth mechanisms can be either purely diffusion controlled or interface controlled model. The kinetics in the interface controlled model is purely controlled by the the movement of the interface between the parent phase and the transformation product. Under the diffusion controlled model, an allotriomorphic ferrite grain grows in a parabolic fashion as

$$S = \frac{b}{2} = \alpha_1 \sqrt{t} \quad \text{Eq.39}$$

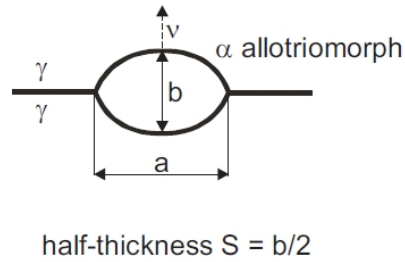


Fig. 8 A schematic description of a parabolic growth of allotriomorphic ferrite according to Eq.39

S is the half-thickness of the ferrite allotriomorph. α_1 is the parabolic rate constant and t is the growth time. Its growth rate can be achieved from [Chr75, Zen49, Bha85, Aar70]

$$\alpha_1 \exp\left(\frac{\alpha_1^2}{4D_C^\gamma}\right) \operatorname{erfc}\left(\frac{\alpha_1}{2\sqrt{D_C^\gamma t}}\right) = 2\sqrt{\frac{D_C^\gamma}{\pi}} \frac{C_{\text{nominal}} - C^{\gamma\alpha}}{C^{\alpha\gamma} - C^{\gamma\alpha}}. \quad \text{Eq.40}$$

D_C^γ is the diffusion of carbon in austenite. $C^{\gamma\alpha}$ is the carbon content at the interface on the austenite side. $C^{\alpha\gamma}$ is the carbon content at the interface on the ferrite side. Such the diffusion controlled model is the core of the well-known simulation software DICTRA™, which solves the problems with simple geometry such as planar, cylindrical or spherical.

The case in between is also possible and is called mixed mode controlled. Several findings from the researchers at TU Delft led by van der Zwaag [Kri97, Kop00] confirm that common cases of austenite to ferrite transformations conforms the mixed mode model. The transformation interface velocity, $v(T)$, in both the interface and mixed mode controlled models employ the following equation for the growth of ferrite

$$v(T) = M_0 \exp\left(\frac{-Q}{RT}\right) \Delta G_v. \quad \text{Eq.41}$$

M_0 is the interface mobility. Q is the activation energy 140-168 kJ/mol [Hil75, Kri98, Thi06, Faz05].

In some modelling works [Kop00, Hua06], nucleation is not treated as time-dependent process. But all nuclei are introduced at the beginning because of the very short interval of nucleation. Namely, the nucleation rate is not really taken into account and the

transformation is controlled mainly by growth kinetics. It is also called '*site saturation model*'.

2.5.3.1 Spatial model

Further approach to reduce the greyness and increase the predictiveness of modelling is a spatial model, which simulates the transformation on space domains such as Monte Carlo-Potts (MC-P) or cellular automata (CA) as well as the phase field (PF) model. In these cases, the calculation domains are extended to 2 and 3 dimension so that the simulations represent small areas or volumes of the microstructures. Therefore, the distribution in microstructure such as grain size distribution can be taken into account, while all the models in sections 2.5.1 and 2.5.2 can give only for mean values. The ferrite nucleation is based on the probability and space on the domain. The Monte Carlo method generates inputs randomly from a probability distribution over the domain [Jan07] and applies to every field. In the context of grain growth simulation, the probability of transition based on the change in free energy determines the movement of the grain boundary [Bey05]. Cellular Automaton works on a collection cells on a grid of specified shape. A neighborhood of each cell is defined, for example cells which are in the distance of 2 or less cell away. Each cell has the status of '*on*' and '*off*' with the simulation time by deterministic or probabilistic transformation rules, regarding its neighborhood [Bey05]. Multiphase field model has a different concept other than the other models in this group and is on the focus of this dissertation and will be explained in details.

2.5.4 Phase field modelling

In this model, the change of phases across the phase boundaries is continuous and it is defined as '*diffuse interface*' while the other models are based on '*sharp interface*'. This makes more sense in metallic system as the transition is gradual especially in the solidification problem [Rap04]. The diffuse interface in most systems has a thickness in order of a few angstrom to a few nanometer [Moe08], but is multiplied by in order of 100 for the sake of numerical calculation [Rap04]. Without tracking the interfaces explicitly, complex grain morphologies can be predicted regardless of the assumption of the grain shape [Moe08, Militzer2010], such as Widmanstätten [Log04]. It can therefore treat cases with different solute distribution due to the deviation from local equilibrium [Str05, Ahm98, Log03] such as NPLE (non partitioning local equilibrium), which is very advantageous. A well-known commercial code MICRESS™ (MICRostructure Evolution Simulation Software) also couple this feature.

A phase field is a local order parameter field that distinguishes a broken symmetry between two distinct phases. It is based on the approach of Ginzburg-Landau, who expressed the free energy of a superconductor as a complex order parameter. Metallurgists simply interpret the order or phase field parameter into phase fractions. The simplest case can be explained such as shown in Fig. 9. Each phase has an extreme phase field parameter value, in this case solid has $\phi_i = 0$ and liquid has $\phi_i = 1$. At the interface in between, the phase field value varies from between 0 and 1. The evolution of the microstructure is controlled by the minimisation of the free energy of the system, which is respect to the phase field parameter

$$\frac{\partial \phi}{\partial t} = M \frac{\partial G}{\partial \phi'} \quad \text{Eq.42}$$

where M is a mobility and G is the free energy, which is the function of the phase field parameter. The information about the interface velocity from the physically based growth model in section 2.5.3.

Steinbach [Ste96, Ste99] has developed it further for systems containing more than 2 phases since 1996 and called it '*multi-phase field modelling*'. Every single grain has its own field parameter and the interaction between grains is described in a pairwise fashion. The standard multiphase field equation is described by:

$$\frac{\partial \phi_i}{\partial t} = \sum_j M_{ij} \left\{ \gamma_{ij} \left[\phi_i \nabla^2 \phi_j - \phi_j \nabla^2 \phi_i + \frac{\pi^2}{2\eta^2} (\phi_i - \phi_j) \right] + \frac{\pi}{\eta} \sqrt{\phi_i \phi_j} \Delta G_{m_{ij}} \right\} \quad \text{Eq.43}$$

M_{ij} is the interface mobility of adjacent grains. γ_{ij} stands for the interfacial energy for different pair of interface. η represents the width of the transition boundary. $\Delta G_{m_{ij}}$ is the difference of the molar Gibbs free energy between adjacent ferrite and austenite grains. The evolution of the phase field parameters is controlled by the Gibbs free energy minimisation.

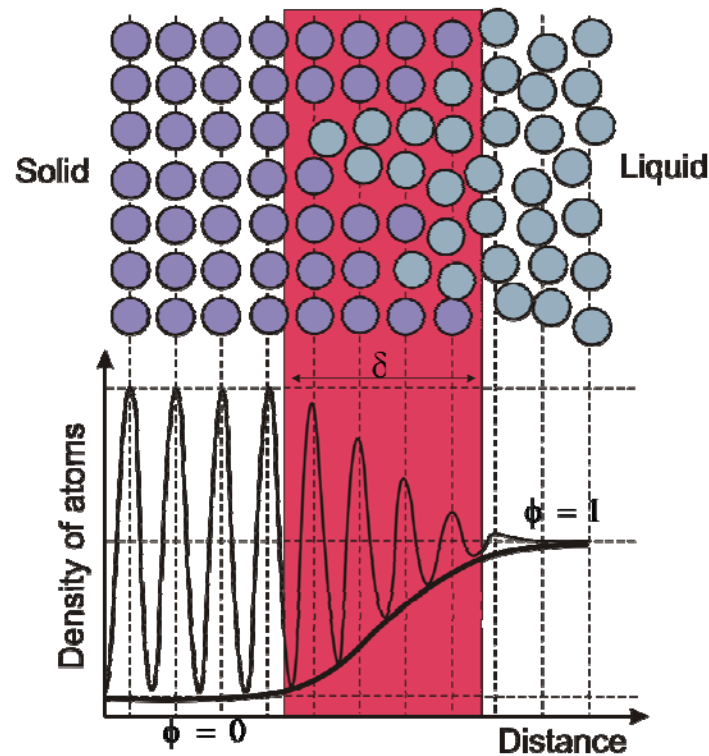


Fig. 9 The representation of phases by the phase field parameter and its variation inside the 'diffuse interface'

Steinbach's approach results in the possibility to describe multiple grains and phases during microstructure evolution and it is adopted in the commercial code MICRESS™. Within this code, the driving force of the phase transformation can be taken directly from the thermodynamic database in the software ThermoCalc™ through a Gibbs Energy System (GES) or from a self-defined linearised phase diagram. In case of the simulation of austenite recrystallisation and austenite grain growth, this term turns to be zero.

It can be seen from Eq.43 that during the austenite to ferrite phase transformation, the nucleation is not within the phase field formalism and has to be modelled separately, which unfortunately means more number of adjusting parameters.

The diffusion of the solute atoms is solved separately by

$$\frac{\partial \bar{x}}{\partial t} = \nabla \sum_{i=1}^N [\phi_i D_i \nabla \bar{x}_i]. \quad \text{Eq.44}$$

The terms \bar{x}_i and D_i stand for the mixture composition and multicomponent diffusion coefficient matrix in phase i .

The phase field equation (Eq.43) results in interface-controlled model transformation but when coupled with diffusion, it was found to be equivalent to the mixed mode model [Mec05].

The grid size has to be small with respect to the diffuse interface thickness and the diffuse interface thickness has to be small with respect to the typical radius of curvature of the microstructure. Generally 5-10 grids points within the diffuse interface are required for the stability of the numerical calculation. Therefore, the simulation in a large microstructure domain requires high computational resources.

There is an increasing number of work applying the phase field model to the solid state transformation such as austenite to ferrite. Nonetheless, it is still not common that the effect of austenite conditioning such as that in the hot rolling is taken into account.

2.5.5 Thermodynamic modelling

The CALculation of PHase Diagrams or CALPHAD is an approach to represent the Gibbs energy expressions as a function of system properties: temperature, pressure and compositions. It is derived by fitting the parameters in a thermodynamic model using the thermodynamic properties and phase equilibria derived by experiments. Therefore, it requires very good databases for reliable results. This modelling class can be categorised as no scale, either in time or distance with higher predictiveness and insight.

The modelling with CALPHAD approach should be the first step to be done if an adequate thermodynamic database for the interested material is available. One can evaluate the transformation behaviours of the interested alloys before selecting the alloying concepts or producing melts. One can calculate the critical temperatures under equilibrium, namely, A_{e1} and A_{e3} , critical temperatures under non-equilibrium, phase diagram, the equilibrium fraction of phases as well as other thermodynamic properties without any extra experimental fitting. The well-known commercial programs with database utilising the CALPHAD approach are ThermoCalc™, FactSage™, MTDATA™, PANDAT™ and MatCalc™. Within MTDATA™, a number of open-source databases such as SGTE for solution [Hac08] can be found. ThermoCalc™ employs the common tangent method (section 2.5.5.1) and the Gibb's energy minimisation technique [TCC] and is so far considered by the community to be one of the best. Thanks to the very general algorithm to find the equilibrium state of a system based on the work of Hillert [Hil99], which was implemented by Jansson [Jan84].

ThermoCalc™ is more flexible for the users to define the external conditions for their equilibrium state [And02]. With the comprehensive descriptions of the equations of state and all thermodynamic functions of pure substances and solution phases contained in various database, it is able to formulate the Gibbs energy expressions as well as its second derivatives. By means of the global minimisation technique, in which the common tangent plane giving the absolute lowest Gibbs energy is made for the calculation, the truly stable phase equilibria can be derived.

Different modes of equilibrium result in different partitioning of solute atoms. There are certainly differences between the substitutional and interstitial solute atoms. This solute partitioning under different equilibrium modes are show in Fig. 10. The negligible partitioning local equilibrium (NPLE) and paraequilibrium are constrained equilibria (or also called non-equilibria) by which the substitutional solute atoms partition very little or not at all. The cases of partial carbon supersaturation and martensitic phase transformation have no partitioning of the substitutional solute atoms either and are depicted here just for comparison.

2.5.5.1 Local equilibrium (or orthoequilibrium)

It is clear from the thermodynamics point of view that a system can lower its free energy the most if the instable phase is separate into 2 phases whose tangents of the free energy curves lie on a common tangent line, as illustrated for an Fe-C system in Fig. 11. In this case, the γ phase, at composition X_{γ} , is decomposed into the stable enriched the γ phase, at composition $X_{\gamma'}$, and α phase at composition X_{α} . The free energy of the system, will be therefore, $G^{\gamma'+\alpha}$ (at composition X_{γ} on the tangent line). Fe and C will have the same chemical potential in both α and γ phases so that

$$\mu_{Fe}^{\alpha} = \mu_{Fe}^{\gamma} \quad \text{and} \quad \mu_C^{\alpha} = \mu_C^{\gamma}. \quad \text{Eq.45}$$

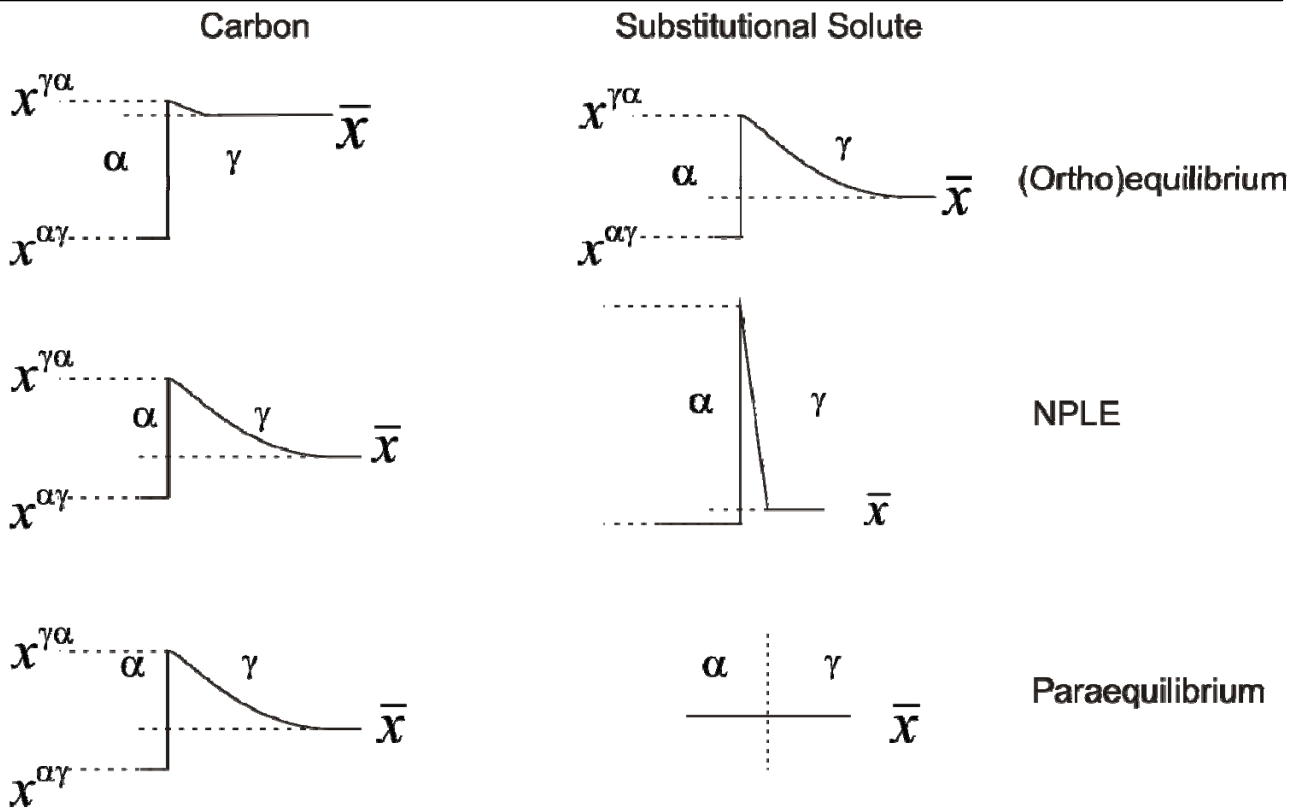


Fig. 10 The distribution of solute atoms according to different equilibriums [Bha01]

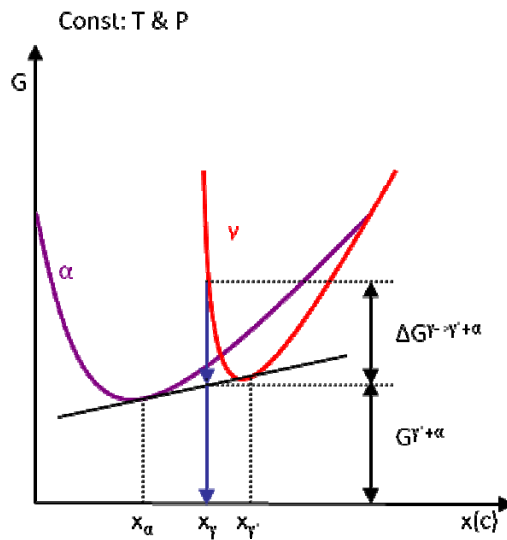


Fig. 11 The common tangent concept

This mode of equilibrium is sometimes called ortho-equilibrium, which was discussed by Hillert [Hil04], that this term is rather misleading.

Fig. 12(a) depicts an isothermal section of Fe-C-Mn system revealing the distribution of each alloying element. The concentration profiles of carbon and manganese at the transformation front follow points *c* and *d*. The dark filled black circle shows the chemical composition of the bulk. Note that in this case it lies on the carbon isoactivity line (long dash line).

2.5.5.2 Paraequilibrium

Paraequilibrium is an equilibrium-deviated condition or a partial equilibrium or a constrained equilibrium, in which the chemical potential of interstitial component(s), i.e. C, N, O, S, are the same in two specific phases in a multicomponent system and the combined chemical potentials of iron and all substitutional elements are equal on both sides of the transformation front. This means $u_{Fe}\mu_{Fe} + u_{M1}\mu_{M1}$ and $u_{Fe}\mu_{Fe} + u_{M2}\mu_{M2}$ and so on are constant.

The *u* fraction is defined by

$$u_{M_1} = \frac{x_{M_1}}{x_{Fe} + x_{M_1} + \dots}, \quad \text{Eq.46}$$

which means the ratio of the mole fraction of the substitutional atom component to the sum of the mole fraction of all substitutional atoms.

Therefore, the mole ratio between the substitutional elements and iron stays constant under paraequilibrium phase transformation.

Generally speaking, the interstitial components diffuse fast enough that they can partition among two phases according to thermodynamics while those of substitutional type could hardly diffuse and have the same composition both in the parent phase and the product phase. Therefore, the carbon content in ferrite is as low as predicted by thermodynamics and the content which is rejected from ferrite is piled up behind the transformation front in austenite. In contrast, the content of other substitutional elements remains the same in both phases. As a result, the transformation under paraequilibrium is much more rapid than that under (ortho)equilibrium.

2.5.5.3 Negligible partitioning local equilibrium, NPLE (or quasi-paraequilibrium)

This happens when the the substitutional solute atoms do not partition during the transformation. Similar to paraequilibrium, the composition of the substitutional solute atoms remains the same in the parent and the product phases. The difference is that the equilibrium holds at the interface and it results in a small peak of the substitutional specie(s), which is depicted in Fig. 10.

As shown in Fig. 12b, which shows an example of Fe-C-Mn, the concentration profiles of carbon and manganese at the interface follow points *c* and *d* as they have to keep the equilibrium at the transformation front. Point *c* determines the carbon and manganese concentrations at the interface on α side and point *d* determines those on γ . Note that during the transformation, the concentration of manganese in the bulk of both α and γ phases is kept constant at the nominal composition, except at the interface. On the other hand, the carbon and manganese in the bulk of γ start with the nominal composition as indicated by the filled black circle. During the transformation, the carbon in γ will increase and eventually reach the carbon isoactivity line which is shown by the long dash line. The intersection between this line and the level of the manganese content determines the final carbon content in austenite.

Fig. 12 Schematic isothermal sections of the Fe-C-Mn showing the solute redistributions under a) local equilibrium (PE) b) negligible partitioning local equilibrium (NPLE) The long dash line is the carbon isoactivity line. *ef* and *cd* are tie lines. The dark filled black circle indicates the bulk composition.

This mode of equilibrium is sometimes called quasi-paraequilibrium, for example, in Hillert's text book [Hil99].

a)

It was reported [Faz05] that the transformation does not follow a single approach. It is shifted from the PE at the beginning to NPLE and finally to LE.

b)

2.6 Martensite transformation

Martensite formation is widely accepted that it is a diffusionless transformation. It consists of very rapid nucleation and growth that the transformation time can be neglected. Moreover, it is well established that it is athermal transformation, namely, the fraction transformed does not depend on time but only the difference between the martensite transformation start temperature and the current temperature. The most common way to calculate the martensite fraction at a specific temperature is by utilising the Koistinen-Marburger law [Koi59] as follows:

$$m_{KM}(T, C_\gamma) = 1 - e^{-C_{KM}(M_s(C_\gamma) - T)} \quad \text{Eq.47}$$

M_s is the martensite start temperature. C_γ is the carbon content in austenite. The constant C_{KM} is taken usually as 0.011 for steels [Koi59] as it was derived by pure iron-carbon. Almost every literature follows this equation form. At most other coefficients are proposed [Hou78, Wil87].

The M_s temperature is a function of chemical composition, which is generally derived by regression analysis [And65, Bra75, Kul80, Kun98, Lor04] and is summarised in Table 2.6 together with B_s temperature (bainite start temperature). The most important element on the M_s temperature is carbon as can be seen from the coefficient in the empirical equations. In the hot rolled DP steels, it corresponds to the carbon content of the enriched remaining austenite after the ferrite formation. It is obvious from the Koistinen-Marburger law that in many cases, the entire remaining austenite will not transform into martensite except at very low temperatures, in other words, sub-zero temperatures. The untransformed austenite is termed '*retained austenite*'.

The driving force of the nucleation of martensite is related to the T_0 locus as

$$\Delta G^{\gamma \rightarrow \alpha} = \Delta H^{\gamma \rightarrow \alpha} \frac{(T_0 - M_s)}{T_0} \quad \text{Eq.48}$$

T_0 is the locus where austenite and the product phase (martensite in this case) have the same composition and free energy. $\Delta H^{\gamma \rightarrow \alpha}$ represents the enthalpy change.

2.7 Bainite transformation

Bainite can be regarded as the most complicated microstructure in steels. In German language, it is also called '*Zwischenstufe*' which means '*the stage in between*' due to the fact that its transformation temperature lies in between that of pearlite and of martensite. Its transformation has both diffusional growth and shear. It composes of 2 components: sheaf of ferrite platelets and carbide (or other carbon rich second phases), which can either precipitate in the ferrite platelets or outside. In the so-called upper bainite, which forms at relatively higher temperatures, the second phases precipitate between the ferrite platelets. In contrast, the carbide precipitates inside the ferrite plates in lower bainite.

The physically-based microscopic modelling can be therefore divided into 2 approaches: nucleation-controlled and diffusion-controlled models. Both have a number of followers but the latter got more attention in the recent years after the initiation by Bhadeshia [Bha82] and improved several years later by Rees and Bhadeshia [Ree92, Ree92b]. Under the diffusion-controlled approach, the final volume fraction of bainitic ferrite can be straightforwardly deduced by the carbon content of the steel. It works well if the growth of bainitic ferrite and the carbide precipitation are simultaneous. But an additional mechanism such as solute drag by molybdenum needs to be introduced to take into account the observed transformation arrest. On the other hand, the maximum amount of bainitic ferrite under the nucleation-controlled approach is calculated by means of the T_0 locus [Tak91]. It has been found that the carbon content in the retained austenite observed by experiments is closed to that calculated from the T_0 locus [Jac02, Mat02]. This approach focuses on the displacive and diffusionless formation of the bainitic ferrite platelet, which is also called sub-unit. It is believed that the overall transformation rate is controlled purely by the nucleation of the sub-units as its growth is fast enough and can be considered to be '*instantaneous*'. The primary sub-units originate from austenite grain boundaries. New sub-units form continuously at the tip of the previous sub-units. As the nucleation proceeds, the austenite matrix is more enriched in carbon and results in carbide precipitation. Several models for bainite transformation from the literature are tabulated in Table 2.5. The B_s temperatures from the literature are listed together with the M_s temperatures in Table 2.6.

Table 2.5 Summary of recent bainite kinetics models [Gro08].

Model and related references	Year	Controlling process	Type of heat-treatment	Carbide precipitation	Chemical composition limitations	Comments
Rees-Bhadeshia [Ree92]	1992	Nucleation control	Isothermal	No	Si + Al > 1%*	Accounts for autocatalytic nucleation, austenite grain size, incomplete reaction phenomenon, does not provide quantitative information for M ₃ C
Quidort-Brechet [Qui02], [Qui01, Qui02b]	2002	Diffusion control	Isothermal & continuous cooling	No	Si + Al > 1%*	Calculated α_B sub-unit growth-rates significantly higher than experimental, does not account for incomplete reaction phenomenon, does not provide quantitative information for M ₃ C
Matsuda-Bhadeshia [Mat04]	2004	Nucleation control	Isothermal & continuous cooling	No	Si + Al > 1%*	Accounts for autocatalytic nucleation, austenite grain size, incomplete reaction phenomenon, does not provide quantitative information for M ₃ C
Azuma et al. [Azu05]	2005	Nucleation control	Isothermal	Yes	Fundamentally none	Accounts for autocatalytic nucleation, incomplete reaction phenomenon, sub-unit refinement, calculates vol. fraction, size & distribution of carbides, identifies upper & lower bainite

Model and related references	Year	Controlling process	Type of heat-treatment	Carbide precipitation	Chemical composition limitations	Comments
Gaude-Fugarolas-Jacques [Gau06]	2006	Nucleation control	Isothermal	No	Si + Al > 1% *	Accounts for autocatalytic nucleation, austenite grain size, incomplete reaction phenomenon, does not provide quantitative information for M ₃ C
Katsamas [Kat08]	2006	Nucleation control	Isothermal	No	Si + Al > 1% *	Semi-empirical model for calculation of retained austenite in multiphase TRIP steels, can calculate vol. fraction of α_B indirectly

* Since these models neglect carbide precipitation, they would be more realistically applicable in steels containing Si and/or Al in excess of 1% mass, in order for cementite precipitation to be drastically suppressed.

2.7.1 Thermodynamics modelling for the non-equilibrium phases

The critical temperatures for all the phases deviated from (ortho)equilibrium, although not straightforward, are also possible with the CALPHAD approach. The calculations of the bainite start temperature (B_s) and martensite start temperature (M_s) as well as the start temperature of the Widmanstätten ferrite (W_s), are also suggested in the literature [Bha01, Lee92]. It can be done either by common tangent, parallel tangent and diffusionless transformation concept, depending on how a scientist defines his system.

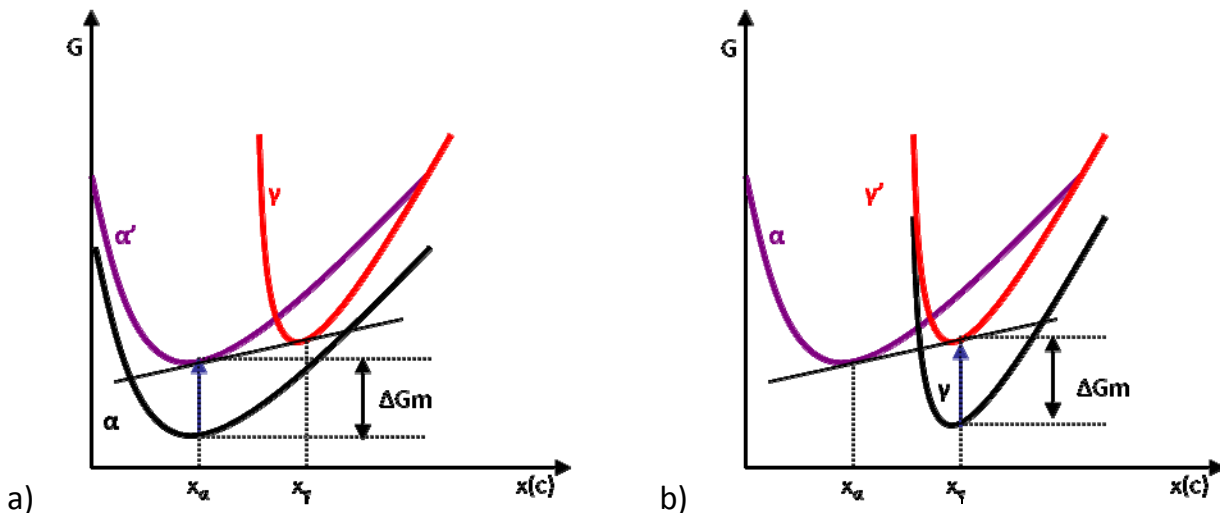


Fig. 13 The parallel tangent concept a) for example in case of bainite and Widmanstätten ferrite formation, in which the product phase has an additional stored energy b) for example in case of the deformed austenite, in which the parent phase contains a stored energy

The parallel tangent concept comes into the play when the product phase is defined to contain some stored energy, in comparison with the closest equilibrium phase, or when the parent phase is defined to contain additional free energy. The former case is therefore applied to the case of Widmanstätten ferrite and bainite transformation according to some researchers [Lee92]. They are considered to store some extra energy compared with ferrite, as illustrated in Fig. 13a. The latter case can be applied to, for example, the austenite with retained strain, which results in the increase in A_{e3} . This case is shown in Fig. 13b. The stored energies in Widmanstätten ferrite and bainite were proposed by Nanba [Nan90, Lee92] to be 300 and 600 J/mol, respectively. On the other hand, the stored energy in the austenite depends on the magnitude of the retained strain.

This approach can be also considered as the method to calculate the maximum change in free energy between 2 phases [Hil99]. In this case, it can be proven that:

$$-\Delta G_m = G_{Fe}^{\gamma} - G_{Fe}^{\alpha} = G_C^{\gamma} - G_C^{\alpha} \quad \text{Eq.49}$$

Bhadeshia [Bha01] employs this approach for the nucleation of both bainite and Widmanstätten ferrite and established the so-called universal nucleation function, which is the criterion for their nucleation as follows:

$$\begin{aligned} G_N &= C_1(T - 273.18) - C_2 \text{ J/mol} & \text{Eq.50} \\ C_1 &= 3.637 \pm 0.2 \text{ J/mol.K} \\ C_2 &= 2540 \pm 120 \text{ J/mol.K} \end{aligned}$$

and the nucleation follows if $\Delta G_m < G_N$.

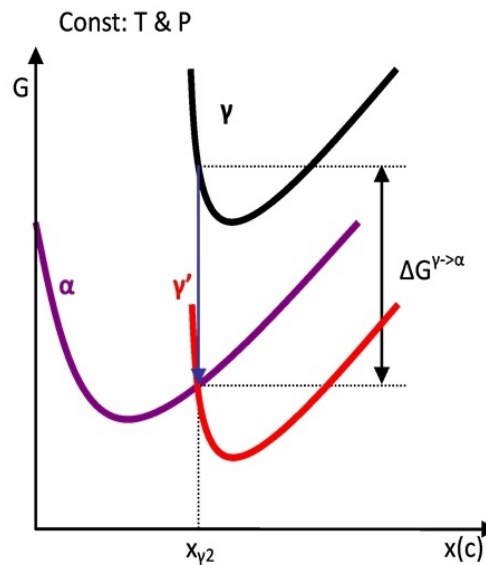


Fig. 14 The diffusionless transformation approach

He defines the growth of bainite as diffusionless. But if it does not sustain, it will allow the diffusional growth of the Widmanstätten ferrite. In this case, he employs the common tangent method with the free energy of transformation ($-\Delta G_m^{\gamma \rightarrow \gamma' + \alpha}$) of 50 J/mol.

The last approach is for the diffusionless transformation, where the parent and the product phases have the same composition. It can therefore be described as in Fig. 14. Porter [Por92] described the martensite transformation with this approach. The change in

the free energy for martensite transformation was reported by Guénin [Gué79] to be 1260 J/mol. The bainite transformation by Bhadeshia follows this method and is assumed to have a stored energy of 400 J/mol.

Table 2.6 The empirical bainite and martensite start temperatures from the literature.

Authors	Steel, mass%	Ref.	Equations, °C	No.
Suehiro	Low C and C-Mn	Sue87	$B_s = 718 - 425 C - 42.5 Mn$	Eq.50
Zhao and Zha	No accurate information	Zha92	$B_s = 720 - 585.63 C + 126.6 C^2 - 66.34 Ni + 6.06 Ni^2 - 0.232 Ni^3 - 31.66 Cr + 2.14 Cr^2 - 91.68 Mn + 7.82 Mn^2 - 0.3378 Mn^3 - 42.37 Mo + 9.16 Co - 0.1255 Co^2 + 0.000284 Co^3 - 36.02 Cu - 46.15 Ru$	Eq.51
Li	0.2-0.41 C	Li98	$B_s = 637 - 58 C - 35 Mn - 34 Cr - 15 Ni - 41 Mo$	Eq.52
Kunitake and Okada	0.11-0.56C	Kun98	$B_s = 732 - 202 C - 85 Mn - 47 Cr - 37 Ni - 39 Mo - 216 Si$	Eq.53
Lee	0.1-0.8 C	Lee02	$B_s = 745 - 110 C - 59 Mn - 39 Ni - 68 Cr - 106 Mo + 17 Mn Ni + 6 Cr^2 + 29 Mo^2$	Eq.54
Kirkaldy	0.1-0.55C	Kir83	$B_s = 656 - 58 C - 35 Mn - 75 Si - 15 Ni - 34 Cr - 41 Mo$	Eq.55
Steven and Haynes	0.1-0.55C	Ste56	$B_s = 830 - 270 C - 90 Mn - 37 Ni - 70 Cr - 83 Mo$ $M_s = 561 - 474 C - 33 Mn - 17 Cr - 17 Ni - 21 Mo$	Eq.56
Andrews	$\leq 0.6C, \leq 4.9Mn,$ $\leq 5.0Cr, \leq 5.0 Ni,$ $\leq 5.4Mo$	And65	$M_s = 539 - 423 C - 30.4 Mn - 17.1 Ni - 12.1 Cr - 11.2 Si - 7.0 Mo$	Eq.57
Carapella	0.0-5.0C, Mn, Si, Cr, Mo, Ni, W, Co	Car44	$M_s = 494(1 - 0.62 C)(1 - 0.092 Mn)(1 - 0.033 Si)(1 - 0.045 Ni)(1 - 0.07 Cr - 0.029 Mo - 0.018 W - 0.012 Co)$	Eq.58

Authors	Main alloying elements, mass%	Ref.	Equations, °C	No.
Eldis	0.1-0.8C, 0.35-1.80Mn, <1.50Si, <0.90Mo, <1.50Cr, <4.50Ni	Bar82	$M_s = 531 - 391.2 C - 43.3 Mn - 21.8 Ni - 16.2 Cr$	Eq.59
Grange and Stewart	0.29-1.02C, 0.29-1.85Mn, 0.15-0.70Si, 0.2-3.41Ni, 0.4-1.41Cr	Gra46	$M_s = 538 - 350 C - 37.7 Mn - 18.9 Ni - 27 Mo$	Eq.60
Kulmburg	0.1-1.1C, 0.25-0.5Si, 0.35-1.45Mn, 11-17.7Cr, 0.05-1.65Mo, 0.25-2.45Ni, 0.01-0.35V	Kul80	$M_s = 492 - 125 C - 65.5 Mn - 10 Cr - 29 Ni$	Eq.61

Authors	Main alloying elements, mass%	Ref.	Equations, °C	No.
Lorenz	0.01-0.919C, 0.005-1.74Si, 0.017-4.5Mn, 0.011-3.67Cr, 0.01-4.15Mo	Lor04	$M_s = 506.6 - 338.7 C - 18.3 Mn - 14.5 Cr + 1.3 Si$	Eq.62
Nehrenberg	0.17-1.28C, 0.29-1.21Mn, 0.15-1.89Si, 0.1-3.41Ni, 0.05-8.81Cr, 0.03-0.33Mo, 0.0-0.16V	Neh46	$M_s = 499 - 292 C - 32.4 Mn - 16.2 Ni - 22 Cr - 10.8 Si - 10.8 Mo$	Eq.63
Rowland and Lyle	0.35-1C	Row46	$M_s = 499 - 324 C - 32.4 Mn - 27 Cr - 1632 Ni - 10.8 Si - 10.8 Mo - 10.8 W$	Eq.64

3 LABORATORY PROCESS SIMULATION

3.1 Material selection, melt production and sample preparation

In this work, two DP steels will be mentioned. Their chemical compositions are listed in Table 3.1

Table 3.1 The chemical compositions of the investigated DP steels, mass%

Material Name	C	Si	Mn	P	S	Cr	Mo
Mn-Mo DP	0.073	0.03	1.44	0.004	0.002	0.02	0.150
Mn-Si DP	0.064	0.41	0.93	0.005	0.002	0.48	0.005

The molybdenum containing grade, whose composition is similar to those in the cold rolled DP steel grades, was selected especially for the modelling so that the ferrite transformation kinetics is rather retarded. The effect of the processing temperatures as well as the retained strain on the transformation kinetics is expected to be more obvious. It also serves the purpose to evaluate the possibility to produce hot rolled DP steel from a cold rolled grade. The Mn-Si DP concept acts as the opposite case as the ferrite formation kinetics is expected to be much more favourable as both chromium and silicon are ferrite formers

Both steel grades were produced at the Department of Ferrous Metallurgy, RWTH Aachen University, in a vacuum furnace. This furnace operates with a middle frequency of 2 kHz and a maximum power of 100 kW. At room temperature, the vacuum chamber can achieve a pressure of 10^{-5} bar. The ingots had the weight of 80 kg and the dimensions of $520 \times 140 \times 140 \text{ mm}^3$. The top part of the ingots where obvious shrinkage appeared was discarded. They were forged and rolled into intermediate bars with the dimensions of $430 \times 70 \times 23 \text{ mm}^3$ at the Institute for Metal Forming (IMF), TU Bergakademie Freiberg, and prepared further to the samples with dimensions according to Table 3.2

Table 3.2 Summary of the samples used, classified by experiments

Size of final samples	Preparation method	Experiment
Cylindrical samples, $\varnothing 5 \text{ mm} \times 10 \text{ mm}$	Machining	Transformation kinetics with/without deformation in dilatometer (Baehr DIL-805A/D)
Flat samples, $7 \times 4 \times 1 \text{ mm}^3$		Transformation kinetics without deformation in dilatometer (Baehr DIL-805A/D)
		Austenite grain size determination
Cylindrical samples, $\varnothing 10 \text{ mm} \times 15 \text{ mm}$		Double hit test at hot deformation Simulator (Schlenck)
Rectangular samples, $70 \times 20 \times 8 \text{ mm}^3$		Plane strain hot deformation simulation at a plane strain hot deformation simulator (TTS820)
Bar, $90 \times 55 \times 9.5 \text{ mm}^3$	Rolling	Rolling experiment

3.2 Process simulation in deformation dilatometer

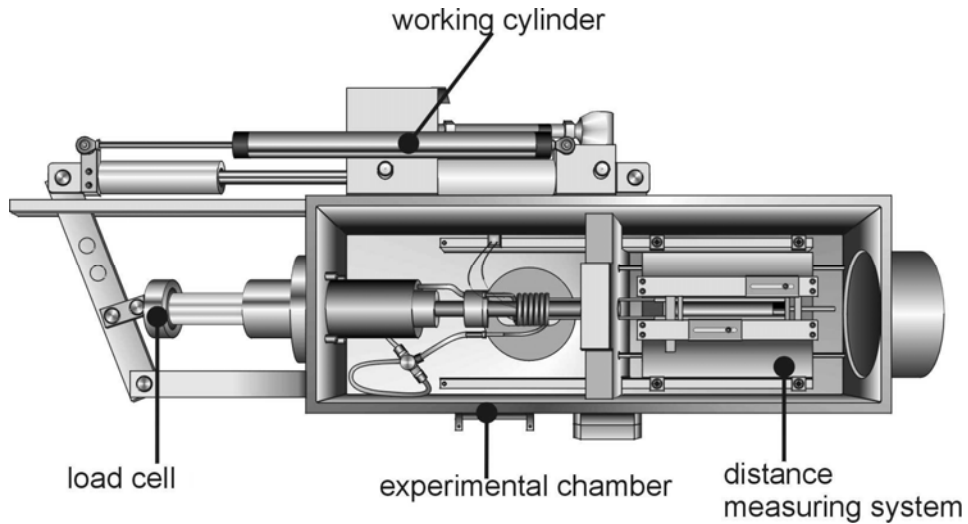


Fig. 15 A drawing of the deformation dilatometer (Baehr DIL-805A/D)

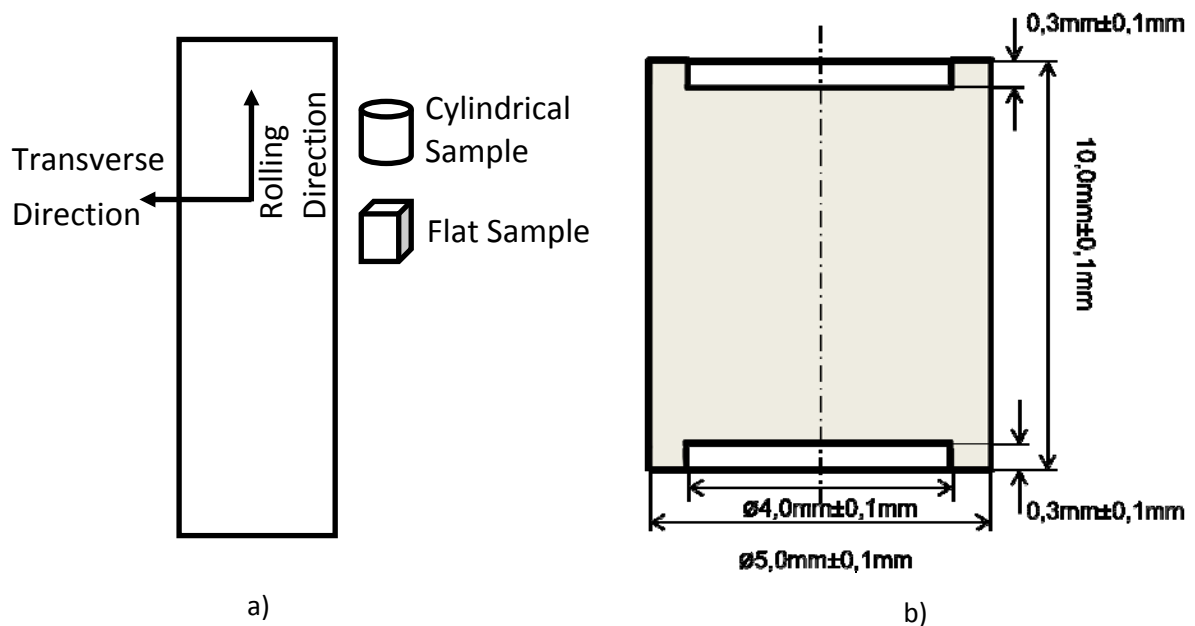


Fig. 16 The description of the dilatometer samples. a) The orientation of the samples along the intermediate bars. b) The drawing of cylindrical dilatometer samples showing the space on the top and bottom sides where the glass powder lubricant is put in.

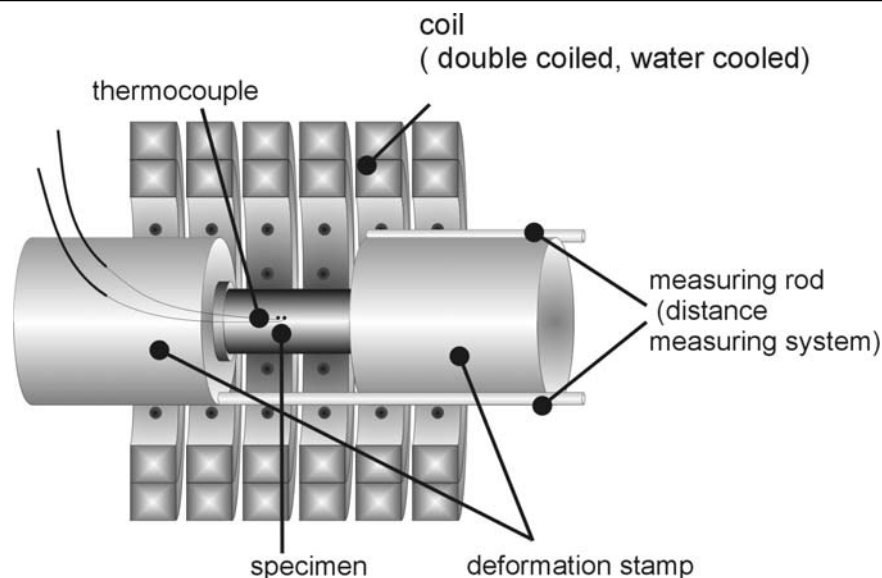


Fig. 17 A drawing depicting the layout of the experiment chamber in the deformation dilatometer. A cylindrical sample is shown in this picture.

Firstly the rough hot rolling process window for each steel grade was determined by trial and errors in a deformation dilatometer (Baehr DIL-805A/D, Fig. 15) with numerous combinations of austenite conditioning i.e. different austenitisation temperatures and durations as well as different degrees of deformation. The deformation varied from none to 4 steps of deformation with total logarithm strain of 1.2, which is the maximum logarithm strain allowed in the machine.

Cylindrical samples with a diameter of 5 mm and a length of 10 mm must be used in cases of having deformation. But flat samples with dimensions of $7 \times 4 \times 1 \text{ mm}^3$ were used in case of no deformation or if an extremely high cooling rate was necessary. As shown in Fig. 16, cylindrical samples have some space on the top and bottom faces, where glass power lubricant was put into to reduce the friction and facilitate a homogenous deformation. A molybdenum platelet was also put topmost on each side of the samples for the same purpose. Also shown in Fig. 17, a thermocouple was spot-welded to the middle of the length of the sample to record the thermal history during the experiments and allow the temperature control of the samples. In the same fashion, a thermocouple was welded to the middle of the face of the flat samples.

Owed to the inert gas atmosphere used in the machine, the samples is protected from oxidation and can be also quenched with the gas with a cooling rate up to $600 \text{ }^\circ\text{C/s}$ in flat geometry, $100 \text{ }^\circ\text{C/s}$ in non-deformed cylindrical geometry (or heavily deformed (bulged)

cylindrical samples in the modernised Baehr DIL-805A/D) and 70 °C/s in heavily deformed (bulged) cylindrical geometry in the old Baehr DIL-805A/D. Helium was used for higher cooling rate and argon was used for general cases. The pressure in the experiment chamber was 5×10^{-2} Pa or 5×10^{-4} mbar.

The simplest experiments started with different austenitisation temperatures with at most a single deformation step as shown as *Option A* in Table 3.3. *Option B* has been done to make a trial and error to transfer to the rolling experiment on a pilot 4-stand rolling mill. The most promising sets of parameters, which realise the DP steel microstructure within the process window of the pilot rolling mill, were selected and separated as *Option D: 'Rolling Option'*.

The thermomechanical cycles are schematically illustrated in Fig. 18. For all cases, the last deformation step, ε_5 , was intended to be under the recrystallisation stop temperature, T_{nr} . The thermal cycle was then held at different isothermal temperatures, T_{ROT} , and for different durations, t_{ROT} , in the γ - α intercritical region. The determination of the austenite grain size after reheating (T_1, t_1) will be explained in section 3.2.1. The samples under

Table 3.3 Summary of the thermomechanical cycles carried out in the deformation dilatometer according to the Fig. 18.

	<u>Option A:</u> Different D_γs from Reheating	<u>Option B:</u> Different D_γs from Repeated Recrystallisations	<u>Option C:</u> Large D_γs	<u>Option D:</u> Rolling Option
\dot{T}_1, T_1, t_1	200 °C/minute; 900/950/1000/1050/1100/ 1150/1200 °C; 120, 300, 600, 900 s	200 °C/minute; 1150 °C; 900 s	200 °C/minute; 1200 °C; 300 s	200 °C/minute; 1150 °C; 900 s
\dot{T}_2, T_2, t_2	-	4.3 °C/s; 1100 °C; 3 s	5 °C/s; 1150 °C; 3 s	4.3 °C/s; 1100 °C; 3 s
$\varepsilon_2, \dot{\varepsilon}_2$	-	0.2; 5 s ⁻¹	0.2; 5 s ⁻¹	0.2; 5 s ⁻¹
\dot{T}_3, T_3, t_3	-	15 °C/s; 1000 °C; 3 s	-	15 °C/s; 1000 °C; 3 s
$\varepsilon_3, \dot{\varepsilon}_3$	-	0.4; 12 s ⁻¹	-	0.4; 12 s ⁻¹
\dot{T}_4, T_4, t_4	-	30 °C/s; 950 °C; 3 s	-	30 °C/s; 950 °C; 3 s
$\varepsilon_4, \dot{\varepsilon}_4$	-	0.3; 12 s ⁻¹	-	0.3; 12 s ⁻¹
\dot{T}_5, T_5, t_5	50 °C/s; 900 °C; 3 s	50 °C/s; 900 °C; 3 s	4.3 °C/s; 830°C; 3 s	50 °C/s; 900 °C; 3 s
$\varepsilon_5, \dot{\varepsilon}_5$	0.0-0.9; 12 s ⁻¹	0.0-0.3; 12 s ⁻¹	0.0-0.6; 12 s ⁻¹	0.3; 12 s ⁻¹
$\dot{T}_{ROT}, T_{ROT}, t_{ROT}$	60 °C/s; 680°C; 0-10 s	60 °C/s; 600-800°C; 0-10 s	60 °C/s; 680 °C; 3, 7 s	60 °C/s; 680°C; 7 s
\dot{T}_{coil}	5-270°C/s	5-100 °C/s	60 °C/s	60 °C/s

cycles with deformation were further proved for the recrystallisation as will be explained in section 3.2.2 and modelled in 5.2.

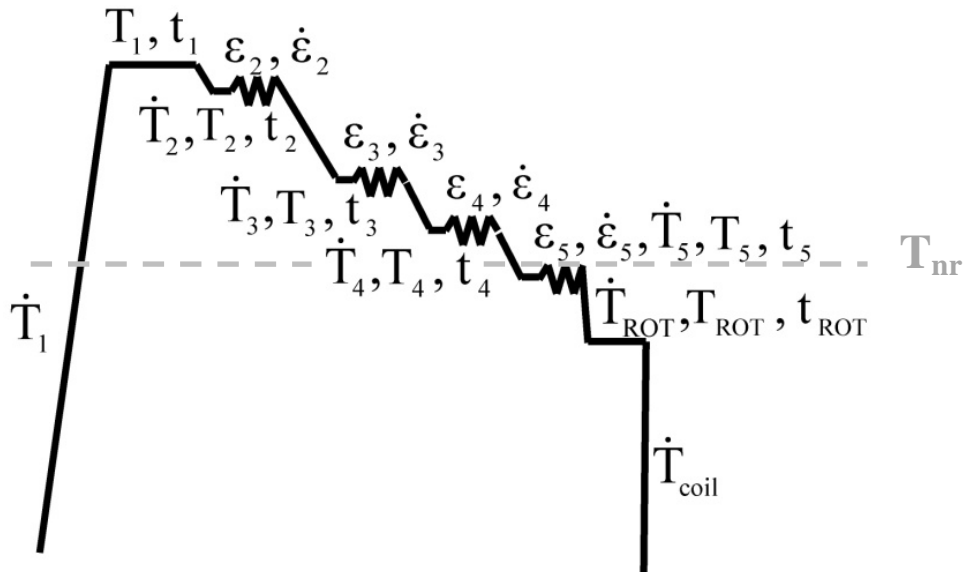


Fig. 18 The thermomechanical cycles carried out in the deformation dilatometer

For an easy understanding, the through process simulation is separated into austenitisation, recrystallisation and ferrite formation respectively and described in the following sections and chapter 4.

3.2.1 Austenite grain size determination

The initial austenite grain size was determined by different methods as follows:

- *Quenching and etching method*: for general cases
- *Ferrite decoration method*: for large austenite grain sizes
- *Oxidation method*: for a very small austenite grain size
- *Measurement of recrystallised fraction and calculation with an empirical equation (Eq.16)*: for the austenite grain sizes created by repeated recrystallisations between the deformation passes

Good results in this section were striven for due to the fact that the prior austenite grains (PAGs) in such the low carbon steels cannot be always simply revealed by quenching and etching. Revealing the recrystallised grain sizes are the most difficult because it must be tested with cylindrical samples, in which the cooling rates obtained after being heavily deformed reach only 60 °C/s. This level of cooling rate provokes the formation of low carbon bainite which obscures the prior austenite grain boundaries significantly. Slower cooling rates induce some ferrite transformation.

Cases having large prior austenite grain sizes were additionally revealed by the ferrite decoration method, by which the grain boundaries are visualised after little ferrite formation as the grain boundaries are nucleation sites. On the other hand, a very small grain size in Mn-Si DP steel was additionally observed by means of the oxidation method.

Quenching and etching method

Small flat samples (dimensions of 7×4×1 mm³) were austenitised by reheating in the dilatometer to different temperatures, T_1 , with a heating rate of 600 °C/minute and held for different durations, t_1 , as shown in Table 3.4. Then they were quenched with helium with a cooling rate as high as 600 °C/s. Finally, the samples were annealed at 550 °C for 20 hours in a salt bath to promote the carbon diffusion to the grain boundaries. The details of the metallographic work will be described in section 3.5.1.

Table 3.4 The experiment plan for determining the initial austenite grain sizes

Reheating temperature, °C (T_1)	Reheating time, s, (t_1) for Mn-Mo DP	Reheating time, s, (t_1) for Mn-Si DP
900	-	300
950	300	120, 300
1000	300	120, 300
1050	300	300
1100	300, 600, 900	300, 900
1150	300, 600, 900	300, 600, 900
1200	300, 600, 900	300, 600

Ferrite decoration method

After the austenitisation, the samples were cooled down to the intercritical temperatures and held shortly as only ferrite transformation at the grain boundaries is expected. Finally the samples were quenched with helium so that the transformation was ceased.

Oxidation method

Only the case of Mn-Si steel austenitised at 900 °C for 300 s was further performed by this method as it is the most time consuming. Oxygen was let in at the latter stage of austenitisation. The best combination of oxidation duration and air pressure was searched for by trial and errors. Cylindrical dilatometer samples were ground until a small flat area was achieved. It was further polished with diamond suspension to a 1 µm finish. This polished flat surface on a side of cylindrical samples will be observed the grain size.

3.2.2 Determination of the recrystallised fraction and the grain size after recrystallisation

Proof for dynamic recrystallisation

The dynamic recrystallisation was analysed only from the flow curves during the deformation. The curves were taken from the hot compression simulator (Schenck, Fig. 16). If no plateau or no drop appeared in the curves, the dynamic recrystallisation was neglected.

Measurement of static recrystallisation

The recrystallised fraction between deformation steps was analysed from double hit tests carried out in the above mentioned hot compression simulator (Schenck) for each rolling temperature. It gives superior quality of flow curves to that obtained by the deformation dilatometer (Baehr DIL-805A/D) in that the elastic part of the flow curve is obvious. The evaluation of the double hit tests is shown schematically in Fig. 20. The time between hits was varied to measure different softening fraction, F_s , which was calculated by [Tam88] as follows

$$F_s = \frac{\sigma_m - \sigma_2}{\sigma_m - \sigma_1}. \quad \text{Eq.65}$$

The statically recrystallised fraction was measured from the softened fraction, subtracted by the recovered fraction. The double hit tests were carried out at the temperature at each rolling pass and employed to characterise the recrystallisation kinetics at isothermal temperatures.

The yield point of each deformation step was determined at the intersection of the stress-strain curve and a line parallel to the elastic part of the curve shifted by an offset of 0.2% along the strain axis as shown in Fig. 20(b). Then both the fractions of recovery of 0.2 and 0.25 were deducted from total softening fraction. Therefore, the fraction recrystallised can be compared between both criterions. The fraction recrystallised, F_x , is calculated as

$$F_x = \frac{F_s - 0.2}{0.8}$$

Eq.66

The deformation temperatures and interpass times for the double hit tests are shown in Table 3.5.

temperature range (°C)	RT - 1500
heating rate (K/s)	1 - 100
cooling rate (K/s)	0.01 - 60
heating source	inductive
heating power (kW)	15
max. deformation force (kN)	160
max. equivalent strain	1.2
deformation rate (1/s)	0.001 - 30
min. delay time (s)	0.1
cross head rate (mm/s)	500

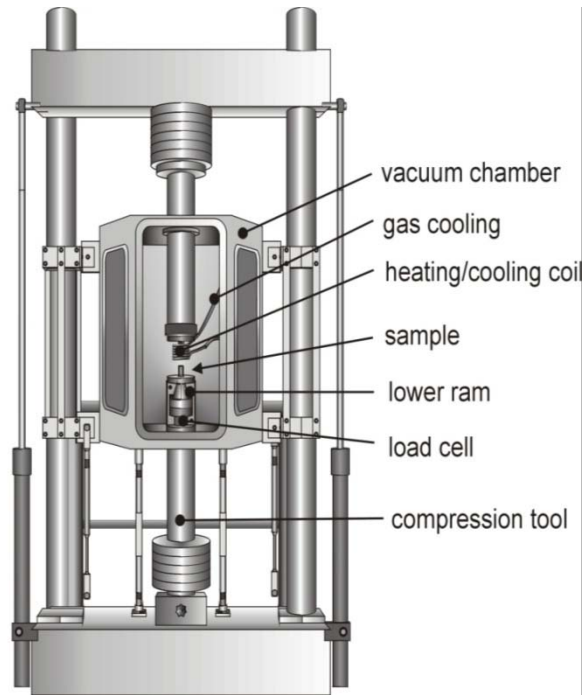


Fig. 19 The hot compression simulator (Schenck)

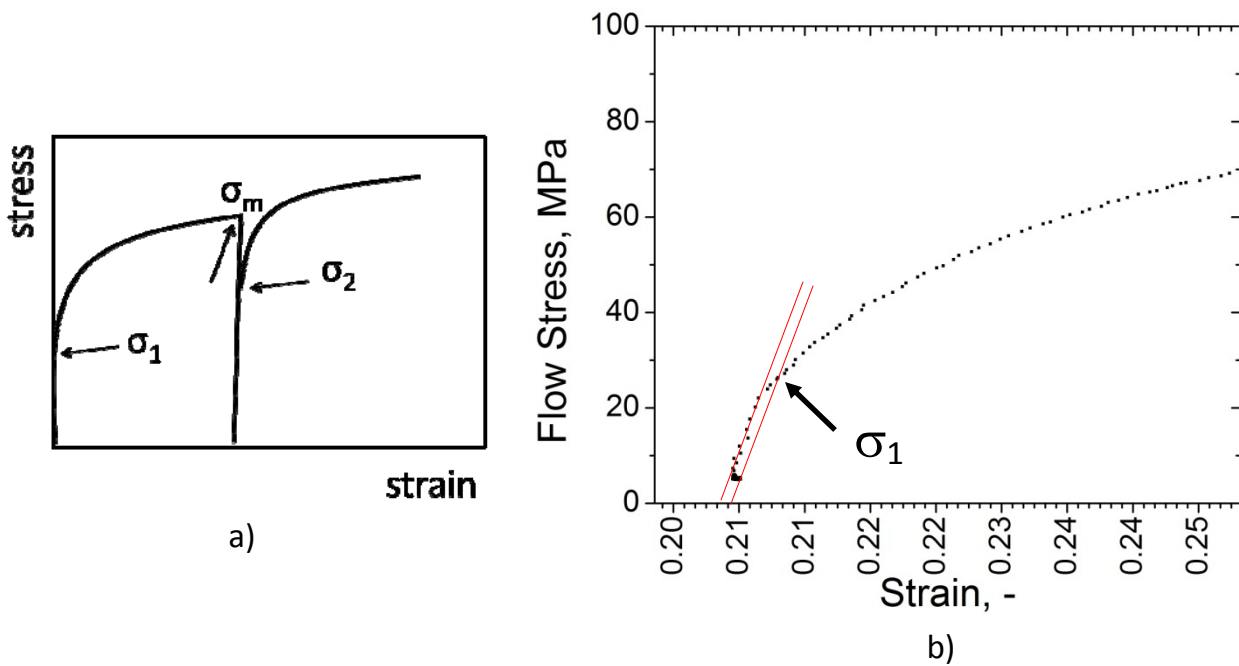


Fig. 20 The evaluation of the double hit tests. (a) σ_1 and σ_2 represent the yield strength from the first and second hit, respectively. σ_m represents the maximum stress from the first hit. (b) The offset method used for measuring the yield strength.

Table 3.5 The summary of the testing conditions of the double hit tests

Temperature, °C	Interpass time for Mn-Mo DP	Interpass time for Mn-Si DP
1100	3, 10, 50 s	3, 10, 50 s
1000	3, 10, 50 s	3, 10, 50 s
950	3, 10, 50 s	3, 10 s

3.2.3 The flow curve for the calculation of the stored energy in austenite

The flow curve of the last deformation step (Fig. 18), which lies in the non-recrystallisation temperature region was measured from the deformation dilatometer. It is useful for the calculation of the stored energy in austenite (section 5.1.2.1 and 5.6.1)

3.2.4 Ferrite formation kinetics

All samples under the thermomechanical cycles in Table 3.3 were measured for the phase fraction. The ferrite formation kinetics were obtained by plotting the ferrite fraction with their isothermal transformation times. Some were further analysed for the ferrite grain size.

3.2.5 The hardenability of austenite after the carbon partitioning

The carbon partitioning after the ferrite formation totally changes the hardenability in the remaining austenite and is expected to enable the martensitic transformation and avoid the bainitic to realise the DP steel microstructure. This cannot be measured from the traditional CCT diagrams which observe the transformation kinetics from a fully austenitic state. But it can be investigated only by a continuous cooling after different amount of ferrite formations and after ferrite formation has stopped, which result in different degrees of carbon enrichment in the remaining austenite, with different cooling rates. The combination of ferrite fractions and the cooling rates for this investigation is listed in Table 3.6. The cooling rates here are averages from 600°C down to 200 °C. As the ferrite takes a volume of 50-80% of the samples, the signals achieved by dilatometry during further phase transformations to martensite and/or bainite are rather weak. The hardenability was therefore deduced from the martensite and bainite fraction by metallographic observation. It was represented here as '*modified CCT diagrams*', in which the critical temperatures were calculated from the empirical equations. The bainite start temperature was taken from Lee (Eq.54) [Lee02]. The martensite start temperature was taken from Lorenz (Eq.62) [Lor04]. The martensite finish temperature (Mf) was taken to be 215 °C lower than the calculated martensite start temperature (Ms) [Pet70].

Table 3.6 The varying amount of ferrite and the cooling rates for the measurement of the hardenability of the remaining austenite after different degrees of carbon partitioning. The cooling rates were measured from 600 °C to 200 °C.

Ferrite fraction	Cooling rate, °C/s	
	Mn-Mo DP	Mn-Si DP
0.5	-	57, 263, 287
0.6	-	262, 284
0.7	7, 27, 48, 60	50, 53, 58, 95, 262
0.8	7, 40, 60	49, 58, 60, 96, 274
0.9	-	6, 22, 34, 47, 62, 97

3.3 Process simulation in 4-stand rolling line

The pilot scale hot rolling was performed at the Institute for Metal Forming (IMF), TU Bergakademie Freiberg, whose rolling line is depicted in Fig. 21. The best hot rolling parameters with multiple deformation steps proven by the deformation dilatometer were selected for this (*Option D: 'Rolling Option'* in Table 3.3). The hot rolling experiment started with reheating the bars with dimensions of $90 \times 55 \times 9.5 \text{ mm}^3$ at 1150°C for 15 minutes, followed by mechanical descaling. It was followed by rolling in the above mentioned rolling mill to a thickness of 3.5 mm.

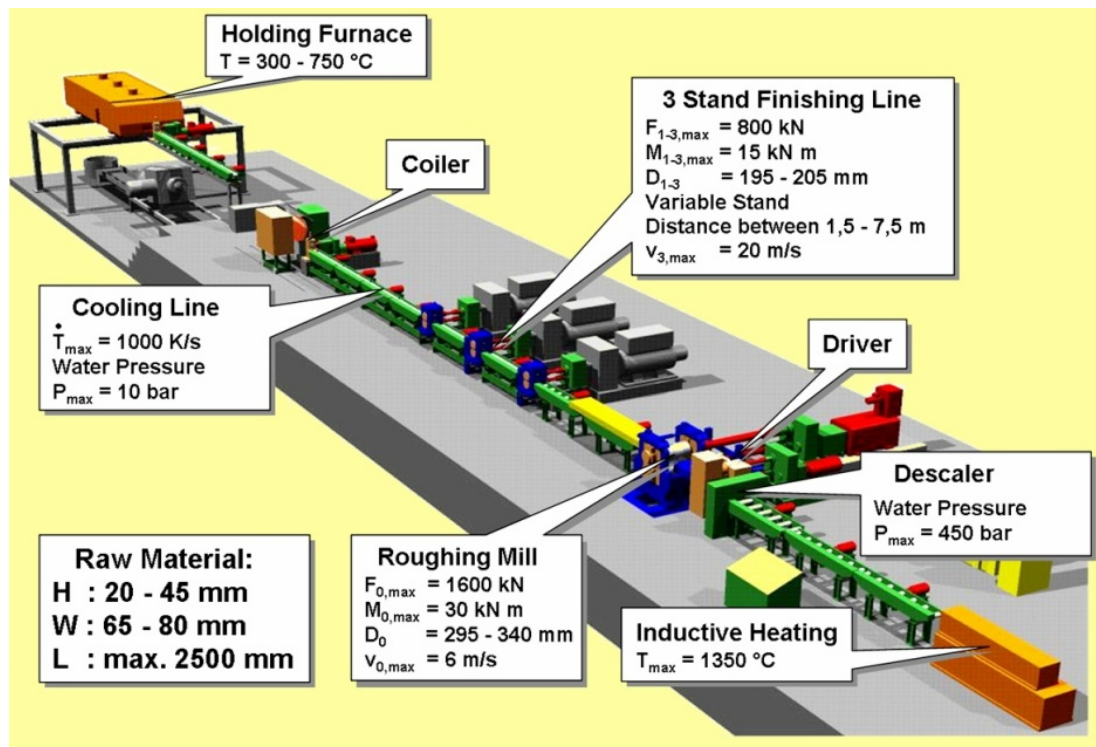


Fig. 21 The configuration of the pilot rolling mill at IMF, TU Bergakademie Freiberg. The bars were bypassed from the induction furnace to the roughing mill manually. The rolled strips were quenched into a water bath at the end of the cooling line.

All the experimental heating/rolling parameters are shown in Table 3.7. The rolled strips were transported through four sections of the cooling line. Each section has a length of 1600 mm. The cooling water only in the first cooling section was turned on. Therefore the first section will be mentioned as '*cooling line*' while the other three sections will be named as '*ROT*'.

Table 3.7: The rolling parameters adopted into the hot rolling experiments. The time for each rolling pass means the interpass time after that pass.

Materials	Parameters	Reheating	Pass1 (F0)	Pass2 (F1)	Pass3 (F2)	Pass4 (F3)	Cooling Line	ROT
Mn-Mo DP	Temperature, °C	1150	1100	1000	950	900	-	680
	Time, s	900	10	3	3	0.5	1.5	7
	Strain (ε_{thick}), -	-	0.173	0.346	0.26	0.26	-	-
	Equivalent Strain (ε_{eq}), -	-	0.2	0.4	0.3	0.3	-	-
	Strain rate ($\dot{\varepsilon}_{thick}$), s ⁻¹	-	4.96	11.76	12.36	14.07	-	-
	Initial Thickness, mm	9.5	9.5	8.0	5.7	4.4	3.4	3.4
	Rolling speed, m/s	-	0.5	0.8	0.8	0.8	-	-
	Water amount, l/minute	-	-	-	-	-	143	-
	Predicted Austenite Grain Size (D_γ), μm	100	72	42	34	-	-	-
	S_v , mm ⁻¹	-	-	-	-	70	-	-

(Int. No.090722_2)

Materials	Parameters	Reheating	Pass1 (F0)	Pass2 (F1)	Pass3 (F2)	Pass4 (F3)	Cooling Line	ROT
Mn-Si DP	Temperature, °C	1150	1100	1000	950	900	-	680
	Time, s	900	10	3	3	0.5	1.5	7
	Strain (ε_{thick}), -	-	0.173	0.346	0.26	0.26	-	-
	Equivalent Strain (ε_{eq}), -	-	0.2	0.4	0.3	0.3	-	-
	Strain rate ($\dot{\varepsilon}_{thick}$), s ⁻¹	-	4.96	11.76	12.36	14.07	-	-
	Initial Thickness, mm	9.5	9.5	8.0	5.7	4.4	3.4	3.4
	Rolling speed, m/s	-	0.5	0.8	0.8	0.8	-	-
	Water amount, l/minute	-	-	-	-	-	140	-
	Predicted Austenite Grain Size (D_γ), μm	270	100	46	35	-	-	-
	S_v , mm ⁻¹	-	-	-	-	70	-	-

(Int. No.090514_1)

The strain in the thickness direction was calculated by the fact that rolling has a plane strain compression condition and the logarithm strains in the direction of the uniaxial load in deformed dilatometer samples should be equal to the equivalent strain in the plane strain compression, using the yield condition from von Mises,

$$\epsilon_{thick} = \frac{\sqrt{3}}{2} \epsilon_{eq} \tag{Eq.67}$$

The variable ϵ_{thick} represents the logarithm strain in the thickness direction of the rolled strip. The ϵ_{eq} was transferred from the uniaxial degree of deformation in the dilatometer. It was done with the best care to keep the strain rate and rolling speed as close as possible to those in the process simulation in the deformation dilatometer.

During rolling, the cooling of the bars was controlled purely by the heat transfer to the ambient atmosphere and the roll surfaces. The temperatures of the bars at all rolling stands were determined by five pyrometers at the entrance and/or exit of the rolling stands above the bar surface (approximately 350 mm above), shown schematically in Fig. 22. The accuracy of the pyrometer was improved by pressured air blow to eliminate the steam. The transport velocity on the cooling line and ROT was 1 m/s. Within 1.5 s, the sheets were cooled down by one high pressure cooling unit from the final rolling temperature to the aimed temperature, 680°C. Further, the sheets moved along the ROT for 7s, followed by quenching into water bath whose temperature was constant at 20°C.

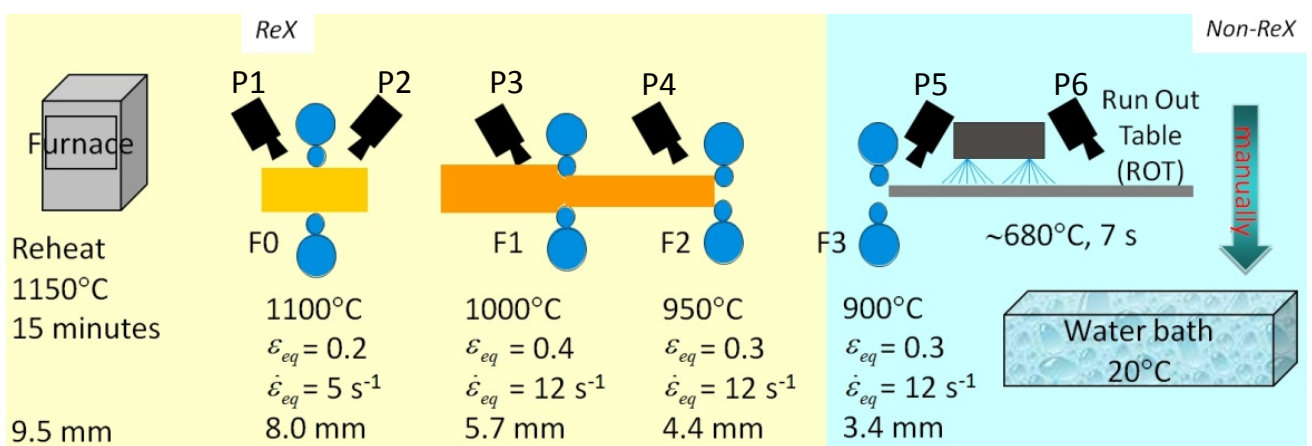


Fig. 22 Schematic description of the rolling line and rolling experiments, including the arrangement of the pyrometers. P1 to P6 represent the pyrometers

3.4 Plane strain compression at hot deformation simulator

A small bar sample with dimensions of $70 \times 20 \times 8 \text{ mm}^3$ was used to simulate a plane strain compression as that in the rolling experiment in another hot deformation simulator (TTS-820, Fig. 23). The thermomechanical cycle is as in Option D: 'Rolling Option' in Table 3.3. A flat compression head whose width is 10 mm, was employed to deform only in the middle of the bar along the rolling direction as depicted in Fig. 24. The maximum cooling rate after deformation was $25 \text{ }^\circ\text{C/s}$.

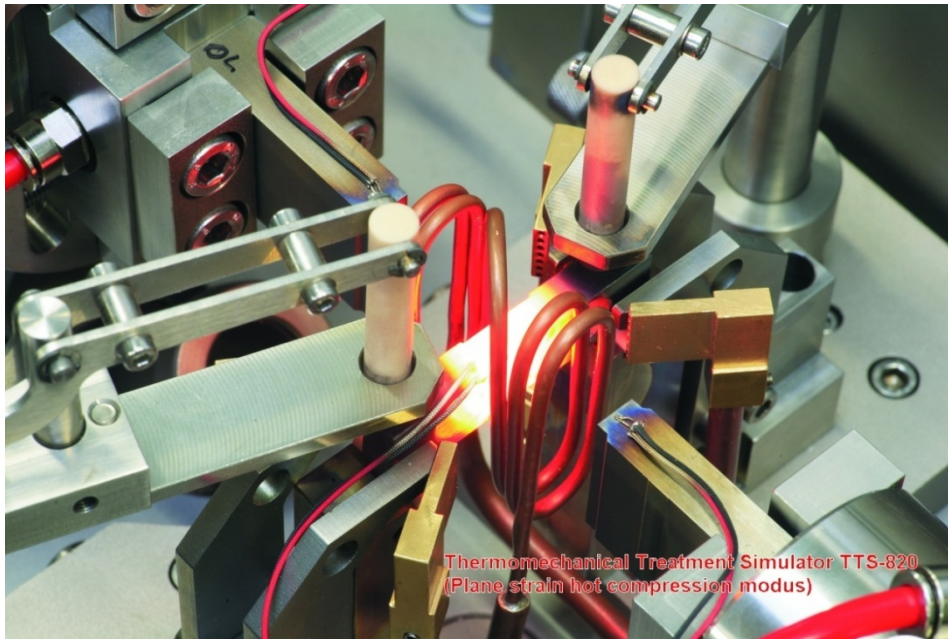


Fig. 23 The plane strain hot deformation simulator

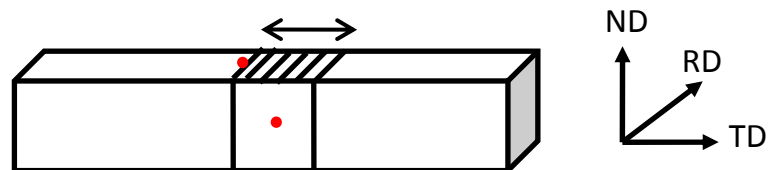


Fig. 24 The bar sample for the plane strain hot compression test. The area under deformation is shaded. The positions of thermocouple are at the red dots.

3.5 Microstructure analysis

3.5.1 Austenite grain size determination

As listed in section 3.2.1, the austenite grain size was investigated by different methods according to the level of grain size and the occurrence of the recrystallisation. With the absence of recrystallisation, the austenite grain size was investigated by the metallography.

The samples undergone quenching and etching method were etched with the picric acid solution. The austenite grain boundaries were then drawn and the measured grain surface area was converted into the Equivalent Area Diameter (EQAD). For the smaller grain sizes, the dark field illumination method helped to reveal the grain boundaries. Only one sample of the Mn-Si DP was etched with the hot picric acid at 75°C. Nital acid solution was used for the samples undergone ferrite decoration method. The grain surface area was measured similarly to calculate the EQAD.

The samples after the oxidation method were further prepared with care. They were polished very lightly without grinding to maintain the oxidised surface. The oxide scale was therefore removed only partly to ensure minimum removal of the oxidised surface. No further chemical was used. The grain size was measure also as EQAD.

3.5.2 Ferrite fraction, morphology, grain size, grain size distribution and nucleation density

The ferrite phase was mainly observed with a light optical microscope (LOM) by the standard preparation procedure: the samples were mounted in epoxy resin, grinded and polished until diamond suspension with the particle size of 1 µm. They were then etched with the nital solution. The ferrite fraction was analysed visually with the aid of the program ImageJ™ [IMJ]. All the investigations under LOM were made at the Department of Ferrous Metallurgy (IEHK), RWTH Aachen University.

As some strain inhomogeneity can occur in bulged cylindrical samples, it is recommended [Lor03] to observe the microstructure at the positions where the effective strain value can be represented at best. These positions are shown in Fig. 25

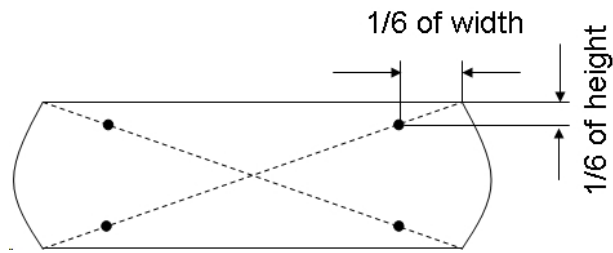


Fig. 25 The positions predicted to contain the effective strain in bulged deformed cylinder dilatometer samples by Lorenz [Lor03]

Some interesting cases were selected for the simulation with phase field model. Namely, the samples having the final recrystallised austenite grain size of $35\ \mu\text{m}$ from both steels were further measured for the ferrite grain size distribution. Each ferrite grain was measured manually by drawing its periphery with the commercial program Digimizer™[Dig]. Then the ferrite grain size was converted into the EQAD. This data was forwarded for the phase field simulation in section 5.6.

3.5.3 Identification of bainite, martensite and retained austenite constituents

Light optical microscope (LOM)

Some cases in which the microstructures contain the mixture of bainite and martensite or in some cases also of retained austenite, the Le Pera etchant was used to help to distinguish these phases by showing the martensite part containing carbon from 0.4% as well as retained austenite in white [Ang06]. Others are shown in brown.

If the existence of retained austenite is expected, the samples were also investigated by deep nital etching, in which they were etched by nital acid solution for a minute.

Scanning electron microscope (SEM)

A scanning electron microscope (SEM) with the magnifications of 1000-3000X reveals and distinguishes phases especially the bainite and martensite from the surface roughness of phases. Martensite is expected to appear smooth while bainite is expected to have much more roughness showing the lath structure obviously. The fractions of bainite and martensite were then measured manually from the SEM micrographs. The areas showing smooth surface count to martensite while those showing rough surface count to bainite.

Electron backscatter diffraction patterns (EBSD)

Phase mappings by electron backscatter diffraction patterns (EBSD) were performed to observe the retained austenite, as it has a different crystal structure from the ferrite/martensite matrix. After the samples were polished until 1 μm diamond suspension, they were electro-polished with the potential of 34 Volt for 15 s. The EBSD was done at 25 keV with standard step size of 120 nm and also 40 nm in some necessary cases. The SEM and EBSD investigations were done at Central Facility for Electron Microscopy (GFE), RWTH Aachen University.

Field emission electron microprobe (FEG EPMA)

The solute redistribution during the ferrite transformation was analysed further by means of the new generation high resolution field emission electron microprobe (FEG EPMA). This technique consists of rastering a beam of electrons over a given region of interest. The interaction of the incident electrons with the sample produces characteristic x-rays which are simultaneously collected by five wavelength dispersive spectrometers. Hence, five elements: C, Mn, Mo, Cr, Si were mapped. The detected x-ray intensity is proportional to the concentration of the elements in the sample. Higher resolution measurements can be achieved with a field emission electron gun than with the traditional tungsten filament as the diameter of the electron beam is significantly smaller.

The samples were mounted in a Cu-containing holder for the conductivity. They were polished up to colloidal silica and left unetched. The measurements were performed on a JEOL JXA-8530F microprobe at 15 keV with a probe current of 100 nA. The dwell time for the line analyses was 10 s, whereas the one for the mappings was 100 ms.

For the line measurements, the sensitivity of the carbon concentration and resolution are approximately 0.05 mass%C and 0.4 μm , respectively. To avoid the carbon contamination, it was performed on a fresh area before the EBSD measurement or the element mapping.

X-ray diffraction method (XRD)

The amount of retained austenite was measured also separately by the X-ray diffraction method (XRD). The XRD was carried out in a Bruker D8 Advance XRD instrument with Hi-Star 2 θ detector with $\text{CoK}\alpha$ with a wavelength of 1.79 \AA . It was carried out at the Department and Chair of Physical Metallurgy and Metal Physics (IMM), RWTH Aachen University.

Magnetic induction

The magnetic induction measurement was carried out by the company voestalpine Stahl GmbH. With this method, a much more accurate fraction of retained austenite is expected as the whole volume of sample is measured.

3.6 Mechanical properties of the hot rolled sheets

3.6.1 Tensile testing

The mechanical properties of the hot rolled strips were determined with a universal tensile rig Zwick Z100. The sample dimensions were according to DIN 50125 standard as the strips had a thickness of 3.5 mm. The drawing of the tensile sample is shown in Fig. 26 and Table 3.8. The length of the samples lies along the rolling direction.

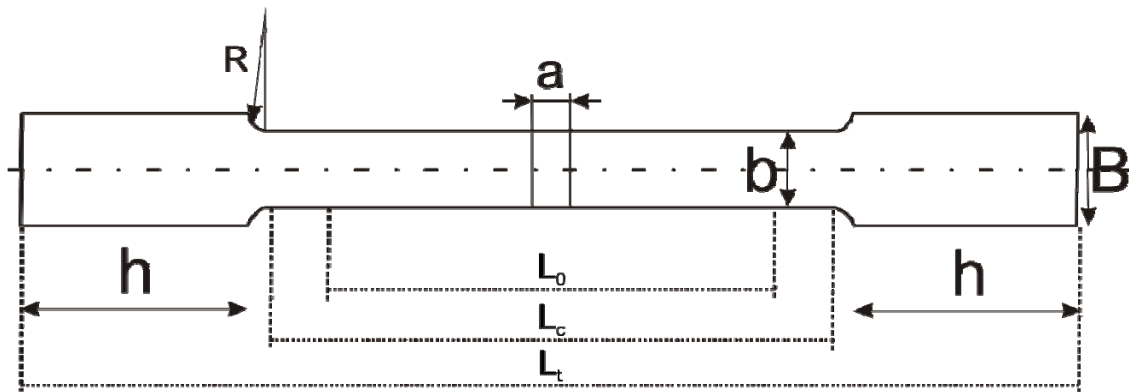


Fig. 26 Tensile samples with rectangular cross sections according to DIN EN 10002 (L_0 =initial length, L_c =test length, L_t =total length, a =thickness of the flat test piece, b =width).

Table 3.8 The sample geometry of the tensile samples with rectangular cross section shown in Fig. 26.

$$L_0 = k \sqrt{a \cdot b}$$

Standard	k	a	b	L_0	L_c	L_t	B	h	R
DIN 50125	11.3	4	10	70	80	200	15	50	20

The testing was carried out at ambient temperature and at a testing speed of 2 mm/minute. The characteristic values: yield strength (YS), ultimate tensile strength (UTS), uniform elongation (e_u), total elongation (e_f) and strain hardening exponent (n), are measured automatically. On the other hand, the true stress-true strain curve was determined manually. The samples which broke outside the gauge length were not included in the results.

3.6.2 Hardness mapping

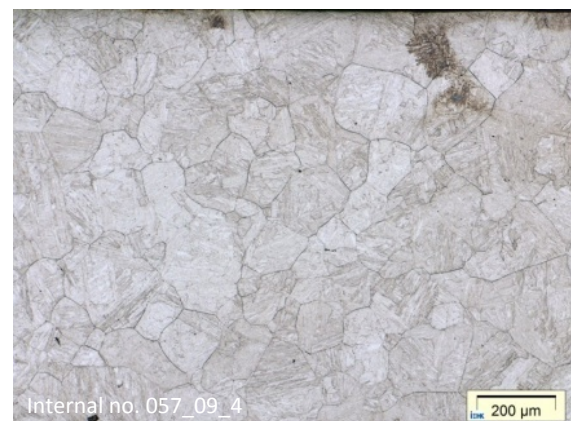
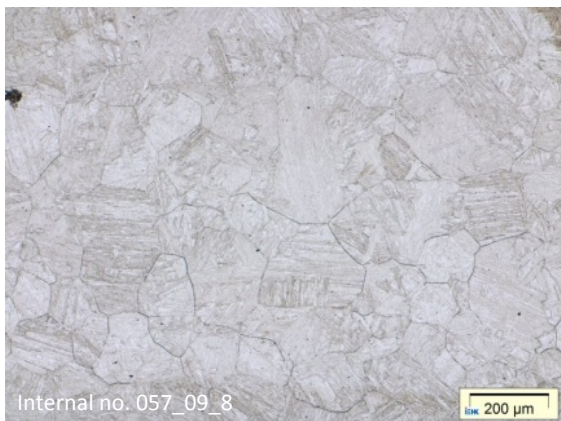
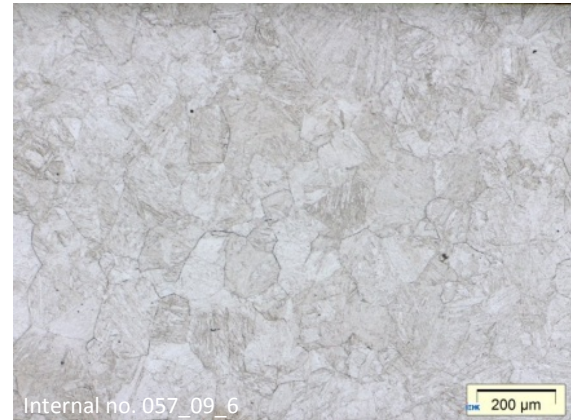
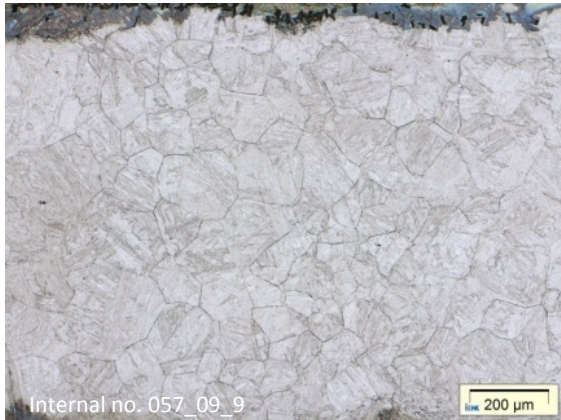
Selected samples were measured for the hardness value across the whole surface where other metallographic observations were performed. The hardness indenter exerted a 0.8 g force and had a step size of 0.3 mm.

4 RESULTS FROM LABORATORY PROCESS SIMULATION

4.1 Process simulation in deformation dilatometer

4.1.1 Austenite grain size by quenching and etching

The austenite grain sizes after different reheating conditions are tabulated with the metallographic results in Fig. 27 to Fig. 30.



1200°C 900 s, 128 μm

1150°C 900 s, 111 μm

Fig. 27 The austenite grains in the Mn-Mo DP steel revealed by the quenching and etching method after the austenitisation at 1200 °C and 1150 °C

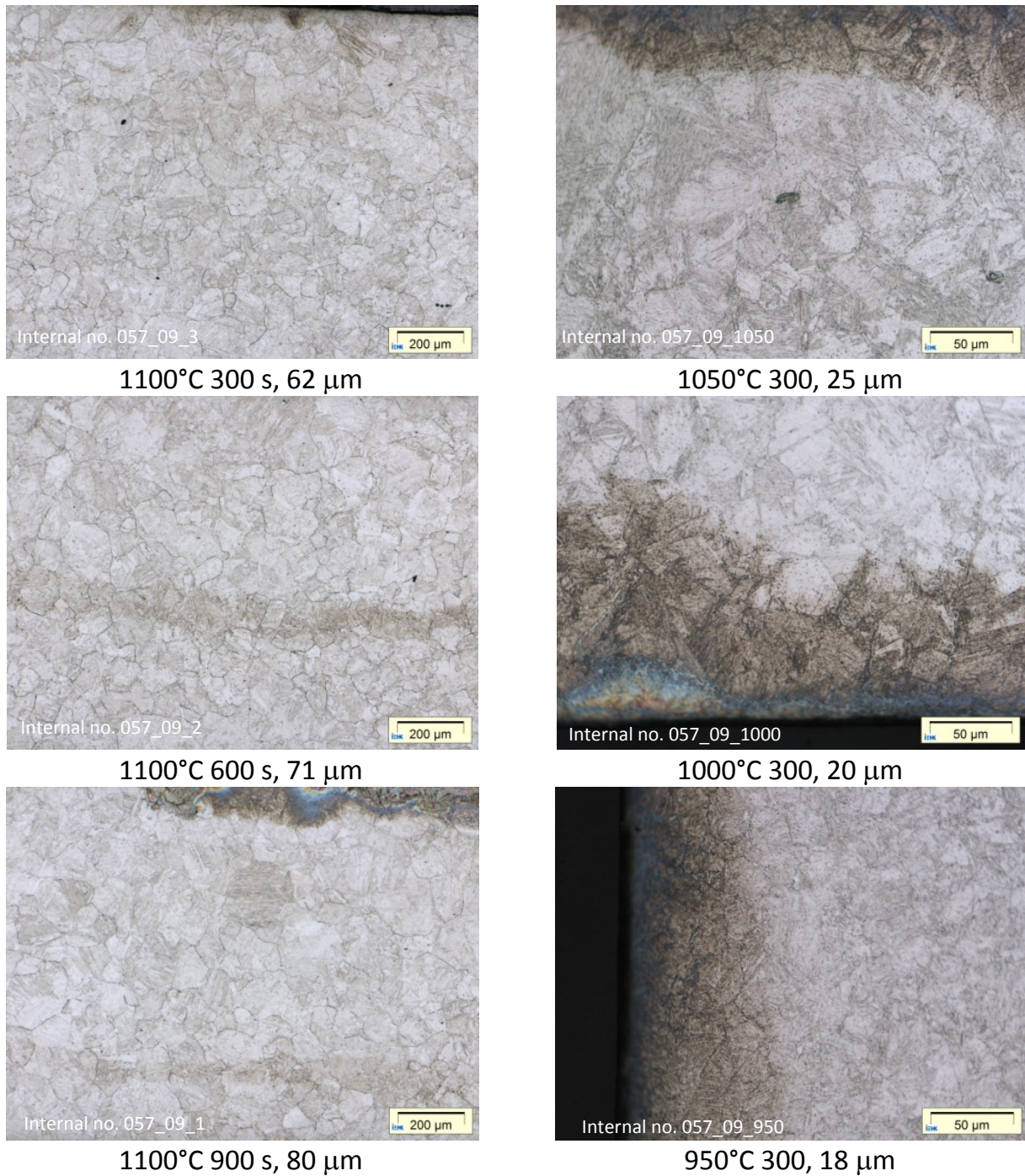
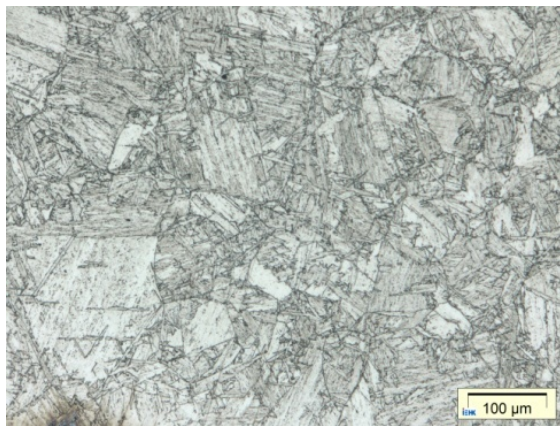
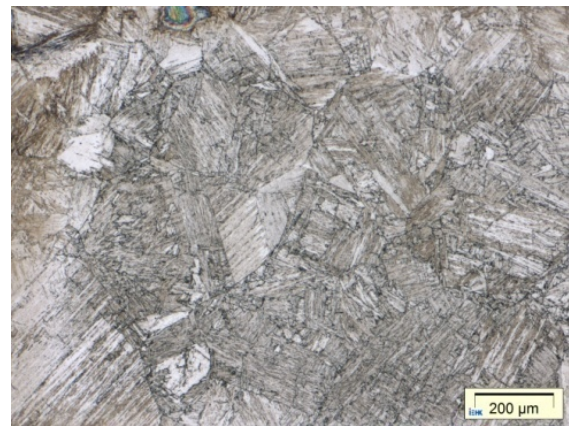


Fig. 28 The austenite grains in the Mn-Mo DP steel revealed by the quenching and etching method after the austenitisation at 1100 °C, 1050 °C, 1000 °C and 950 °C

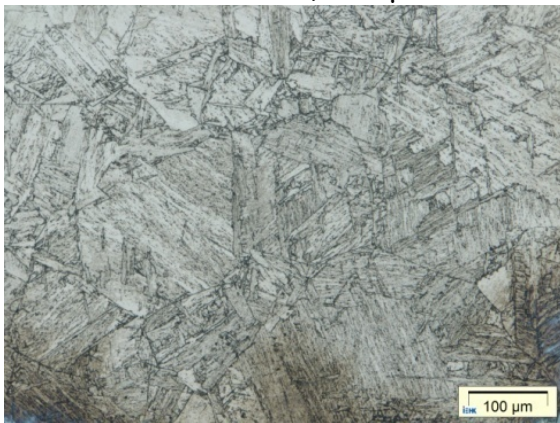
The austenite grain boundaries in the Mn-Mo DP steel are apparent after reheating under different reheating conditions and quenching, especially at larger austenite grain sizes. The grain boundaries in case of very small grain sizes are much less manifest. On the other hand, the grain boundaries in Mn-Si DP are strongly obscured by the irregularities in the low carbon martensitic structure. However, the grain size measurement as EQAD was done with



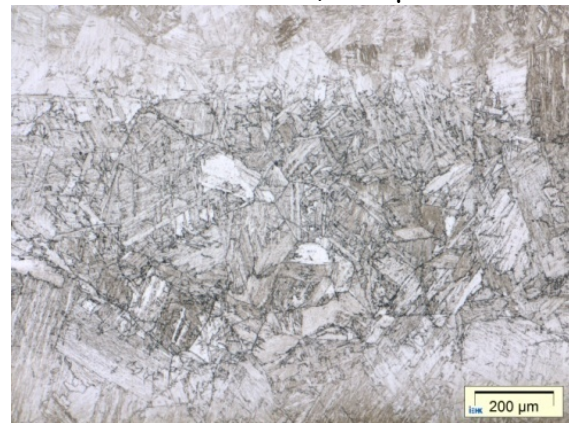
1200°C 300 s, 102 μm



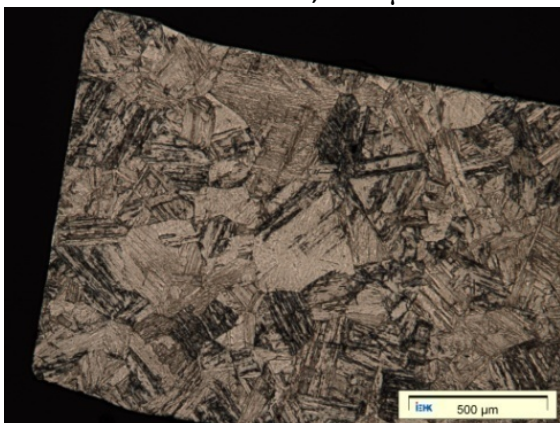
1200°C 600 s, 240 μm



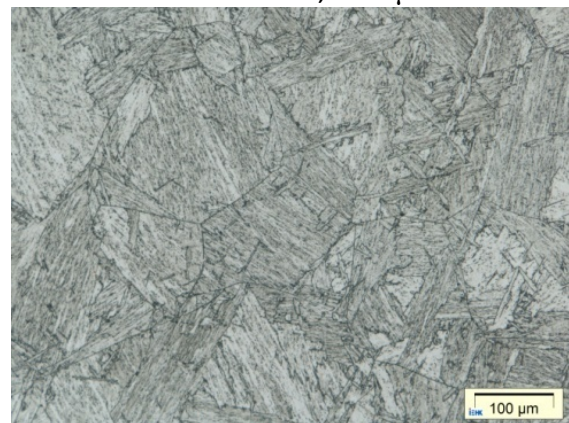
1150°C 300 s, 150 μm



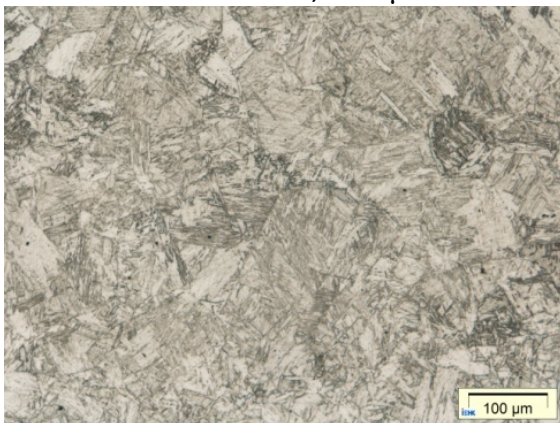
1150°C 600 s, 198 μm



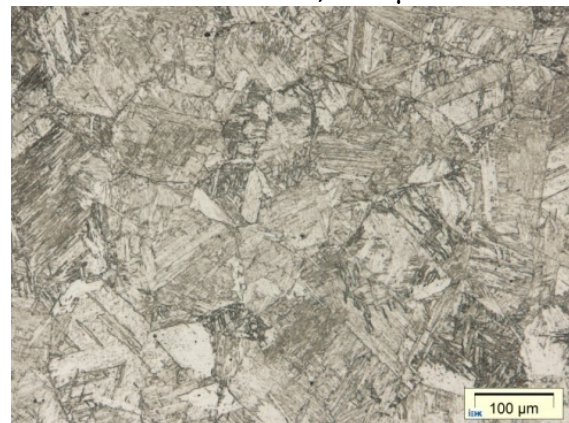
1150°C 900 s, 300 μm



1100°C 900 s, 180 μm



1000°C 120 s, 115 μm



950°C 300 s, 120 μm

Fig. 29 The austenite grains in the Mn-Si DP steel revealed by the quenching and etching method after different austenitisation temperatures and durations

best care. The smallest grain sizes could not be revealed after quenching and etching. But etching with the hot picric acid at 75°C improves the results significantly. It was therefore performed for the case of austenitisation at 900 °C for 300 s.

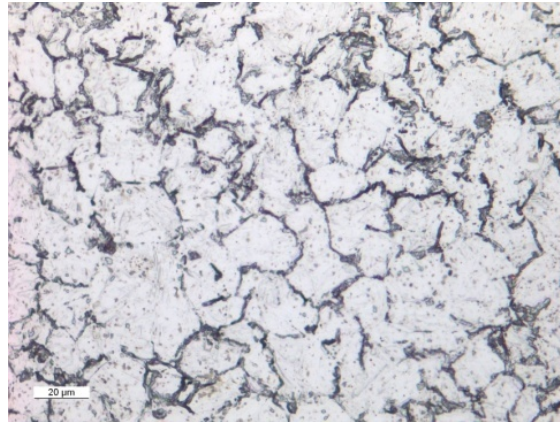


Fig. 30 The austenite grains in the Mn-Si DP steel revealed by quenching and etching with the picric acid at 75 °C after austenitisation at 900 °C for 300 s. The grain size of 22 μm was evaluated.

4.1.2 Austenite grain size by ferrite decoration

As mentioned in section 3.2.1 and 3.5.1, the ferrite decoration method was used in some samples with large austenite grain sizes.

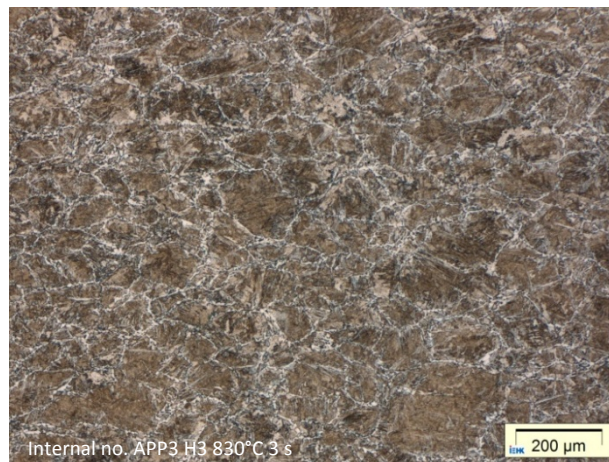


Fig. 31 The result from the attempt to reveal the deformed austenite grains in the Mn-Mo DP steel by the ferrite decoration method. The sample was reheated at 1200°C for 300 s, deformed at 1150°C with a strain of 0.2, then deformed at 830 °C also with a strain of 0.2. Then the ferrite decoration was performed at 680°C for 3 s. The austenite grain size of 100 μm was estimated.

Fig. 31 shows an attempt to use the ferrite decoration method to lineate the deformed austenite grains in the Mn-Mo DP steel which was reheated at 1200°C for 300 s, then deformed at 1150°C with a strain of 0.2 and was finally deformed at 830°C with a strain of 0.2. The ferrite decoration was induced at 680°C for 3 s. The grains cannot be shown by quenching and etching. Although most of the PAGs are shown in this case, the result can help only to estimate the PAGs roughly due to the fact that too many ferrite lines were induced near the PAGs, especially at smaller grains. Incomplete recrystallisation at 1150°C can rationalise for this. The ferrite decoration method is therefore not suitable for the observation of deformed austenite grains. It is not suitable for smaller austenite grain sizes too as ferrite transformation is rather fast and too many ferrite lines obscure the PAGs.

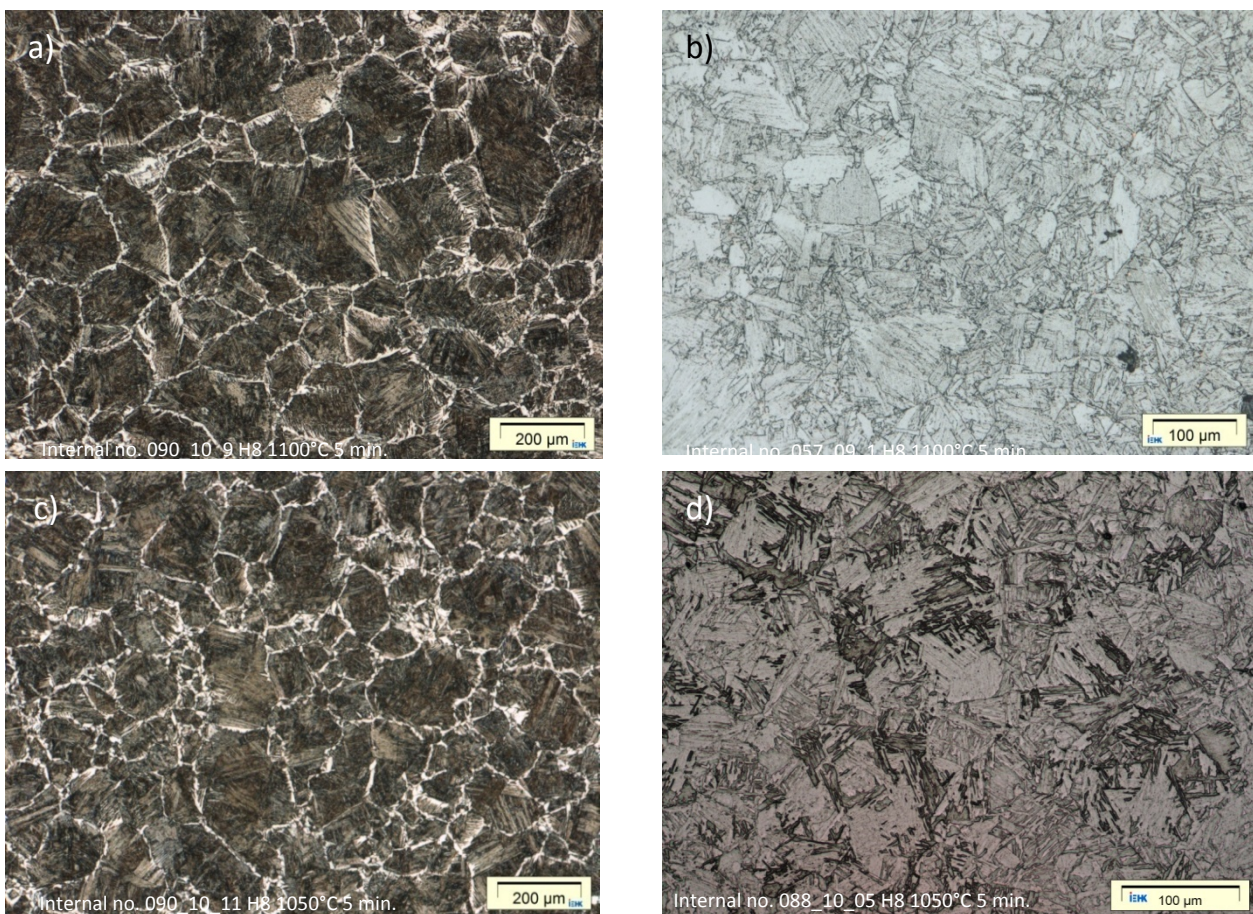


Fig. 32 The investigation of austenite grain sizes in the Mn-Si DP by the ferrite decoration method, compared with the results from quenching and etching method. a) and b) The sample was reheated at 1100°C for 300 s. a) The sample was quenched to 680 °C and held for 3 s. The austenite grain size of 135 μm was evaluated. b) The sample was quenched and etched with picric acid and not evaluated quantitatively. c) and d) The sample was reheated at 1050°C for 300 s. c) The sample was quenched to 680 °C and held for 3 s. The austenite grain size of 130 μm was evaluated d) The sample was quenched and etched with picric acid and not evaluated quantitatively.

The Mn-Si DP steel has relatively large grains after reheating. The ferrite decoration was therefore employed together to obtain more reliable results due to the unclear grain boundaries from the quenching and etching method. In contrary to the above mentioned case in Fig. 31, the ferrite decoration method shows the PAGs evidently.

4.1.3 Austenite grain size by oxidation method

It is the most time consuming method among all the methods to determine the austenite grain size as the optimum combination of experimental parameters, i.e. oxidation time and pressure of oxygen, varies significantly on the steel type, oxidation temperature [Akb95]. It was therefore carried out only for the Mn-Si DP steel due to the unclear grain boundaries. The smallest grain size created by the austenitisation at 900°C for 300 s was selected as it is not revealable by etching with the picric acid at the room temperature.

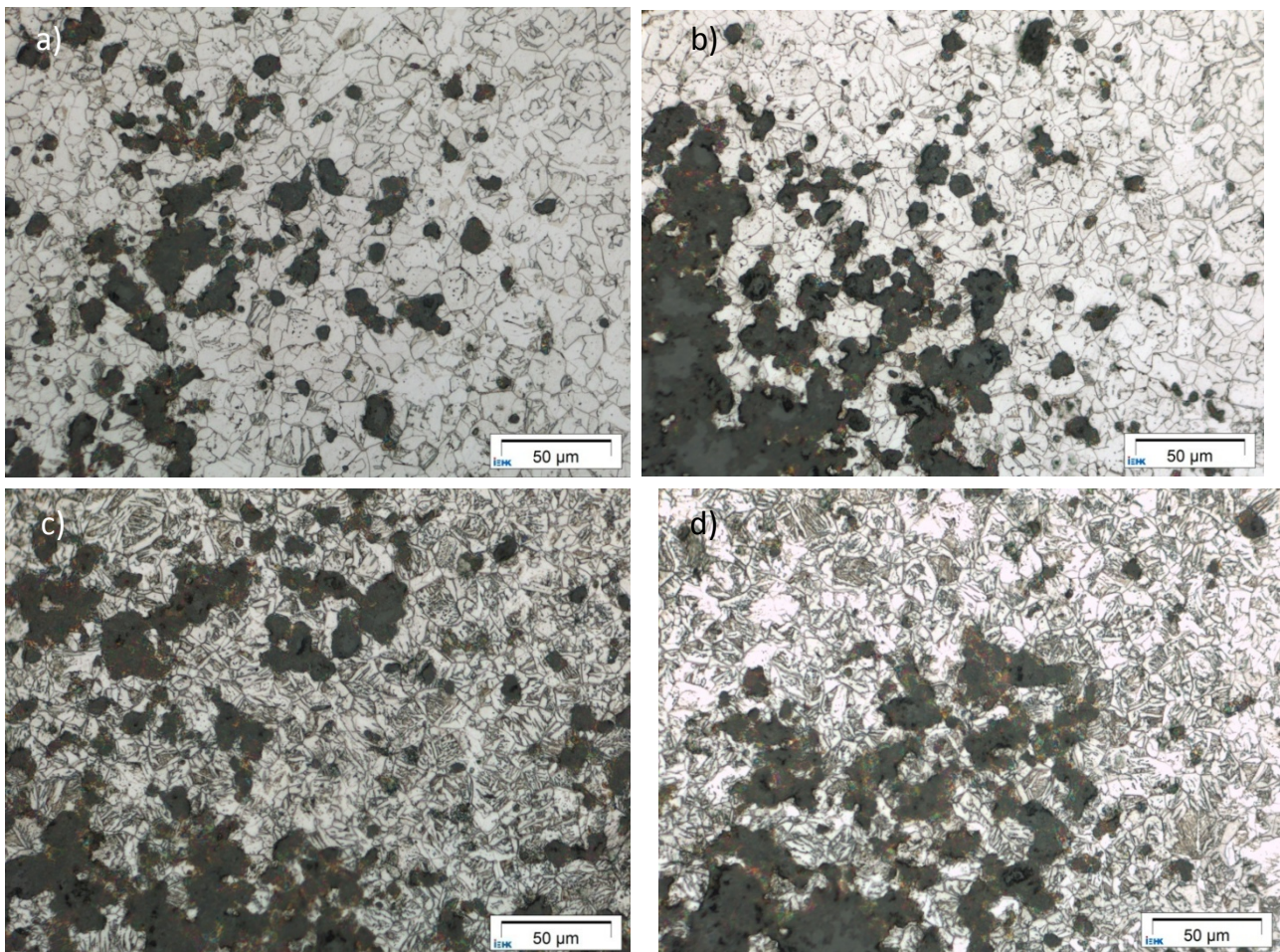


Fig. 33 The polished samples after the oxidation. The black parts are the oxide layers, which were intentionally left. The austenite grain size was evaluated to be 17 µm. a) and b) with pressure of 0.1 bar. c) and d) with pressure of 0.5 bar.

The cylindrical dilatometer samples were austenitised in the dilatometer at 900 °C. The oxidation was performed by stopping the flow of helium and letting oxygen in. The oxidation started during the reheating period and continued until quenching.

The oxygen pressures of 0.1 and 0.5 bar with the oxidation time of 180 s give the best results, which are shown in Fig. 33. The oxide layer was polished very carefully and lightly that the trace of the oxidised layer can be still seen (dark parts). Using cylindrical samples is advantageous for the polishing as mounting and grinding is not possible in this case and the flat sample is too small for polishing without mounting. The evaluation of the grain size is not straightforward in this case as there are a number of irregularities inside the grains, which can be also seen in quenched and etched samples and must be excluded. The grain size was finally evaluated to be 17 μm .

4.1.4 Fraction recrystallised between rolling passes

This section concerns only the thermomechanical routes *Option B* and *D* in Table 3.3 only as the significant recrystallisations between the deformation steps are expected.

The proof of dynamic recrystallisation

The dynamic recrystallisation was analysed purely from the flow curves during the deformation in Schenck hot deformation simulator. Fig. 34 shows the flow curves during all the deformation steps in *Option B* and *D*. There is neither plateau nor drop in all curves and therefore no dynamic recrystallisation is concluded for the context of this work.

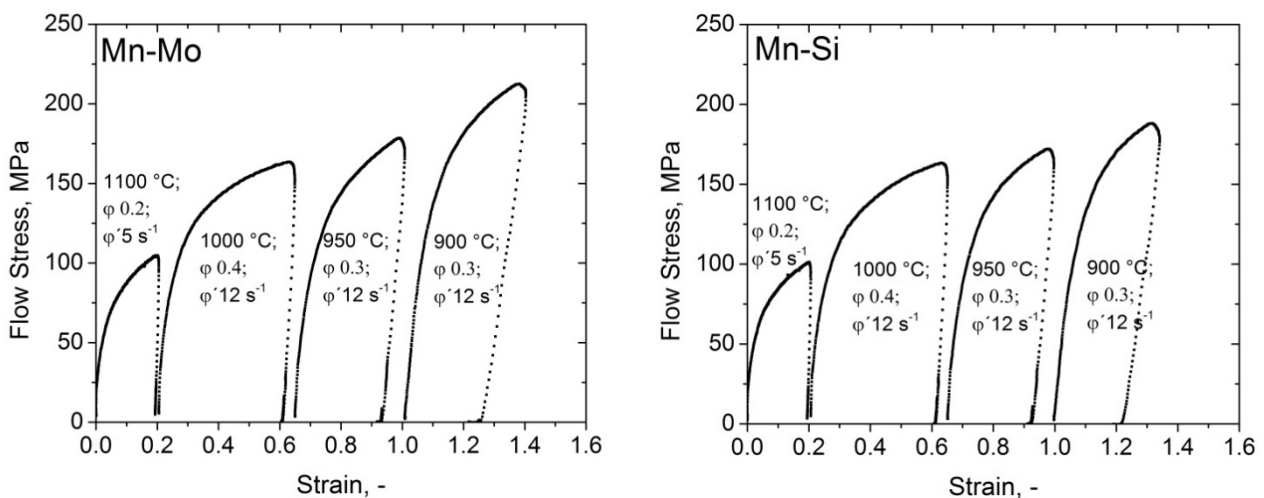


Fig. 34 The flow curves of a) Mn-Mo DP steel and b) Mn-Si DP steel during the four deformation steps in the processing route *Option B* and *D*.

The measurement of static recrystallisation

Represented in Table 4.1 to Table 4.4 are the softening and recrystallised percentages of the studied steels measured by means of the double hit tests described in section 3.2.2 and calculated by Eq.66 The recrystallised percentage was calculated under both the assumptions with recovery fraction of 0.2 and 0.25 as compared in Table 4.2 and Table 4.4.

Table 4.1 Softening percentage obtained from the double hit tests for the Mn-Mo DP steel

Auftrag 021	Temperature, °C		
Interpass time, s	1100	1000	950
3	94.37	96.86	80.24
10	93.54	99.66	92.87
50	97.63	98.70	97.11

Table 4.2 The calculated recrystallisation percentage for the Mn-Mo DP steel

	Temperature, °C		
Interpass time, s	1100	1000	950
With recovery fraction of 0.25			
3	92.49	95.81	73.65
10	91.39	99.55	90.49
50	96.84	98.27	96.15
With recovery fraction of 0.2			
3	92.96	96.08	75.30
10	91.92	99.58	91.09
50	97.04	98.38	96.39

Table 4.3 Softening percentage obtained from the double hit tests for the Mn-Si DP steel

Auftrag 007	Temperature, °C		
Interpass time, s	1100	1000	950
3	98.45	96.37	86.86
10	99.20	99.87	88.67
50	102.06 (taken as 100)	98.22	-

The recrystallised fractions in all cases are relatively large that the recrystallised austenite grain size after each deformation pass can be reasonably calculated by Eq.16. Only the third deformation step in the Mo-Mn DP steel with the shortest interpass time (3 s) has relatively large unrecrystallised fraction.

Table 4.4 The calculated recrystallisation percentage for the Mn-Si DP steel

Interpass time, s	Temperature, °C		
	1100	1000	950
With recovery fraction of 0.25			
3	97.93	95.16	82.48
10	98.93	99.83	84.89
50	100.00	97.63	-
With recovery fraction of 0.2			
3	98.06	95.46	83.58
10	99.00	99.84	85.84
50	100.00	97.78	-

4.1.5 The flow curve for stored energy of austenite

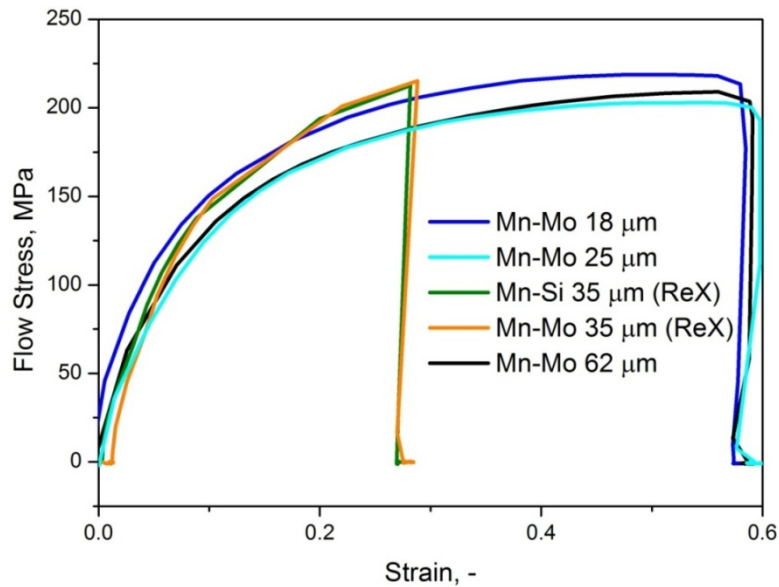


Fig. 35 The flow curves of the studied materials having different austenite grain sizes. The deformation was at 900 °C. The inscription 'ReX' means the deformations were performed on the recrystallised austenite. The grain size assigned in this case is a predicted grain size according to the recrystallised fraction and Eq.16.

Represented in Fig. 35 are the flow curves during the deformation at 900 °C. Different austenite grain sizes in both the studied materials yield similar flow stresses. At the total logarithm strain of 0.3, which yields around the plastic strain of 0.28, the flow stress is

approximately 215 MPa. This stress level will be forwarded to the modelling sections 5.1.2.1 and 5.6.1 to take into account the stored energy of the austenite induced by the deformation.

4.1.6 Ferrite formation kinetics

The results described in this section are derived by the stepwise quenching after different short holding intervals in the ferrite transformation region temperature in the deformation dilatometer. The dilatation curves were not utilised to quantify the phase fraction directly. An argument for this is that the experiments on the ferrite transformation focus on very short holding periods according to the industrial process window. Due to the complex processing steps combining both quenching to the required temperatures and deformation, especially the processing route in *Option B*, many relative length change curves show some discontinuities and irregularities. From all the reasons, the ferrite transformation kinetics was derived by quenching after different transformation times. The ferrite fraction was analysed by means of the metallographic work. Additionally, it is also

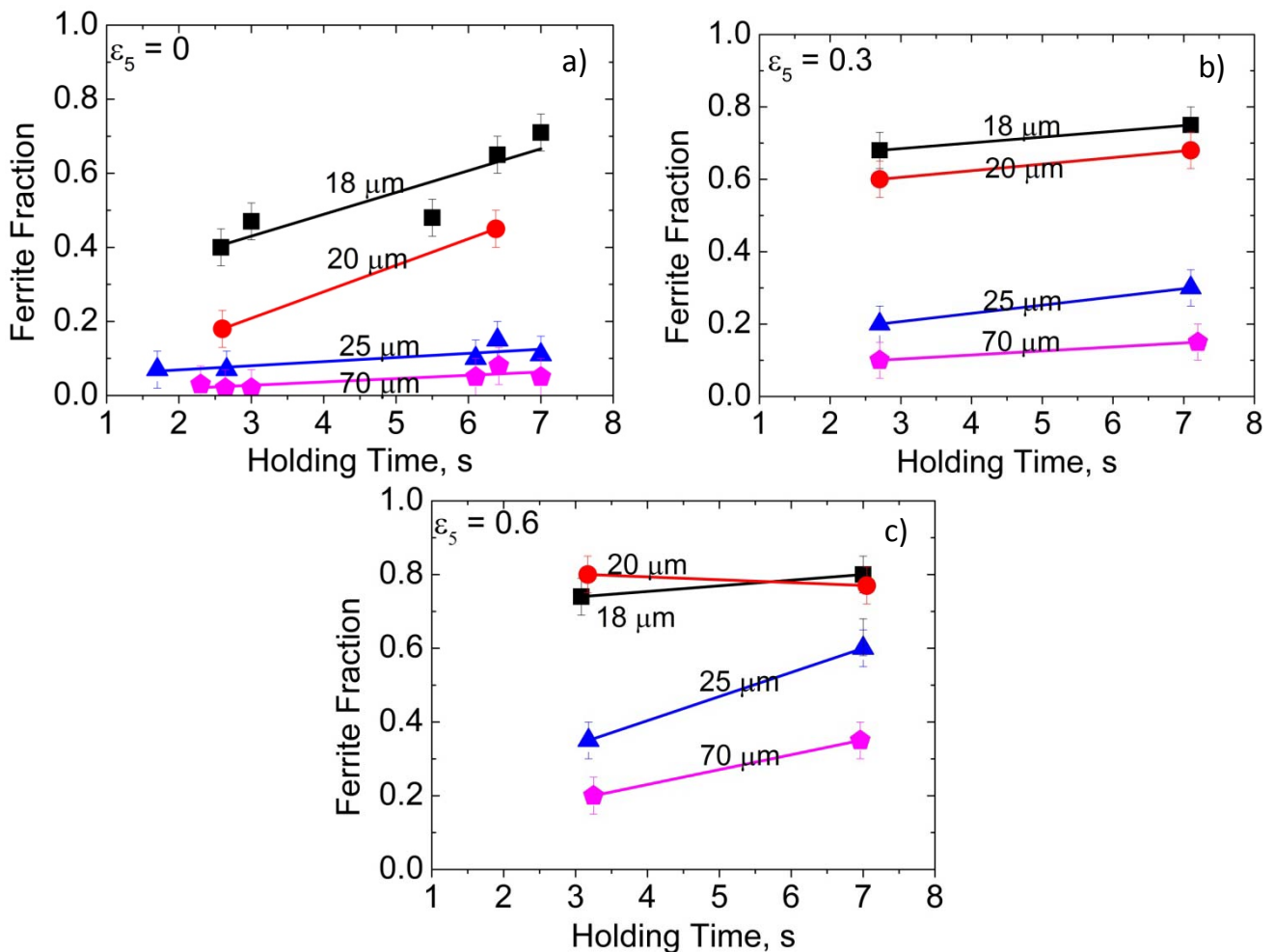


Fig. 36 The ferrite transformation kinetics at an isothermal temperature of 680 °C in the Mn-Mo DP steel according to different degrees of retained strain and austenite grain sizes, separated by the degree of

retained strain. ε_5 indicates the deformation at 900 °C. a) no retained strain b) retained strain of 0.3 c) retained strain of 0.6

interesting to observe the bainite and martensite transformation in the samples with different ferrite fraction, namely in samples after short and long ferrite transformation time as the degree of carbon enrichment in austenite varies with the ferrite fraction.

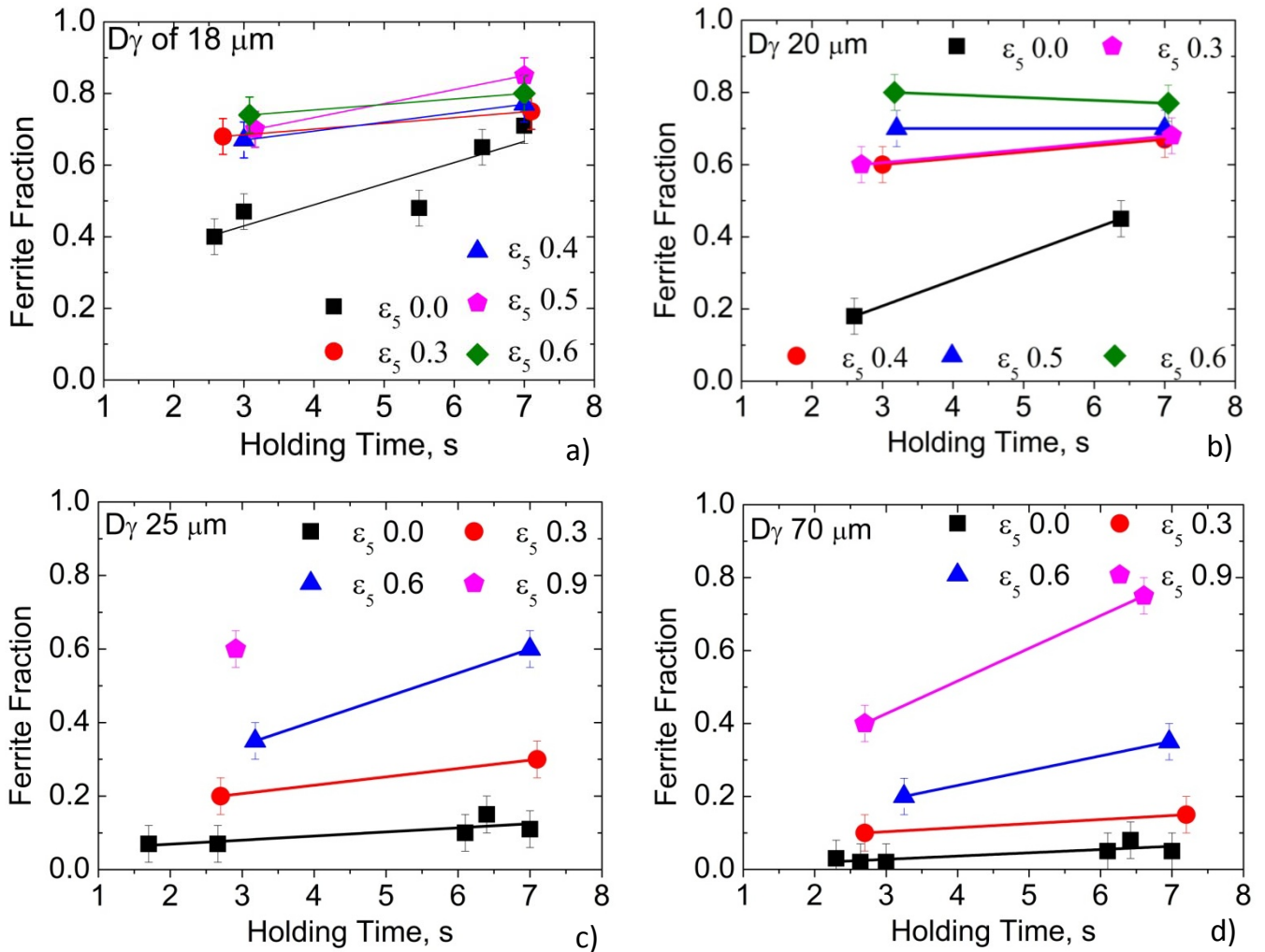


Fig. 37 The ferrite transformation kinetics at an isothermal temperature of 680 °C in the Mn-Mo DP steel according to different degree of retained strain and austenite grain size, separated by the austenite grain size. ε_5 indicates the deformation at 900 °C. a) austenite grain size of 18 μm b) austenite grain size of 20 μm c) austenite grain size of 25 μm d) austenite grain size of 70 μm

Fig. 36 to Fig. 39 show the effect of the austenite conditioning: prior austenite grain size (created by different austenitisations) and retained strain, on the ferrite transformation at 680°C in the two studied steels. They correspond to the processing route *Option A* in Table 3.3.

It is evident that at the same austenite grain sizes, higher degrees of retained strain promote the ferrite transformation kinetics. The effect is more pronounced in cases of larger austenite grain sizes. Comparing Fig. 36a with Fig. 36b and Fig. 36c when the retained strain involves and increases from 0.0 to 0.3 and to 0.6, the ferrite transformations in the Mn-Mo steel samples with austenite grain sizes of 25 and 70 μm rise up significantly. But those with austenite grain sizes of 18 and 20 μm increases only slightly.

As visualised differently for the same steel in Fig. 37, the same conclusion can be drawn. At the smallest austenite grain size of 18 μm , different retained strains do not bring large difference in the transformation kinetics. But the retained strain accelerates the kinetics at the larger austenite grain sizes much more apparently.

The ferrite transformation kinetics of the Mn-Si steel are shown separately in Fig. 38 and Fig. 39. In the strain-free case, the transformation kinetics shows a sharp increase as soon as the austenite grain size becomes smaller than 130 μm . It is interesting that the kinetics does not vary much within a big range of austenite grain size between 120-70 μm . But the retained strain of 0.3 accelerates the kinetics in cases of the austenite grain sizes of 130 and 135 μm significantly.

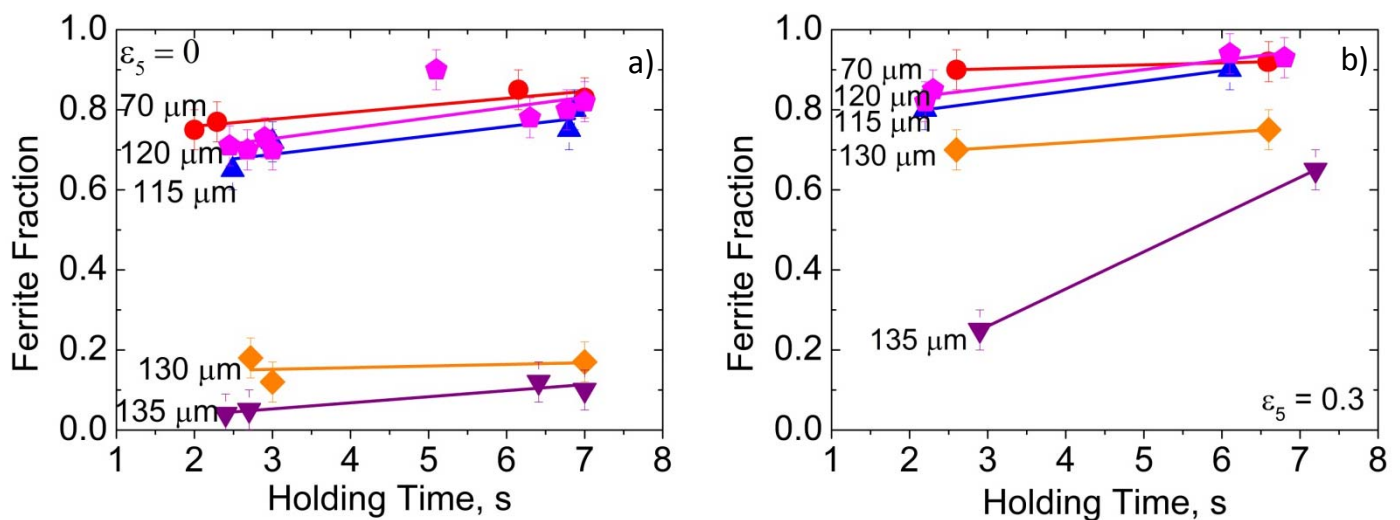


Fig. 38 The ferrite transformation kinetics at an isothermal temperature of 680 °C in the Mn-Si DP steel according to different degrees of retained strain and austenite grain sizes, separated by the degree of retained strain. ϵ_5 indicates the deformation at 900 °C a) no retained strain b) retained strain of 0.3

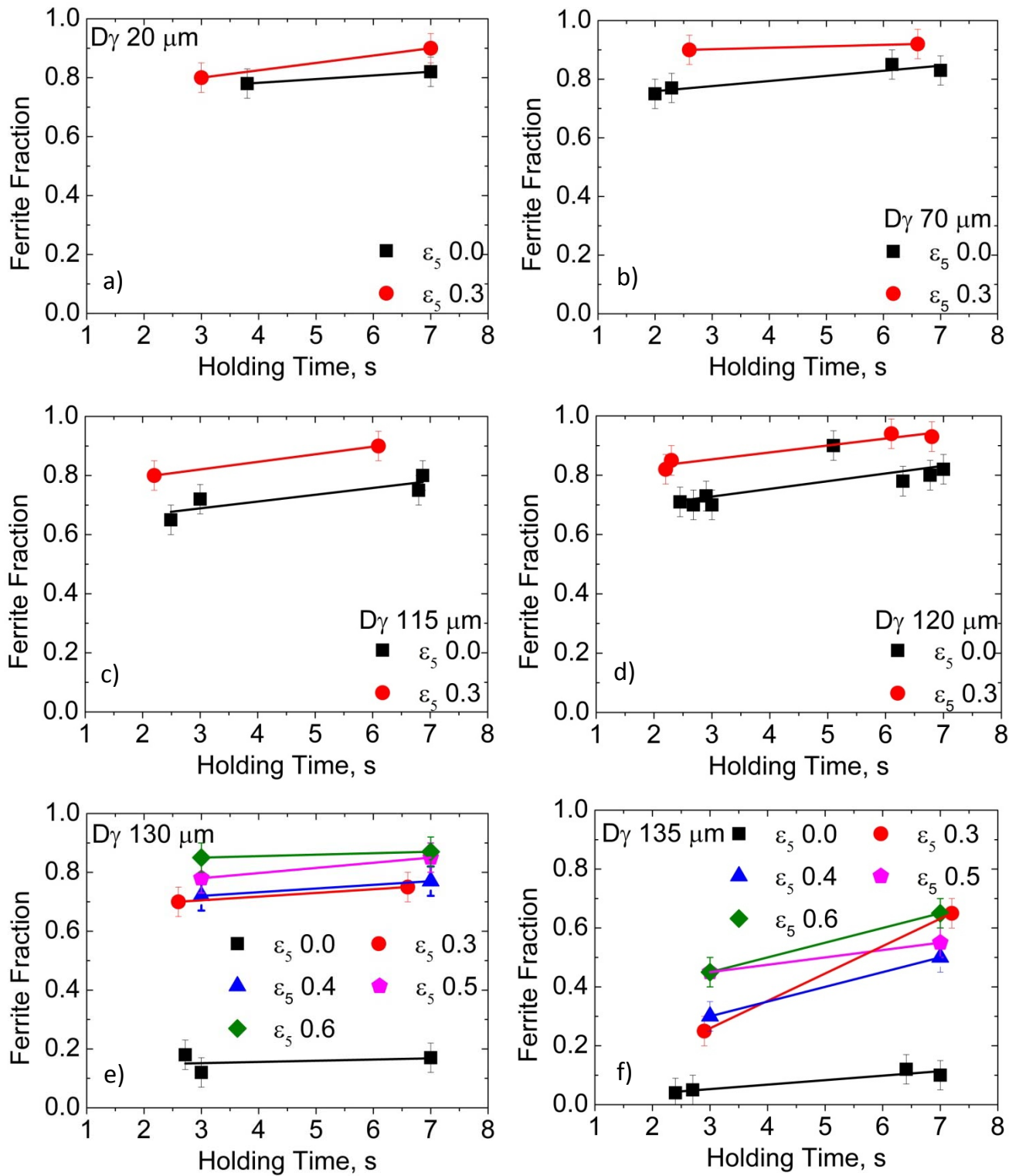


Fig. 39 The ferrite transformation kinetics at an isothermal temperature of 680 °C in the Mn-Si DP steel according to different degrees of retained strain and austenite grain sizes, separated by the austenite grain size. ϵ_5 indicates the deformation at 900 °C a) austenite grain size of 20 μm b) austenite grain size of 70 μm c) austenite grain size of 115 μm d) austenite grain size of 120 μm e) austenite grain size of 130 μm f) austenite grain size of 135 μm

Plotting the austenite grain size separately in Fig. 39, it can be seen that insufficient ferrite fraction according to the general requirement for DP steels comes only from the austenite grain size of 135 μm at all retained strains and from the austenite grain size of 130 μm without strain. Ferrite forms in other cases rather rapidly and can facilitate the hot rolling production properly.

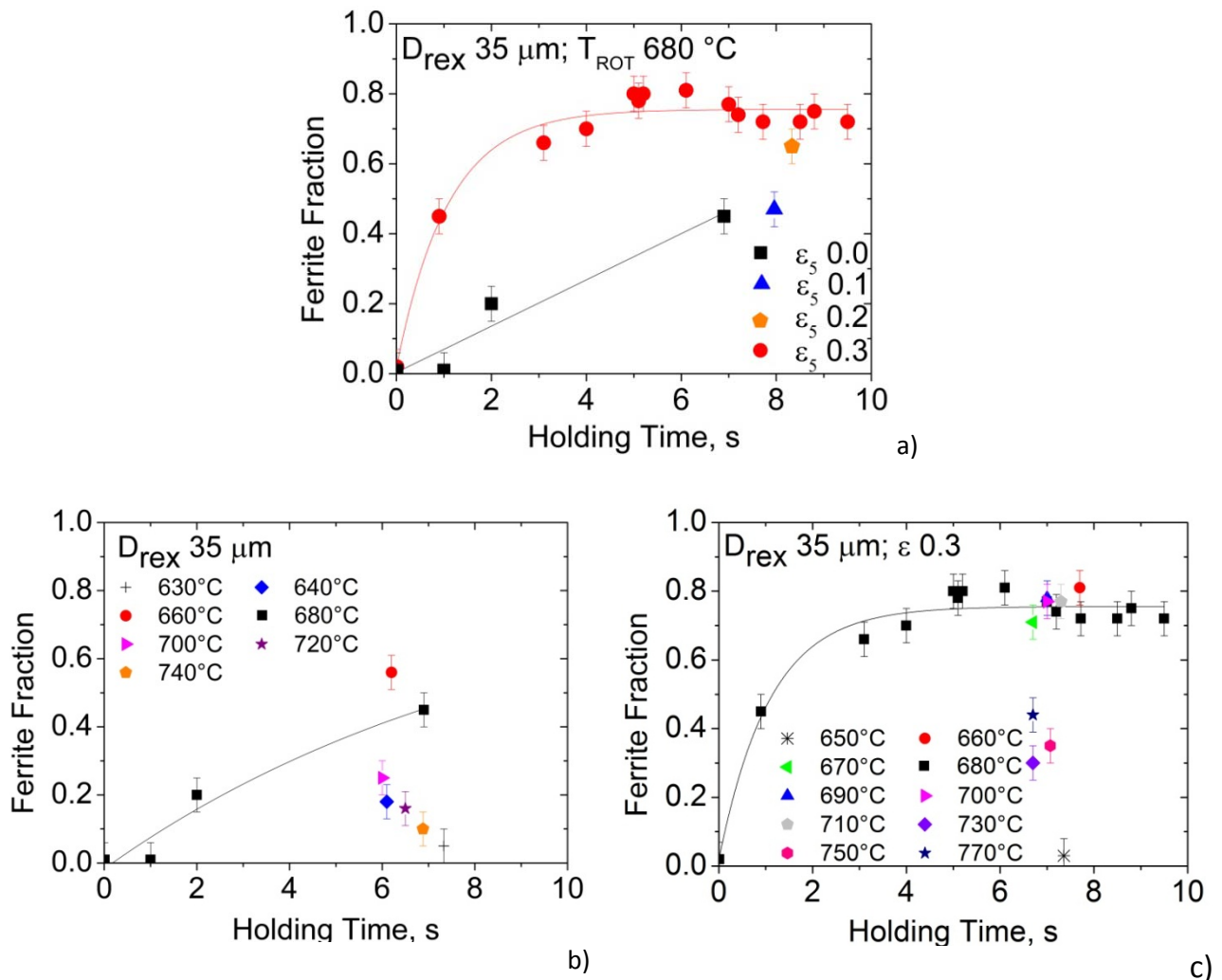


Fig. 40 The ferrite transformation kinetics in the Mn-Mo DP steel from the austenite grain size of 35 μm , which is the result of repeated recrystallisations according to the processing routes *Option B* and *D*. ϵ_5 indicates the deformation at 900 $^\circ\text{C}$ a) the effect of the retained strain on the transformation kinetics at 680 $^\circ\text{C}$ b) the effect of transformation temperature, in case of no retained strain c) the effect of the transformation temperature, in case of a retained strain of 0.3.

A large number of experiments focus on the case of prior austenite grain size of 35 μm , which is evolved by repeated recrystallisations (*Option B* and *D* in Table 3.3), because it corresponds to the experimental rolling conditions. Fig. 40 and Fig. 41 show the kinetics under this condition with different retained strains and transformation temperatures. The

ferrite fraction in the Mn-Mo DP steel under the retained strain of 0.3 rises up to around 0.7-0.8 within 5 s, after which it starts to saturate. On the other hand, the Mn-Si steel needs only 3 s to produce a ferrite fraction as high as 0.9, also under a retained strain of 0.3.

Note that each data point is derived from a sample held at a specific transformation temperature followed by quenching. Therefore the datapoints with longer holding times do not always show higher fraction than those having shorter holding times. Some extent of ferrite results during the quenching. This is much more significant in Mn-Si DP and will be discussed later.

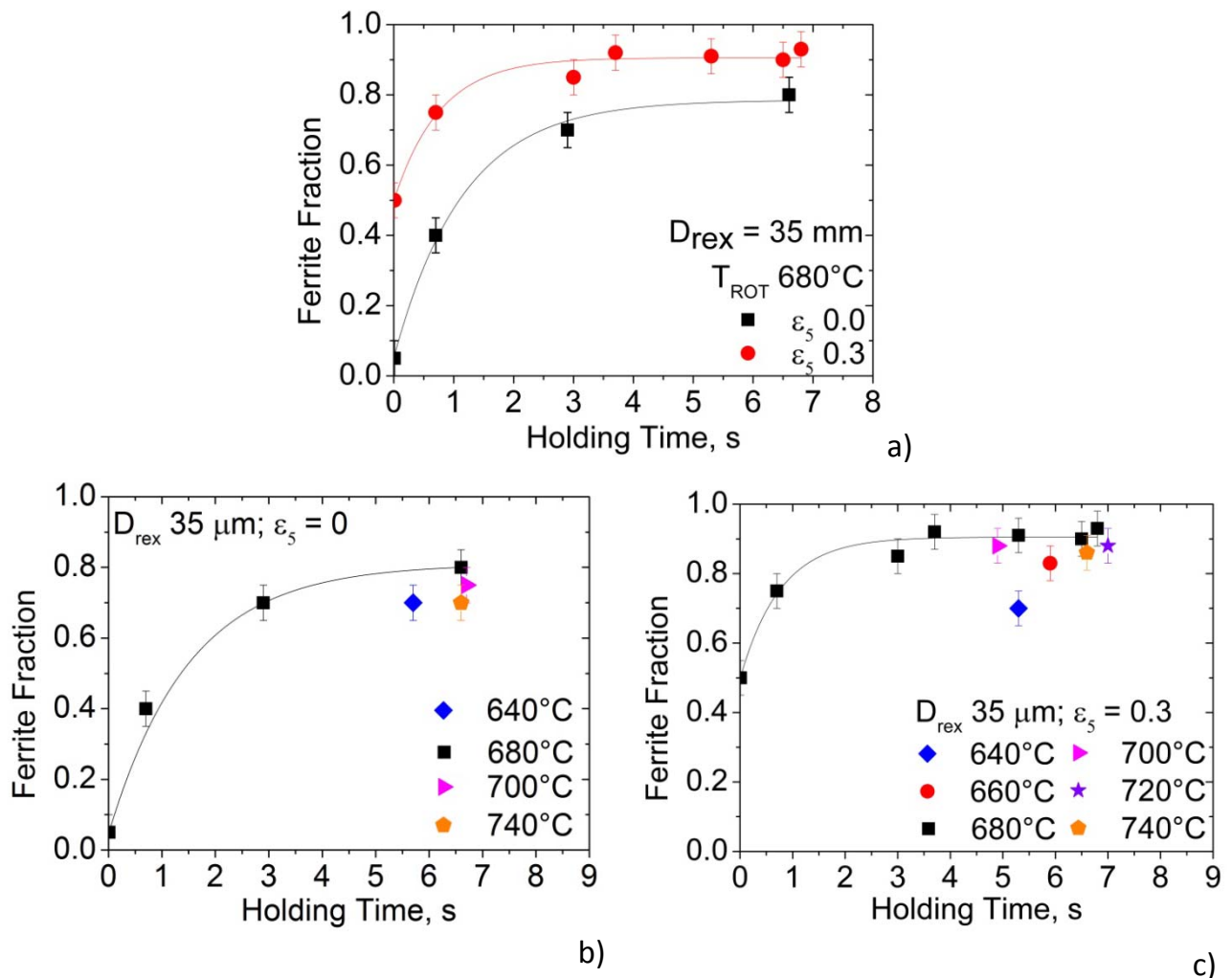


Fig. 41 The ferrite transformation kinetics in the Mn-Si DP steel from the austenite grain size of $35 \mu\text{m}$, which is the result of repeated recrystallisations according to the processing routes *Option B* and *D*. ε_5 indicates the deformation at 900°C . a) the effect of the retained strain on the transformation kinetics at 680°C b) the effect of transformation temperature, in case of no retained strain c) the effect of the transformation temperature, in case of a retained strain of 0.3.

Fig. 40b, Fig. 40c, Fig. 41b and Fig. 41c show the effect of the transformation temperature. The transformation kinetics in the Mn-Mo steel is the most prompt at 660 °C, if no retained strain supports. The transformation temperatures from 660 to 710°C give comparable results under the strain of 0.3 while those outside the range give a much lower ferrite fraction.

Comparing Fig. 40a with Fig. 36b, the transformation kinetics in Mn-Mo with austenite grain size of 25 μm are somewhat contradict to the results from 35 μm from the repeated recrystallisations. They predicted lower ferrite fraction at similar retained strain. This can refer to the incomplete recrystallisation, especially at the third deformation step at 950 °C as mentioned in section 4.1.4, which can leave some accumulated retained strain and therefore the actual retained strain can be higher.

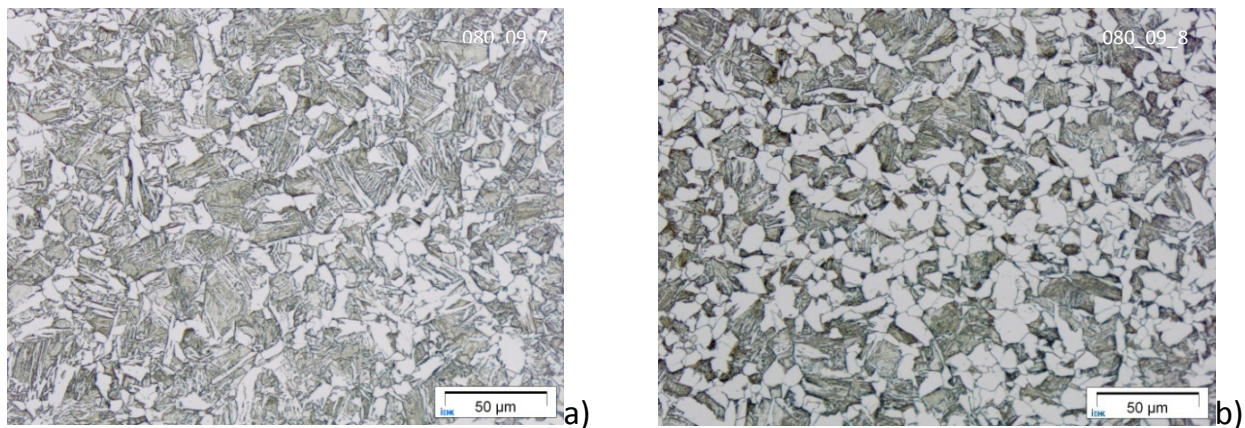


Fig. 42 The development of microstructure in Mn-Mo DP from an (calculated recrystallised) austenite grain size of 35 μm under no retained strain after the transformation time of a) 3 s and b) 6.9 s.

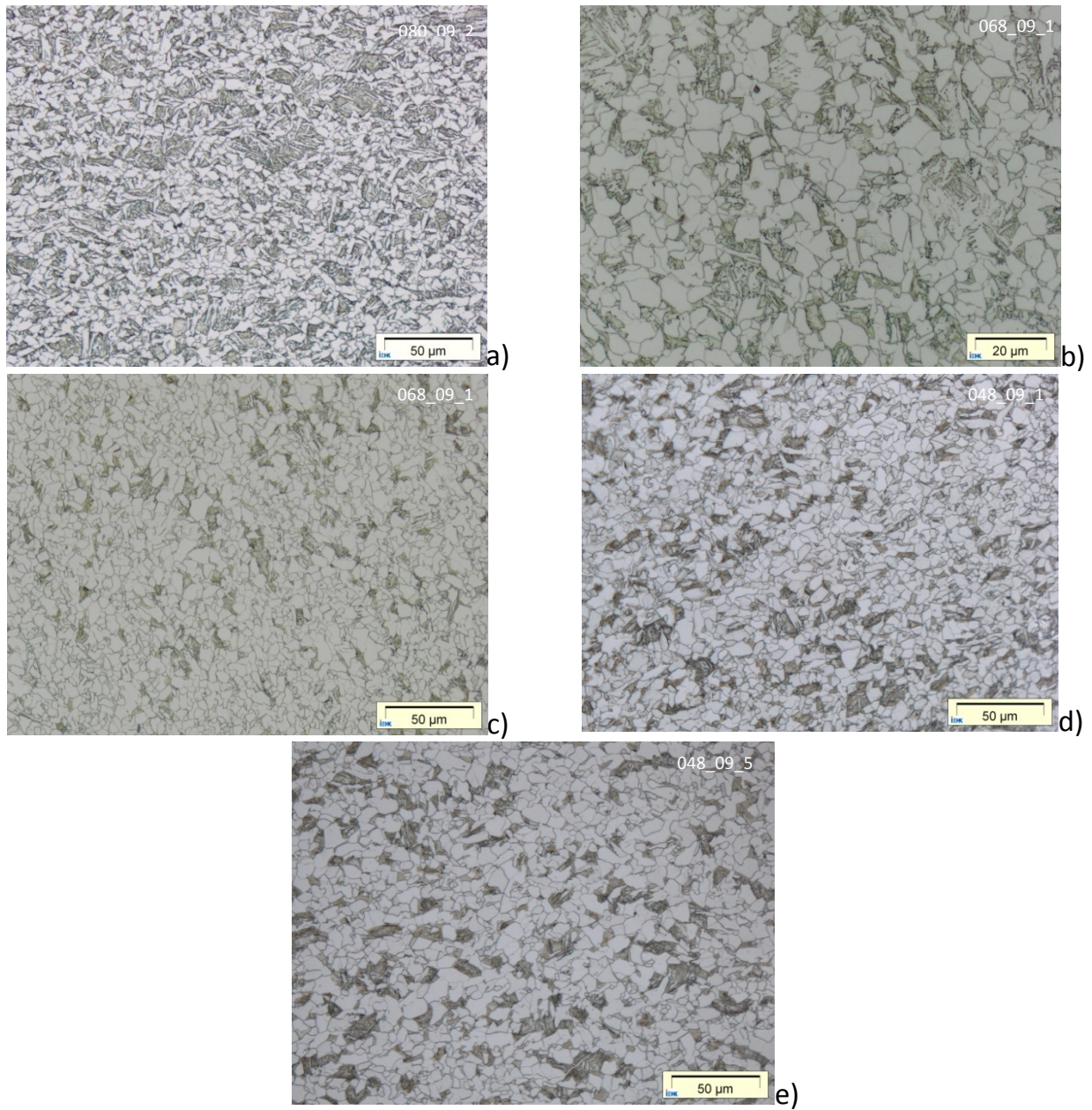


Fig. 43 The development of microstructure in Mn-Mo DP from an (calculated recrystallised) austenite grain size of 35 μm under a retained strain of 0.3 after the transformation time of a) 0.9 s b) 3.1 s c) 5 s d) 7.2 s and e) 9.5 s

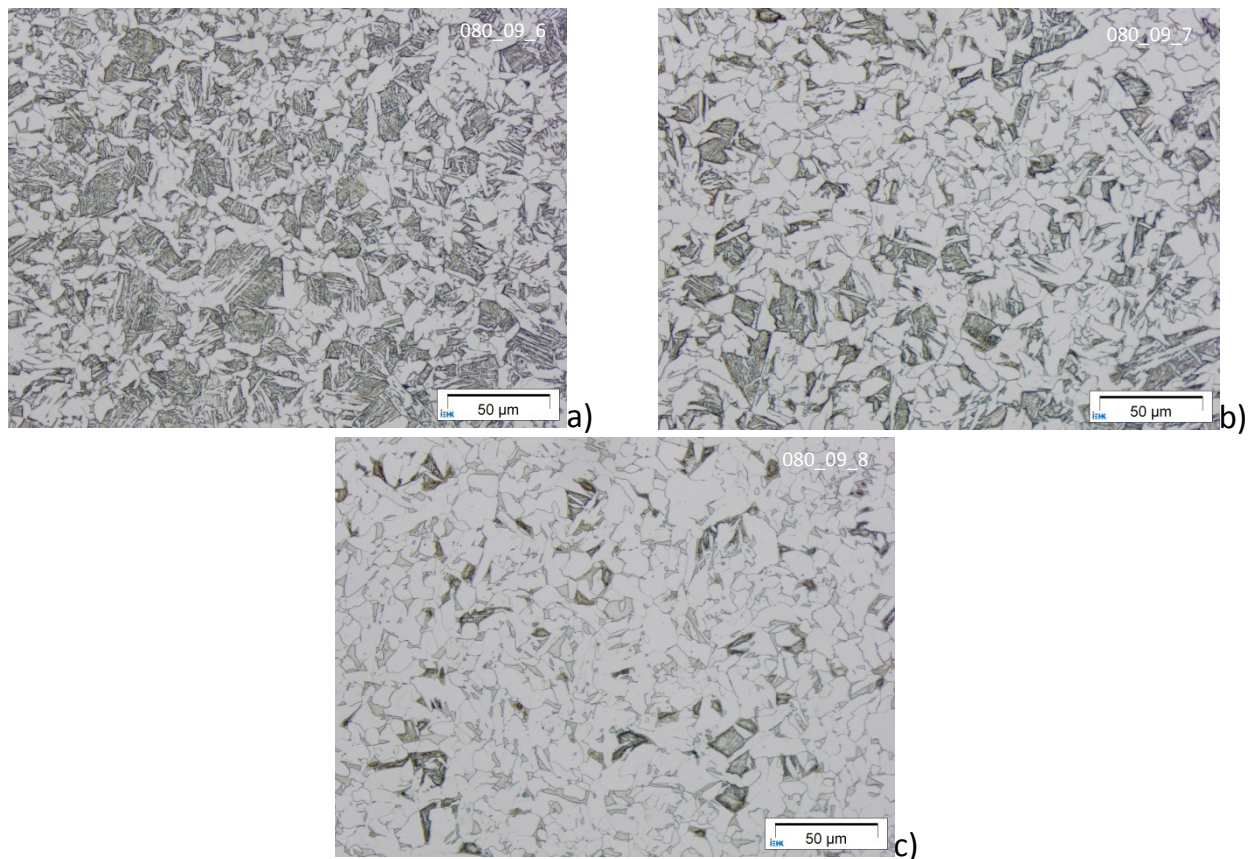


Fig. 44 The development of microstructure in Mn-Si DP from an (calculated recrystallised) austenite grain size of 35 μm under no retained strain after the transformation time of a) 0.7 s b) 2.9 s c) 6.6 s

Fig. 42 to Fig. 45 reveal the microstructure development in both the Mn-Mo and Mn-Si DP steels, whose transformation kinetics are quantitatively summarised previously in Fig. 40 and Fig. 41. These microstructures were also used to investigate the ferrite nucleation density in the studied rolling process and for the phase field simulation in section 5.6. The initial stage of ferrite formation, namely after only a small ferrite fraction, for example Fig. 42a, helps to prove the prior austenite grain boundaries after the repeated recrystallisations. The rough estimation of the recrystallised grain size as 35 μm by using Eq.16 from Liu [Liu07] repeatedly after each deformation step should be adequate.

Due to the high number of nucleation sites at such the refined austenite grains, the trace of the prior austenite grain boundaries is obscured just after a few further seconds of transformation (Fig. 42b). The retained strain accelerates it intensively so that the sequence of nucleation cannot be seen anymore in Fig. 43a to Fig. 43e.

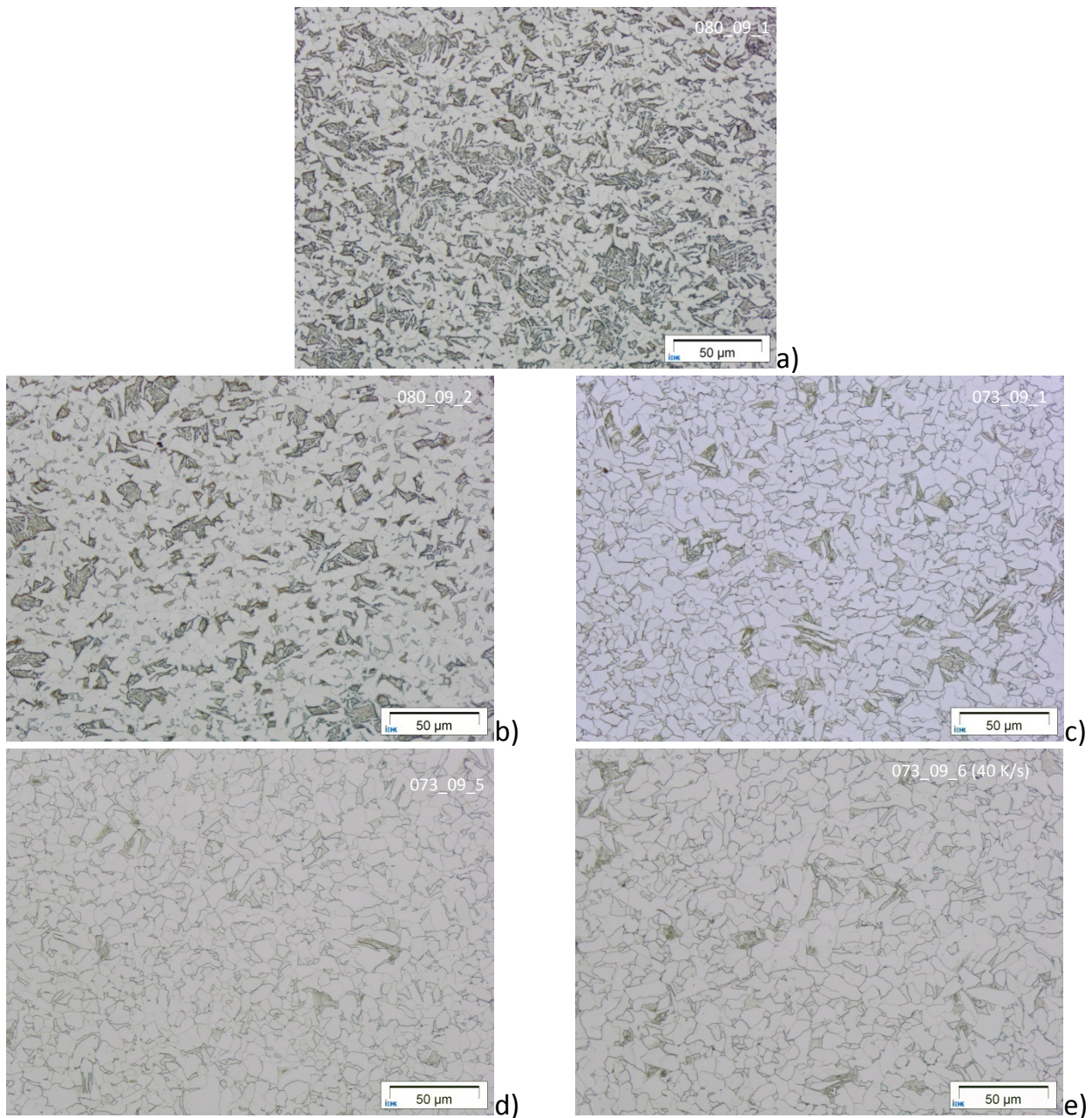


Fig. 45 The development of microstructure in Mn-Si DP from an (calculated recrystallised) austenite grain size of 35 μm under a retained strain of 0.3 after the transformation time of a) 0.01 s b) 0.7 s c) 3 s d) 3.7 s and e) 6.5 s

The stepwise quenching can ‘freeze’ the nucleation sequence in the Mn-Si steel only to a little extent as demonstrated in Fig. 44 and Fig. 45 as the transformation is nearly complete within only the first few seconds. It is also very likely that ferrite formation starts before the temperature reached the isothermal transformation temperatures.

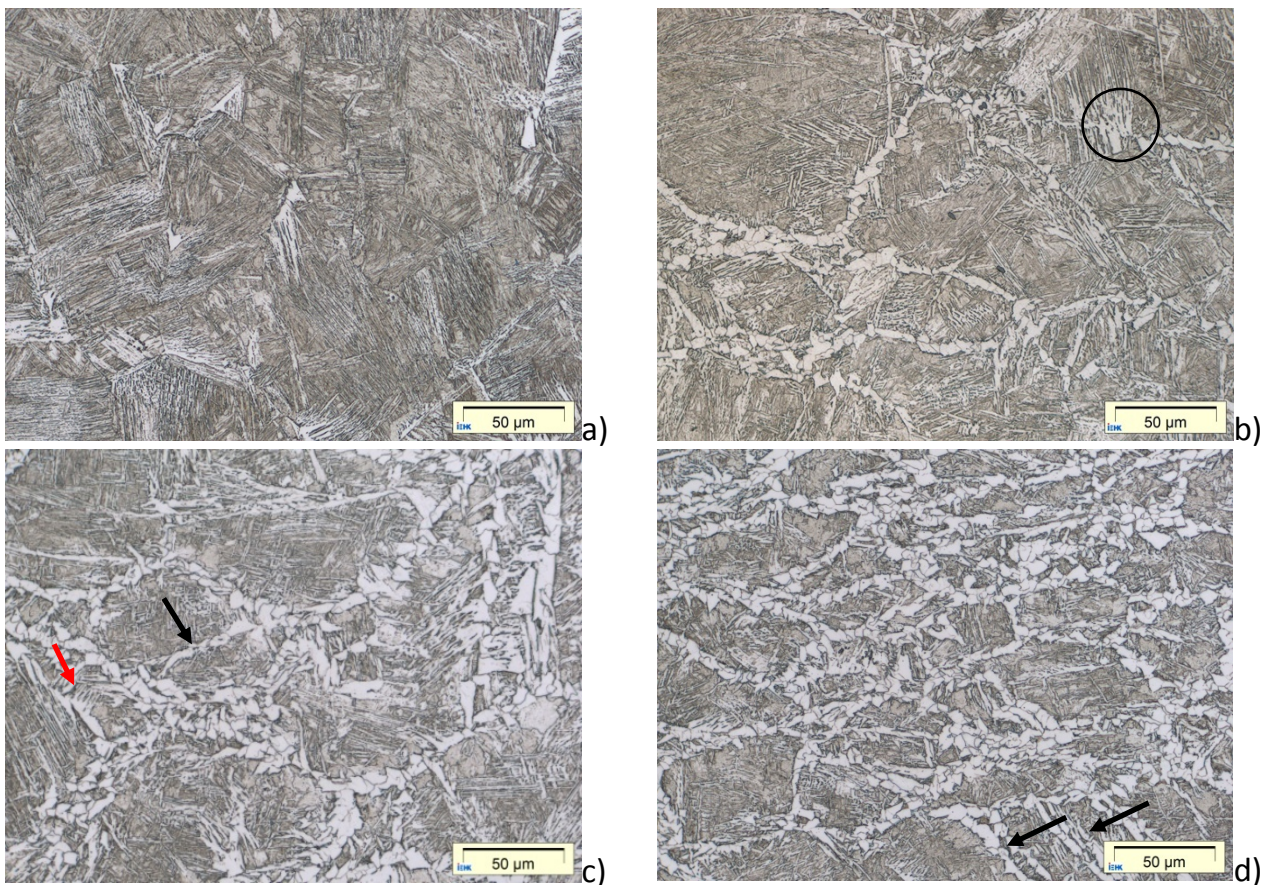


Fig. 46 The microstructure development after 3 s of transformation in the Mn-Mo DP having the austenite grain size of 100 μm with different degree of deformation. ε_5 indicates the deformation at 830 $^{\circ}\text{C}$. a) ε_5 of 0.0; trace of ferrite b) ε_5 of 0.2; 7% ferrite c) ε_5 of 0.4; 20% ferrite d) ε_5 of 0.6; 25% ferrite

A different microstructure development in the Mn-Mo DP steel can be seen Fig. 46 (3 s) and Fig. 47 (7 s). The austenite conditioning was done as listed as *Option C* in Table 3.3. The prior austenite grain size before the ferrite transformation is 100 μm . It is not directly relevant to the hot rolling process window but shows a significant influence of the retained strain on the ferrite transformation. The nucleation sites, which are the triple junction/grain boundaries and bulk, can be differentiated clearly. This case was therefore selected to study the austenite to ferrite transformation under the influence of deformation by phase field modelling as published elsewhere [Suw09]. At lower degrees of retained strain and/or shorter holding times, only single rings of ferrite grains decorate the prior austenite grain boundaries. It can be seen that afterwards, more ferrite grains nucleate next to the existing ferrite rings, as the boundary between austenite and ferrite can be fresh nucleation sites. The ferrite fraction rises only up to 0.62 after 7 s transformation time under the retained strain of 0.6. This indicates that this austenite conditioning is not the most appropriate for the process window of hot rolled DP steels.

Pointed by black arrows in Fig. 46, some ferrite grains nucleate at some straight lines making some angles to the prior austenite grains, which are now surrounded by ferrite grains. These straight lines can be most probably deformation bands, which appear more at higher strains.

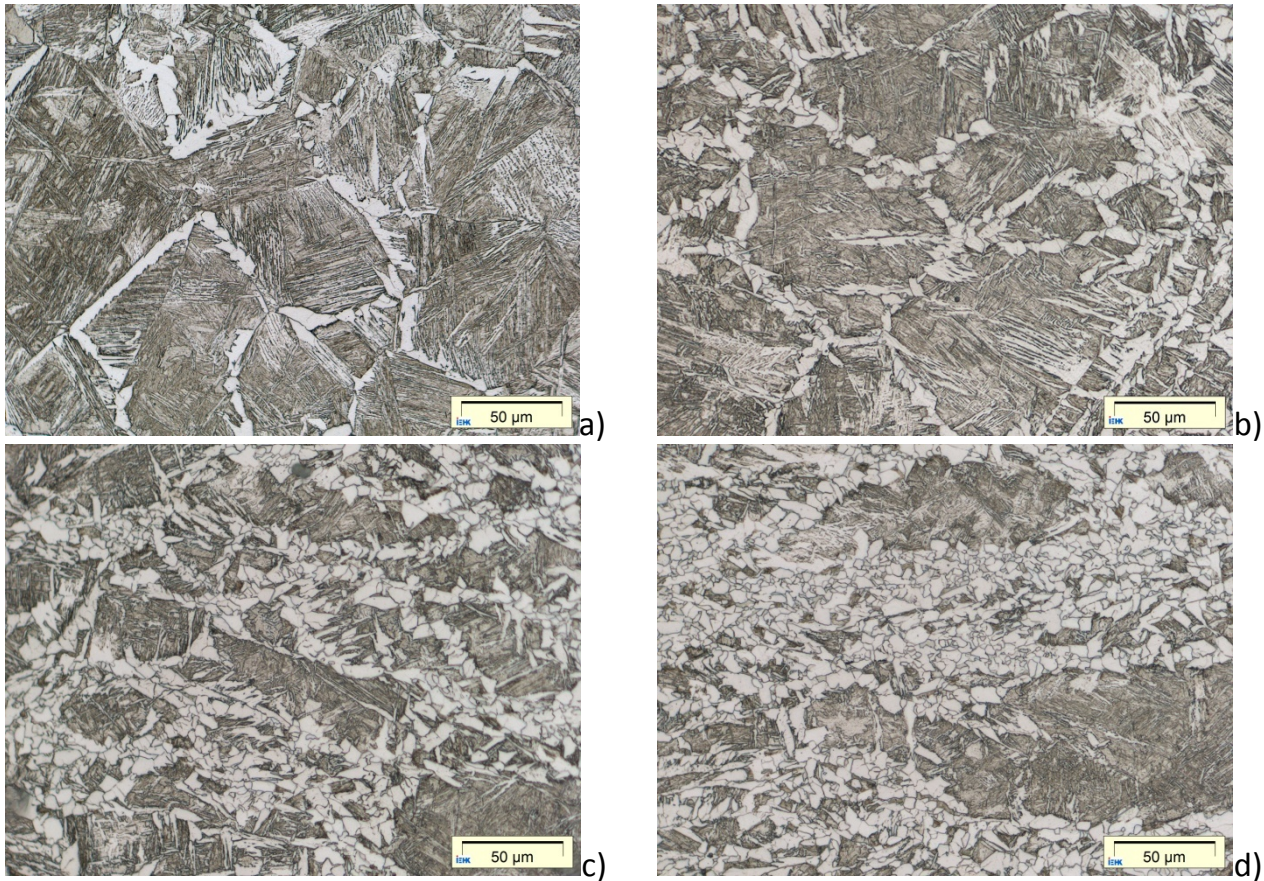


Fig. 47 The microstructure development after 7 s of transformation in the Mn-Mo DP having the austenite grain size of 100 μm with different degree of deformation. ε_5 indicates the deformation at 830 $^{\circ}\text{C}$. a) ε_5 of 0.0; 4% ferrite b) ε_5 of 0.2; 23% ferrite c) ε_5 of 0.4; 39% ferrite d) ε_5 of 0.6; 62% ferrite

At the initial stage of ferrite formation, a few different morphologies of ferrite appear. The prior austenite grain boundaries are dominated by allotriomorphic ferrite and Widmanstätten ferrite (or ferrite sideplate). A Widmanstätten ferrite has a longer grain along the prior austenite grain boundary and has some spikes perpendicular to the alignment of its grain and is pointed out by a red arrow in Fig. 46c. Some grains appear as globular bainitic ferrite and are highlighted with circles. Both side plate ferrite and bainitic ferrite should have transformed during quenching down to the room temperature as their critical temperatures are lower than the holding temperature of 680 $^{\circ}\text{C}$.

4.1.7 Plane strain compression at hot deformation dilatometer

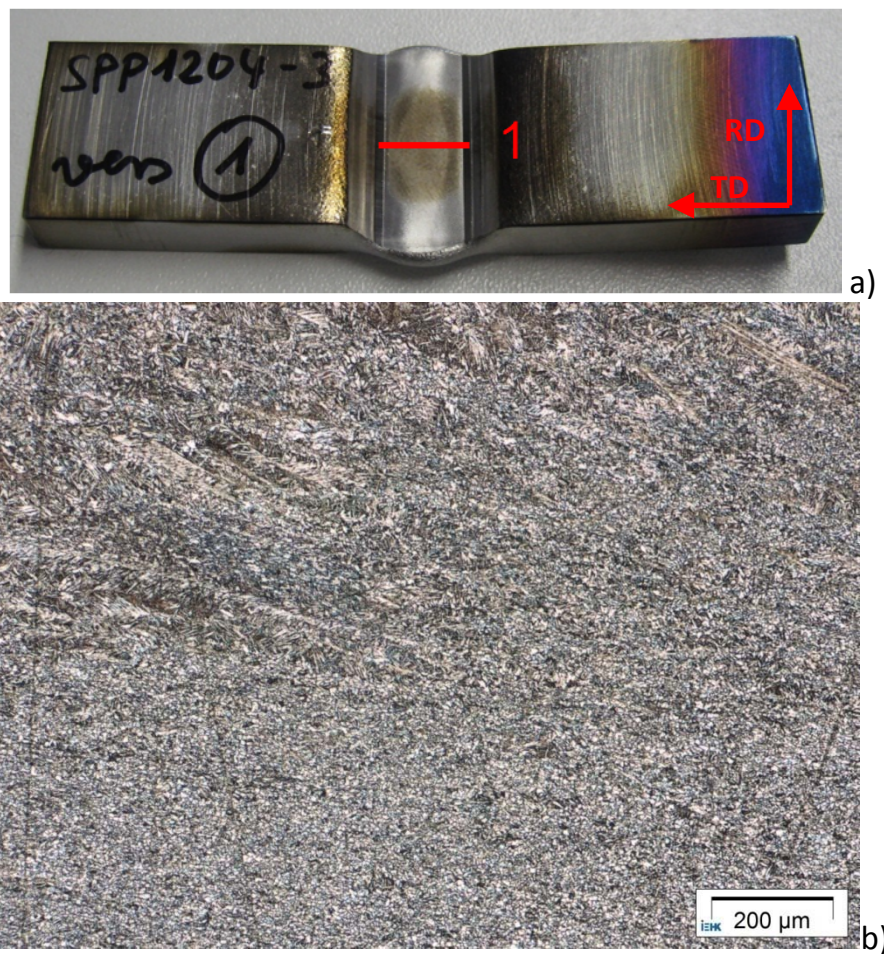


Fig. 48 The microstructure yielded from the thermomechanical process *Option D* in Table 3.3 performed in a small bar sample in the hot deformation dilatometer TTS820 with plane strain compression heads. a) the deformed sample b) the microstructure at the cross section number 1.

The thermomechanical process *Option D: 'Rolling Option'* in Table 3.3 was forwarded to a plane strain compression test at the hot deformation dilatometer TTS820. The sample was deformed only at the middle of the sample length with a flat deformation punch along the sample width, (here rolling direction). Cross sections along the sample length, or transverse direction, were investigated for the microstructure. The microstructure at cross section no.1 is illustrated in Fig. 48. The microstructure on the top part of the micrograph represents the part farer away from the centre line of the cross section and reveals less ferrite fraction. The lower part, which is closer to the centre line, shows more homogenous microstructure.

4.1.8 Ferrite grain size and the ferrite nucleation density

All the ferrite grains from the microstructures in Fig. 42 and Fig. 45 were measured manually by converting the area of the grain surface into EQAD. The number of ferrite grains (or nucleation density) and ferrite nuclei/grain size in both steels are summarised in Fig. 49. It is not possible to differentiate the ferrite grains nucleated at the triple points, grain surfaces/boundaries and in the bulk, especially at the latter stage of transformation. Therefore only the total nucleation densities are taken.

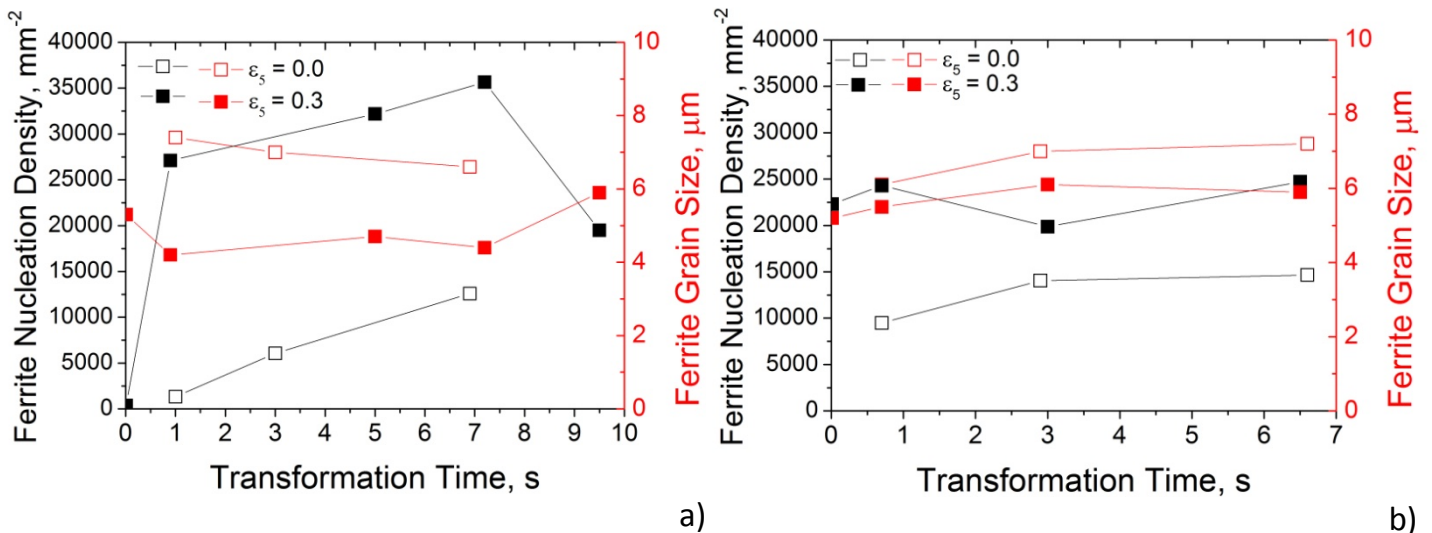


Fig. 49 The ferrite nucleation density and nuclei/grain size in a) the Mn-Mo DP steel and b) the Mn-Si DP steel

It is obvious that the ferrite nucleation is extremely enhanced by deformation especially in the Mn-Mo DP steel. Moreover, deformation refines the ferrite grain size to less than 1 μm. The large drop in the number of ferrite grains at 9.5 s in the Mn-Mo DP steel can be a result of the agglomeration. It results in the increase of the grain size for more than 1 μm.

4.1.9 The hardenability of austenite after carbon partitioning

The CCT diagrams of the remaining austenite after the ferrite transformation, which are called ‘*modified CCT diagrams*’ are displayed in Fig. 50 and Fig. 52 for the Mn-Mo and Mn-Si DP steels respectively.

Fig. 50 points out the hardenability of the remaining austenite in the Mn-Mo steel with the carbon content of 0.12%, after a ferrite fraction of 0.4 is formed, with the carbon content of 0.2%, after a ferrite fraction of 0.7 is formed, and with the carbon content of 0.3%, after a ferrite fraction of 0.8 is formed, respectively. The carbon contents shown here are the

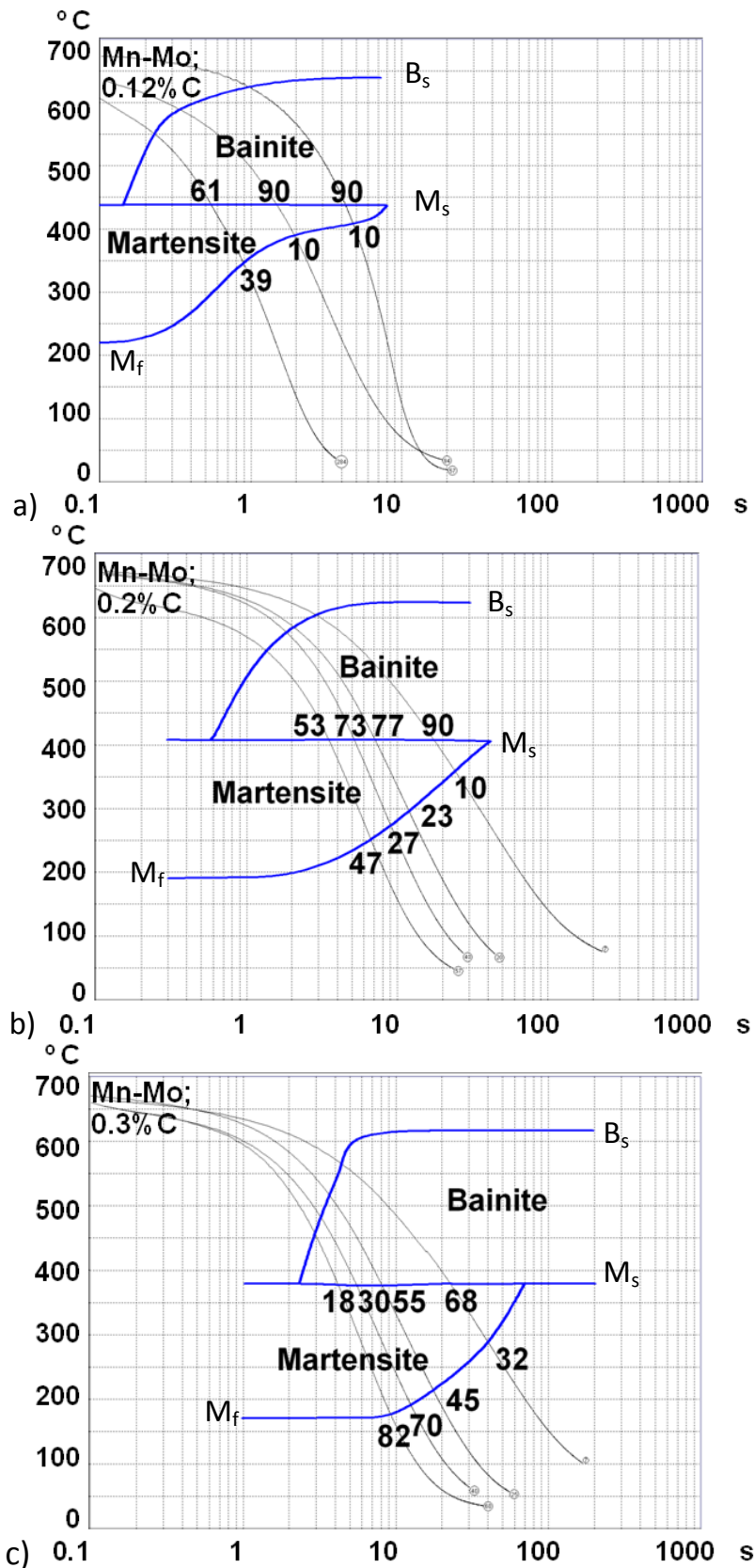


Fig. 50 The 'modified CCT diagrams' of the Mn-Mo DP showing the hardenability of the remaining austenite after the ferrite formation and carbon partitioning. The numbers represent the percentages of bainite and martensite compared only with the volume of the remaining austenite (a) with carbon content of 0.12%, after a ferrite fraction of 0.4 is formed (b) with carbon content of 0.2%, after a ferrite fraction of 0.7 is formed (c) with carbon content of 0.3%, after a ferrite fraction of 0.8 is formed.

calculated average carbon content according to the mean field method, or in other words, carbon mass balance, which will be represented in section 5.4.1.

The critical temperatures were calculated after taking the carbon partitioning into account, which will be shown in the next chapter. The numbers in the diagram indicate the percentages of martensite and bainite transformed through the cooling profiles. The percentages were calculated by ignoring the previously transformed part. A cooling rate up to 60 °C/s was obtained in the cylinder dilatometer samples. The higher cooling rates come from the flat samples.

As the total fraction of martensite and bainite contributes to only 20-30% of the sample volume, the dilatation signal during this transformation is extremely weak. Therefore the critical temperatures were taken from the empirical equations in Eq. 54 and Eq.62. The martensite finish temperature (M_f) was taken to be 215 °C lower than the calculated martensite start temperature (M_s) [Pet70].

It is rather clear that with higher fraction of ferrite, the carbon content in the remaining austenite becomes higher. Bainite and martensite bays move to the right hand side with the higher carbon content, as generally defined as higher hardenability of austenite. With this, the higher cooling rates result in less bainite fraction and larger martensite fraction. In the window of these experimental parameters, the Mn-Mo DP steel still results in at least some bainite even at the highest carbon content and fastest cooling rate. The critical temperatures are also lowered by updating the carbon content in the empirical equations.

Similarly, the hardenability of the Mn-Si DP steel is represented in Fig. 51 and Fig. 52. Contradictory, 100% percent of martensite can be obtained in the Mn-Si DP steel even at the lowest carbon content. More martensite can be achieved at lower cooling rates than those in the Mn-Mo steel. At the carbon content of 0.55%, a little pearlite was discovered at slower cooling rates.

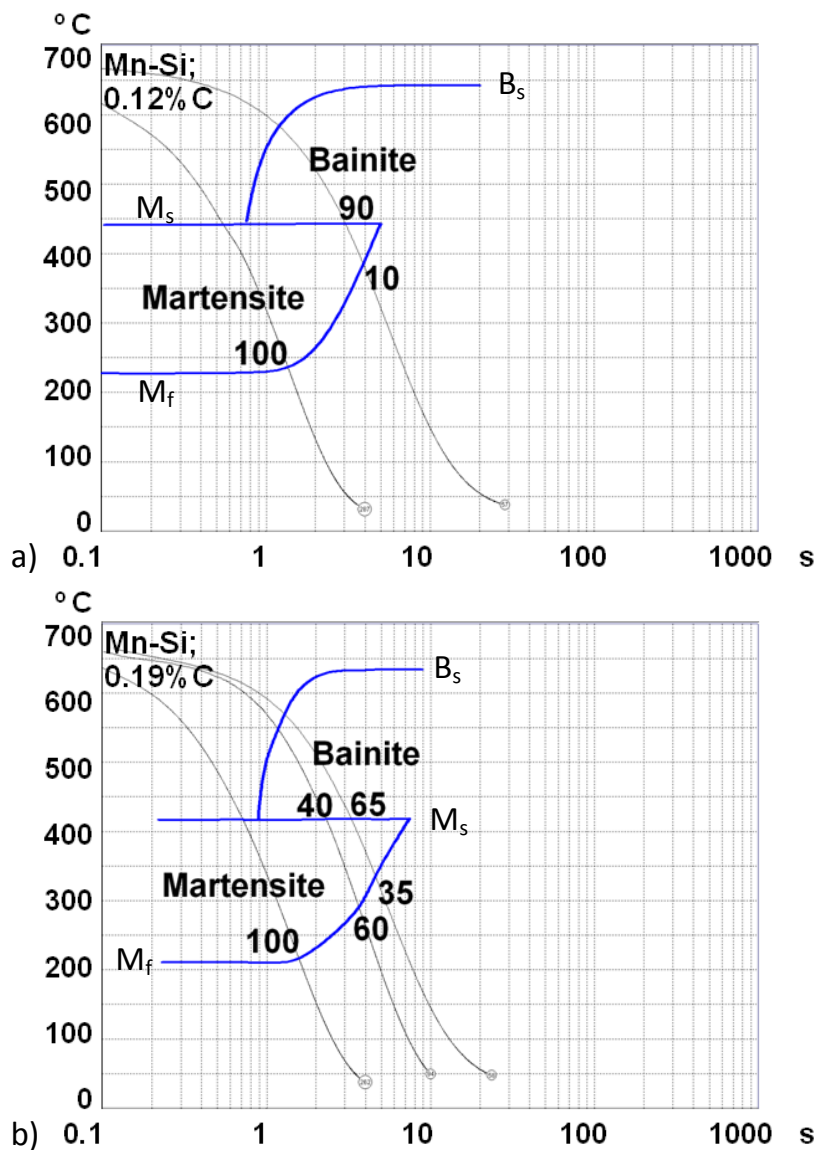


Fig. 51 The 'modified CCT diagrams' of the Mn-Si DP steel showing the hardenability of the remaining austenite after the ferrite formation and carbon partitioning. The numbers represent the percentages of bainite and martensite compared only with the volume of the remaining austenite (a) with carbon content of 0.12%, after a ferrite fraction of 0.5 is formed (b) with carbon content of 0.19%, after a ferrite fraction of 0.7 is formed

Under different cooling rates, the area inside the martensite/bainite (and possibly retained austenite) (here M/B/RA) constituent has different morphologies of bainite as shown in Fig. 53 and Fig. 54. Low carbon bainite appears in the middle of large M/B/RA islands obviously at lower cooling rates such as in Fig. 53 (7 °C/s). Only the narrow outer region of the islands becomes martensite. This is the best evidence of the carbon gradient profile austenite islands. The austenite islands in the Mn-Mo steel are relatively large because of the lower ferrite fraction. It is therefore advantageous for the investigation of such the carbon profile.

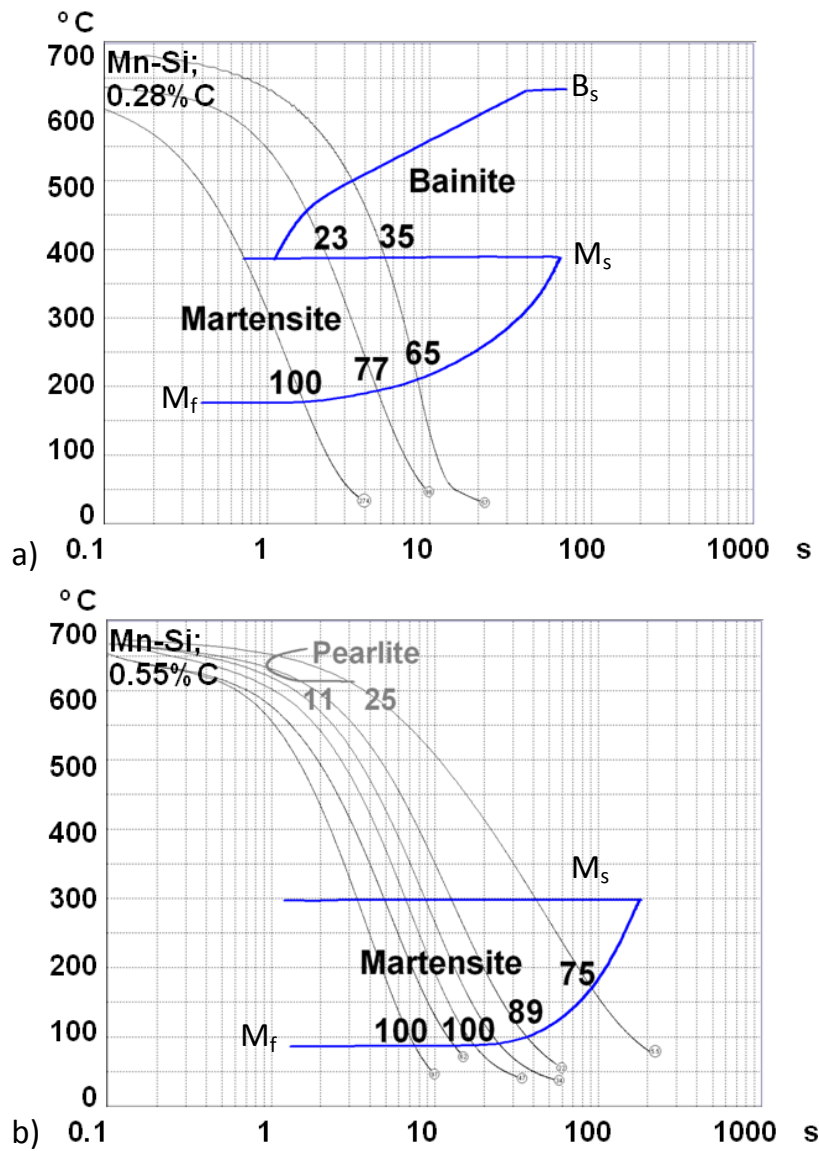


Fig. 52 The 'modified CCT diagrams' of the Mn-Si DP steel showing the hardenability of the remaining austenite after the ferrite formation and carbon partitioning. The numbers represent the percentages of bainite and martensite compared only with the volume of the remaining austenite (a) with carbon content of 0.28%, after a ferrite fraction of 0.8 is formed (b) with carbon content of 0.55%, after a ferrite fraction of 0.9 is formed.

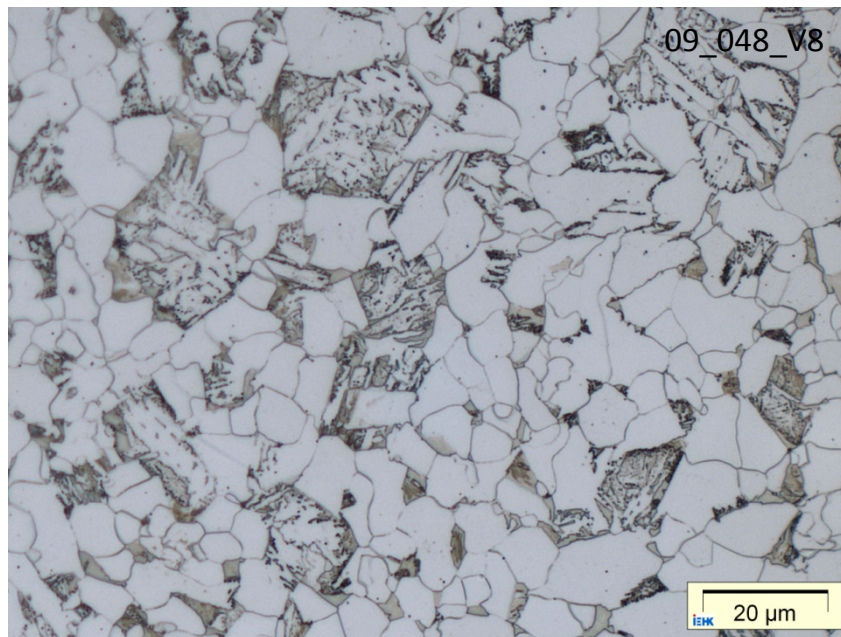


Fig. 53 The microstructure of the Mn-Mo DP steel after the processing route *Option B* in Table 3.3. Ferrite formed at 680 °C for 7.7 s. Then the sample was cooled slowly with a total cooling rate of 7 °C/s, measured from 600 °C to 200 °C. Low carbon bainite dominates the inner part of large former remaining austenite island while martensite appears only in the narrow outer ring. Small former austenite islands become martensite islands. Trace of pearlite can be seen in the higher carbon area, say, the outer ring of large austenite islands or in the small austenite islands.

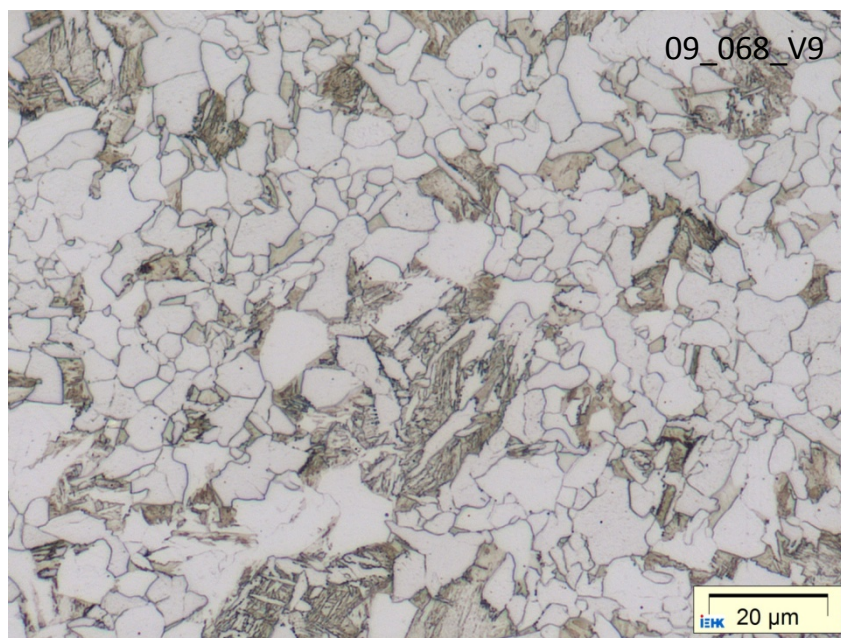


Fig. 54 The microstructure of the Mn-Mo DP steel after the processing route *Option B* in Table 3.3. Ferrite formed at 660 °C for 7.7 s. Then the sample was cooled with a total cooling rate of 58 °C/s, measured from 600 °C to 200 °C.

Only slight difference in the phases in the austenite island can be seen at a high cooling rate such as 58 °C/s such in Fig. 54. The islands consist of the mixture of martensite and bainite, which can be little distinguished at some locations. But the tendency to have only martensite in the smaller islands remains and it is evident that bainite still appears in the middle in very large islands.

The samples from the Mo-Mn steel were further analysed for the more accurate bainite and martensite fraction by means of SEM, especially for higher accuracy of the modified CCT diagrams. Fig. 55 and Fig. 56 are examples of the results. They are from the same sample but different locations. Fig. 55 focuses on the area with large M/B/A islands and Fig. 56 shows the area with small islands.

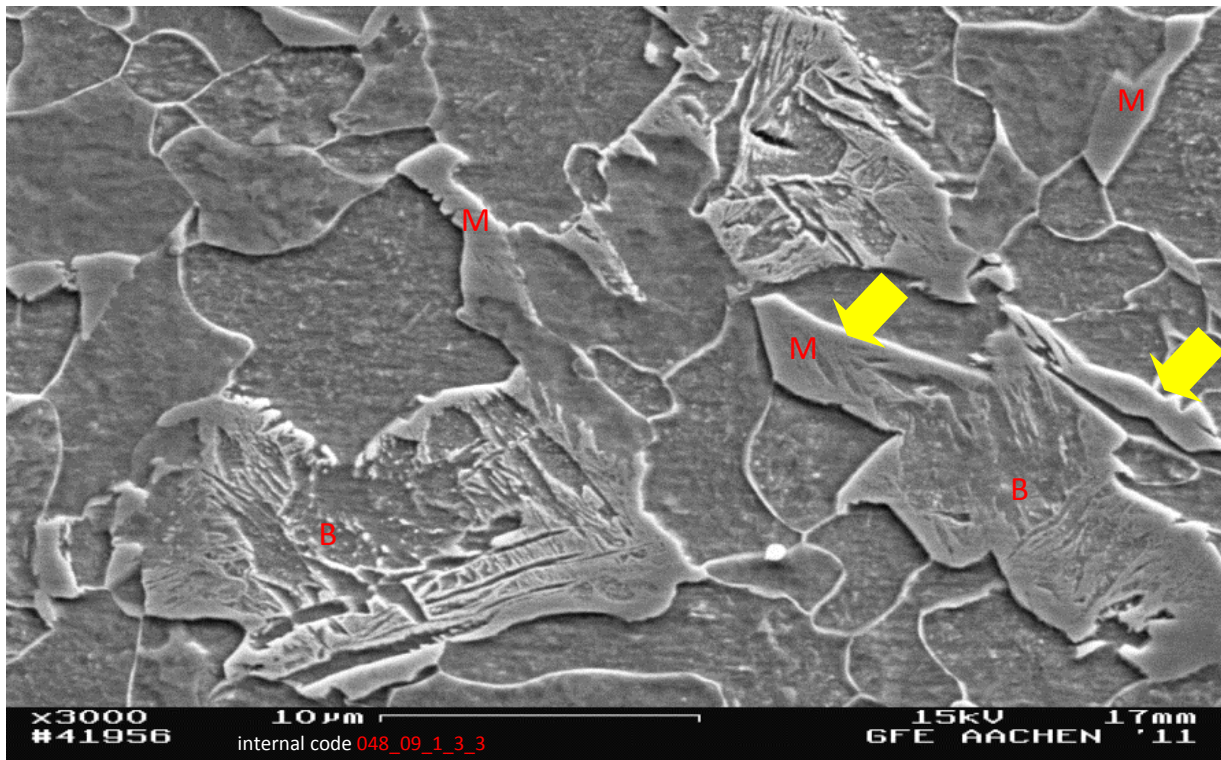


Fig. 55 The microstructure under SEM of Mn-Mo DP steel containing ferrite fraction of 0.74 which was quenched with a cooling rate of 67 °C/s after the ferrite formation. This micrograph shows the area with large M/B/A islands. B – area of bainite, M – area of martensite, the yellow arrows show the areas suspicious to contribute to retained austenite fraction.

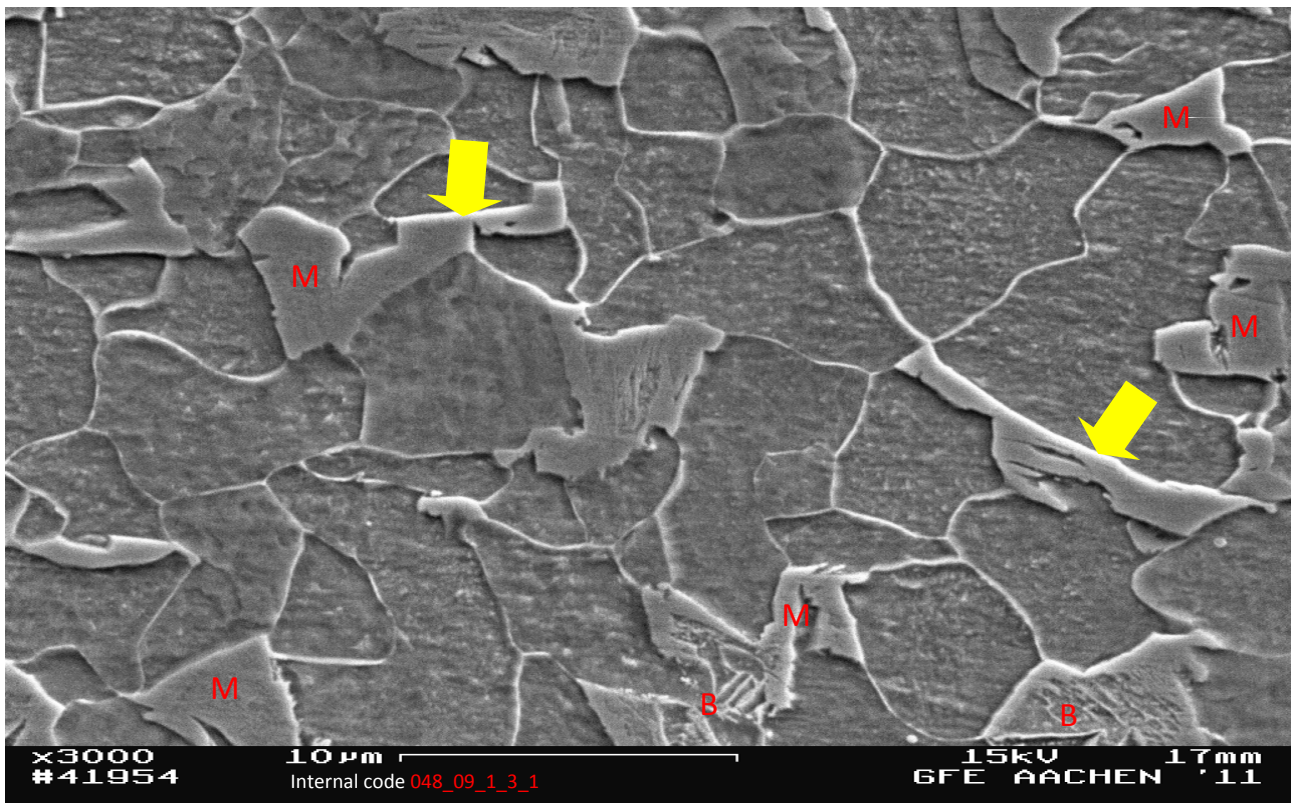


Fig. 56 The microstructure under SEM from the same sample as in Fig. 55. (Mo DP steel containing ferrite fraction of 0.74, quenched with a cooling rate of 67 °C/s). This micrograph shows the area with small M/B/A islands. B – area of bainite, M – area of martensite, the yellow arrows show the areas suspicious to contribute to retained austenite fraction.

It is clear that in Fig. 55, the rough lath-like areas correspond to bainite while the smoother areas belong to martensite. Less difference in roughness is seen in Fig. 56. The outer edge of the M/B/RA constituents appears shiny in both cases. Many are also straight or rectangular. These areas are suspected to contain some retained austenite. The retained austenite was further proven by other characterisation techniques for this reason.

The phase map by EBSD, presented in Fig. 57, performed on the same sample as shown in Fig. 54. It shows the retained austenite as green area, whose total is 0.4% by the step size of 120 nm and 0.8% with by the step size of 40 nm, respectively. The alternative measurement of retained austenite by means of XRD reports the retained austenite in order of 4%.

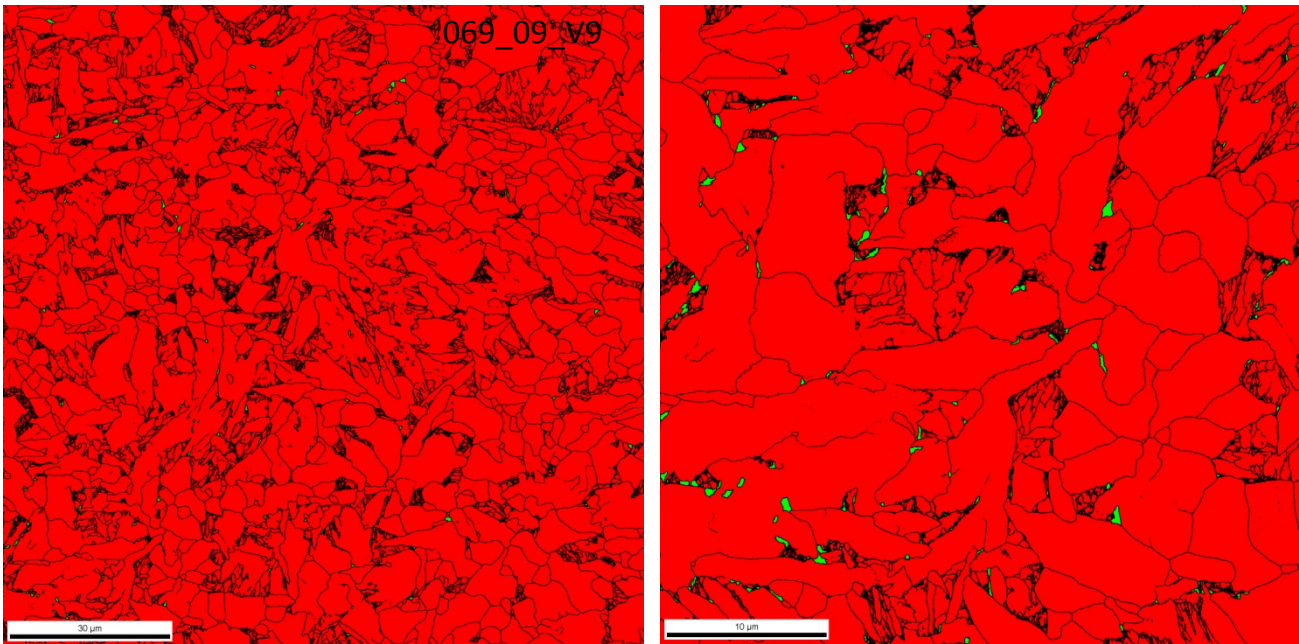


Fig. 57 The phase maps by means of EBSD carried out in the sample shown in Fig. 54. The green area represents the retained austenite. a) 0.4% by the step size of 120 nm b) 0.8% by the step size of 40 nm

Astonishing results come from the magnetic induction measurement, which discovers 14-19% of retained austenite in some samples of the Mn-Mo steel. The percentage of retained austenite in the sample in Fig. 54 (and Fig. 57) was determined to be 9.8.

A simple further investigation was therefore carried out as a trial by etching some samples with nital solution for a minute. Some topography can be detected due to the fact that the retained austenite, having the highest carbon content among all the constituents, is etched to a lesser degree. Fig. 58 reveals again a microstructure of the sample in Fig. 54 (and Fig. 57) after the deep etching. The white thin layers adjacent to the martensite/bainite islands, can most probably correspond to the retained austenite. The percentage of the white layer amounts to approximately 5%.

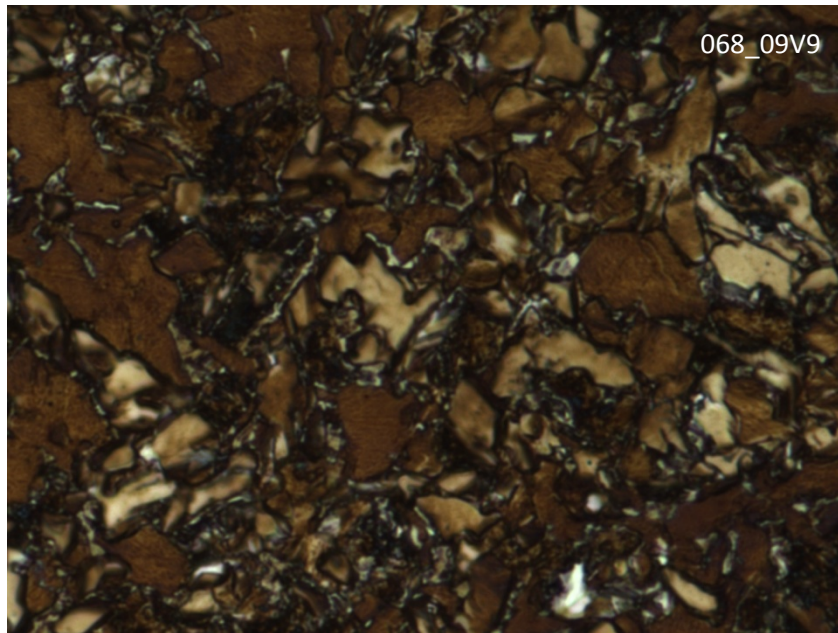


Fig. 58 The microstructure of the sample in Fig. 54 and Fig. 57 etched with nital solution for a minute. White thin layers are the suspicious areas of the retained austenite.

Other results come from the new generation FEG EPMA, by which the relatively exact carbon content in the microstructure can be measured due to the small electron beam. However, it was employed to measure the carbon content only in another sample of the Mn-Mo DP steel, whose retained austenite of 18.1% was detected by the magnetic induction and of 4.6% by XRD.

The quantitative measurement (Fig. 59) scanned through an area composed of several ferrite grains and M/B/RA constituents, for which the backscattered electron and secondary electron micrographs acted as a guideline. The scan length is 20 μm . The islands showing topography are expected to be the M/B/RA constituent. Its boundary, which corresponds to position 1 and 2, shows higher carbon content, up to 0.6% C. This can be a good proof for the retained austenite. Between position 1 and 2, namely in the middle of the M/B/RA constituent island, the carbon content as low as that of the nominal carbon content (0.073% C) is detected. This can be illustrated in more details in Fig. 60 and Fig. 61, in the qualitative element mapping, which has been done on different areas to avoid carbon contamination. All the substitutional solute elements have relatively homogenous distribution, which is not the case of cold-rolled DP steels, in which Mn and Si make partitioning [Pin12].

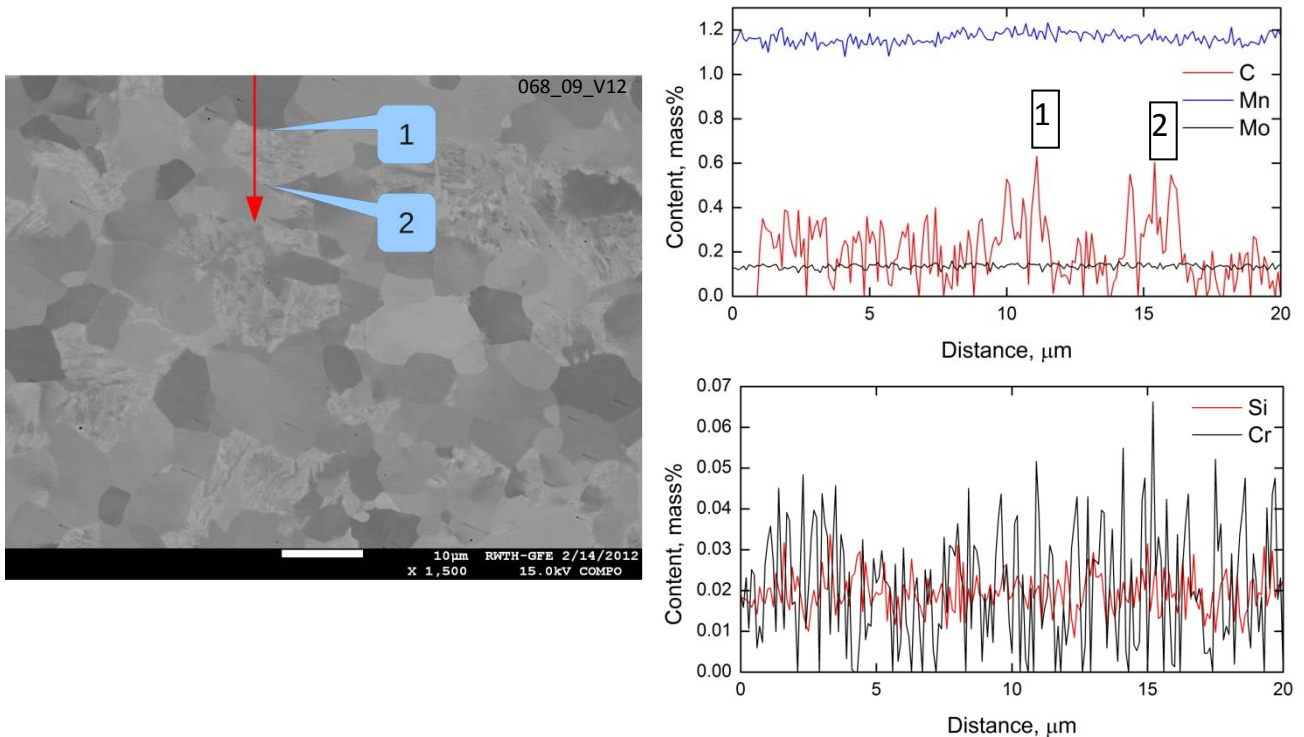
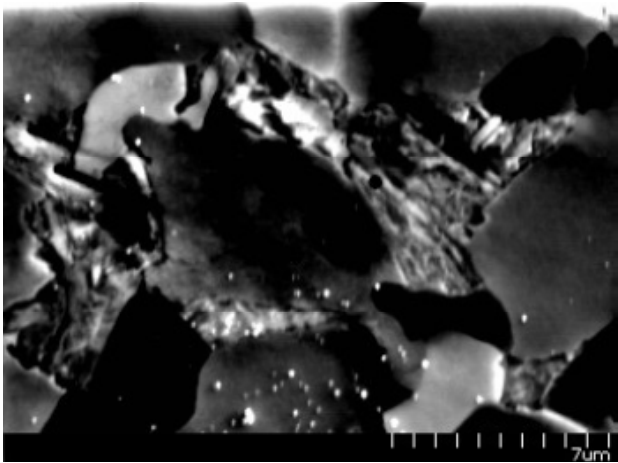


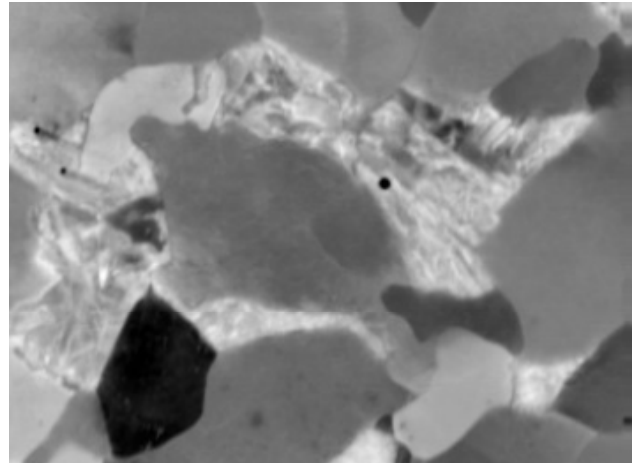
Fig. 59 A quantitative FEG EPMA line scan showing the content of 5 elements across an area including a large M/B/RA islands in a Mn-Mo sample. The areas showing topography relate to the M/B/RA islands. The total length of the line scan is 20 μm . The retained austenite was measured by magnetic induction as 18.1% and by XRD as 4.6%.

The picture from the backscattered electron shows the M/B/RA islands as rough areas and shows ferrite grains flat. The analysis of the carbon distribution consequently focuses on the rough areas.

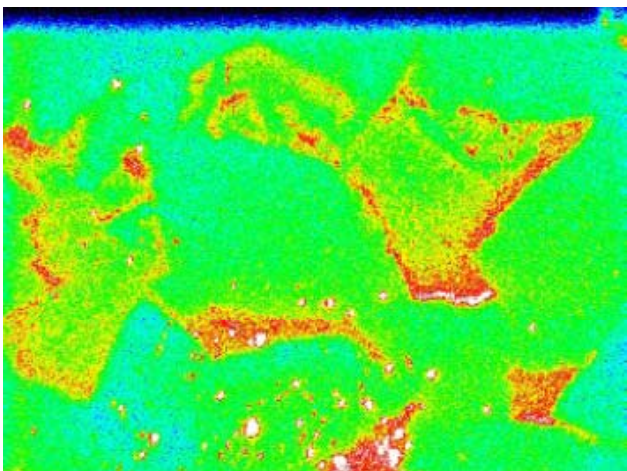
Red colour shows the areas with the highest level of carbon content and some parts can represent the retained austenite. They are relatively thin layers encircling the M/B/RA islands, corresponding to the findings in Fig. 53, Fig. 55, Fig. 56 and Fig. 58. The middle of the M/B/RA islands shows as low carbon content as that in ferrite grains. The white spots/areas do not show high carbon content areas but artefacts. In sum, the carbon diffusion distance in this steel during the ferrite formation is surprisingly short and the carbon content in the M/B/RA constituents is not homogeneous. The areas enriched with carbon are only around the M/B/RA islands and it results in the relatively high fraction of retained austenite in such the low carbon steel.



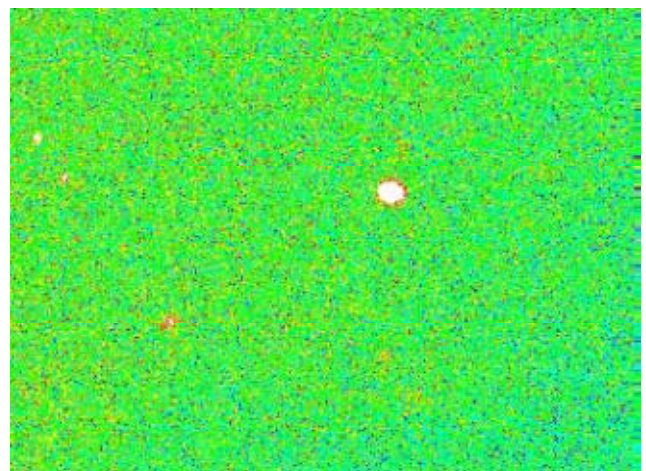
Secondary Electron



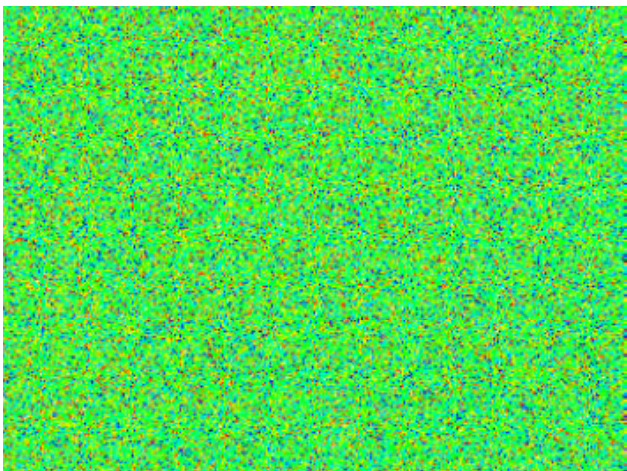
Backscattered electron



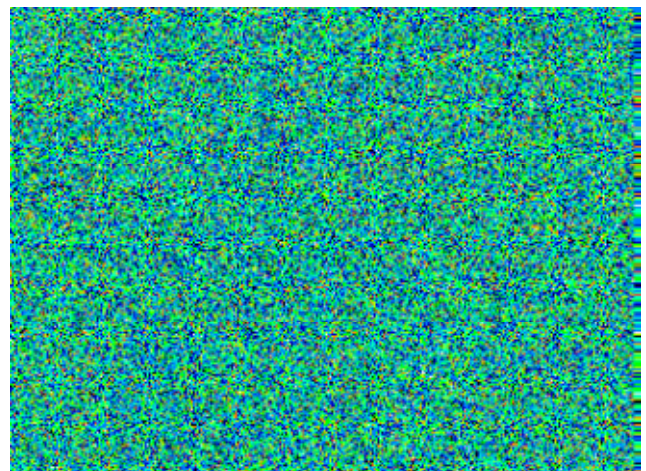
C



Mn

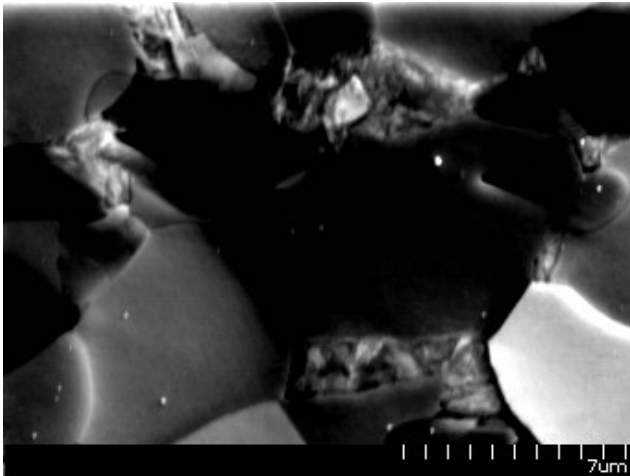


Mo

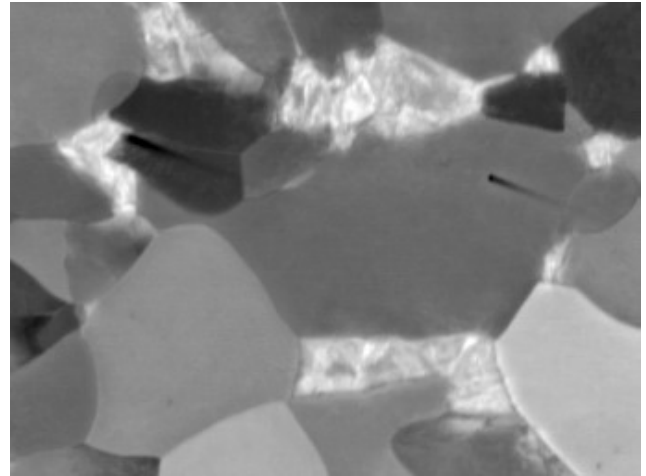


Cr

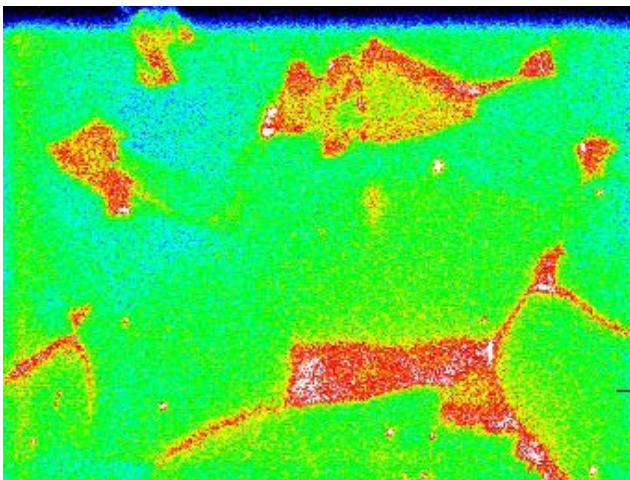
Fig. 60 Qualitative mappings of 5 elements by means of the FEG EPMA on the same sample as Fig. 59. The mappings were performed at 15 keV and 100 nA. The scan position is not related to the line scan in Fig. 59.



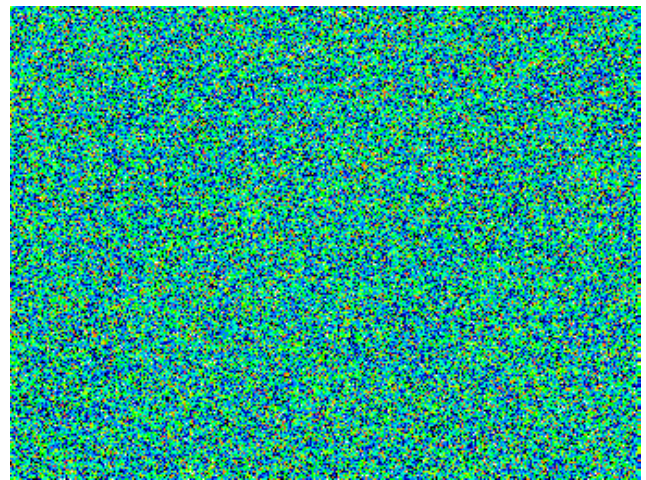
Secondary Electron



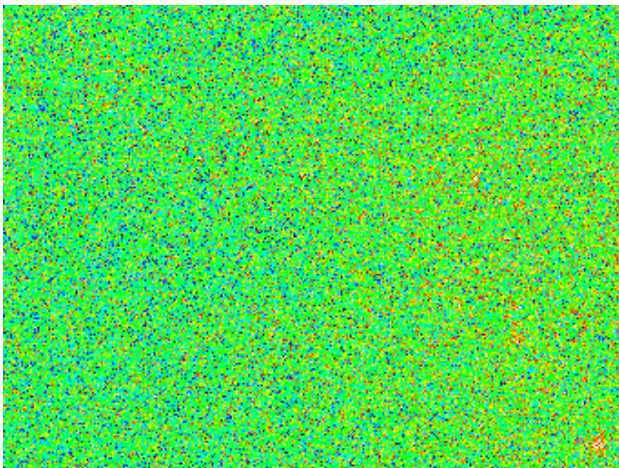
Backscattered Electron



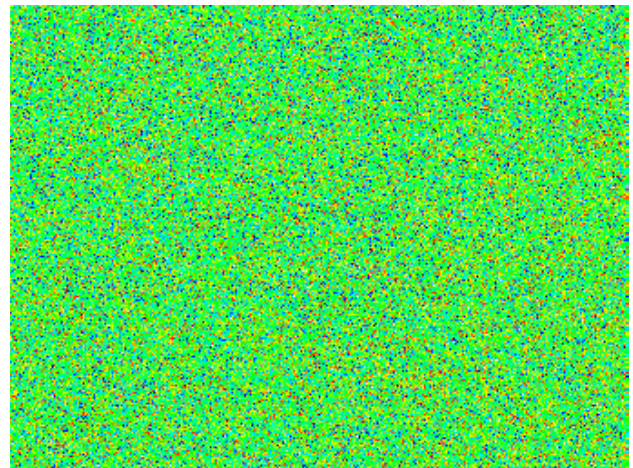
C



Cr



Mn



Mo

Fig. 61 Qualitative mappings of 5 elements by means of the FEG EPMA at a different position than Fig. 60. The mappings were performed at 15 keV and 100 nA. The scan position is not related to the line scan.

The substitutional solute elements show to have homogenous distribution. From superficial analysis, the transformation mode should fall into the paraequilibrium case. However, the NPLE case should not be omitted from the analysis because the small peak of the substitutional solute atoms can disappear easily during diffusion at lower temperatures afterwards.

The quantitative line scans on the Mn-Si DP steel samples are shown in Fig. 62 and Fig. 63. Fig. 62 does not show a distinct difference from the line scan in Mn-Mo DP steel in Fig. 59 as a big island of M/B/RA was selected. Note that this sample had a short transformation time, i.e. 3 s. Fig. 63 which scanned on a very narrow M/B/RA island gives a very interesting result that the carbon content in the island can go even up to over 1mass%. The latter sample has a longer transformation time, i.e. 7 s of total transformation time before quenching. For both cases, no partitioning of substitutional solute atoms is observed.

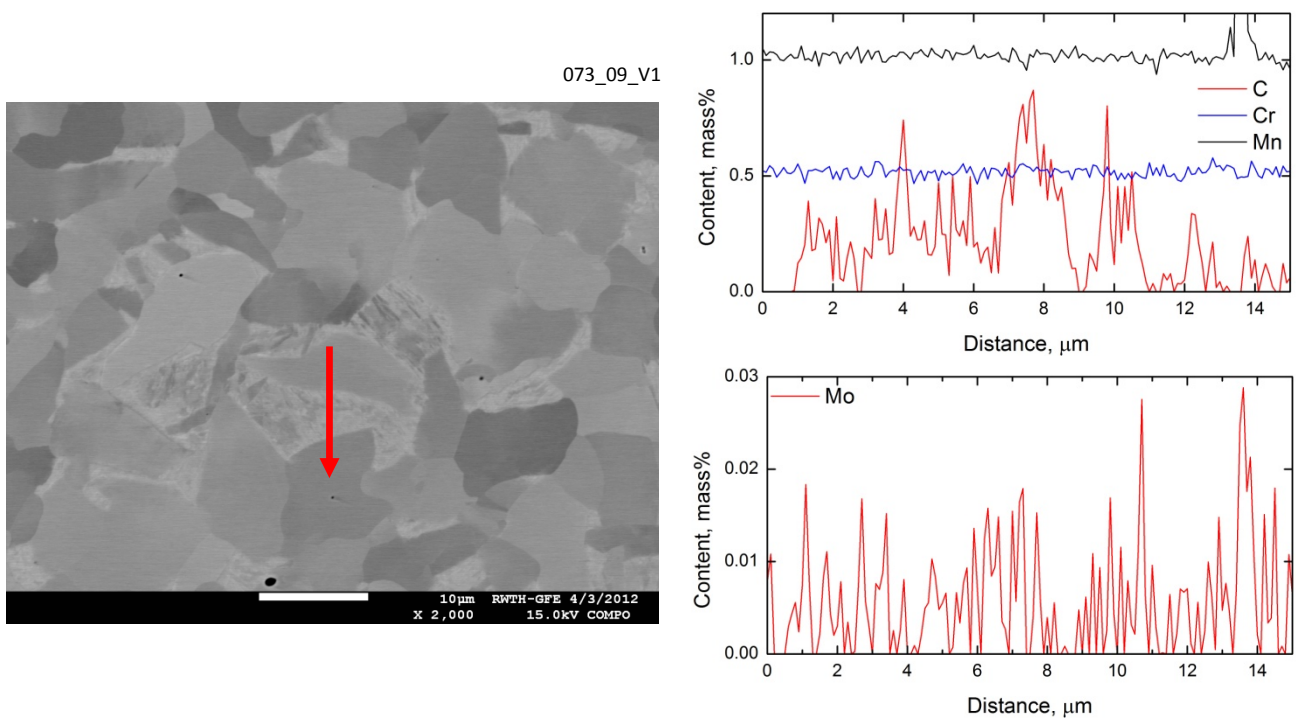


Fig. 62 A quantitative FEG EPMA line scan showing the content of 4 elements across an area including an M/B/RA island in a Mn-Si sample. The areas showing topography relate to the M/B/RA islands. The total length of the line scan is 15 μm . The retained austenite was measured by XRD as 7.4%. A third phase has been found in the sample and can affect the amount of retained austenite.

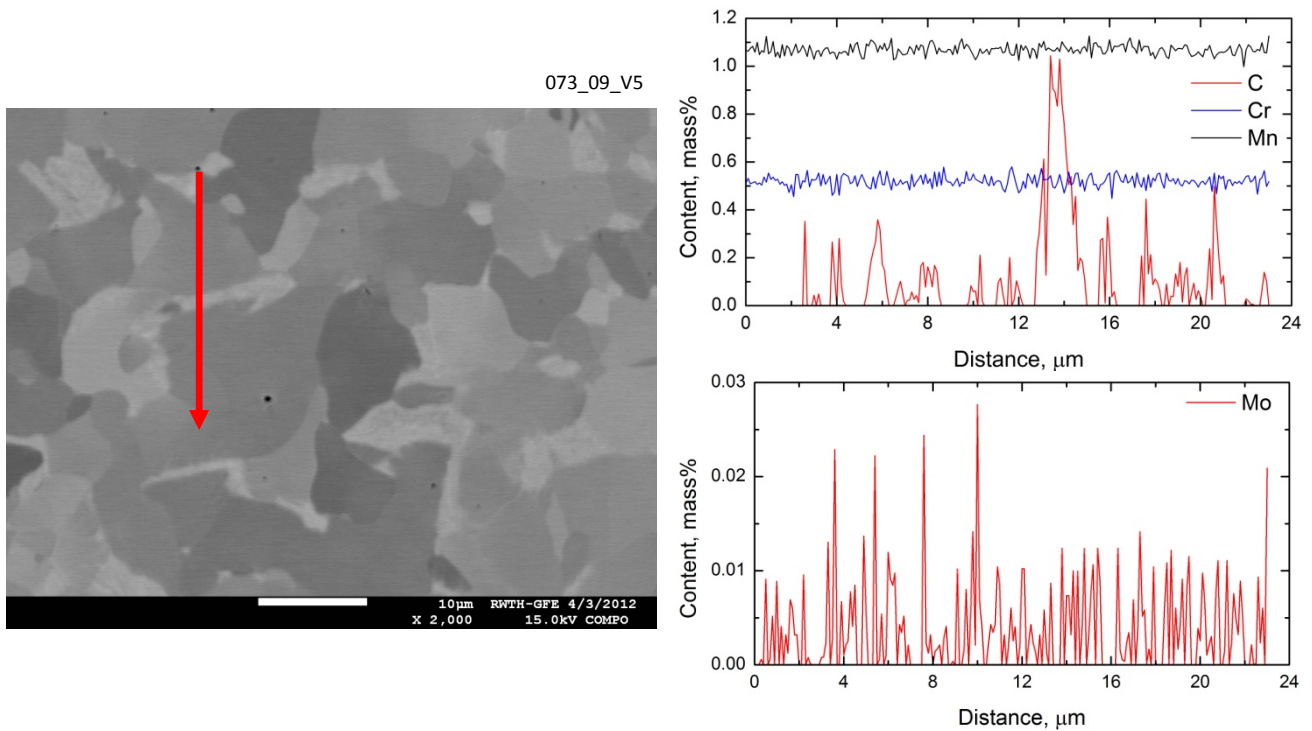
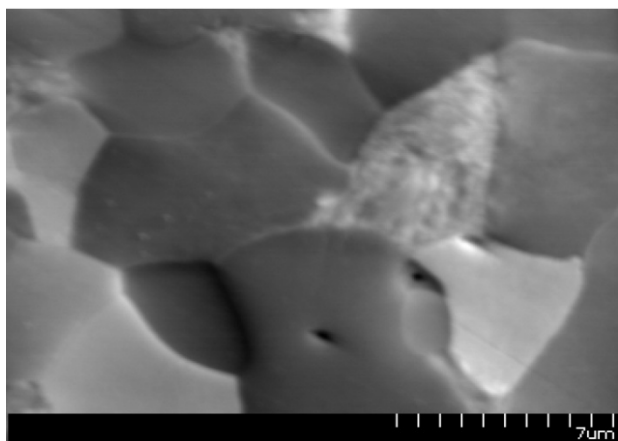
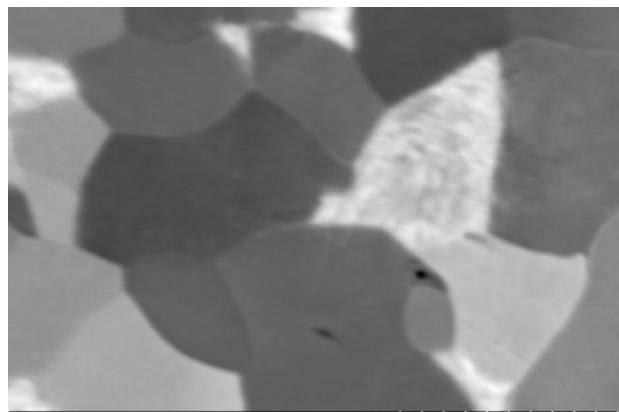


Fig. 63 A quantitative FEG EPMA line scan showing the content of 4 elements across an area including an M/B/RA island in a Mn-Si sample. The areas showing topography relate to the M/B/RA islands. The total length of the line scan is 24 μm . The retained austenite was measured by XRD as 7.7%. A third phase has been found in the sample and can affect the amount of retained austenite.

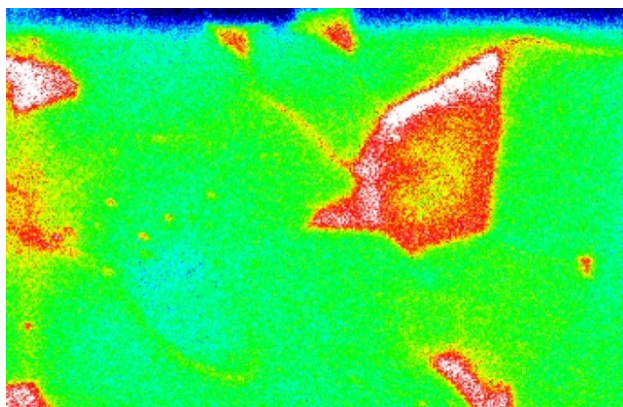
The element mapping in Fig. 64 and Fig. 65 show rather homogenous distribution of carbon as well as the substitutional elements. No large gradient of carbon content can be observed like in the case of Mn-Mo DP steel. The amount of retained austenite measured by XRD in these two samples are 7.4% and 7.7%. During the measurement, a third phase has been found and it can be a main cause of the inaccuracy in the measurement. Although the values from XRD are suspicious, the observed extreme high carbon content can be a good evidence of having some amount of retained austenite, although the M/B/RA islands in the Mn-Si DP steel are relatively small.



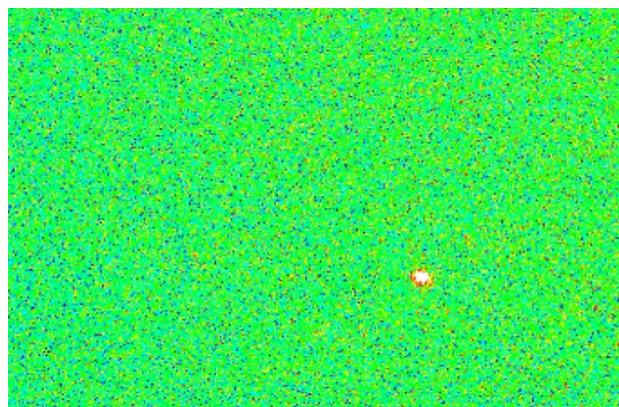
Secondary electron



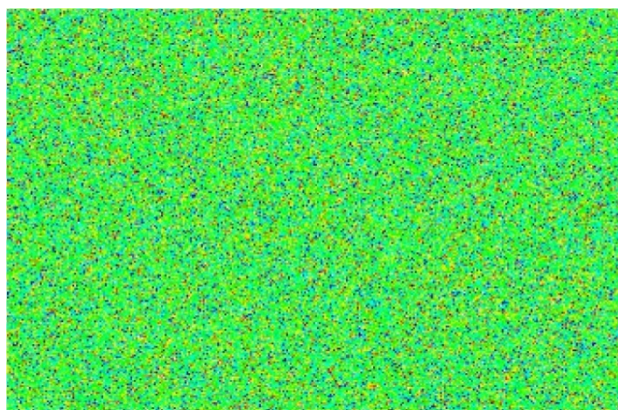
Backscattered electron



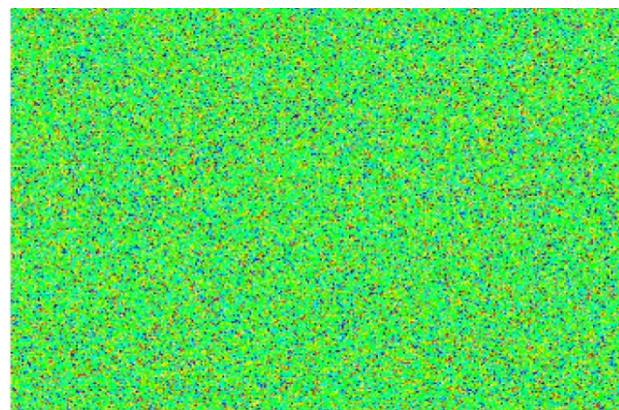
C



Mn

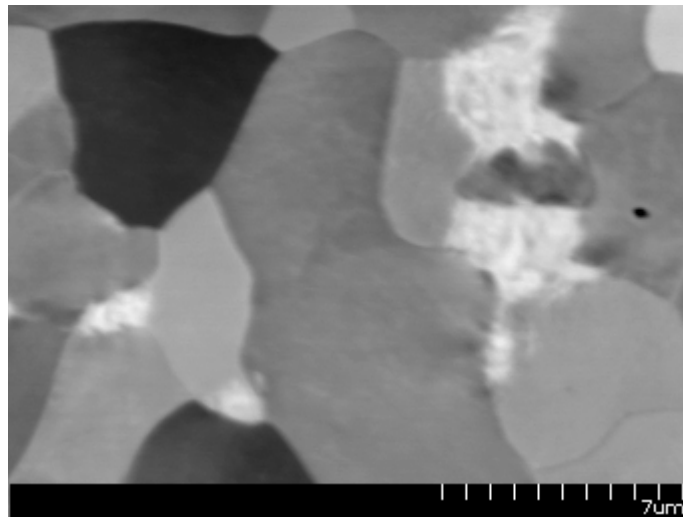


Cr

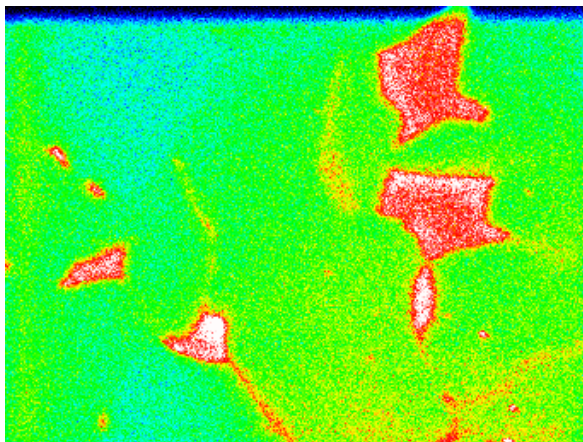


Mo

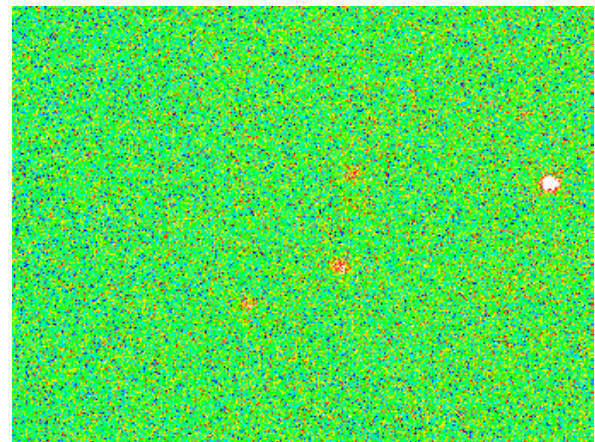
Fig. 64 Qualitative mappings in a Mn-Si samples by means of FEG EPMA on the same sample on which the line scan in Fig. 62 has been performed. The mappings were performed at 15 keV and 100 nA.



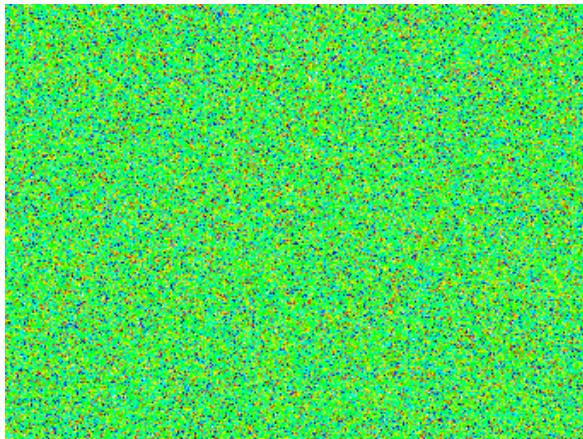
Backscattered electron



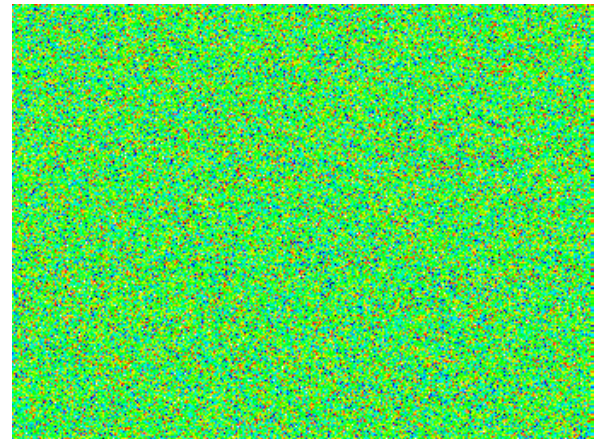
C



Mn



Cr



Mo

Fig. 65 Qualitative mappings in a Mn-Si samples by means of FEG EPMA on the same sample on which the line scan in Fig. 63 has been performed. The mappings were performed at 15 keV and 100 nA. Scattered electron micrograph is not available at this position.

4.2 The rolling experiment and the hot rolled DP steel sheets

The thermal history during the rolling experiment deviated a little from what expected. Say, the temperature at the first pass (F0) (between the first and second pyrometer, P1 and P2) is 50°C lower, i.e., 1050°C instead of 1100°C. All the rolling experiments for both steels had the same rolling schedule. The whole thermal history measured with 6 pyrometers from a rolling experiment is revealed in Fig. 66, as an example.

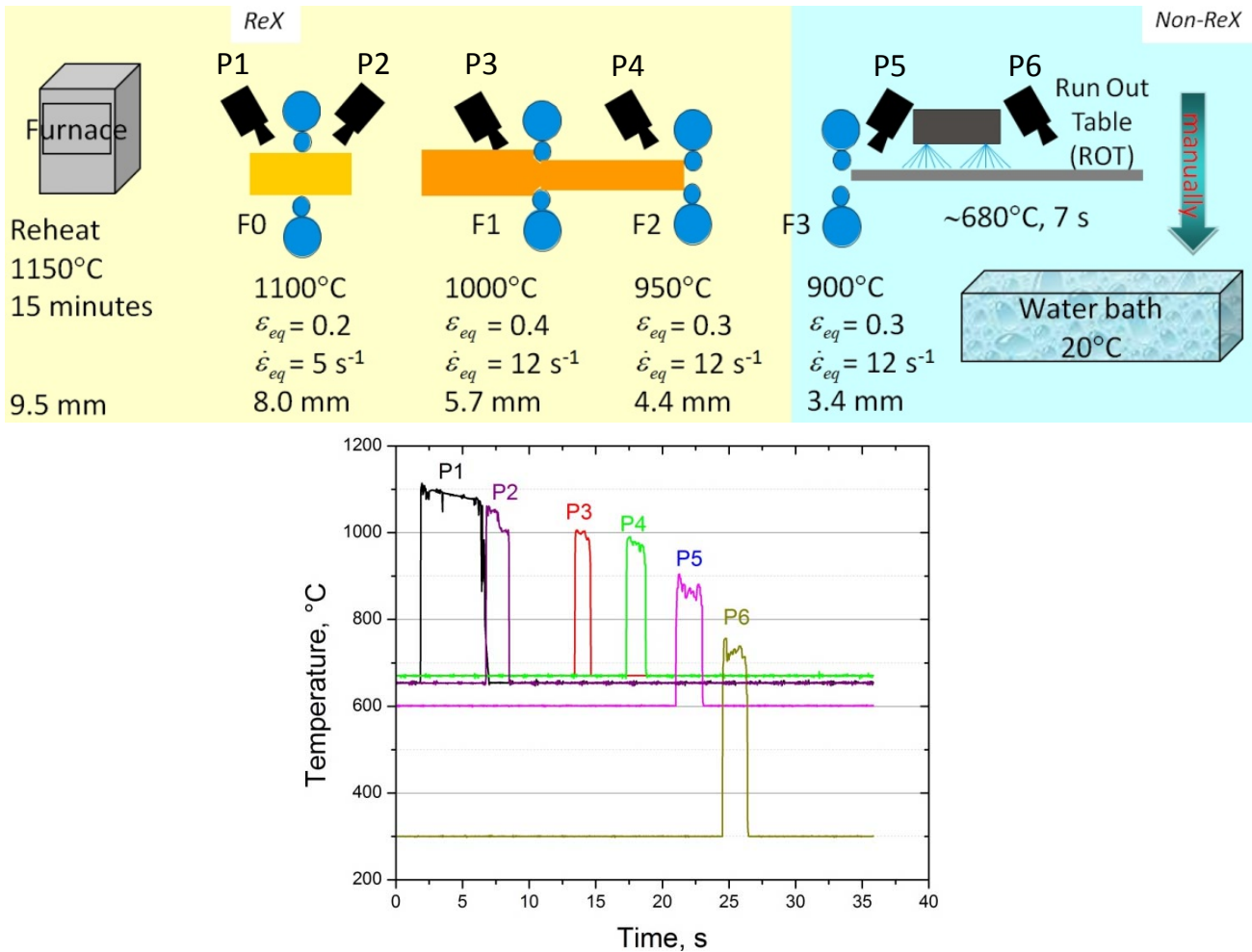


Fig. 66 The thermal history recorded during a rolling experiment.



Fig. 67 The hot rolled strips.

As the rolled strips (Fig. 67) were quenched into water after the 7 s transportation time on the ROT, all the remaining austenite transforms into martensite. The cooling rate by quenching into water was estimated to be around 350 °C/s, which is significantly faster than the fastest cooling rates achievable from in the deformed dilatometer samples in Fig. 50 and Fig. 52.

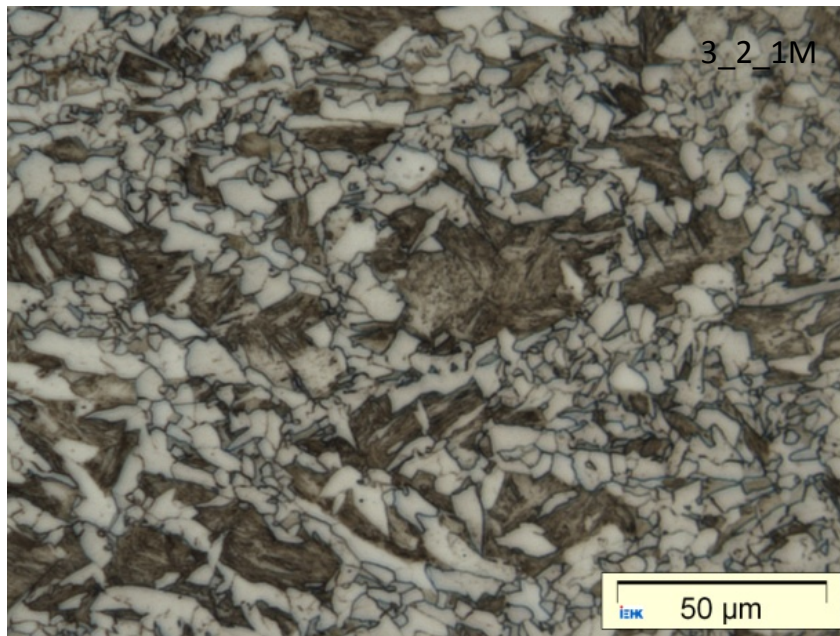


Fig. 68 The microstructure of a Mn-Mo hot rolled steel sheet. The ferrite fraction shows to be as low as 0.50. The martensite fraction sums to 0.35. Some globular bainitic ferrite is seen and amounts to a fraction of 0.15. The ferrite grain size is 5 µm.

The microstructure of the Mn-Mo hot rolled steel sheets has significantly low ferrite fraction, 0.5 ferrite, 0.15 globular bainitic ferrite and 0.35 martensite, as presented in Fig. 68. Its ferrite grain size is 5 μm .

The microstructure investigated by SEM of a hot rolled sheet of Mn-Si DP steel is shown in Fig. 69. Its ferrite grain size is relatively large, i.e. 8.5 μm . The M/B/RA islands appear relatively smooth and therefore almost all of them should represent the martensite. The edge of some martensite islands appears shiny. However, the magnetic induction confirms no retained austenite. This is opposite to the case of the dilatometer samples which were undergone similar thermomechanical cycle and discussed in the previous section but no clear reasoning can be made currently.

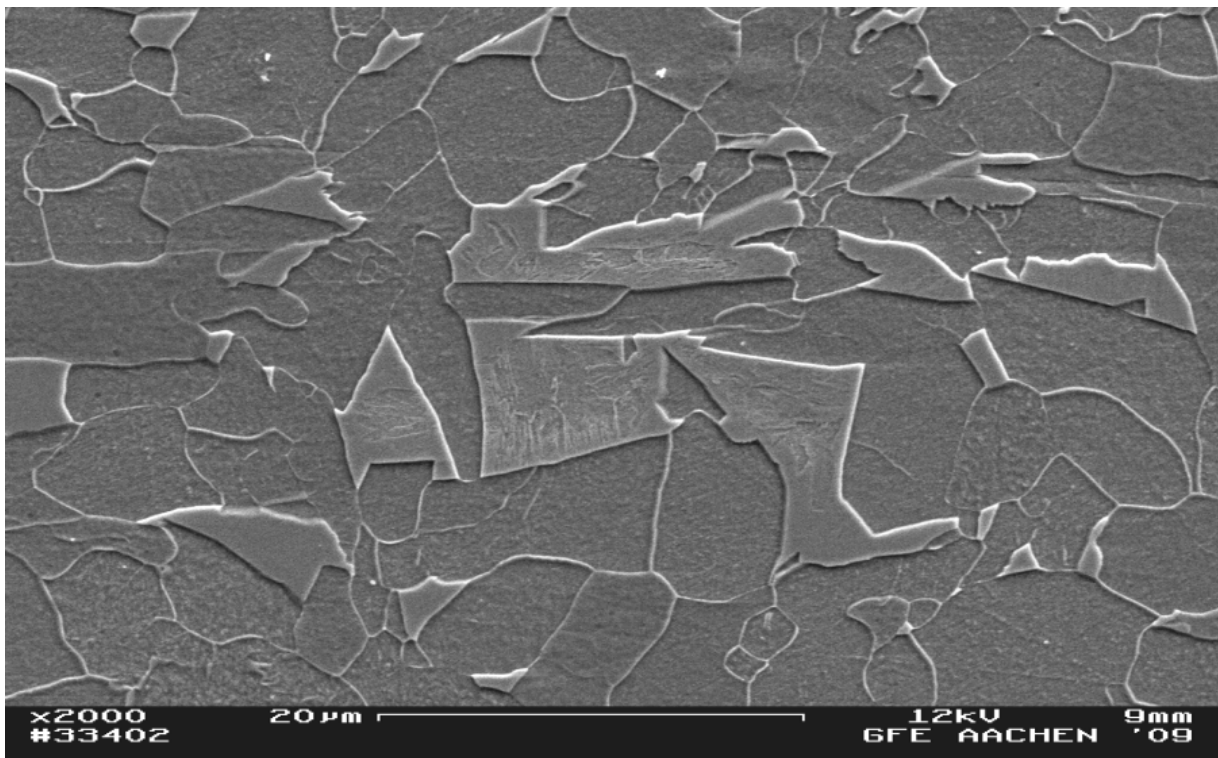


Fig. 69 The microstructure of a Mn-Si hot rolled sheet revealed by SEM containing ferrite fraction of 0.92, martensite of 0.08. The ferrite grain size is 8.5 μm .

4.2.1.1 The mechanical properties of the hot rolled DP steels

The engineering stress-strain curves tested on the a hot rolled sheet of the Mn-Mo DP and Mn-Si DP steels are shown in Fig. 70.

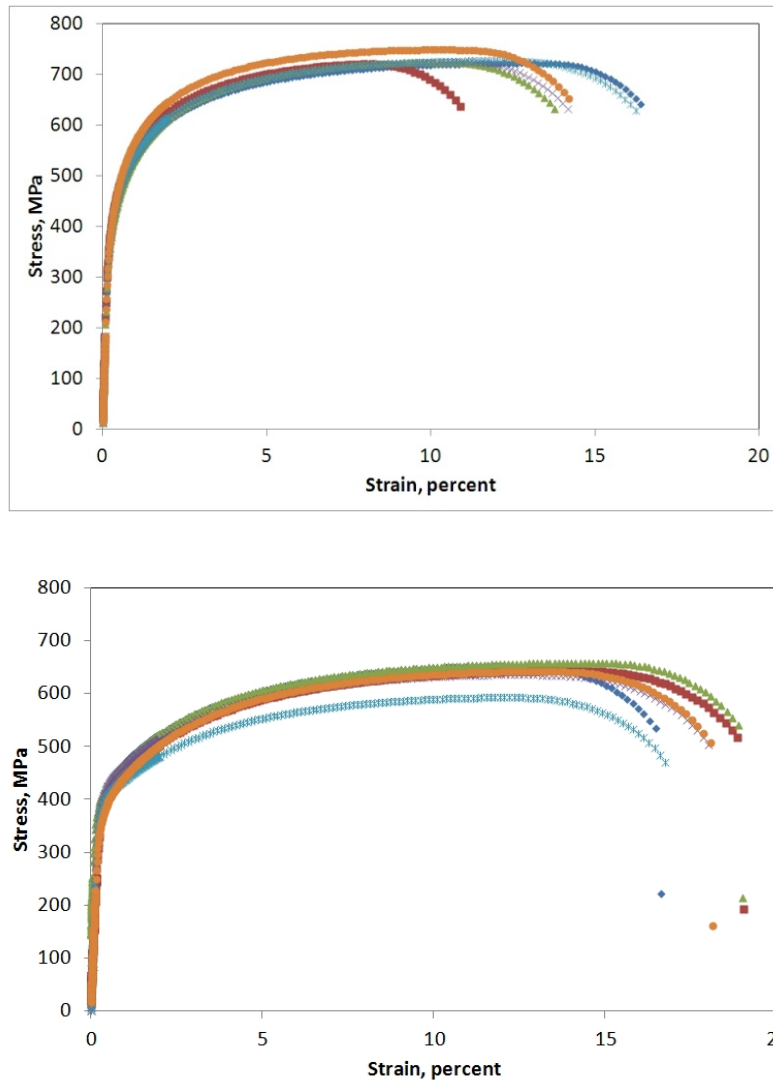


Fig. 70 The engineering stress-strain curves tested on a) the Mn-Mo DP steel sheets b) the Mn-Si DP steel sheets.

Their average mechanical properties as well as the standard deviations are shown in Table 4.5.

Table 4.5 Summary of the mechanical properties of the hot rolled strips

		YS, 0.2 offset, MPa	UTS, MPa	YS/UTS	Uniformed Elongation, %	Total Elongation, %	Strain Hardening Exponent (n), -
Mn-Mo DP (090514_2)	Average	439	729	0.60	10.30	14.02	0.14
	Standard deviation	13	10	0.01	1.53	1.98	0.01
Mn-Si DP (090722_2)	Average	401	637	0.63	12.60	17.79	0.17
	Standard deviation	12	26	0.02	0.92	1.20	0.01

The Mn-Mo DP steel, as it has relatively low ferrite fraction but contains higher fraction of harder phases, i.e. the mixture of martensite and bainite, shows higher yield strength and ultimate tensile strength. Likewise, it has less uniform and total elongations. However, the presence of no sharp yield point satisfies the properties of DP steels. Both steels also have the ratio between the yield strength and ultimate tensile strength in the order of 0.6.

Fig. 71 and Fig. 72 present the hardness mapping of two Mn-Si hot rolled strip samples and two Mn-Mo deformed dilatometer samples, respectively. The Mn-Si steel is composed of ferrite with fraction of 0.92 and its hardness lays mostly in the range 150-200 HV, which is the hardness level of ferrite as also concluded by [127]. The zones at the rims of the samples adjacent to the mounts must be neglected due to the interference from the epoxy resin mounts. Four areas showing lower hardness periodically, say 100-150 HV, can be the result of the interference.

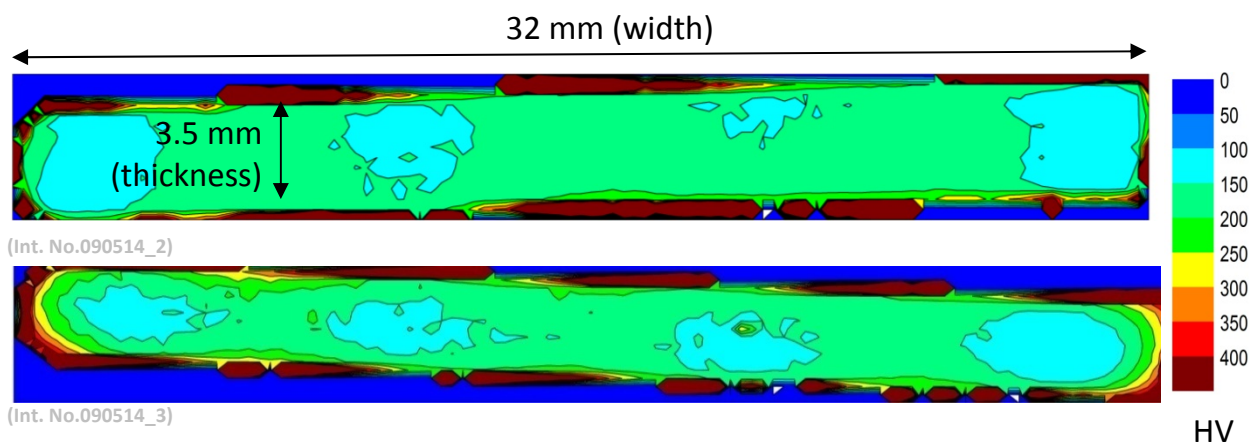


Fig. 71 The hardness mapping in the hot rolled strips of the Mn-Si DP steel. Blue – resin area. Red brown – artefact.

Generally speaking, the hardness level of the sample can be measured as the effective hardness level. The current hardness mapping proves that the hardness in any single M/B/RA island cannot be measured. This is because the M/B/RA islands float in the soft matrix of ferrite.

The hardness mapping tests were carried out for the Mn-Mo steels only with the dilatometer samples. The samples went through the processing route *Option B* with the ferrite transformation time of 7 and 9 s followed by the cooling rate of 57 °C/s. They resulted in similar ferrite fraction, namely, 0.74 and 0.72. Higher hardness was found in this case, say, some regions with 200-250 HV, mixed with the regions with hardness of

150-200 HV. The bigger M/B/RA islands contribute to the higher hardness level. The regions with lowest hardness, 100-150 HV at the outer region of the samples can contribute to the area with higher strain as the strain in the deformed cylindrical sample is not homogenous [Lor03].

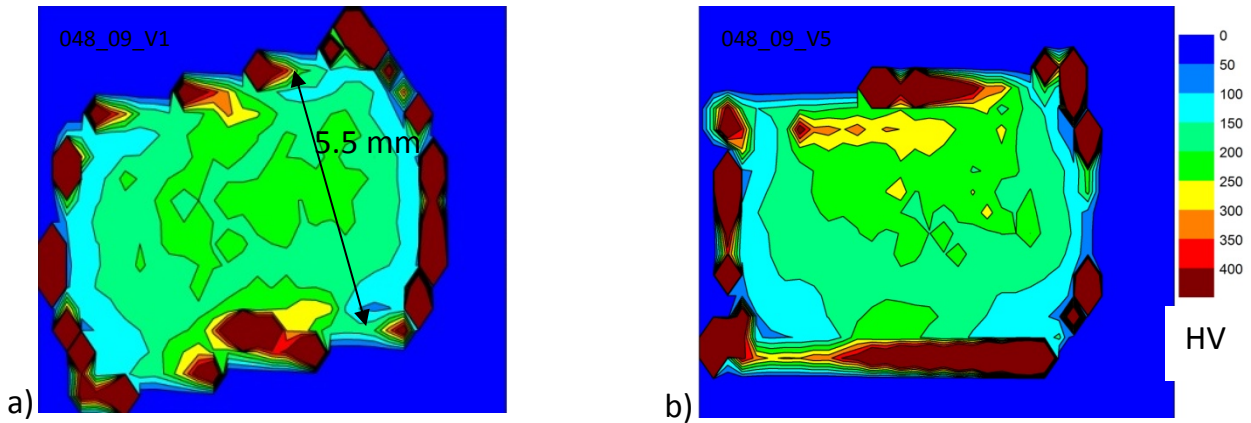


Fig. 72 The hardness mapping carried out on the deformed dilatometer samples of the Mn-Mo DP steel processed through the processing *Option D* in Table 3.3. The cooling rate after the ferrite formation was 57 °C/s. The samples have a ferrite fraction of 0.72-0.74 with a fraction of 0.19-0.2 for martensite. The rest is bainite. Blue – resin area. Red brown – artefact.

Again, this measurement cannot reveal the hardness of a single M/B/RA island separately as it disperses in a soft matrix.

5 MODELLING WORK

5.1 Alloying and process window presumption by CALPHAD

Before selecting the alloying concepts and producing melts, good modelling scientists should start with presuming the transformation characteristics of the interested alloys. Because no experimental data might be available at this stage and the most potential way of modelling which does not require any fitting parameter from the experiments is the thermodynamic calculation. Especially nowadays it can readily perform in commercial softwares such as ThermoCalc™ as employed in this work.

In this section, the calculation of isopleths, and the critical temperatures under equilibrium, A_{e3} , A_{e1} , under paraequilibrium, A_{e3para} , A_{e1para} and for non-equilibriums, W_s , B_s , T_0 , M_s , will be explained. Isopleths are stable phase fields in relation with temperature and one of composition variables. The maximum fraction of ferrite and bainite will be also calculated.

5.1.1 Calculation of the isopleths

Different pseudo binary Fe-X phase diagrams were calculated with ThermoCalc™ for different main alloying elements as an easy tool to support the alloying selection. After giving all the alloying elements, only the element of interest, X, and temperature were stepped to create an Fe-X phase diagram. The calculation was done in the equilibrium calculation module (POLY3) module in ThermoCalc™ version S with the most recent database TCFE6 and the global minimisation was turned off to avoid unnecessary confusing phases. The variation of composition X was mapped against temperature. The pressure was always kept constant at 1×10^5 Pa.

5.1.2 Calculation of the critical temperatures

As carbon influences the critical temperatures significantly and takes the main role in solute partitioning, all the critical temperature were calculated for a selected range of carbon content.

5.1.2.1 Calculation of A_{e1} and A_{e3}

Both the A_{e1} and A_{e3} temperatures were also calculated explicitly in POLY3 module. It was done by both possible different ways of calculation as follows:

1. *'compute-transition'*, which is an instant command (users have to guess which phase will appear/disappear)
2. *'change-status'* command followed by the commands *'set-condition'* and *'compute-equilibrium'* (users know exactly which phase will (dis)appear.)

For the latter case, the phase which is speculated to form must be assigned the status *'fixed'* and temperature should be released as a free variable. In this case the influence of the instantaneous change in a specific chemical composition on the critical temperatures can be derived. It is safer than the other case, on which phase the users are working with.

The calculation under paraequilibrium is possible with the command *'advanced-options'* since ThermoCalc™ version S followed by *'step-with-option'*. From version P and earlier, the command *'special-options'* must be used instead. Afterwards, the option *'paequilibrium'* must be selected. For the context of austenite to ferrite transformation, the fcc and bcc must be given in the command window. Two results will be given: the paraequilibrium temperatures for bcc and fcc structures, which are the A_{e1para} and A_{e3para} respectively.

The calculation for A_{e3} under deformation, in other words A_{e3d} , follows the parallel tangent concept suggested by Lee [Lee92]. Under the parallel tangent concept, the equilibrium is defined by

$$\mu_{\gamma}^i = \mu_{\alpha}^i + \Delta G_m \quad \text{Eq.68}$$

Here, the chemical potential difference of component i between fcc (μ_{γ}^i) and bcc (μ_{α}^i) is constant, and is equal to an additional stored energy ΔG_m . The calculation for its magnitude will be given in the next paragraphs.

The stored energy of deformation contributes additionally to the molar Gibbs free energy of transformation in the austenite. It was derived from the flow curve during the deformation step under the recrystallisation stop temperature, T_{nr} . The flow curve is not sensitive to the austenite grain size but to the strain. The increase in the Gibbs free energy is a result of the elastic strain energy and dislocation core energy and is represented by ΔG_{disl} . It can be calculated per unit volume as

$$\Delta G_{disl} = \mu \rho b^2, \tag{Eq.69}$$

where ρ is the dislocation density; μ stands for the shear modulus of austenite which is taken to be 79 GPa; b means the length of the Burgers vector, which is normally 0.25 nm. This is the case that the constant, k , in Frank's rule (Eq.70), which predicts the total energy of dislocation per unit length, E , is taken to be 1, [Sun98] as follows

$$E = k\mu b^2 = \mu b^2. \tag{Eq.70}$$

The dislocation density is related to the flow stress as

$$\sigma = M\alpha\mu b\rho^{\frac{1}{2}}, \tag{Eq.71}$$

where M is Taylor factor, taken to be 3.11 for FCC metals; α is a constant, taken to be 0.15 for FCC metals [Sun98]. Therefore, the extra term of ΔG_{disl} contributed by the increase in dislocation is related to the flow stress as

$$\Delta G_{disl} = \frac{\sigma^2}{M^2\alpha^2\mu}, \tag{Eq.72}$$

where σ stands for the flow stress.

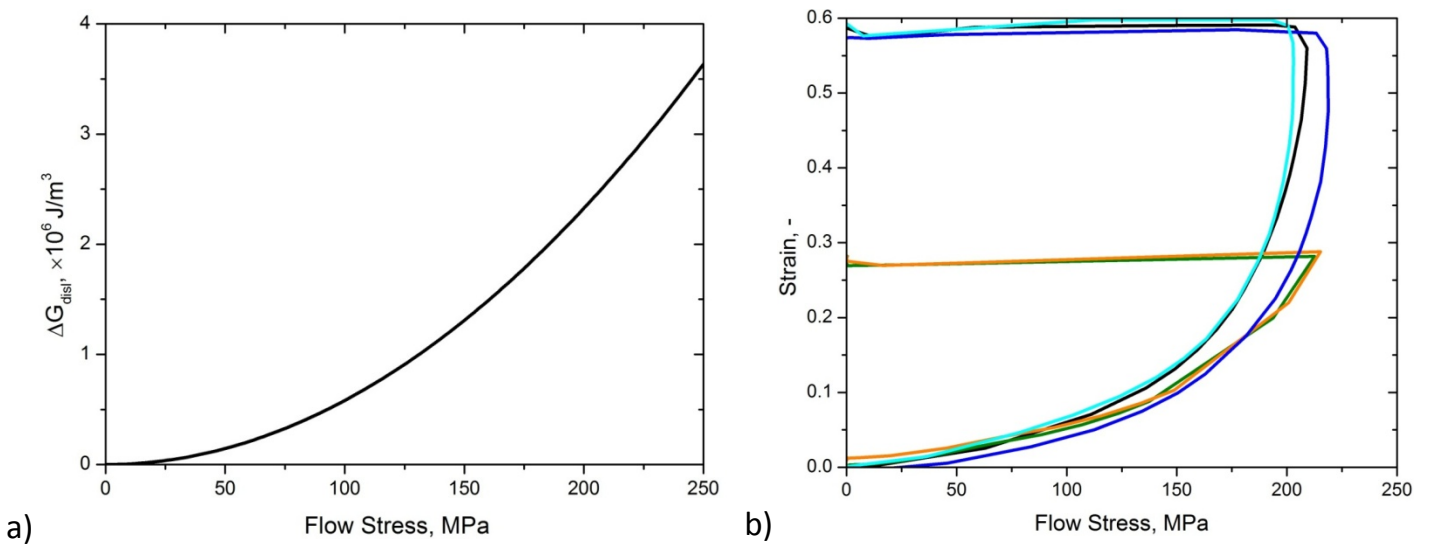


Fig. 73 a) The calculated additional stored energy due to the deformation at different flow stresses which relates to b) The flow curves obtained during the deformation step on samples having different austenite grain sizes as shown already in Fig. 35.

At the retained strain of 0.3, the increase in the molar Gibbs free energy is estimated to be $3.29 \times 10^6 \text{ J/m}^3$. For certain temperature and certain nominal composition, at first, the molar Gibbs free energy of transformation was calculated from the molar volume of austenite (V_m^γ) with the nominal composition as follows:

$$\Delta G_m^\gamma = -3.29 e^6 \left(\frac{\text{J}}{\text{m}^3}\right) x V_m^\gamma \left(\frac{\text{m}^3}{\text{mol}}\right). \quad \text{Eq.72}$$

Note that the molar volume of austenite changes with temperature. Afterwards, by setting the 'phase-addition' of ferrite with the free energy change of ΔG_m^γ , the decomposition of the nominal composition into ferrite and austenite was calculated by establishing equilibrium between ferrite and austenite. Practically, at all temperature steps, the nominal carbon content was stepped from 3 mass% where ferrite phase does not exist with -0.01 wt.% step size until the ferrite phase fraction is larger than zero where the nominal carbon content is then the carbon composition of the A_{e3d} temperature locus. It is more complicated due to the dependency of molar volume of austenite with temperature. Therefore, it was carried out in ThermoCalc™'s MATLAB toolbox.

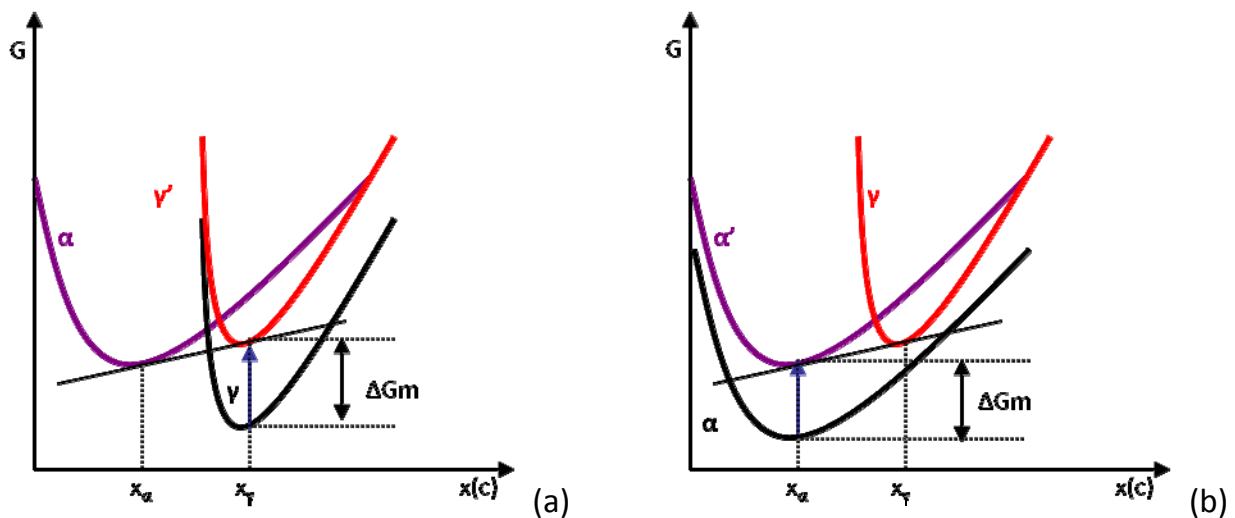


Fig. 74 The parallel tangent concept (a) for the calculation of A_{e3d} and (b) W_s and B_s temperatures

The calculation for the case of NPLE is somewhat more complicated and has been done through MATLAB toolbox interface of ThermoCalc™. Refer to Fig. 12 the u fraction of manganese in ferrite, $u_{Mn}(\alpha)$ and in austenite, $u_{Mn}(\gamma)$, must be equal to the that at the nominal composition. The second condition is that the chemical potential of carbon in austenite must be equal to that in the two phase field as they lie on the isoactivity line of carbon. Setting these conditions together with using the command 'change-status', the

A_{e3_NPLE} can be derived. The energy of deformation in austenite was also added to the molar Gibbs free energy of transformation to investigate the effect of deformation and calculate the A_{e3d_NPLE} temperature.

5.1.2.2 T_0 calculation

T_0 , which is the locus of carbon content and temperature for a diffusionless transformation, can be calculated directly by ThermoCalc™ by choosing 'T-Zero' after the commands 'advanced-option' and 'step-with-option'. This locus is very useful and will be used to calculate the maximum bainite fraction achievable (section 5.1.3). Theoretically, the calculation of T_0 locus with ThermoCalc™ can be applied to all cases of diffusionless transformation, in case of the stored energy of the product phase is known. It would be therefore employed to calculate the B_s and M_s temperatures under the assumption of diffusionless transformation from Bhadeshia [Bha01] and Porter [Por92], respectively, with the stored of 400 J/mol [Bha01] and 1260 J/mol [Gué79].

5.1.2.3 Calculation of W_s and B_s

The calculation of W_s and B_s temperature follows Lee [Lee92], which is rather simple. It adopts the parallel tangent as shown in Fig. 74 again. Lee adopted the stored energy of 300 and 600 J/mol for W_s and B_s respectively [Lee92, Nan90], which was taken as the molar Gibbs free energy for the transformations. It was calculated with varied carbon content purely with the ThermoCalc™ classic version S.

On the other hand, the calculation according to Bhadeshia's concept [Bha01] was also done for a comparison. The nucleation of Widmannstätten ferrite and bainite follows the parallel tangent method. The universal nucleation function was proposed by Bhadeshia as

$$G_N = (3.637 \pm 0.2)(T - 273.18) - (2540 \pm 120) \frac{J}{mol}; \quad \text{Eq.73}$$

$$\Delta G_m < G_N.$$

According to Bhadeshia's approach, the carbon concentration has to be scanned and at every carbon content for each temperature, the single equilibrium must be calculated, until the composition of 2 phase region is found. MATLAB toolbox was again employed for it.

The growth of Widmannstätten ferrite follows the common tangent method while the growth of bainite follows the diffusionless concept. Similarly to A_{e3d} , at every temperature and carbon content, the Gibbs free energies of austenite and ferrite had to be calculated, it was therefore done with MATLAB toolbox. The temperatures at which difference in these energies is equal to the stored energy of the Widmannstätten ferrite are the W_s temperatures being searched.

The growth of bainite under this concept can be calculated more straightforward due to the diffusionless concept and was done directly in ThermoCalc classic version 5 too. The command '*phase_addition*' together with '*step-with-option*' followed by '*T-Zero*' were employed.

5.1.2.4 Calculation of M_s

Porter's method [Por92] of diffusionless transformation was adopted for the calculation of M_s temperature while the stored energy of 1260 J/mol for the transformation follows the finding of Guénin [Gué79]. The calculation method is the same as the calculation for B_s temperature suggested by Bhadeshia described in section 5.1.2.3 except the higher stored energy.

5.1.3 Calculation of the maximum phase fraction

The maximum phase fraction of ferrite, or the thermodynamically equilibrium ferrite fraction, in the interested temperature range was carried out simply by stepping the temperature and calculating the variable VPV (BCC_A2) at every temperature with ThermoCalc™.

According to the nucleation controlled approach, the maximum bainitic ferrite fraction in lower bainite, was calculated according to Takahashi [Tak91], as follows,

$$b_{max} = \frac{X_{T_0} - \bar{X}}{X_{T_0} - X_{Ae1para}} \quad \text{Eq.74}$$

The T_0 locus determines the maximum carbon content allowed in the remaining austenite before the transformation ceases.

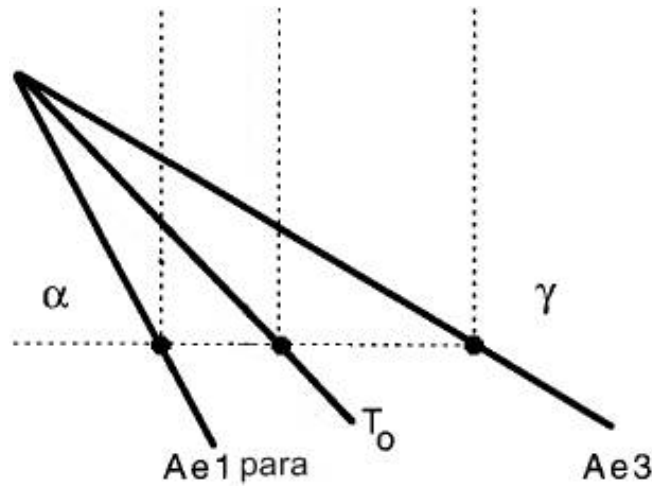


Fig. 75 The calculation of the maximum bainitic ferrite fraction in lower bainite following the T_0 locus according to Takahashi [Tak91]

5.2 Austenite recrystallisation between rolling passes

Firstly the recrystallisation stop temperature was predicted by using the equation proposed by Boratto [Bor88]

$$T_{nr} = 887 + 464C + (6645Nb - 644\sqrt{Nb}) + (732V - 230\sqrt{V}) + 890Ti + 363Al - 357Si$$

Eq.1

Above this temperature, the empirical equation proposed by Liu [Liu07, Sun98] shown as follows was selected to calculate the recrystallised austenite grain size.

$$D_{rex} = 100 \cdot D_0^{1/3} \varepsilon^{-0.37} \exp\left(-\frac{28000}{RT}\right)$$

Eq.16

This is because the measured fraction recrystallised after every deformation step (after deformation step 2-4 in Fig.14) as shown in Table 4.2 and Table 4.4 is relatively large and the effect of the unrecrystallised fraction on the grain size was therefore ignored.

After the recrystallisation in the first pass, the grain size of the newly recrystallised austenite was calculated. Then this grain size was used as the initial austenite grain size for the following recrystallisation after the second deformation step. The calculation was then repeated for the third deformation. The unrecrystallised fraction was not taken into account in the following passes.

The recrystallisation kinetics of each steel was modelled with the t_{50} equation by Sellars [Sel90]

$$F_x = 1 - \exp \left[-0.693 \left(\frac{t}{t_{0.5}} \right)^n \right], \quad \text{Eq.2-9}$$

by using the recrystallised fraction from the experimental work in section 4.1.4.

5.3 Modelling of the effect of austenite grain size and retained strain

The well known mathematical description of the state of austenite before phase transformation or the effective nucleation area, or the so-called S_v , is selected to represent the effect of austenite conditioning on the ferrite transformation kinetics. It determines the grain boundary surface area of austenite in a unit volume and therefore has a unit of mm^{-1} . The equation for the calculation of S_v proposed by Kvač kaj [Kva98] was adopted and is expressed as in Eq.28. Its unit is in mm^{-1} .

$$S_v = 429 \frac{1}{D_\gamma e^\varepsilon} + 1571 \frac{e^\varepsilon}{D_\gamma} + [157.2(1 - e^{-\varepsilon}) - 59.47]_+ \quad \text{Eq.28}$$

In this case, the austenite grain size D_γ refers to the grain size after the (repeated) recrystallisations. The quantity in brackets comes from deformation bands, which are taken into account by Kvač kaj only when the retained strain, ε , exceeds 0.475. Provided that recrystallisation arises during multiple deformation steps, the portion of the retained strain, ε , must be specified and subtracted from the total strain.

5.4 Modelling of the macroscopic ferrite transformation kinetics

The rate form equation of the phase formation propose by Leblond [Leb84, Leb85] was applied to this class of modelling. For ferrite transformation, the rate of ferrite formation can be described as,

$$\dot{f}(t) = [f_{eq} - f]_+ \cdot g_{Temp}(T) \cdot g_{S_v}(D_\gamma, \varepsilon) \cdot g_{Cool}(\dot{T}). \quad \text{Eq.75}$$

The controlling terms of the kinetics are the difference between the equilibrium ferrite fraction, f_{eq} , and the current phase fraction, f ; a function of temperature which is g_{Temp} ; the austenite conditioning g_{S_v} , which is a function of S_v value. The effect of cooling profile, g_{cool} , is kept as 1 for isothermal transformations. The equilibrium ferrite fraction, f_{eq} , was recorded from ThermoCalc™ as explained in section 5.1.3.

The g_{cool} function works for continuous cooling by discretising the g_{Temp} function to the corresponding temperatures along the cooling profile.

$$f(t^{i+1}) = f(t^i) + \Delta t \cdot \left(f_{eq}(T(t^i)) - f(t^i) \right) \cdot g_{Temp}(T(t^i)) \cdot g_{S_v}(D_\gamma, \varepsilon) \quad \text{Eq.76}$$

$f(t^i)$ is the ferrite fraction at the time step t^i ; $f(t^{i+1})$ is the ferrite fraction at the time step t^{i+1} ; Δt is the time interval between the time step t^i and t^{i+1} . $f_{eq}(T(t^i))$ and $g_{Temp}(T(t^i))$ are the equilibrium ferrite fraction and function of the temperature, respectively, at the time step t^i , which corresponds to the temperature $T(t^i)$.

In order to determine the factor g_{Temp} , a pair of the austenite grain size, D_γ and the retained strain, ε , has to be fixed. In this case the (recrystallised) austenite grain size, D_γ of 35 μm and the retained strain of 0 are selected as there are a large number of datapoints. It results in the S_v value of 57.14 mm^{-1} . The value of g_{S_v} was set to be 1 for this condition and g_{Temp} was defined by

$$g_{Temp}(T) = \frac{\ln \frac{f_{eq}-f(t_S)}{f_{eq}-f(t_E)}}{t_E-t_S}. \quad \text{Eq.77}$$

t_S and t_E are the starting point of time and the point of time at the end of the interested course of transformation, respectively. Each experimental data point at the same holding temperature (with different holding time and ferrite fraction) brings different value of g_{Temp} . An average was made to define g_{Temp} for each temperature.

Then the function of g_{S_v} was determined by the experimental data from other conditions: other austenite grain sizes and retained strains, as follows

$$g_{S_v} = \frac{\ln \frac{f_{eq}-f(t_S)}{f_{eq}-f(t_E)}}{(t_E-t_S) \cdot g_{Temp}(T)}. \quad \text{Eq.78}$$

The different g_{S_v} 's from different holding time from the same temperature was calculated as an average. The the values from different temperatures will be made as an average for each S_v value (or each pair of austenite grain size and retained strain).

Both functions g_{Temp} and g_{S_v} were optimised through the least square non-linear optimisation routine '*lsnonlin*' in MATLAB.

5.4.1 Modelling of the carbon partitioning after ferrite transformation

The average carbon content in the remaining austenite, C_γ , has been changed after the ferrite formation and must be calculated before the modelling of martensite formation. An easy way to take care of carbon partitioning between ferrite and austenite is to define C_γ by the mean field method, by which the carbon content in both austenite and ferrite is considered to be uniform, or

$$C_\gamma = \frac{C_{nominal} - C_\alpha \cdot f}{1 - f} \quad \text{Eq.79}$$

where $C_{nominal}$ corresponds to the nominal carbon content in the considered steel. C_α is the carbon content in ferrite, which can be calculated from the empirical formula [Ble10] .

$$C_\alpha = 2.55 \cdot e^{-\frac{4850}{T(K)}} \quad \text{Eq.80}$$

C_γ is the carbon content in the remaining austenite after the ferrite transformation, which is increased due to carbon redistribution.

The '*modified CCT diagrams*' in section 4.1.9 were created as a function of the average C_γ and the diagrams were used for the information for critical cooling rates which result in bainite or martensite during the continuous cooling. If the cooling rate exceeded one of the critical temperatures, the calculation for further ferrite transformation in Eq.79 was stopped.

5.5 Modelling of the macroscopic martensite transformation kinetics

The martensite fraction is described by a variant of the Koistinen-Marburger formula as follows

$$\dot{m}(t) = \frac{1}{\tau_m} [\bar{m}(T, C_\gamma) - m]_+ \quad \text{Eq.81}$$

Assuming that at any time, t , the maximum volume fraction of martensite that can form corresponds to the remaining volume fraction of austenite, i.e., $1-f$. The function \bar{m} is defined by

$$\bar{m}(T, C_\gamma) = \min \{m_{KM}(T), 1 - f\}. \quad \text{Eq.82}$$

Here, m_{KM} describes the volume fraction of martensite according to the Koistinen and Marburger formula [Koi59], i.e.,

$$m_{KM}(T, C_\gamma) = 1 - e^{-C_{KM}(M_s(C_\gamma) - T)}. \quad \text{Eq.47}$$

As the thermodynamic calculation for M_s temperature (section 6.1.2) cannot provide a better result, the M_s was calculated by a selected empirical equation by Lorenz [Lor03],

$$M_s = 506.6 - 338.7C_\gamma - 18.3Mn - 14.5Cr + 1.3Si.$$

5.6 Modelling of the mesoscopic ferrite transformation with phase field modelling

The phase field modelling was performed for the Mn-Mo and Mn-Si DP steels only for the thermomechanical route *Option D: 'Rolling Option'* in Table 3.3 to investigate the isothermal ferrite transformation kinetics at 680 °C. The simulation starts from cooling from the last deformation step at 900 °C down to 680 °C with a cooling rate of 60°C/s. The nucleation takes place during cooling as soon as it reaches the A_{e3d} temperature.

The simulation was performed by the commercial MICRESS™ code version 5.5. The phase field equation (Eq.43) has to be mentioned here again.

$$\frac{\partial \phi_i}{\partial t} = \sum_j M_{ij} \left\{ \gamma_{ij} \left[\phi_i \nabla^2 \phi_j - \phi_j \nabla^2 \phi_i + \frac{\pi^2}{2\eta^2} (\phi_i - \phi_j) \right] + \frac{\pi}{\eta} \sqrt{\phi_i \phi_j} \Delta G_{m_{ij}} \right\} \quad \text{Eq.43}$$

M_{ij} is the interface mobility of adjacent grains. γ_{ij} stands for the interfacial energy for different pair of interface between phase i and j . μ represents the width of the transition boundary

$\Delta G_{m_{ij}}$ is the difference of the molar Gibbs free energy between adjacent ferrite and austenite grains. It was taken from the thermodynamic database TCFE6 through the Gibbs Energy System (GES) file generated by ThermoCalc™ version R. As the simulation considers only the austenite and ferrite phases, the thermodynamic calculation was carried out through ThermoCalc™ as if the cementite phase is suspended.

All the six alloying elements in the selected alloys were considered in the system, which is more advanced than that carried out in [Suw09]. The mode of solute distribution was set up to be '*normal*' which corresponds to the conditions close to NPLE. The diffusion follows Eq.44

$$\frac{\partial \bar{x}}{\partial t} = \nabla \sum_{i=1}^N [\phi_i D_i \nabla \bar{x}_i]. \quad \text{Eq.44}$$

The term \bar{x}_i , the mixture composition in phase i , was derived from the Gibbs energy function taken from the database TCFE6; D_i , the multicomponent diffusion coefficient matrix in phase i , was calculated through the TQ interface to Thermo-Calc™ and a mobility database MOB2 for steels, considering the content of six alloying elements. These are also

transferred to MICRESS code through a GES file. The phase field and diffusion equations were solved by the explicit Euler method. The calculation was carried out by finite differences on a structured cubic grid. The option '*global*' for diffusion was selected and therefore, only the members on the diagonal of the diffusion coefficient matrix are used.

The interface mobility $M_{\gamma-\alpha}$ in the Mn-Si DP is set as a constant at $8 \times 10^{-6} \text{ cm}^4/(\text{J}\cdot\text{s})$ but that in the Mn-Mo varies with the free energy of transformation and it is presented in Fig. 76. This is because the observed microstructure development in section 4.1.6 shows that the phase transformation rate is highest during the first moment of transformation, in which the free energy of austenite is the highest, in order of -60 to -40 J/cm^3 . The phase transformation is slower in latter seconds and becomes sluggish after several seconds of transformation although the equilibrium fraction of ferrite has not been reached. This is not found in the case of the Mn-Si DP steel. The interface mobility in the last period of transformation was therefore set as low as 1.0×10^{-6} to zero.

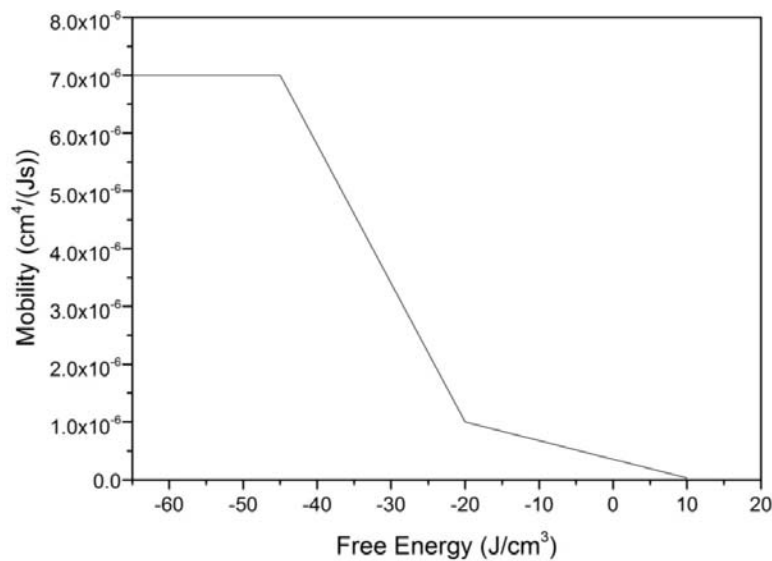


Fig. 76 The non-constant austenite-ferrite interface mobility assigned for the Mn-Mo DP steel.

All the parameters for the calculation are summarised in Table 5.1.

Table 5.1 Summary of the parameters for the calculation, including the derivation method

Parameter	Abbreviation	Derivation method	Value/mode	reference
Interface mobility between ferrite and ferrite	$M_{\alpha-\alpha}$	Value from the literature	$3.3 \times 10^{-6} \text{ cm}^4 (\text{J}\cdot\text{s})^{-1}$	Thi06, Mur75
Interface mobility between austenite and austenite	$M_{\gamma-\gamma}$	Value from the literature	$1.4 \times 10^{-7} \text{ cm}^4 (\text{J}\cdot\text{s})^{-1}$	Thi06, Mur75
Interface mobility between austenite and ferrite	$M_{\gamma-\alpha}$	Will be determined from current simulations	$8 \times 10^{-6} \text{ cm}^4/(\text{J}\cdot\text{s})$ for the Mn-Si DP steel. See Fig. 76 for the Mn-Mo DP steel	-
Interfacial energy between ferrite and ferrite	$\sigma_{\alpha-\alpha}$	Value from the literature	0.5 J m^{-2}	Thi06, Mur75
Interfacial energy between austenite and ferrite	$\sigma_{\gamma-\alpha}$	Value from the literature	0.4 J m^{-2}	Thi06, Mur75
Interfacial energy between austenite and austenite	$\sigma_{\gamma-\gamma}$	Value from the literature	0.7 J m^{-2}	Thi06, Mur75
Width of the transition boundary	η	Arbitrarily adjusted	1 μm or 5 cells	-
Difference in Gibbs free energy between adjacent ferrite and austenite grains	ΔG_{ij}	ThermoCalc™ through TQ interface		-
Additional Gibbs free energy between adjacent ferrite and austenite grains from the stored energy due to retained strain	ΔG_{ijd}	Flow curve during the deformation in the dilatometer experiment (section 3.2.3)	3.29 J/cm^3 at retained strain of 0.3	-

Parameter	Abbreviation	Derivation method	Value/mode	reference
Ferrite Nucleation density	-	Metallographic observation	See Fig. 43 and Fig. 45	
Shield distance	-	Comparison between the ferrite grain size in the simulation and the experiments.	See Table 5.3	-
Shield time	-	Comparison between the ferrite grain size in the simulation and the experiments.	See Table 5.3	-

The distribution of the ferrite nuclei/grain sizes was measured by drawing the grain boundaries of all grains and calculating into EQAD as reported before in section 3.5.2. The number of nuclei assigned to the simulations is listed in Table 5.2 and separated into the three nucleation sites: triple point, interface and bulk. It was used to support the nucleation model in the simulation and to compare with its resulting ferrite grain size. The simulation conditions were adjusted for the best fit of ferrite grain size distribution with the experiment. It is generally controlled by the nucleation density, shield distance and shield time. The shield distance and shield time control a region around a given nucleus for which in a specified time (shield time) no further nucleation occurs.

Table 5.2 The measured ferrite nucleation density compared with those assigned to the simulation at different nucleation sites

	Ferrite nuclei density, mm⁻²			
	Total	Triple points	interface	bulk
Mn-Mo DP steel	3721	195	1200	2326
Mn-Si DP steel	2908	186	861	1861

As the ferrite grain size in the Mn-Si steel was found to distribute rather uniformly, the ferrite nucleation was modelled with phase field method with bigger shield time. On the other hands, it was found that in the Mn-Mo steel, the ferrite grain size varies more. Some grains show to be nucleated together and grow only in the other directions without impingement. It was therefore modelled to have smaller shield distance. The information on the shielding is tabulated in Table 5.3.

Table 5.3 The shield time and shield distance assigned to the simulations.

	Mn-Mo DP		Mn-Si DP	
	Shield time, s	Shield distance, μm	Shield time, s	Shield distance, μm
Triple	0.01	1.5	0.005	6.5
Interface	0.2	2.5	0.1	8.5
Bulk	0.3	3.5	0.15	8.5

5.6.1 The simulation of the pancaked austenite

The austenite grains under deformation were created from random ellipses connected to others under the voronoi criterion. The aspect ratio of axes was adjusted to correspond to the retained strain. The number of grains per area corresponds to the grain size before deformation.

The total number of ferrite nuclei was assigned according to that observed from the metallographic results after different transformation time (Fig. 42 and Fig. 45). The number of ferrite nuclei at the grain interface was calculated to correspond to the S_v value and the observed mean ferrite grain size from the experiment as the S_v function reports the length of austenite grain boundary per area. Those at the triple points have the same number of the triple points appear in the domain. The rest was assigned to the bulk. The nucleation in the bulk was set to start later than at the first two nucleation sites as generally observed. The initial ferrite nuclei size was set to be zero and ferrite started to nucleate as soon as the simulation started. At each specified point/line/area where nucleation is activated, the nucleation is random. The nucleation was completed within a very short time according to the site saturation approach [Tam88].

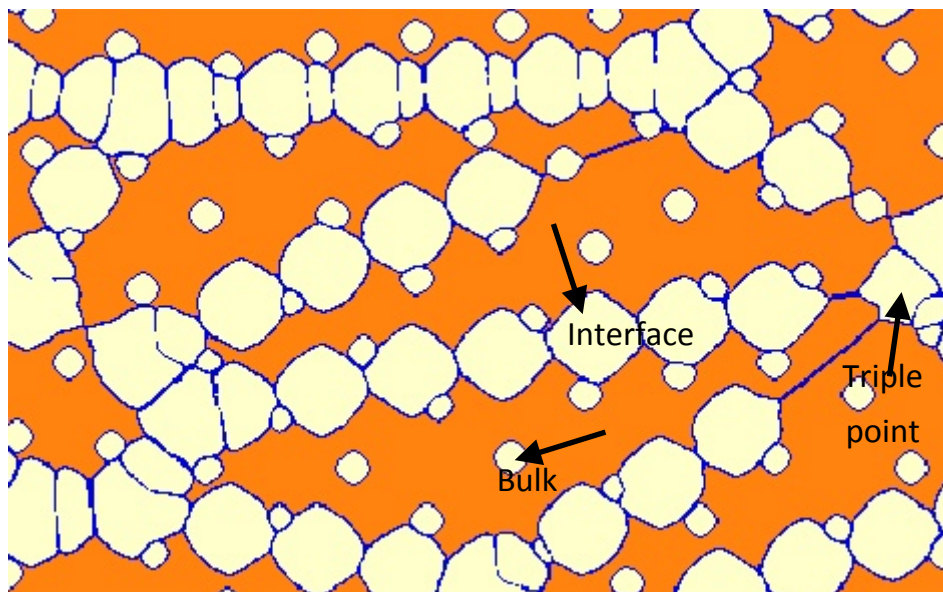


Fig. 77 The three classes of ferrite nucleation sites

A beneficial feature in MICRESS, that it is able to couple the stored energy in austenite, was also employed in the simulation. The stored energy was measured from the flow curve and calculated to be $3 \times 10^6 \text{ J/m}^3$.

The domain size of the calculation is $74 \times 581 \mu\text{m}$ and lies on the cross section of a rolled sheet, as shown in Fig. 78.



Fig. 78 The calculation domain for phase field simulation on the cross section of a rolled strip.

6 MODELLING RESULTS

6.1 Alloying and process window design by CALPHAD

6.1.1 Calculation of the isoplethal phase diagrams

Fig. 79 to Fig. 83 show the isoplethal phase diagrams or pseudo binary phase diagrams of Mn-Mo and Mn-Si DP steels with varying alloying elements.

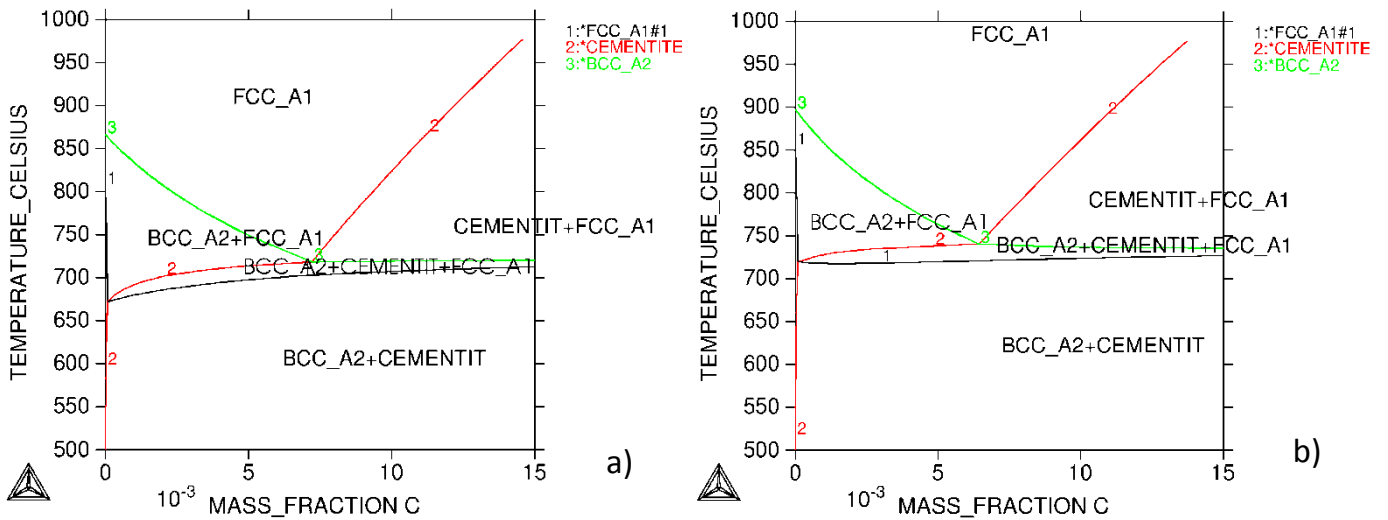


Fig. 79 The isoplethal phase diagrams of a) Mn-Mo and b) Mn-Si DP steels showing the stable phases with the variation of carbon content and temperature. The other alloying contents are kept constant according to Table 3.1.

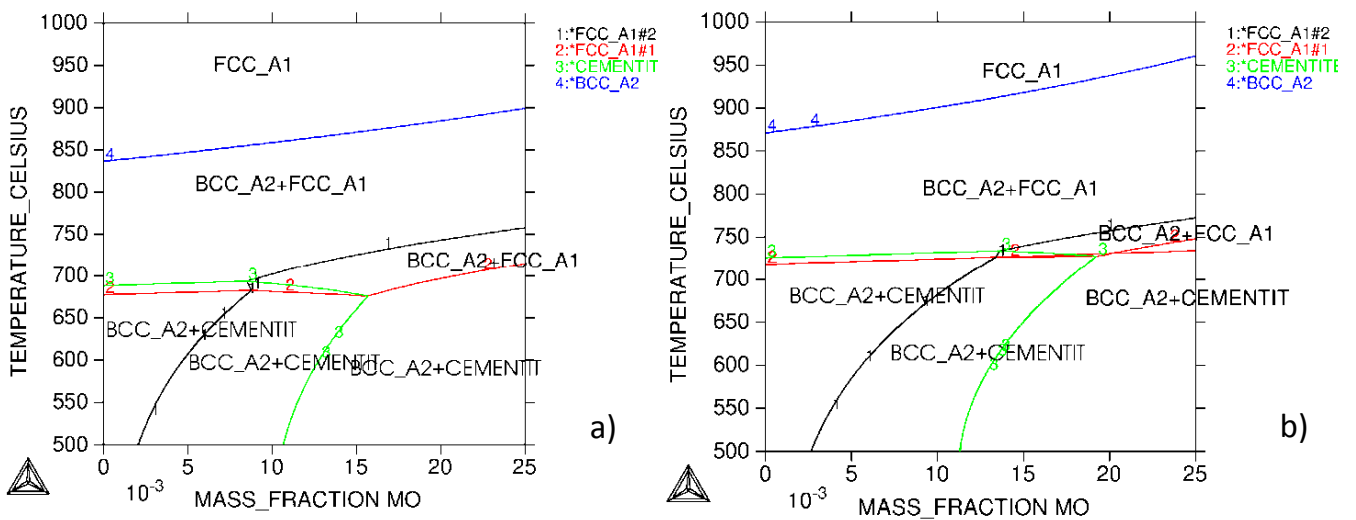


Fig. 80 The isoplethal phase diagrams of a) Mn-Mo and b) Mn-Si DP steels showing the stable phases with the variation of molybdenum content and temperature. The other alloying contents are kept constant according to Table 3.1.

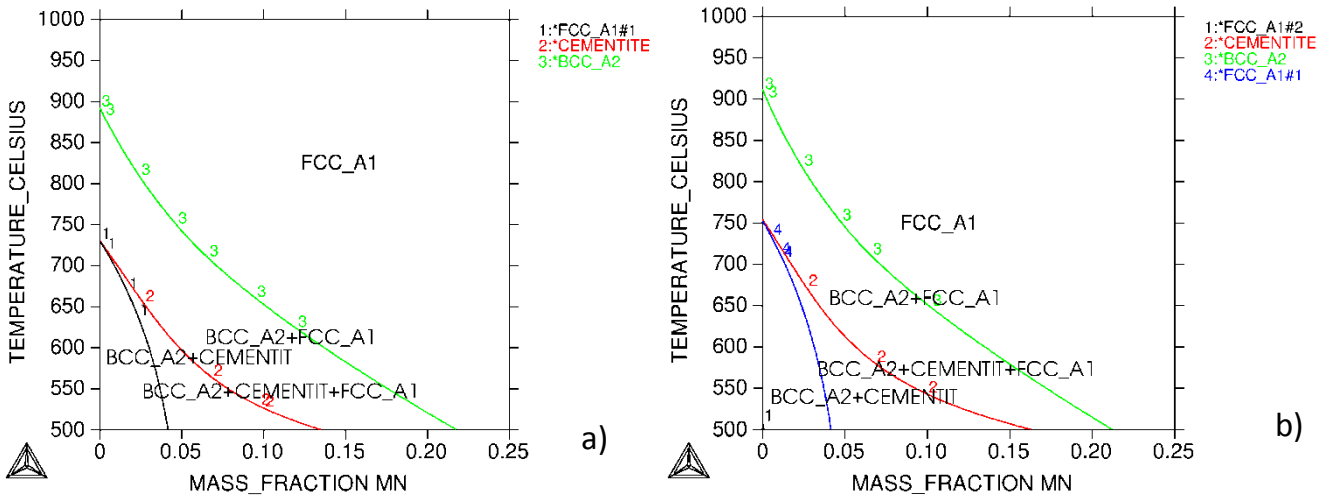


Fig. 81 The isoplethal phase diagrams of a) Mn-Mo and b) Mn-Si DP steels showing the stable phases with the variation of manganese content and temperature. The other alloying contents are kept constant according to Table 3.1.

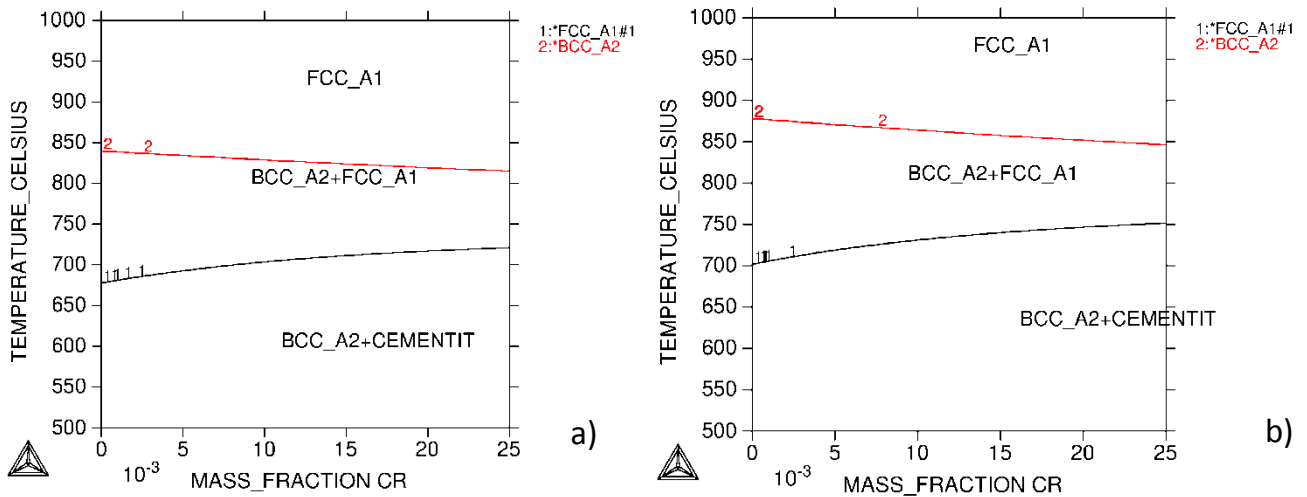


Fig. 82 The isoplethal phase diagrams of a) Mn-Mo and b) Mn-Si DP steels showing the stable phases with the variation of chromium content and temperature. The other alloying contents are kept constant according to Table 3.1.

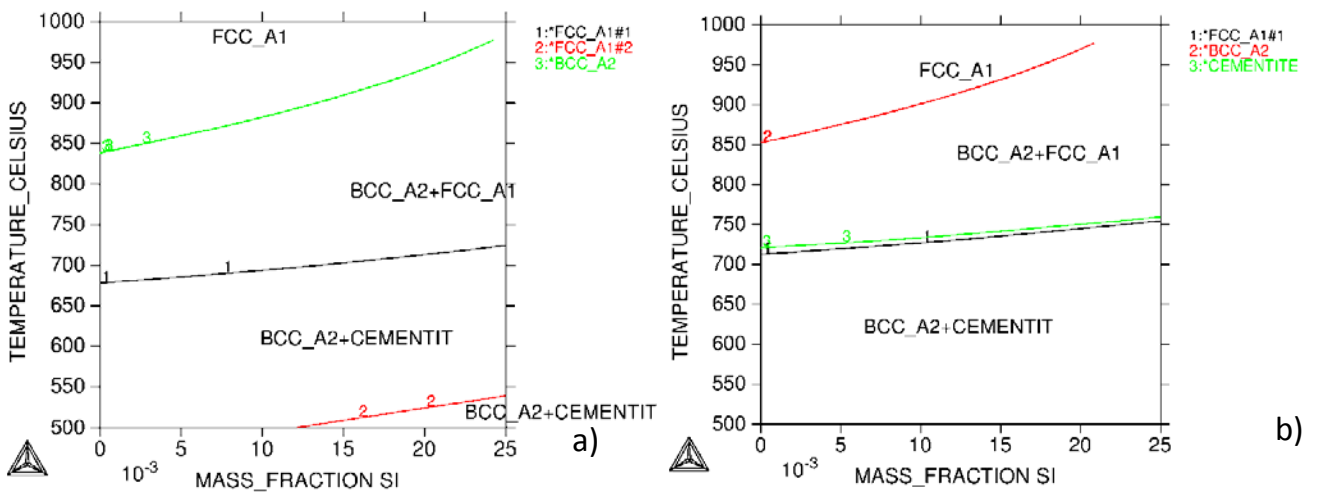


Fig. 83 The isoplethal phase diagrams of a) Mn-Mo and b) Mn-Si DP steels showing the stable phases with the variation of silicon content and temperature. The other alloying contents are kept constant according to Table 3.1.

From these results, the process window can be estimated before the chemical composition of the melt is fixed. The working temperature should, however, not be too close to the phase boundaries as they are for the equilibrium conditions. In the rolling conditions, the critical temperatures will be higher.

6.1.2 Calculation of the critical temperatures

The A_{e1} and A_{e3} under equilibrium condition and paraequilibrium conditions as well as T_0 locus are plotted together in Fig. 84. It can be clearly seen that A_{e3para} is lower than the A_{e3} under (ortho)equilibrium.

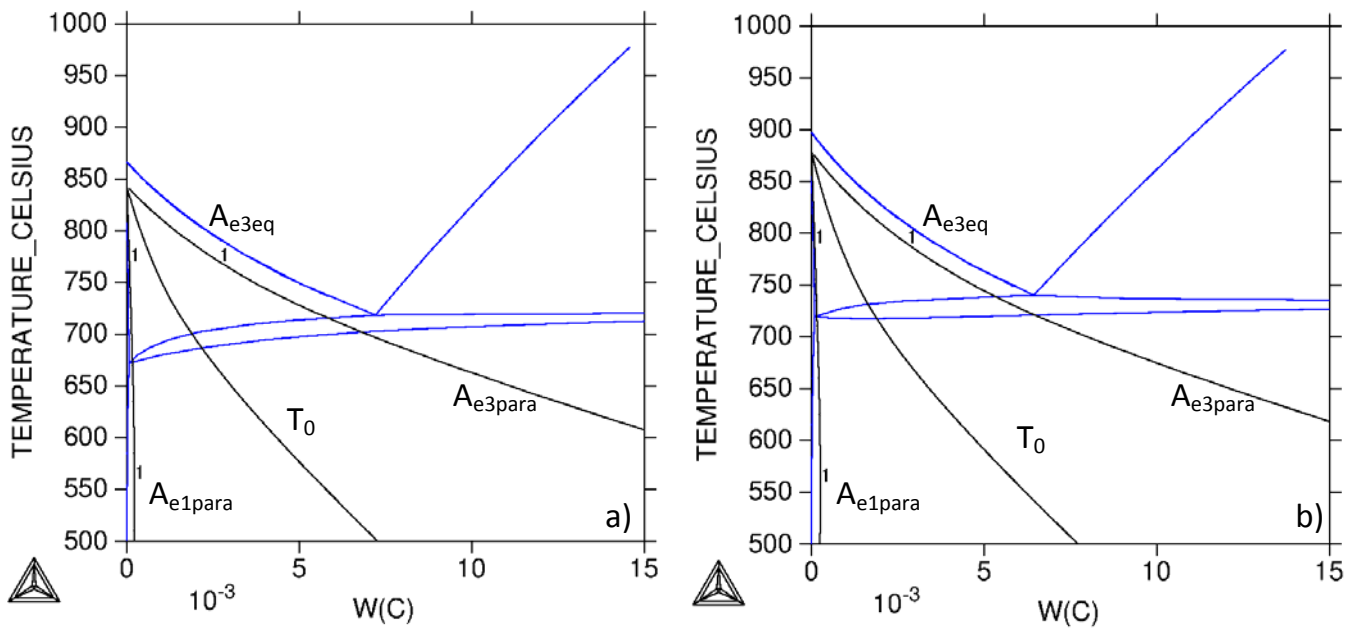
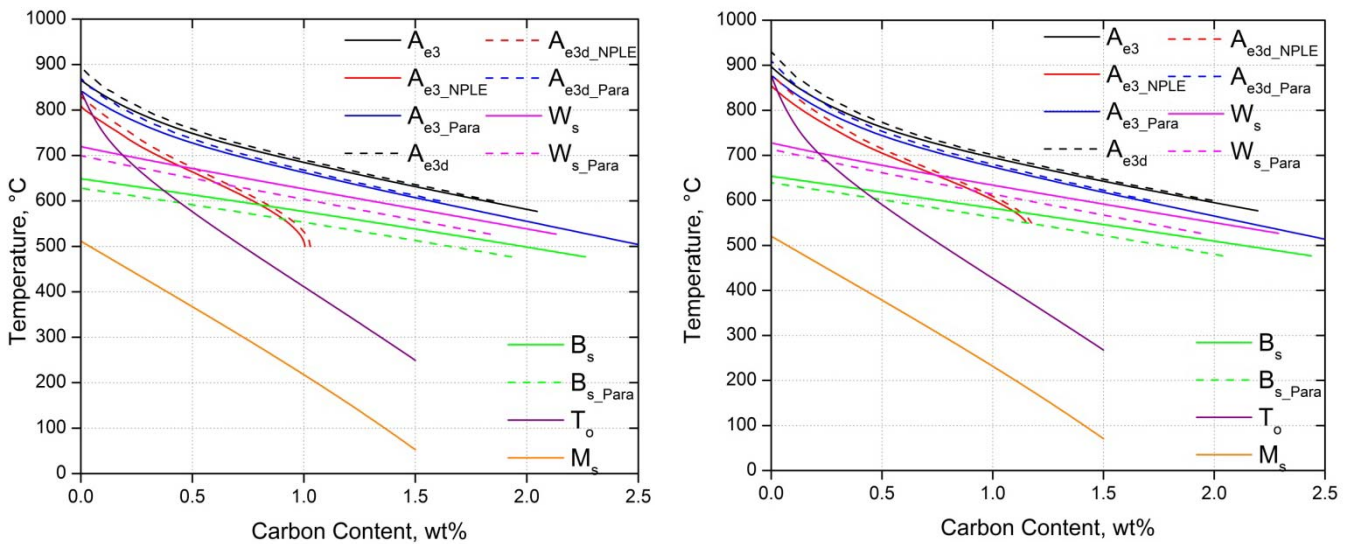


Fig. 84 A_{e1} and A_{e3} under equilibrium and paraequilibrium conditions as well as T_0 superimposed on the pseudo binary phase diagrams of a) Mn-Mo and b) Mn-Si DP steels

Note that the results in Fig. 79 to Fig. 84 were directly calculated from ThermoCalc™. Other calculated critical temperatures including those which were not readily derived from ThermoCalc™ are shown in Fig. 85 and Fig. 86. Those temperatures calculated by the parallel tangent and the diffusionless approaches are represented in Fig. 85 while those according to Bhadeshia's approach are shown in Fig. 86. The A_3 temperatures in the Mn-Si DP steel show to be higher than the Mn-Mo DP steel as can be also seen from the isoplethal phase diagram in Fig. 79. The deformation raises up the A_{e3} temperature only slightly but with a higher degree at the lower carbon content. The A_{e3} and A_{e3d} temperatures under paraequilibrium are approximately 25 °C lower than under the (ortho)equilibrium. Unlikely, the A_{e3NPLE} lies at much lower temperature and has a much

steeper slope. This is the reason why some scientists assume the NPLE transformation mode when the transformation is found to be much slower than other cases.

The W_s and B_s temperatures in Fig. 85 are derived from the parallel tangent approach and seem to give reasonable results. But the M_s temperature calculated from the diffusionless transformation approach coupled with the stored energy proposed by Guénin [Gué79] shows to be unsatisfactory. The highest predicted M_s temperature is somewhat rather high and its slope is too large. Therefore, at the carbon content over 1.5%, the M_s temperature is around at room temperature. This is obviously too low and therefore this modelling approach for M_s shows to be inappropriate.



a)

b)

Fig. 85 The critical temperatures calculated by the parallel tangent and diffusionless transformation approaches for a) the Mn-Mo and b) the Mn-Si DP steel. The A_{e3} , W_s , and B_s temperatures are calculated from the parallel tangent approach. The M_s is calculated from the diffusionless transformation approach.

As both Widmanstätten and bainite have to satisfy the nucleation criterion according to Bhadeshia’s universal nucleation function (G_n), the W_s and B_s temperatures must be interpreted in the relation to the G_n function. In this case, at the higher carbon content behind the intersection between W_s and G_n , the G_n line will be taken as W_s temperature [Ali90]. The highest B_s temperature seems to be realistic but due to the large slope of the curve, at higher carbon contents, the B_s temperature shows to be too low compared with that predicted by Lee [Lee02] as will be shown in Fig. 88.

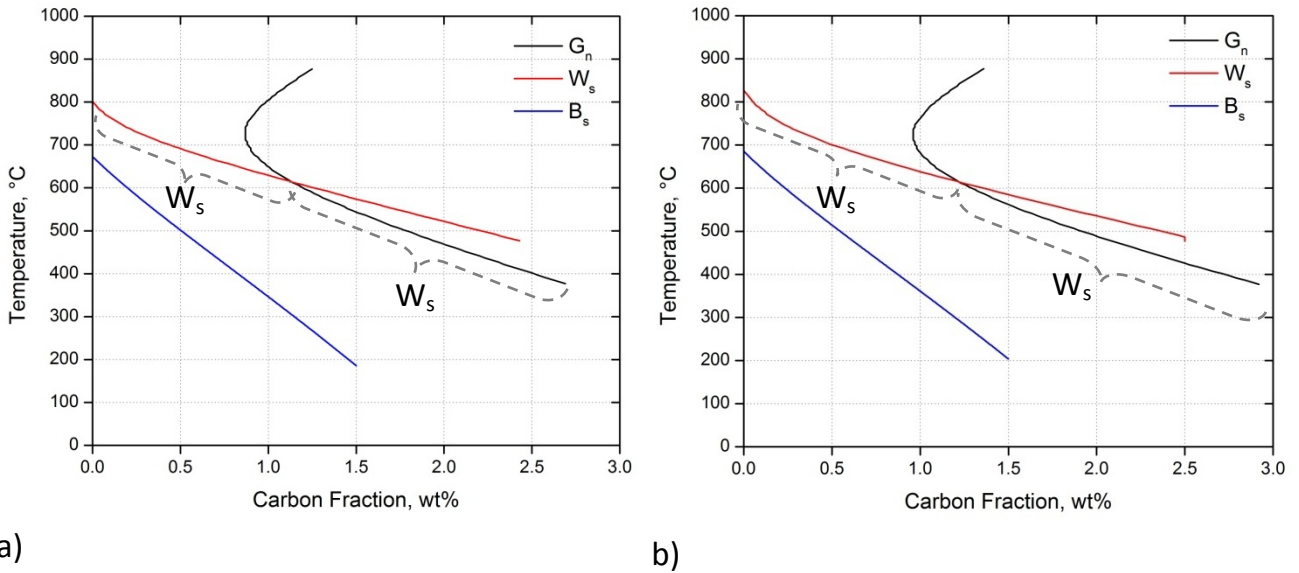


Fig. 86 The calculation results on W_s and B_s temperatures for a) the Mn-Mo and b) the Mn-Si DP steels according to Bhadeshia’s approach.

In conclusions, only the parallel tangent approach for the calculation of A_{3d} , W_s and B_s temperatures are acceptable to be accurate in the context of this work. Nevertheless, as the transformation during cooling is not under equilibrium it is beneficial to observe the A_{r3} temperatures provided from empirical equation from the literature as shown in Fig. 87.

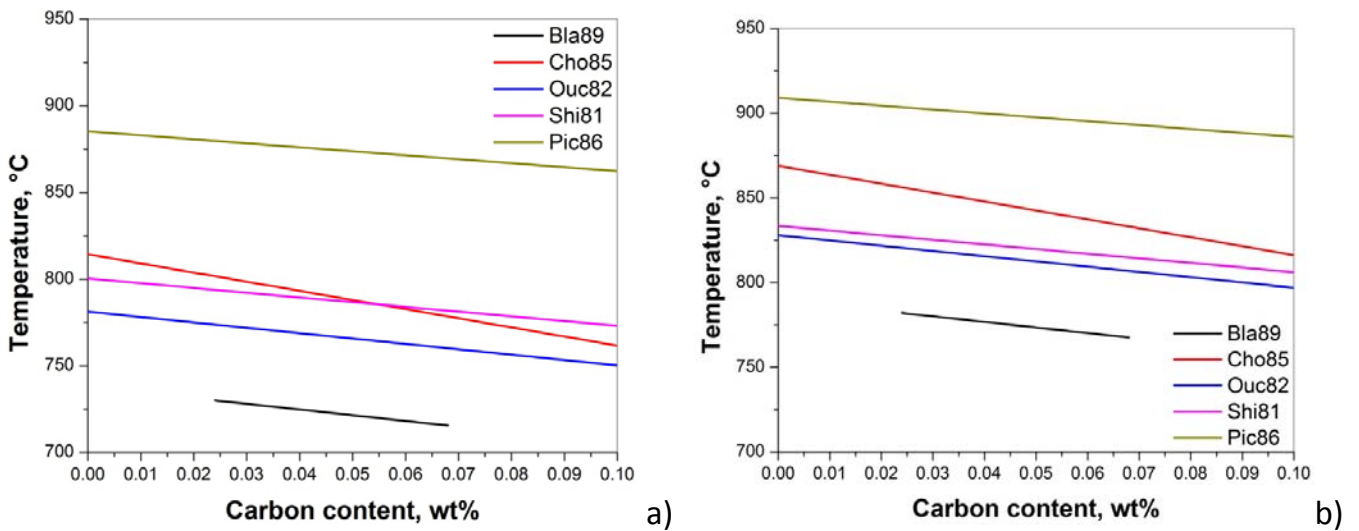


Fig. 87 The A_{r3} temperature plotted from the empirical equations form the literature for a) the Mn-Mo and b) the Mn-Si DP steels.

Fig. 88 compares the B_s temperatures predicted by the empirical equations from different authors in Eq.52 to Eq.54 and Eq.56. They are plotted with those calculated under the (ortho)equilibrium and paraequilibrium conditions, shown already in Fig. 85. The equation proposed by Lee [Lee02] lies in the same range as that calculated under the

paraequilibrium condition. Fig. 89 shows other empirical equations for the B_s temperature shown in Eq.50 to Eq.51 and Eq.55. Similarly, Fig. 90 and Fig. 91 show the empirical M_s temperatures from Eq.56 to Eq.62. All the empirical equations are plotted only in the valid range of carbon content which is reported by the authors.

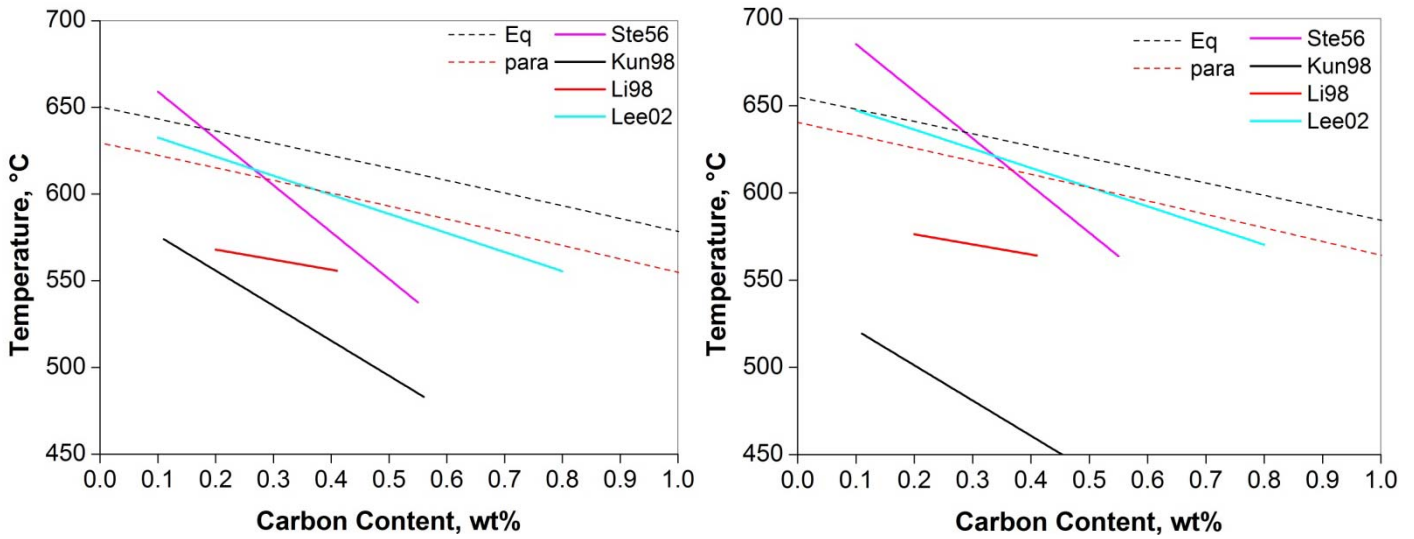


Fig. 88 The predicted B_s temperatures from Eq.52 to Eq.54 and Eq.56 in Table 2.5, compared with those calculated from the thermodynamic approaches. a) the Mn-Mo steel b) the Mn-Si DP steel

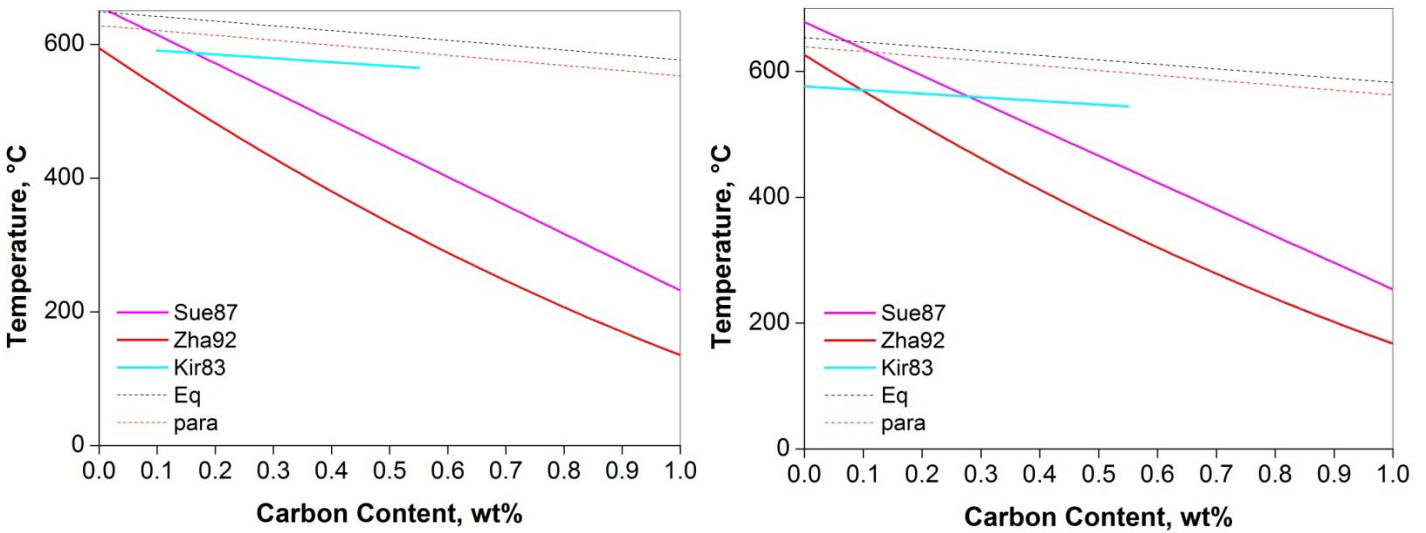


Fig. 89 The predicted B_s temperatures from Eq.50-Eq.51 and Eq.55 in Table 2.5, compared with those calculated from the thermodynamic approaches. a) the Mn-Mo steel b) the Mn-Si DP steel

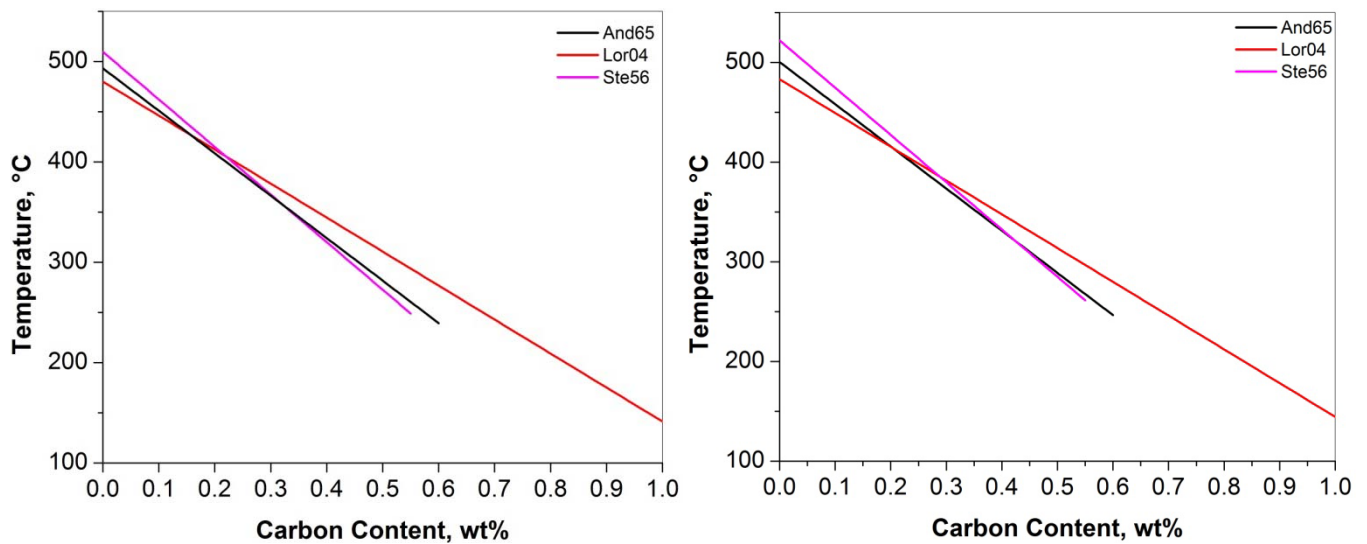


Fig. 90 The predicted M_s temperatures from Eq.56-Eq.57 and Eq.62 in Table 2.5. a) the Mn-Mo steel b) the Mn-Si DP steel

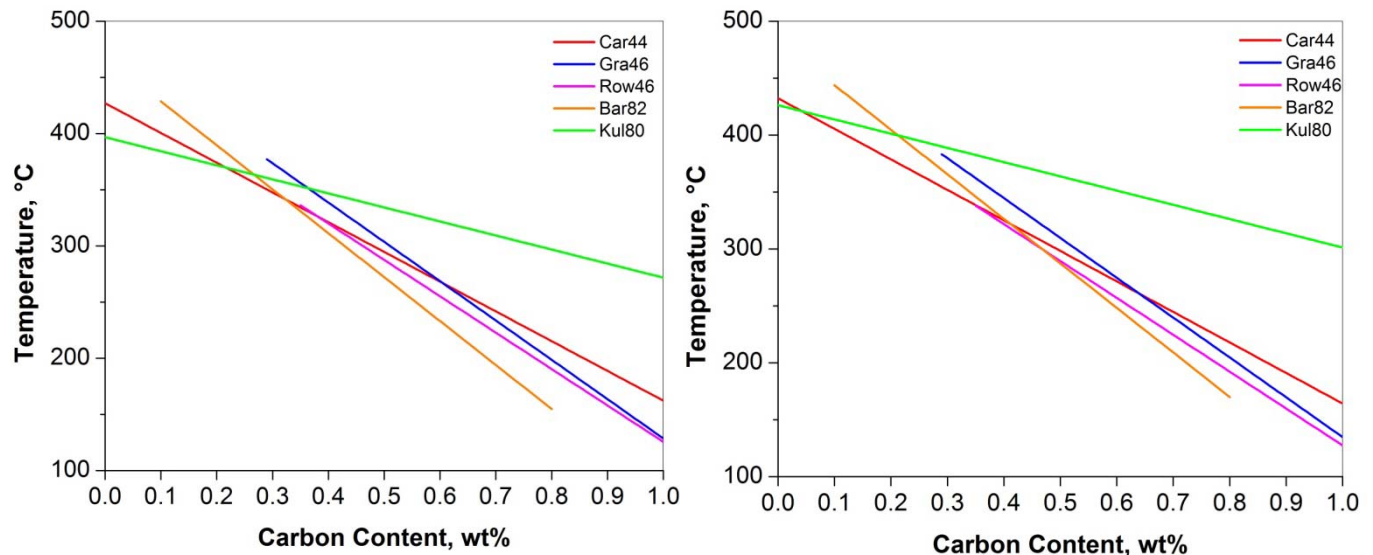
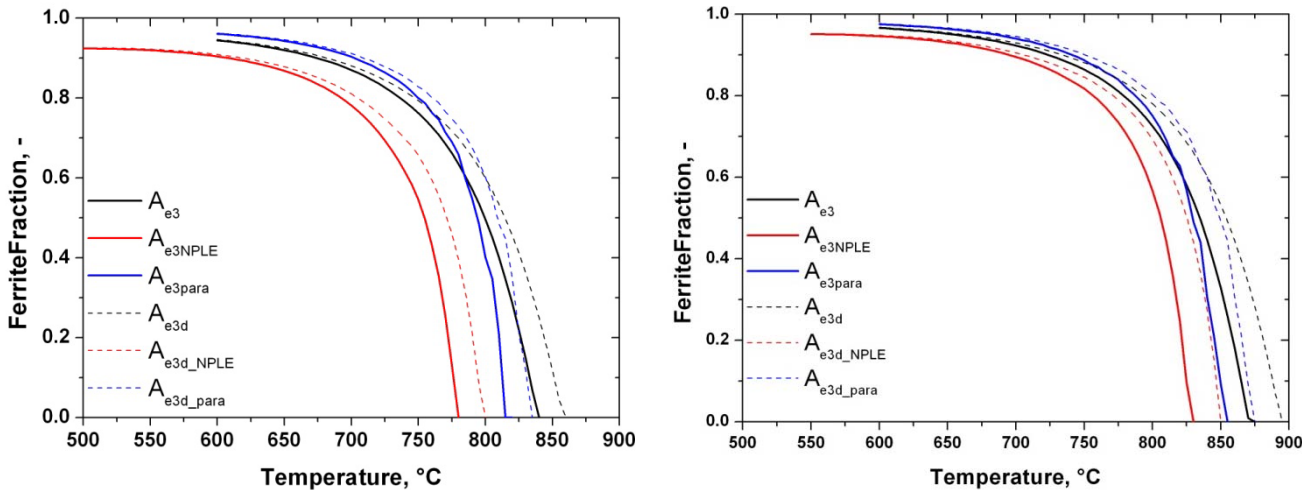


Fig. 91 The predicted M_s temperatures from Eq.58-Eq.61 and Eq.64 in Table 2.5. a) the Mn-Mo steel b) the Mn-Si DP steel

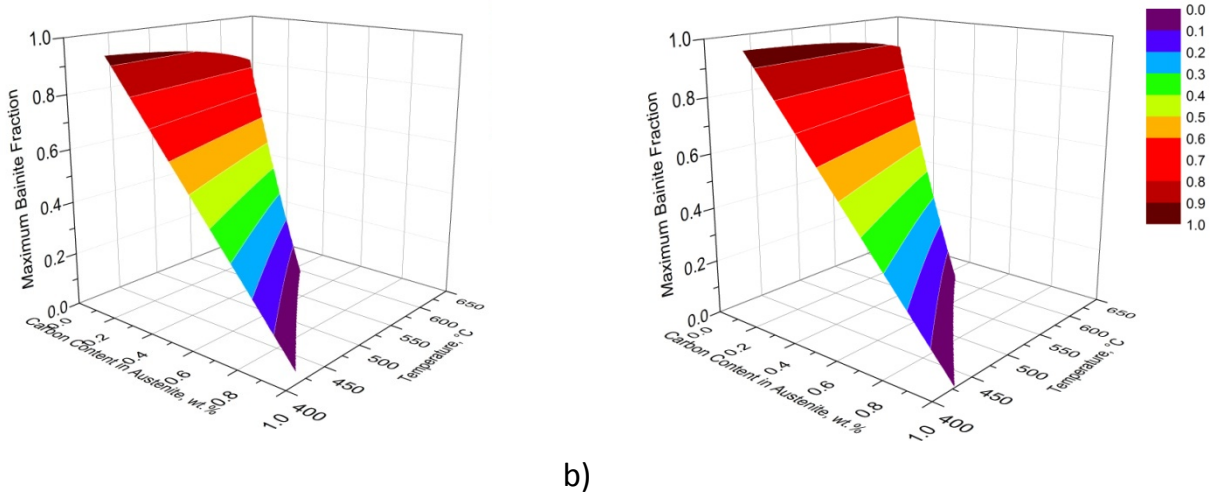
6.1.3 Calculation of the maximum phase fraction

Fig. 92 shows the maximum ferrite fractions for the Mn-Mo and the Mn-Si DP steels at different temperatures calculated from ThermoCalc™ under different modes of equilibria. They are also compared with those affected by deformation in austenite, indicated by the extra subscript 'd'. The value from orthoequilibrium without deformation (A_{e3eq}) will be transferred to the macroscopic modelling for ferrite transformation in section 6.4.



a) b)
Fig. 92 The maximum ferrite fraction at different temperatures calculated from ThermoCalc™ according to different equilibrium conditions. a) the Mn-Mo and b) the Mn-Si DP steels

The maximum bainitic ferrite fraction for the Mn-Mo and Mn-Si DP steels, which is, on the other hand, useful for any further modelling on the bainite transformation, is shown in Fig. 93. It was calculated under the T_0 concept and Eq.74 proposed by Takahashi [Tak91].



a) b)
Fig. 93 The maximum bainite fraction at different temperatures derived from the T_0 concept for a) the Mn-Mo and b) the Mn-Si DP steels

After the ferrite formation, the remaining austenite is taken to have a fraction of 1. The carbon content in austenite shown in the figure (C_γ) is the carbon content partitioned to the austenite. In case of no ferrite transformation, the C_γ is the nominal carbon content. At lower carbon content, bainite is ready to transform at higher temperatures and its achievable maximum fraction is rather high. At higher carbon content, the B_s temperature

lowers. Therefore, the surface tilts to lower temperatures at lower carbon contents and predicts lower achievable fraction. This account for the fact that the austenite tends to transform more to martensite.

In the Mn-Mo DP steel, at the carbon content of 0.073%, which is its nominal carbon content, the achievable bainite fraction is highest at 440°C and amounts to 0.925 while it amounts to somewhat lower fraction of 0.816 at 630°C. On the other hand, in the Mn-Si DP steel, at the carbon content of 0.064%, which is its nominal carbon content, the achievable bainite fraction is highest at 430°C and amounts to 0.955 while it amounts to somewhat lower fraction of 0.927 at 570°C.

6.2 Modelling of the evolution of austenite grain size during recrystallisation

The fraction recrystallised has been measured by the double hit test described in sections 3.2.2 and 4.1.4 and listed in Table 4.2 and 4.4. The t_{50} was estimated from the data in Table 4.2, Table 4.4 and the JMAK form equation for recrystallisation, Eq.2-9. The obtained $t_{0.5}$ s and n values are obtained by means of optimisation and are listed in Table 6.1 and Table 6.2 for the Mn-Mo and Mn-Si DP steels, respectively.

$$F_x = 1 - \exp \left[-0.693 \left(\frac{t}{t_{0.5}} \right)^n \right] \tag{Eq.2-9}$$

Table 6.1 The estimated parameters describing the recrystallisation kinetics for the Mn-Mo DP steel

Deformation temperature, °C	Estimated n-value	Estimated $t_{0.5}$, s	R-square
With recovery fraction of 0.25			
1100	1.922	1.511	0.9872
1000	2.195	1.500	0.9996
950	1.993	2.160	0.9822
With recovery fraction of 0.2			
1100	2.892	1.886	0.9888
1000	2.945	1.777	0.9996
950	2.939	2.363	0.9846

Table 6.2 The estimated parameters describing the recrystallisation kinetics for the Mn-Si DP steel

Deformation temperature, °C	Estimated n-value	Estimated $t_{0.5}$, s	R-square
With recovery fraction of 0.25			
1100	2.253	1.397	0.9998
1000	2.011	1.441	0.9992
950	2.051	1.914	0.9511
With recovery fraction of 0.2			
1100	2.187	1.360	0.9999
1000	2.101	1.424	0.9996
950	2.030	1.756	1.0000

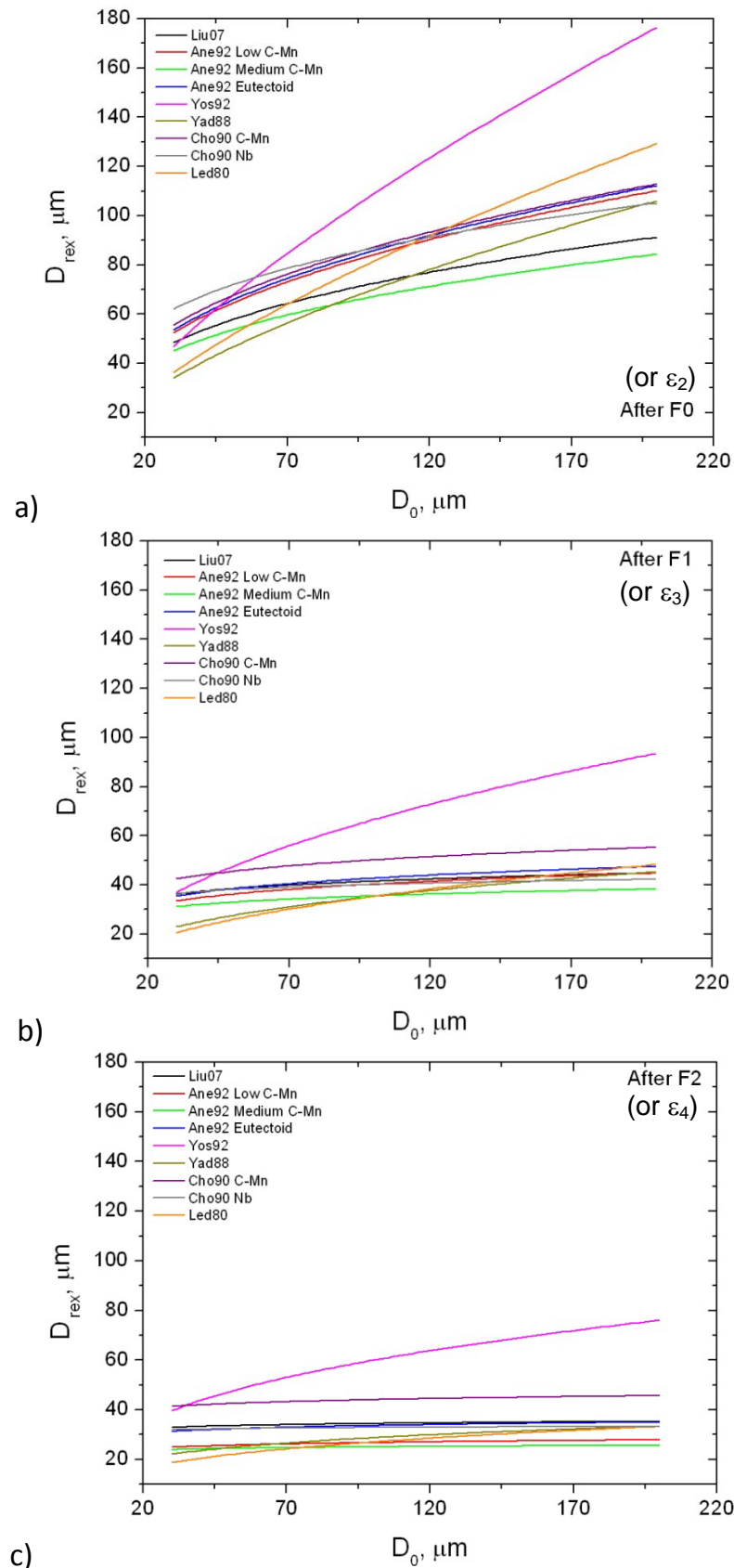


Fig. 94 The evolution of the austenite grain size after the repeated recrystallisations in after 3 rolling passes or deformation steps according to the thermomechanical processing routes *Option B* and *D* in Table 3.3 by using Eq.16 a) after the first (F0 or ε_2) b) after the second (F1 or ε_3) and c) after the third (F1 or ε_3) rolling pass or deformation step. All the deformation parameters are according to those in *Option B* and *D*.

The temperature at the last deformation step, 900°C for the Mn-Si DP steel lies above the predicted T_{nr} temperature by Eq.1, which predicts the T_{nr} at 772 °C. But because after this deformation steps, the samples were quenched down to the isothermal transformation temperature within a short time, the fraction recrystallised is considered minimal. Therefore, the last deformation step was still modelled to be unrecrystallised for both the Mn-Mo DP and Mn-Si DP steels.

Sellars [Sel95] concluded from his modelling results that, with the increasing number of passes, the final austenite grain sizes converge to 35-50 μm and results in fewer discrepancies between the modelled and measured austenite grain sizes. This has been proven in Fig.94 by plotting the recrystallised austenite grain size predicted by several empirical equations from the literature after 3 rolling passes according to the processing routes *Option B* and *D* in Table 3.3. It is therefore, very reasonable to model the austenite grain size of 35 μm at the last deformation step. Kwon [Kwo92] also commented that although each research group has derived different equations to describe the recrystallised austenite grain size, the predicted grain size does not differ much when applied to the repeated recrystallisations between rolling stands.

The recrystallised austenite grain sizes after each deformation pass in the deformation schedule in Table 3.3 has been calculated by the equation from Liu [Liu07], as shown in Table 6.3.

Table 6.3 The calculated recrystallised austenite grain sizes after each deformation pass in the processing route *Option B* and *D* listed in Table 3.3.

Material	Grain Size, μm				S_v, mm^{-1}
	After reheating, T_1	After F0, ϵ_2	After F1, ϵ_3	After F2, ϵ_4	After F3, ϵ_5
Mn-Mo DP	100	72	42	34	70
Mn-Si DP	270	100	46	35	70

6.3 Modelling of the effect of austenite grain size and retained strain

Fig. 95 shows the S_v values result from the combination of different austenite grain sizes and strains, which represent the level of austenite conditioning. It can be seen that the S_v increases sharply with smaller austenite grain size but increases significantly slower with the deformation. This is the reason why the repeated recrystallisations are very effective to increase S_v value in the hot rolling before the austenite grains will be further deformed below T_{nr} by the controlled rolling.

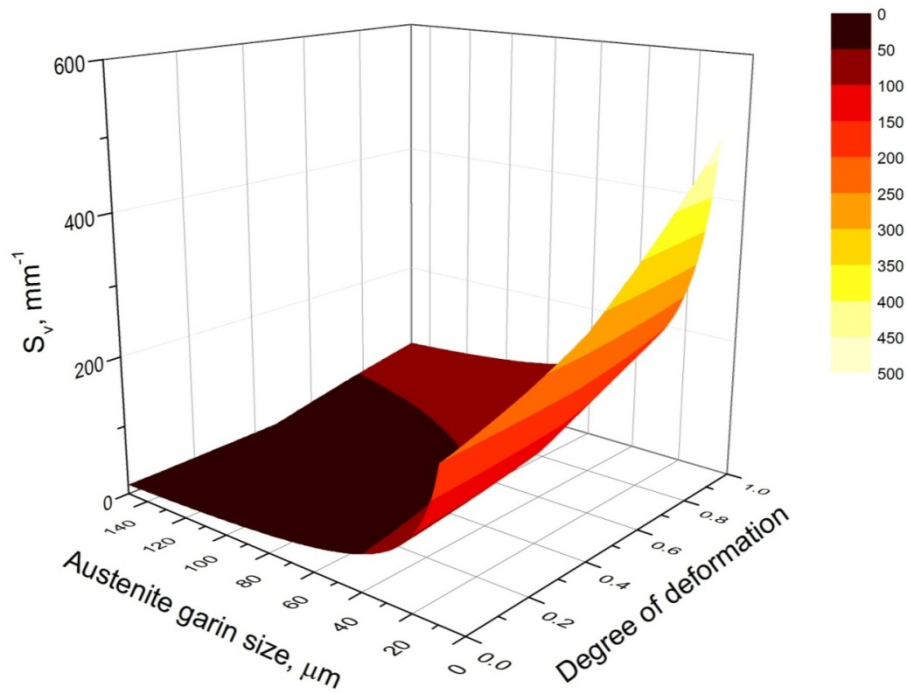


Fig. 95 A surface plot showing the S_v value with the austenite grain size and the retained strain which flattens the austenite grains.

6.4 Modelling of the macroscopic ferrite transformation kinetics

The effect of transformation temperature on ferrite transformation in both the Mn-Mo and Mn-Si DP steel is mapped with the function g_{Temp} in the rate form equation as shown in Fig. 96

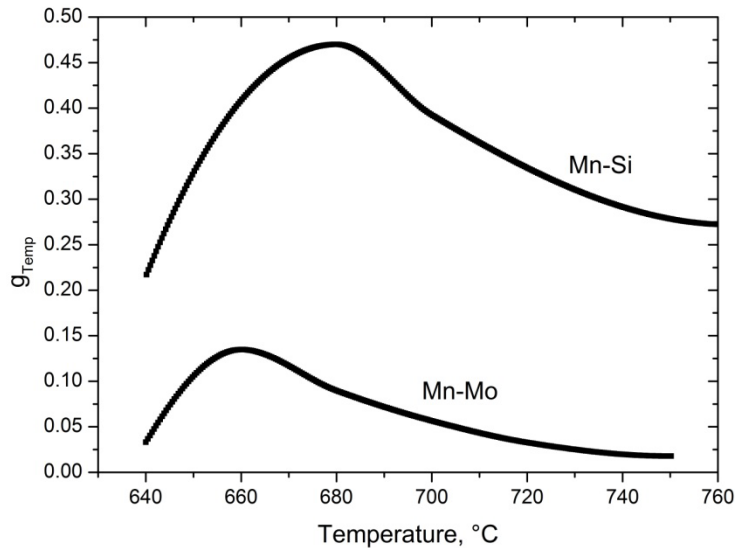


Fig. 96 The g_{Temp} function showing the effect of holding temperature. It was derived from the case of austenite grain size of 35 μm without retained strain.

The g_{Temp} function shows that the most favourable temperatures for the ferrite transformation are 660 and 680°C in the Mn-Mo and Mn-Si DP steels respectively. It is more challenging to define the g_{Temp} values at the highest and lowest temperature regions. Note that these g_{Temp} values are derived from

$$g_{Temp}(T) = \frac{\ln \frac{f_{eq}-f(t_S)}{f_{eq}-f(t_E)}}{t_E-t_S} \tag{Eq.77}$$

At the temperatures where no ferrite fraction can be observed from the isothermal transformation experiment, the g_{Temp} can be numerically zero. But note that it has been derived under the case of strain free (with austenite grain size of 35 μm). As the matter of fact that under deformation, the temperature region for ferrite formation is broader, some ferrite can form under large retained strain at the temperatures where the g_{Temp} might have been defined to be zero under no retained strain.

The effect of austenite grain size and retained strain or, say, the austenite conditioning on the ferrite transformation is shown in Fig. 97. It can be seen clearly that the increasing S_v value raises the g_{S_v} value strongly in the Mn-Mo DP steel which is not the case in the Mn-Si DP steel. This increase in the g_{S_v} value certainly accelerates the transformation rate as described in the rate equation.

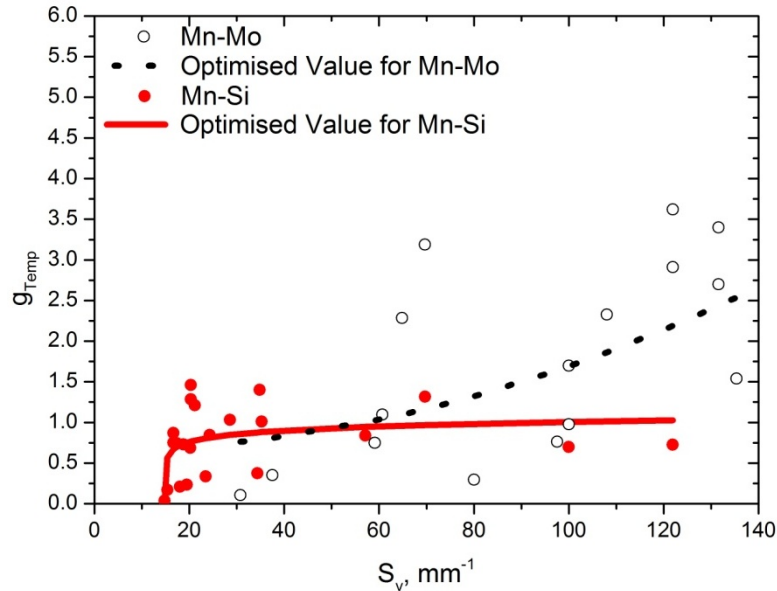
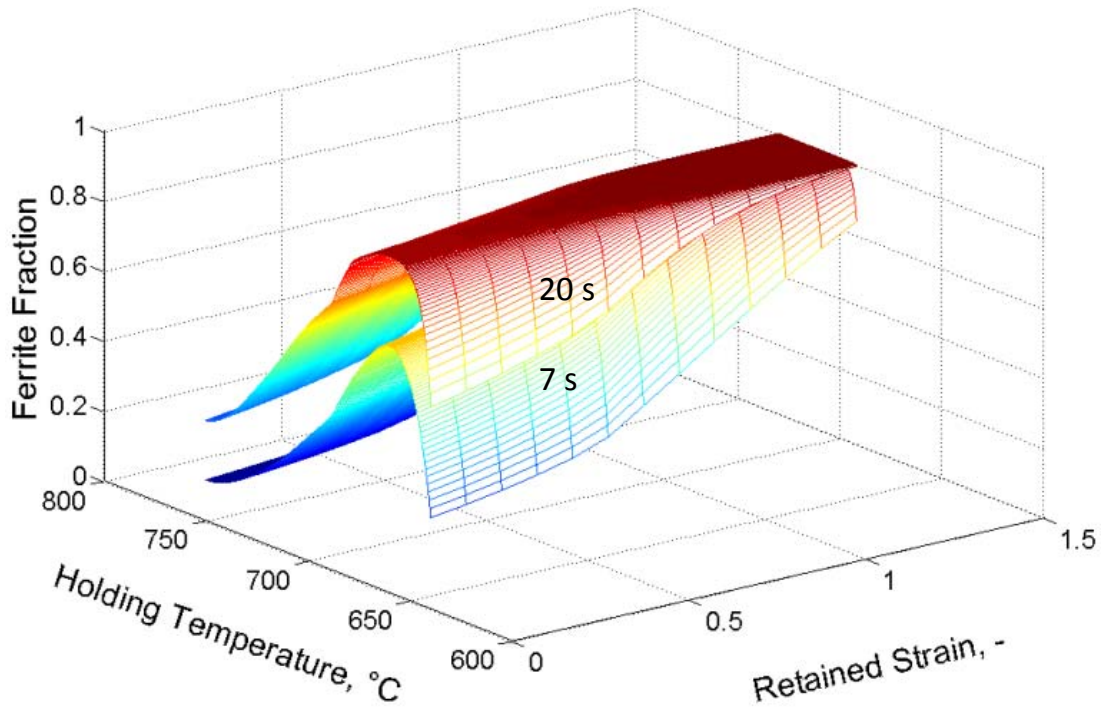


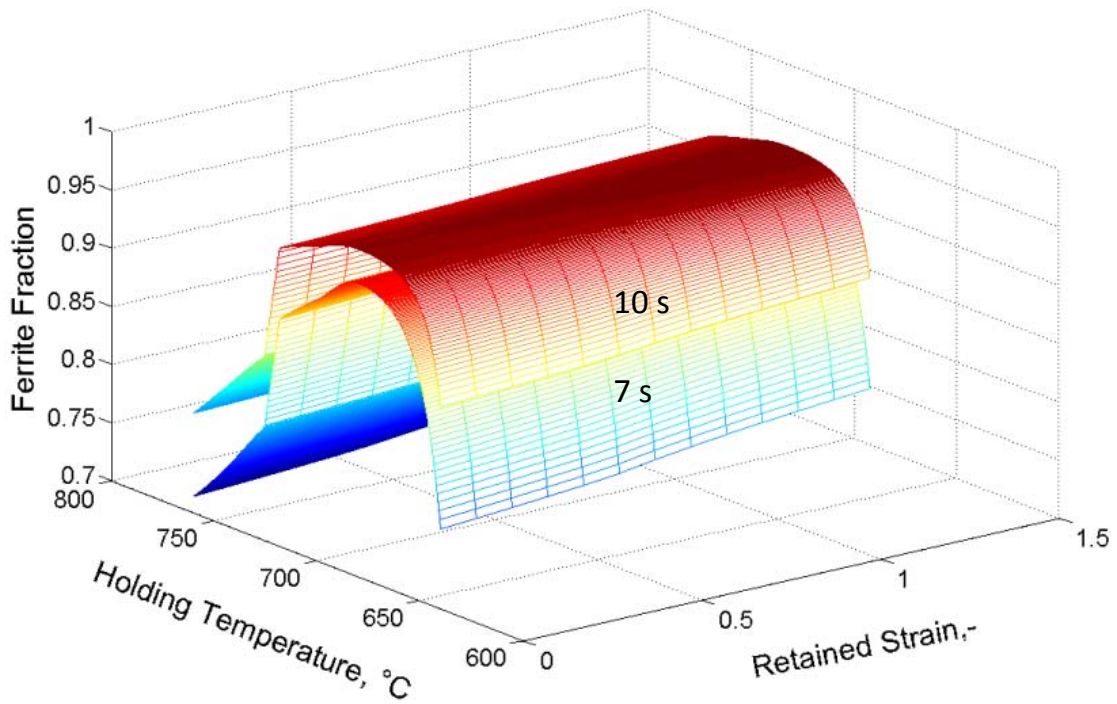
Fig. 97 The g_{S_v} function showing the effect of the S_v value on the transformation kinetics.

The ultimate results from this model can be shown in an arbitrary fashion. For instance, any austenite grain size can be selected from the range where the g_{S_v} function was identified. As an example, the austenite grain size of 25 μm is selected for the illustration in Fig. 98, which shows the effect of the transformation temperature and retained strain on the ferrite fraction.

The process window which conforms the requirement of hot rolled DP steels, in other words, where 70-80% of ferrite can be yielded within 7 s, can be shown better in contours of phase fraction, shown in Fig. 99 and Fig. 100. The ferrite fractions are labelled on the contours. The shaded areas determine the process windows which bring sufficient ferrite fraction for hot rolled DP steels. It is obvious that the feasible process window in the Mn-Mo DP steel is relatively narrow which is opposite to the Mn-Si DP steel. In the latter case, the entire area between 650 to 760°C from a retained strain of 0 to 1.2 becomes the safe process window only after transformation time of 7 s.



a)



b)

Fig. 98 The surface plots showing the ferrite fraction as a function of the transformation temperature and the retained strain. The austenite grain size is 25 μm . a) the Mn-Mo DP steel after 7 and 20 s of transformation time b) the Mn-Si DP steel after 10 and 20 s of transformation time. Note the difference scale of the Z axis.

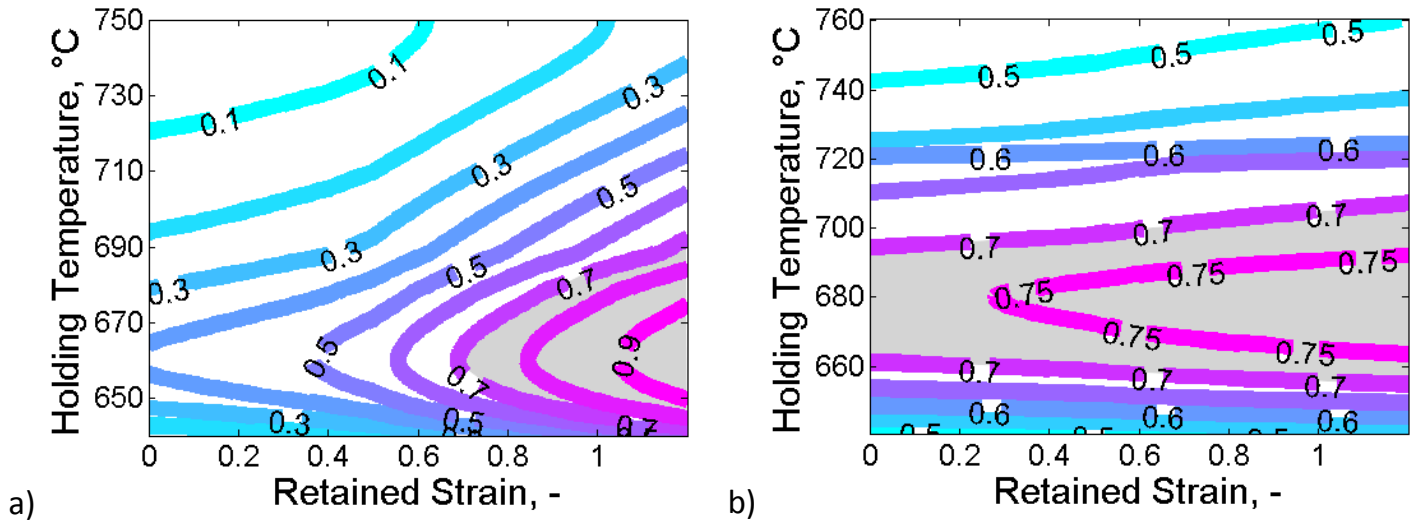


Fig. 99 The contours presenting the ferrite fraction induced within 3 s in a) the Mn-Mo and b) the Mn-Si DP steels. The prior austenite grain size is 25 μm . Note the difference in the temperature axis.

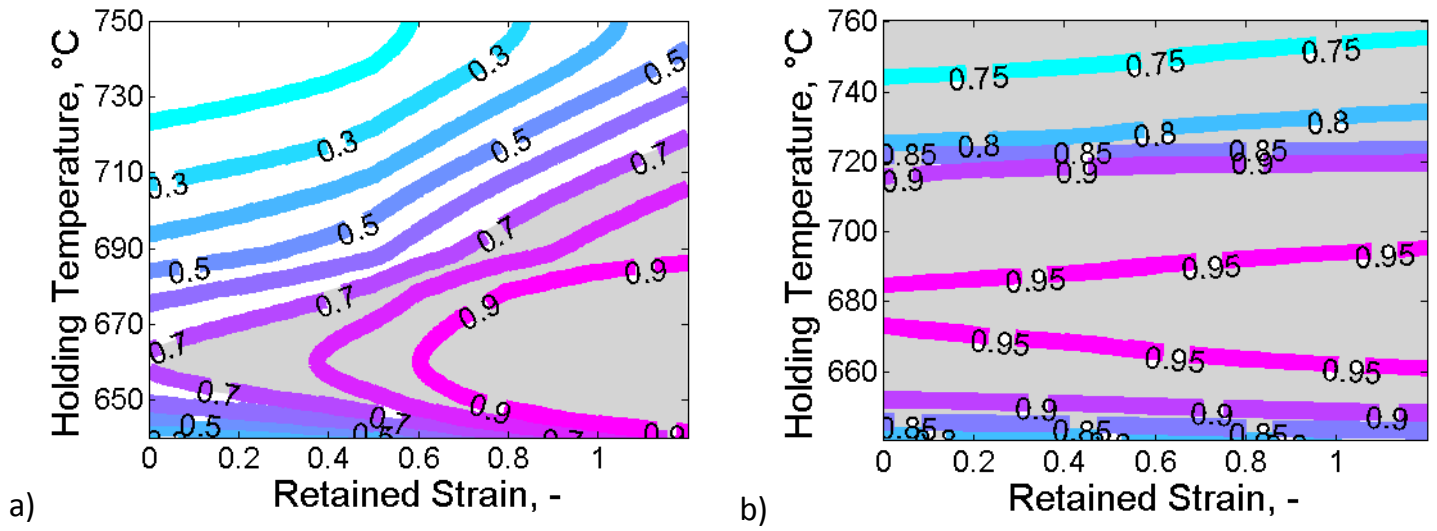


Fig. 100 The contours presenting the ferrite fraction induced within 7 s in a) the Mn-Mo and b) the Mn-Si DP steels. The prior austenite grain size is 25 μm . Note the difference in the temperature axis.

6.5 Modelling of the macroscopic martensite transformation kinetics

The martensite transformation is transformed after quenching to coiling temperatures and plotted together with the course of ferrite transformation in Fig. 101. It visualises the microstructure evolution after the last rolling stand in case of having austenite grain size of 35 μm with a retained strain of 0.3.

Taking into account the ferrite transformation during the continuous cooling results in higher ferrite fraction than taking into account only the isothermal transformation and matches the measured ferrite fraction very well. As a result the prediction of the martensite fraction is also reduced and it corresponds the experimental result very well.

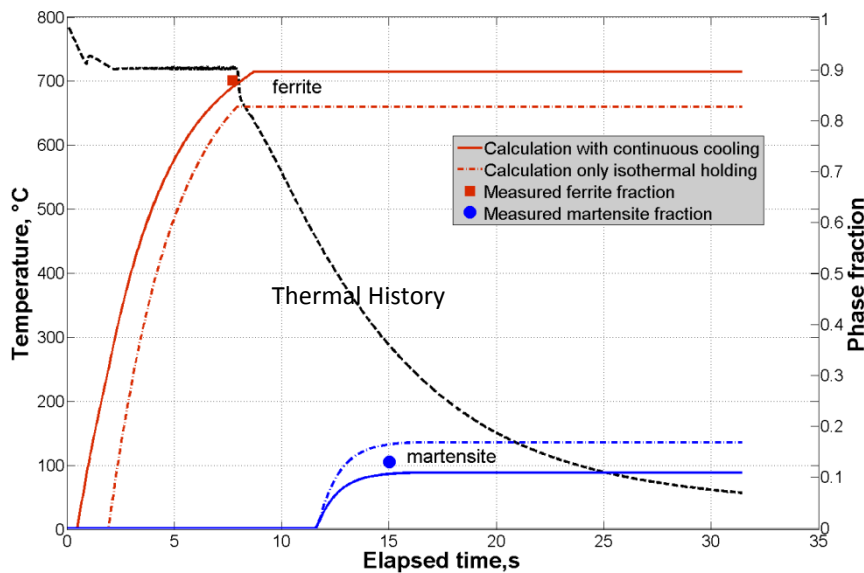


Fig. 101 The development of phases in the Mn-Si DP steel along the thermal history to the ROT at 720 °C after the simulated hot rolling process, followed by quenching to the coiling temperatures. It is the case of austenite grain size of 35 μm with a retained strain of 0.3.

Note that such the modelling employs an average value for both the functions g_{Temp} and g_{S_v} . As soon as there is large scattering in the experimental data, the simulated transformation curves will show some deviation from some data points. An example is shown in Fig. 102. A number of experimental data have been utilised for the calculation of g_{Temp} and g_{S_v} . At the same S_v value, samples have different transformation temperature and time and an average value for each S_v value has to be made before the optimisation for the g_{S_v} function for the whole range of S_v . The green symbols in Fig. 102b represent the mean value at each S_v while the blue line is the optimised values. Fig. 102 explains that

using either the mean value or the optimised value of g_{S_v} can result in some discrepancy from the experimental results accordingly.

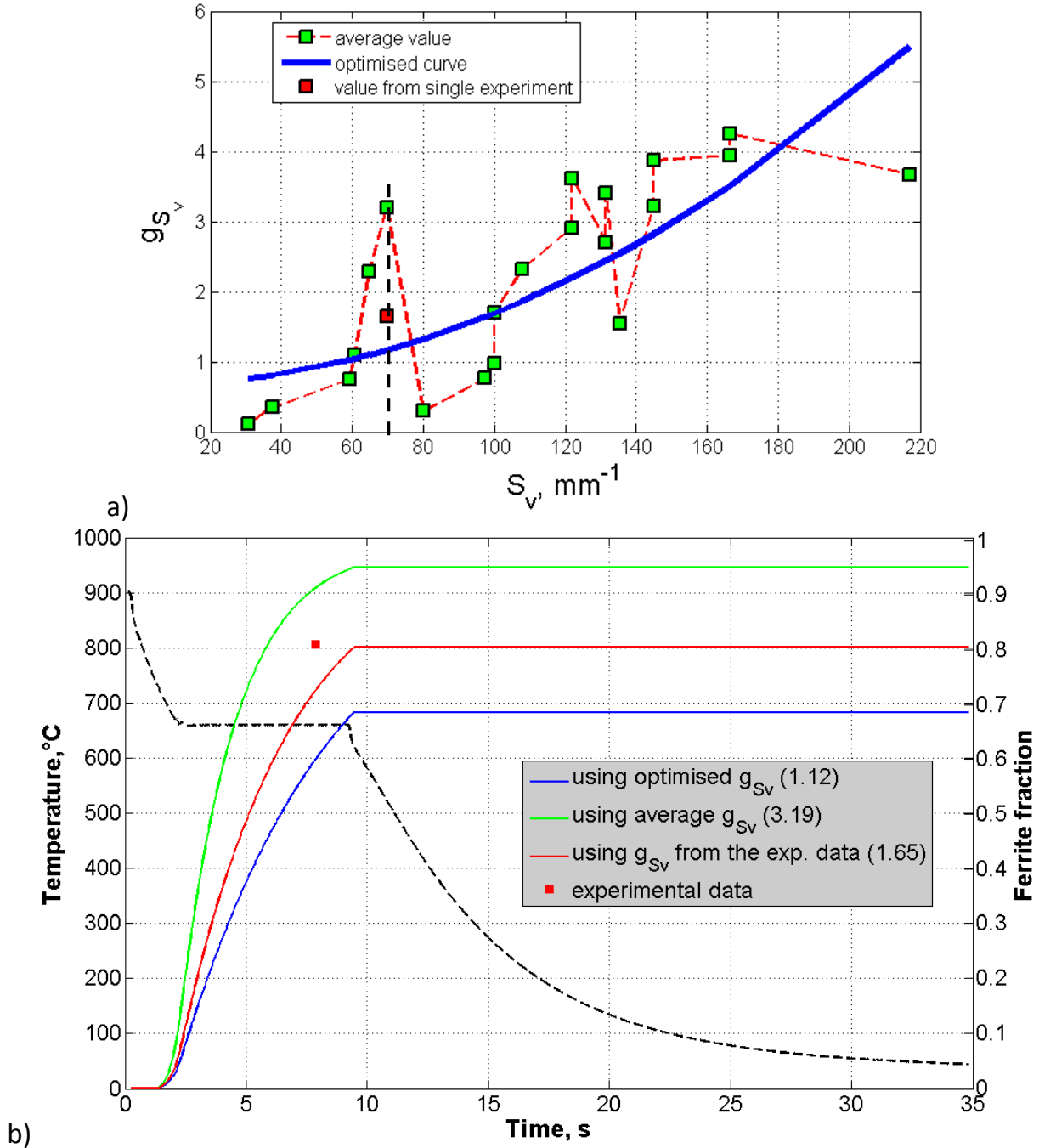


Fig. 102 A comparison between the simulations using different g_{S_v} values with experiment. a) The g_{S_v} values over a range of S_v . The red symbol means a single g_{S_v} value a single experimental data point. The green symbols mean the average value from different experimental datapoints having the same S_v values. They are from different transformation temperatures and time. The blue line is the optimised g_{S_v} values through the whole range of S_v . b) Large discrepancy between the experimental result and the simulations using g_{S_v} values at S_v of 70mm^{-1} from blue line and green dot in a)

6.6 Modelling of the mesoscopic ferrite transformation with phase field modelling

Fig. 103a) and Fig. 103b) show a good agreement of ferrite fractions between those obtained from the phase field simulations and from the experiments in the Mn-Mo steel and Mn-Si DP steels respectively. It is obvious that the ferrite transformation kinetics of the Mn-Mo steel is significantly slower while the one of the Mn-Si steel is extremely prompt at the beginning and then saturates quickly. Some discrepancy at the latter stage of transformation in the case of Mn-Mo steel should be contributed from the experiments. This is because the transformation curve is not from a dilatation curve from a single experiment but from several samples undergone the stepwise quenching for the microstructure.

Fig. 104 helps prove that the ferrite grain size distribution in the simulation fits fairly well with the experiment. Nevertheless it can be seen that the grain size distributions in the experiments cover all classes of grain size but the simulations result in ferrite grains with similar sizes. Note that it is very likely that tiny ferrite nuclei/grains have been overlooked from the metallographic work. Additionally, the grain agglomeration was absolutely not taken into account in the simulation.

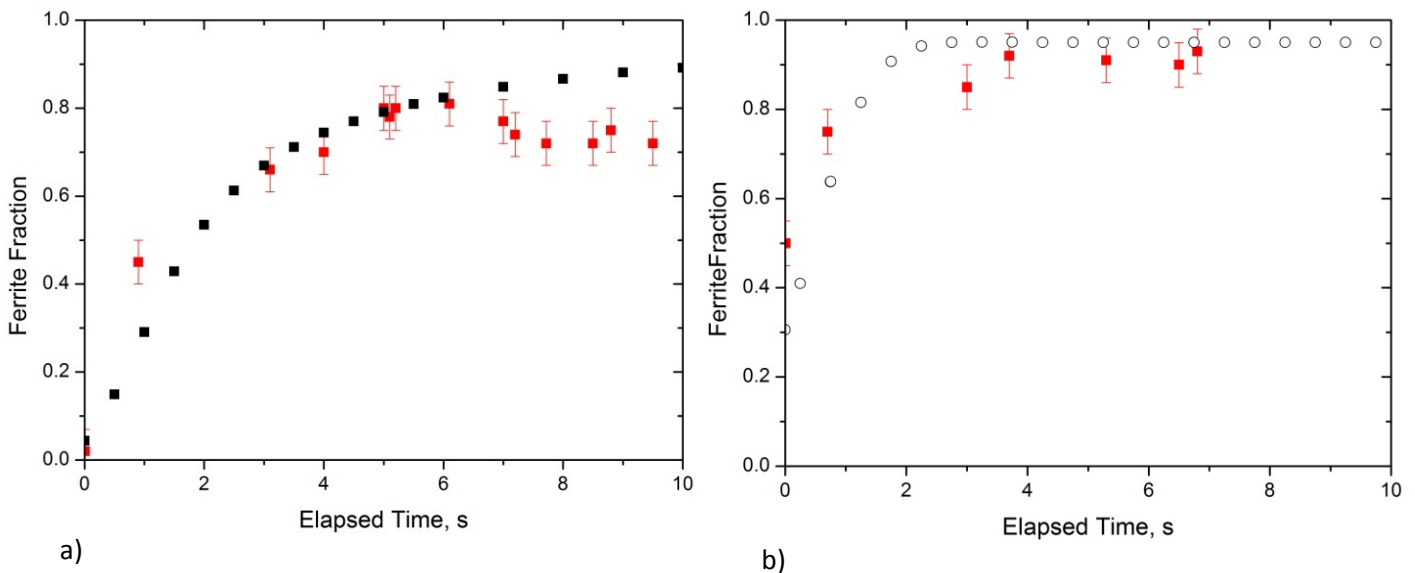


Fig. 103 The phase fraction from simulation compared with from experiment
 a) the Mn-Mo steel b) the Mn-Si DP steel

Depicted in Fig. 105 and Fig. 108 are the simulated microstructures after different phase transformation times for both steels, compared with the carbon redistribution in the

microstructure, Fig. 106-Fig. 107 and Fig. 109 and Fig. 110. The nucleation in the Mn-Mo steel is rather inhomogenously due to the effect of small shield distance. This results in some areas with no ferrite precipitation as the number of nuclei is limited. The large M/B/RA constituent islands, which will be formed during quenching, can be simulated with these areas. After longer transformation times, the ferrite grains adjacent to these islands grow towards inside and these grains become larger while the other grains which have full neighbors cannot grow. The microstructures in Fig. 43 should be taken for a comparison.

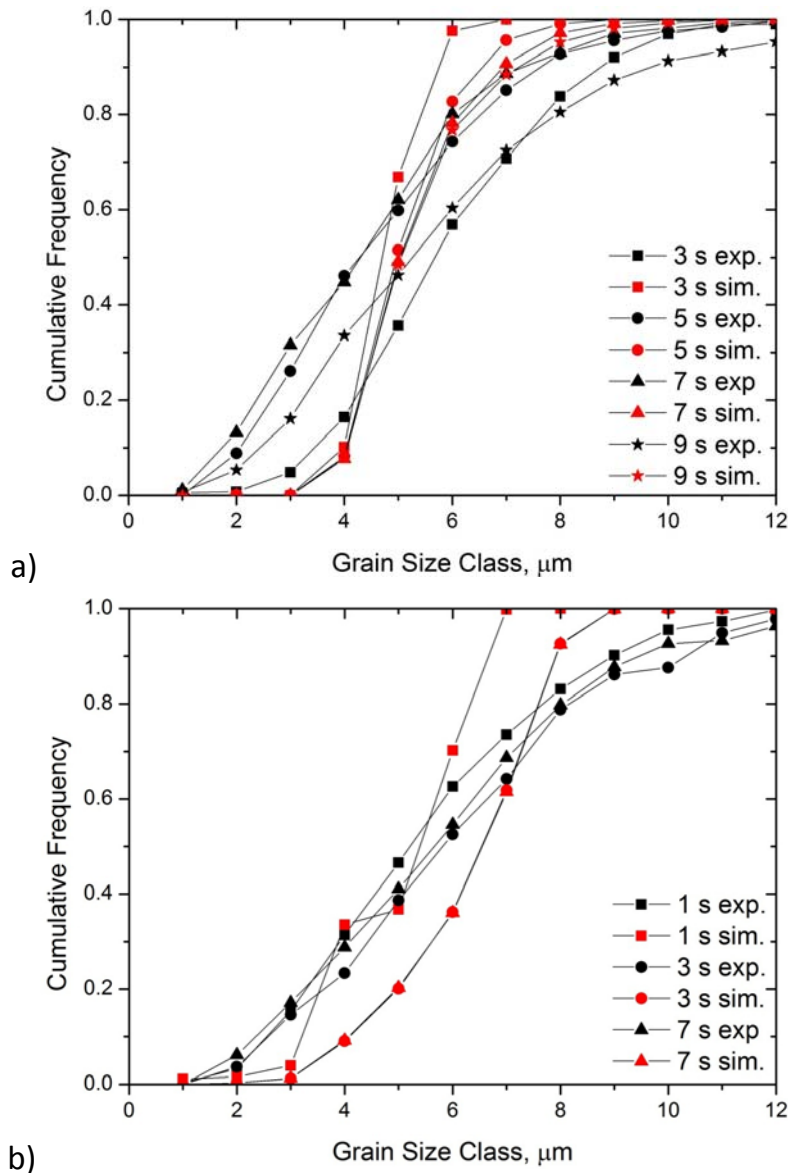


Fig. 104 The ferrite grain size distribution during the phase transformation from the phase field simulation, compared with the experimental results a) the Mn-Mo DP steel b) the Mn-Si DP steel

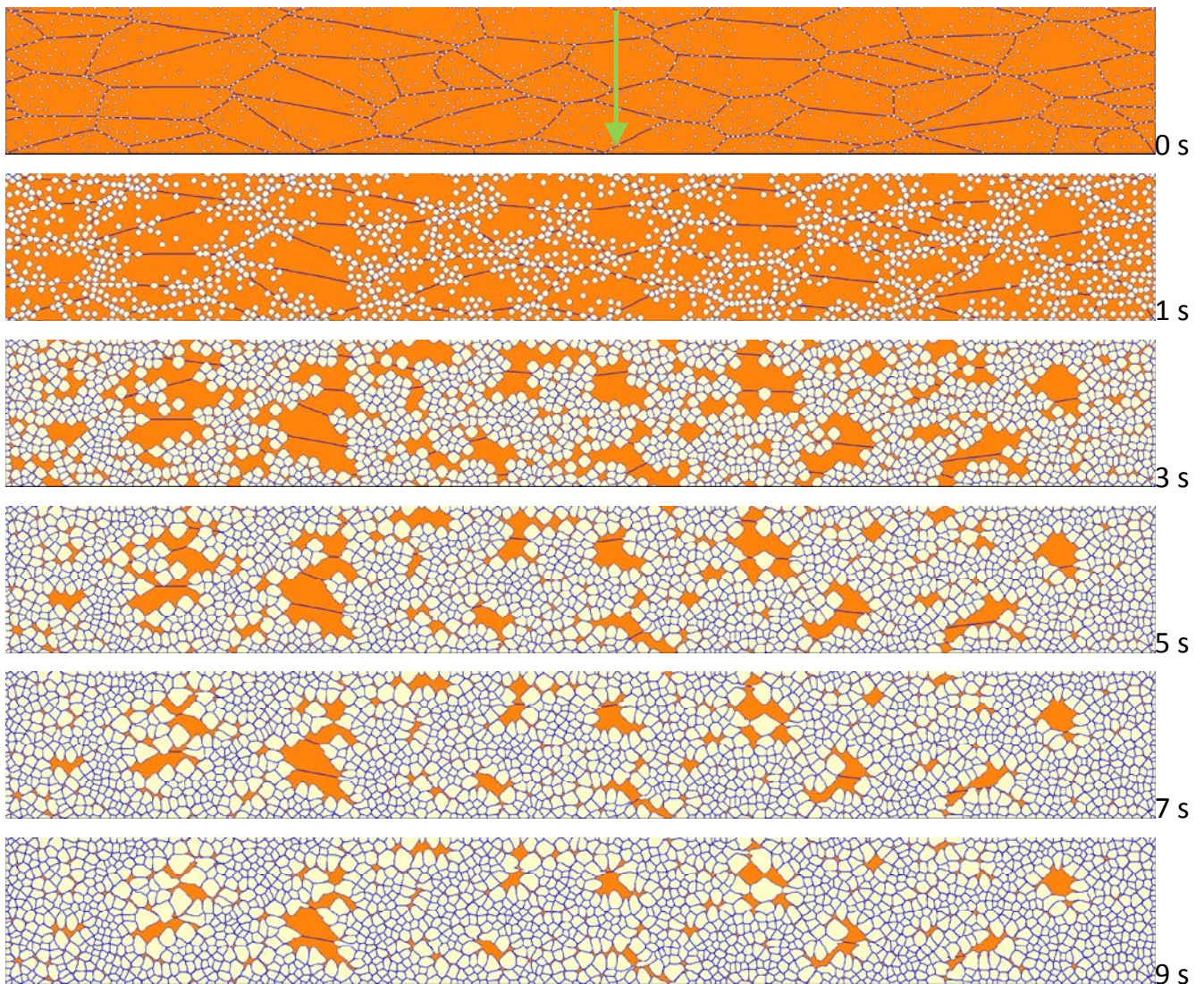


Fig. 105 The microstructure development in the Mn-Mo DP steel from the phase field simulation

On the other hand, Fig. 108, the simulation of Mn-Si DP steel shows that the ferrite grains nucleate at the triple points first, then at the grain surfaces/boundaries followed by in the bulk. The nucleation is rather homogenous and the grain size is uniform, as shown in Fig. 104b. The ferrite fraction itself after 3 s is very high, say 0.94. It looks like there is almost no austenite grains left. This is because the interface between austenite and ferrite as well as the one between ferrite and ferrite has a thickness and occupies the volume being left. It looks therefore a slightly different than that from the microstructure in Fig. 45.

The carbon gradient in the remaining austenite can be observed obviously and it becomes the highlight of this section. The color scale determines the carbon content in mass%. In large islands of the remaining austenite in the Mn-Mo steel, the higher carbon content appears only at the outer region. The smaller islands show a high carbon level through the

whole islands. In contrast, the carbon gradient in the Mn-Si steel shows to be little even in larger austenite islands at the early stage of transformation.

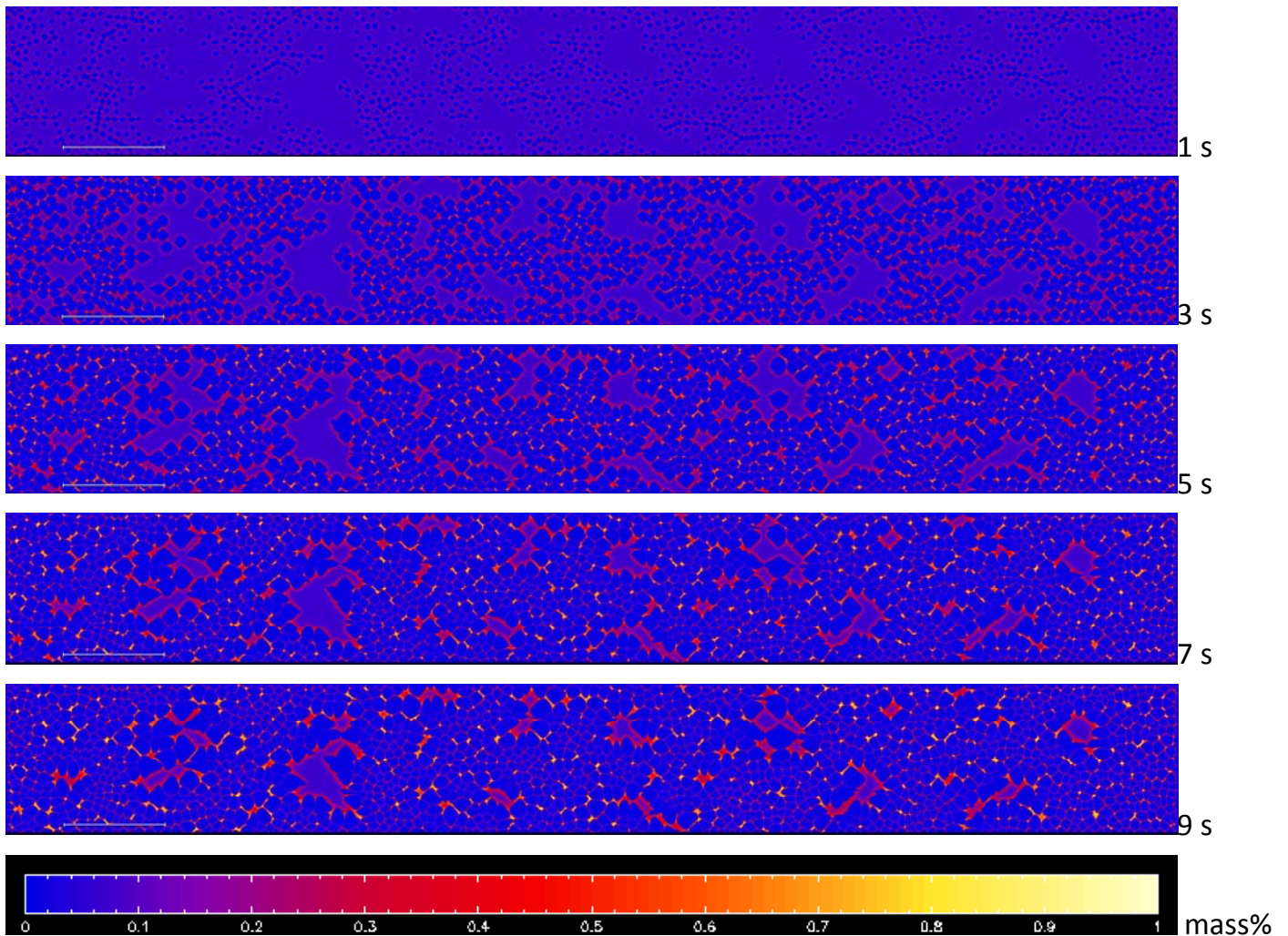


Fig. 106 The distribution of carbon content from the phase field simulation on the Mn-Mo DP steels. Refer to Fig. 105 for the microstructure evolution.

A virtual elemental distribution was measured from the simulation results and the carbon profiles along the arrow in the normal direction in the middle of the strip width are shown in Fig. 107 and Fig. 110 for the Mn-Mo and Mn-Si DP steels, respectively. The scan position in the strip of the Mn-Mo DP steel was shifted from the middle to the right side slightly to pass through 2 larger austenite islands.

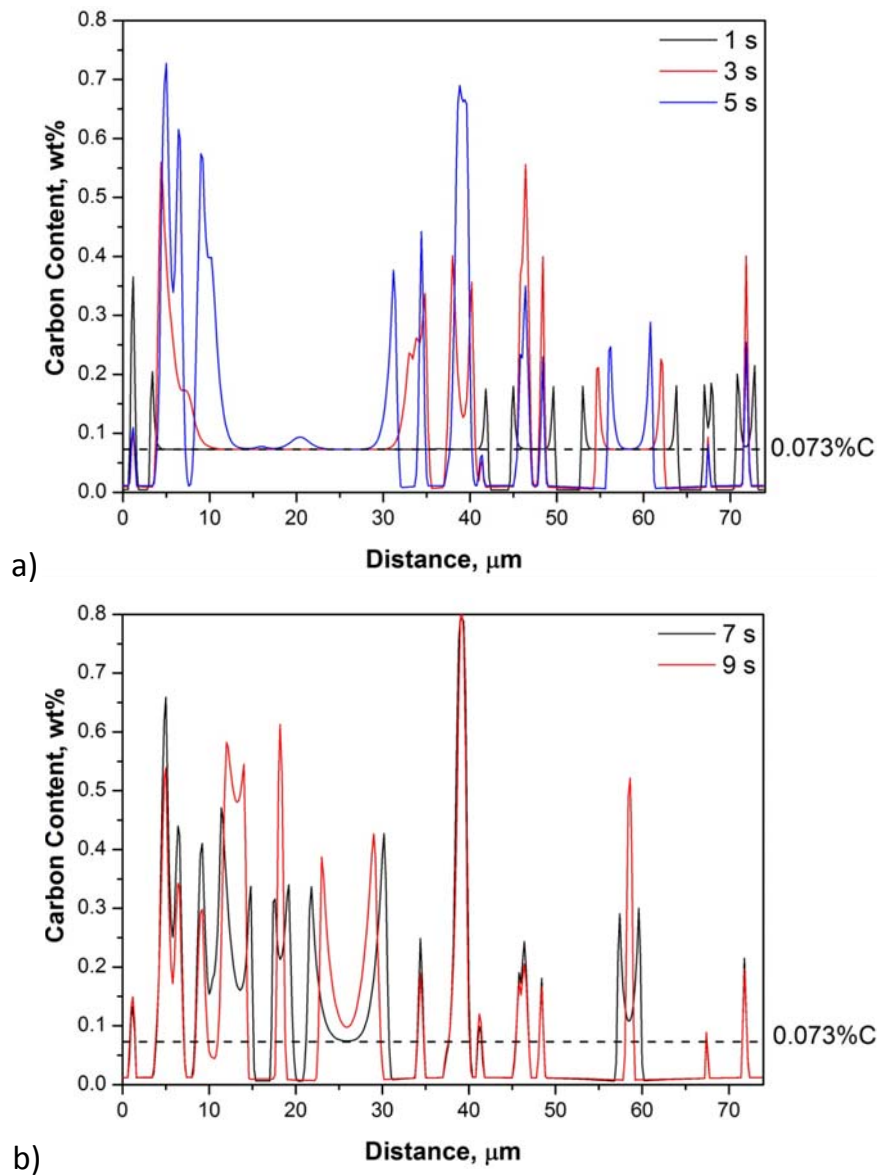


Fig. 107 The carbon profile scanned through the arrow across the microstructure of the Mn-Mo DP steel in Fig. 105.

It is obvious in case of the Mn-Mo DP steel that carbon piles up strongly only near the austenite island boundary. The carbon content inside the islands is the same as the nominal composition, in this case 0.073%. The pileup in the biggest island reaches 0.55% after 3 s. After the growth of ferrite the carbon peaks are trapped in the smaller austenite island the carbon content in some positions reaches 0.7%, which is theoretically high enough to result in some retained austenite. Fig. 107b) shows that at 7 and 9 s, the areas having high carbon content have also significant thickness. This means that if these areas can become retained austenite, it should have also significant volume. It is worth to look back to the carbon mapping results by FEG EPMA in the same materials of a similar case in Fig. 60. The phase field simulation gives a very good agreement.

On the other hand, the carbon peaks in the Mn-Si steel are rather periodically, due to the homogeneously distributed ferrite grains. Some peaks reach the level of 0.7% but their areas are very thin. This means although they result in the retained austenite, the volume should be much less than the former case.

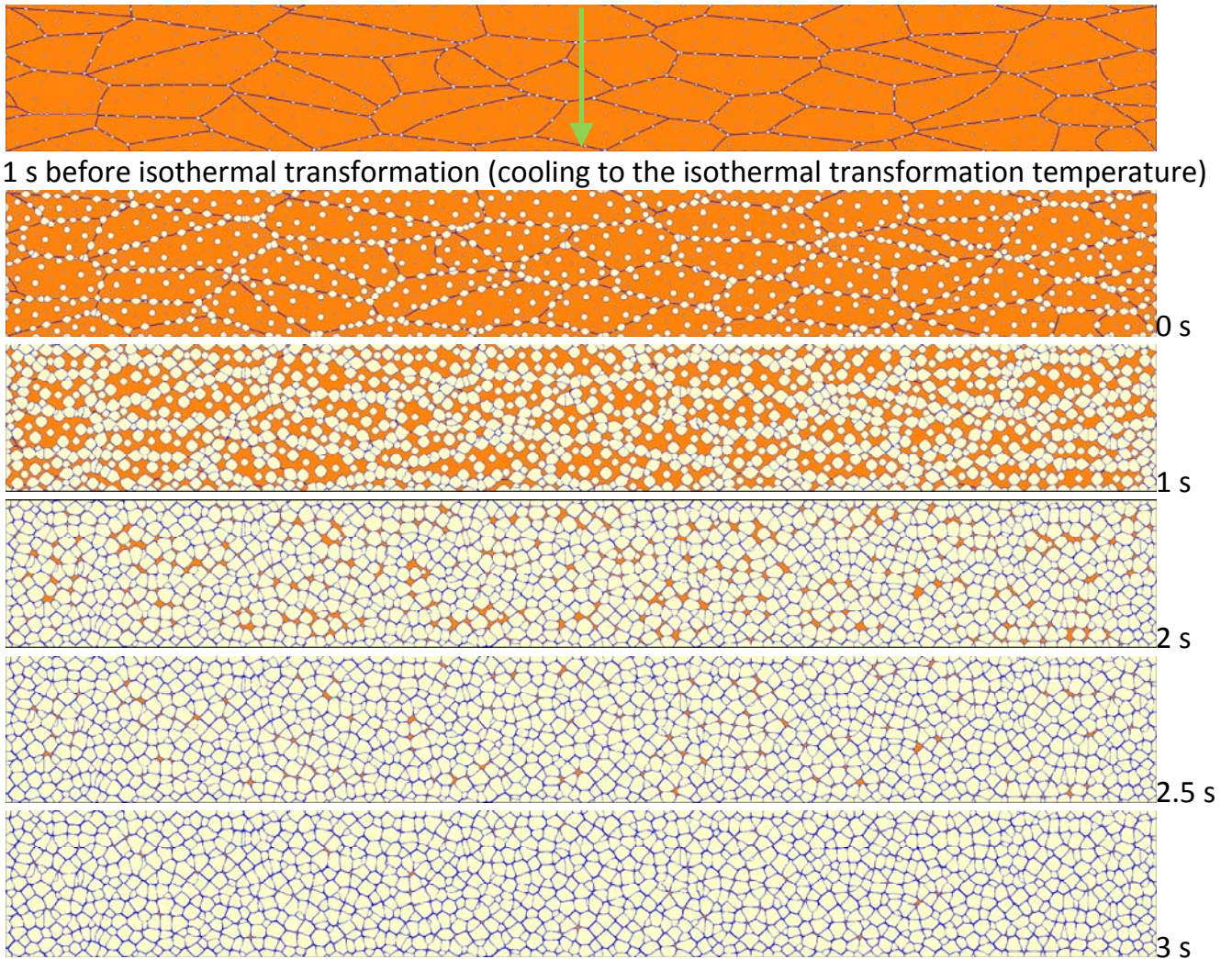


Fig. 108 The microstructure development in the Mn-Si DP steel from the phase field simulation

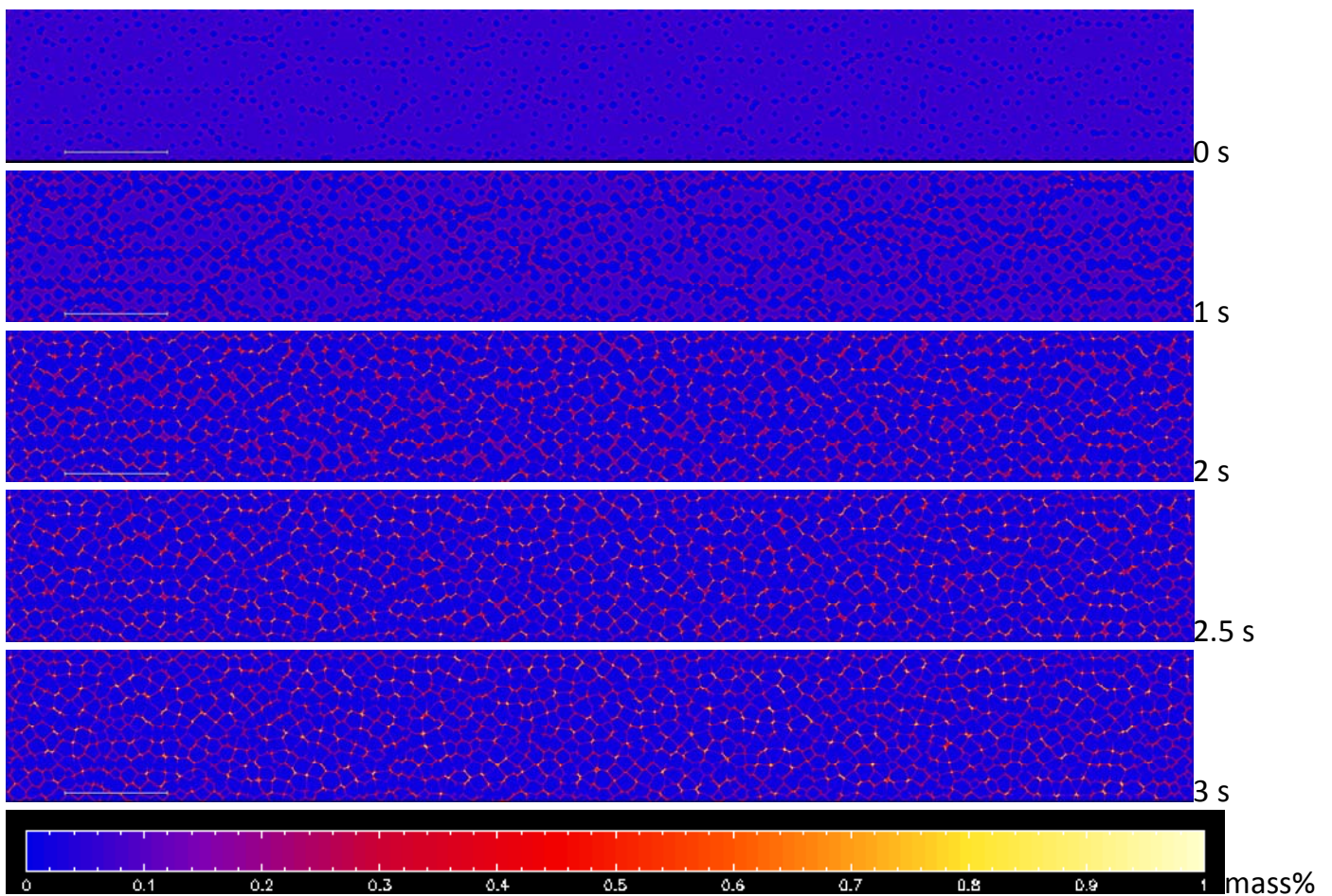


Fig. 109 The distribution of carbon content from the phase field simulation on the Mn-Si DP steels. Refer to Fig. 108 for the microstructure evolution.

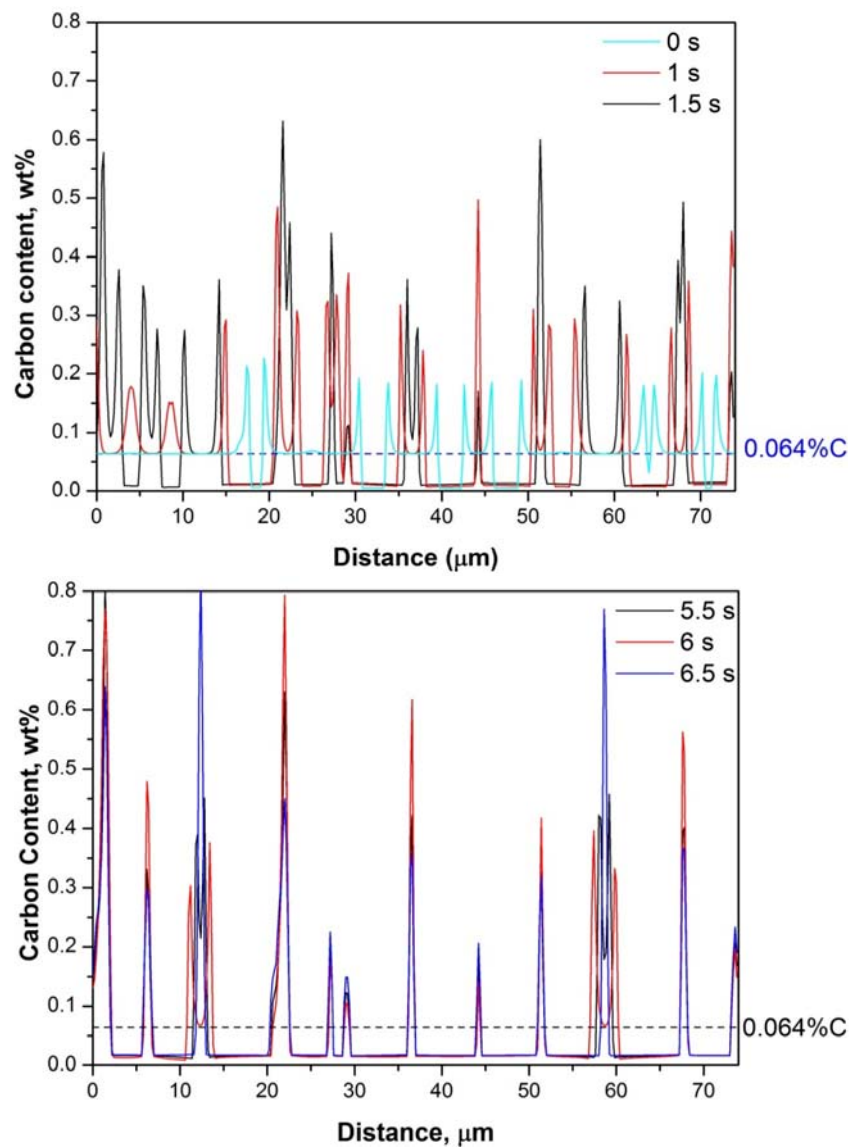


Fig. 110 The carbon profile scanned through the arrow across the microstructure of the Mn-Si DP steel in Fig. 109

A question can arise if the stronger carbon gradient in the Mn-Mo DP steel is simply a result of the higher nominal carbon content. Hence, another computer experiment has been performed. The Mn-Mo DP steel was changed its carbon content into 0.064%, which is the nominal carbon content of the Mn-Si DP steel. The carbon content of the Mn-Si DP steel was switched into 0.073% from the other. A nice result was achieved and is shown in Fig. 112. The stronger carbon gradient still exists although the carbon content in the Mn-Mo DP steel is lower.

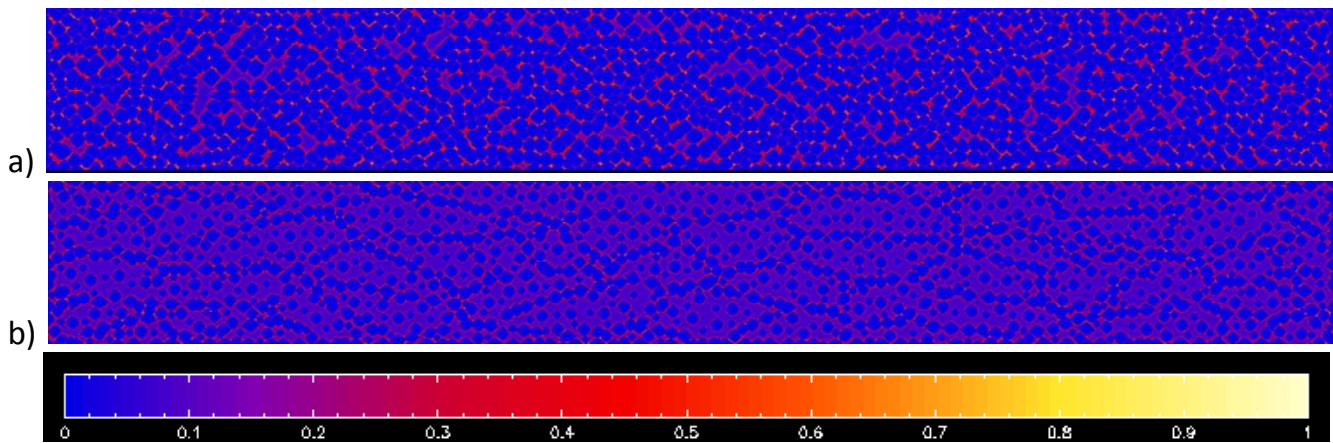


Fig. 111 The carbon content in both steels with new carbon contents. a) Mn-Mo DP steel with 0.064%C b) Mn-Si DP steel with 0.073%C.

New simulations to observe the effect of molybdenum have been tried. The strong carbon gradient has not been found in the simulation on Mn-Mo DP steel without molybdenum nor the Mn-Si DP with the addition of molybdenum.

From all the analyses, molybdenum should not be the main cause of the carbon gradient. The morphology of the austenite islands should be a better reason. The deformation in the Mn-Mo DP steel enhances the nucleation of ferrite much more at the triple junctions and grain boundaries but to lesser degree in the bulk of the grains. Carbon rejection into the austenite grains takes place intensively around the ferrite grains. In contrast, much less carbon partitioning contributes to the middle of large austenite grains. The distribution of ferrite nuclei in the Mn-Si DP, on the other hand, is rather homogeneous and leaves very few large austenite. As the ferrite grains grow, the peaks of the carbon diffusion profile are trapped in the small austenite island and only the high carbon content appears.

7 DISCUSSION

This section discusses the methodology of the experimental process simulation, the input parameters for the modelling and their accessibility as well as some facts to be aware of. Some suggestions for further improvement are also given.

7.1 *Comments on the experimental process simulation*

The experimental process simulation does not only verify the processing window but also yields the necessary input parameters for the modelling. The macroscopic kinetics model needs the resulting phase fraction with the information of transformation temperature and time as well as the austenite conditioning. The phase field model needs additional information of ferrite grain size and distribution to fulfil the nucleation model. On the other hand, the thermodynamics model needs only the chemical composition of the interested alloys.

As pointed out in the experimental result chapter, the transformation kinetics in this work were not achieved by means of the conventional dilatometry. Instead, they were extracted from the phase fraction from the stepwise quenching and the obtained microstructure. Special care must be paid to the dilatometry from such the very low carbon steel especially in case of the processes with several deformation steps and high strain rate. Some dilatation signals become poor due to a few reasons:

1. A different configuration is needed: SiN deformation head, Al₂O₃ push rod and lubricant slot on the sample. They result in higher thermal expansion in the system, compared with the standard experiment without deformation or with deformation under slow strain rate: Quartz glass deformation head and measuring rod without lubrication slot on the sample.
2. The phase transformations are rather fast, which is in order of only several seconds. Steels having higher content of carbon and other alloying elements transform to ferrite in order of a few minutes. Given that the phase transformation is prompt and the intended holding temperature fluctuates, the phase transformation will take place already at the deviated temperatures. The dilatation curve becomes not smooth.
3. The heavily deformed samples became thin in the axial direction, from which the dilatation curves are taken. Therefore the total length change becomes smaller and more difficult to be detected. The new dilatometer (Baehr DIL 805 A/D) at the

Department of Ferrous Metallurgy, RWTH Aachen University, can detect also the dilatation curves from the diameter direction. However, it has been also proven that the curve is not much improved if a high cooling rate in the sample is required as the intensive gas blow interferes the laser measurement.

4. The active volume in the samples is little. This situation happens in case of the second and/or third transformation, after the ferrite transformation. Note that the ferrite fraction is already in order of 0.8. This means that there is only 20% of the total volume left for the martensite and/or bainite transformation. The dilatation signals during this secondary transformation are therefore negligible. This is more severe if the sample is also heavily deformed.
5. There are a few quenching steps before and after the transformation period. This is carried out by switching the quenching gas on and off. The signals became broken during the moments of switching the gas. This feature has been improved later with a gas ramp program from the company Baehr.

The stepwise quenching method is nevertheless very beneficial for the information of the morphology of the M/B/RA islands as shown already in section 4.1.9.

In case that a dilatation curve for the ferrite transformation is really necessary, and to avoid spending too many samples, it is recommended that the quenching rate to the intended transformation temperature be moderate. It should be just fast enough that no significant transformation during quenching will take place. The interested cases should be at best with only a single deformation step and with moderate degree of deformation and strain rate so that the standard machine configuration can be used. Cases with larger austenite grain size, namely, with slower transformation, tend to give more stable dilatation curves. Continuous cooling generally eases the dilatometry evaluation.

A long ferrite transformation time should be done to record the total transformation kinetics from the dilatation curve. But it should not be long enough to pronounce the decarburisation and severe grain coarsening. It is common that people let the transformation curves saturate until a plateau. Before reaching the plateau, the last transformation fraction can be contributed only by the transformation at the sample surface, where the decarburisation takes place. It is more profitable to quench the sample before reaching the plateau, analyse the microstructure and calculate the transformation curve by taking the maximum ferrite fraction investigated from the microstructure.

The cooling rate on the ROT in a rolling mill, including the pilot rolling line employed in this work, is around 20 °C/s. Hence, the required transformation time from the simulation of isothermal transformation time should not be transferred to this case directly. Additionally, some plants allow more transformation time as their ROTs have greater length. The rolling speed of thin strips is slightly higher than 10 m/s. If the ROT is 140 m long and the rolling speed is 14 m/s, the transformation time on the ROT is 10 s. If so, the simulation on the pilot rolling line in this work can be taken as a lower limit.

The evaluation of the austenite grain size and the recrystallised grain size should be also discussed. The austenite grain size influences the ferrite transformation kinetics significantly. It is very important for a macroscopic model to map the transformation kinetics in materials with homogeneously distributed austenite grain size as it takes into account only the single average value of the austenite grain size. Note that larger austenite grains tend to have larger deviation in the grain size as soon as some little grains form. It is also very important that before producing the samples, the ingot should be deformed heavily enough so that the cast structure is completely destroyed. Given that the homogeneity should be improved, a normalising process is recommended before the reheating stage.

It has been proven and also confirmed from the literature that after the repeated recrystallisations, the austenite grain size approaches to a small range of value, 20-50 μm in case of hot rolling. This reduces the inhomogeneity in the austenite grain size also to a lesser degree. The proof of the exact austenite grain boundaries in this case is very difficult by quenching and etching as the cooling rate in such the heavily deformed cylindrical samples is not high enough to avoid the bainite transformation, which obscures the prior austenite grain boundaries severely. The micrographs confirm, nonetheless, that the microstructures after the transformation are rather homogenous. This can imply that the prior austenite grain size should be also homogeneous.

A big difference between those in the industrial rolling and those in the laboratory work, is the fact that the initial austenite grain sizes after the bar reheating are extremely large, approximately a millimetre to a few millimetres. This is due to the long bar reheating duration, approximately 2 hours, to ensure homogenous temperature distribution in the massive bars, weighing 20 tons in case of traditional hot rolling mills. Those in the laboratory are, on the other hand, in order of a few hundred micrometres.

This work estimates the recrystallised grain size after each deformation step provided that the recrystallised fraction is significant, i.e. at least 0.75 and in almost all cases at least 0.85. The grain size is calculated by an empirical equation without taking into account the unrecrystallised fraction. The retained strain was taken only from the last deformation step, which is planned to perform under the T_{nr} temperature. (Although the empirical prediction T_{nr} for the Mn-Si DP steel is lower than the temperature at the last deformation step). If the austenite grain sizes can be more easily revealed such as in cases of steels with higher carbon content, it is recommended that the austenite conditioning before the phase transformation is investigated purely as a function of the measured S_v value, which expresses the total effect of the austenite conditioning.

Traditional CCT diagrams in handbooks focus on a specific austenite grain size which is usually much larger than that before the phase transformation in case of hot rolling. This should not be used to interpret the phase transformation in the hot rolling directly. Besides, the secondary phase transformation products should not be read from the diagrams too much either as the thermal history in the CCT diagrams is totally different than that in the hot rolling.

7.2 Comments on the macroscopic kinetics modelling

A macroscopic model works with average values in the samples, which are in this case the phase fraction and the mean field carbon content after carbon partitioning. A homogenous starting microstructure is favourable indeed. It is not inevitable to have some scatters in the experimental results and all the functions in this work: $g_{Temp}(T)$ and $g_{S_v}(D_\gamma, \varepsilon)$ are calculated through the non-linear least square optimisation method. Therefore it is beneficial to have more number of experimental data points for the model. This class of modelling is hence favourable in industrial plants, from which a numerous data points are available. Moreover, it provides the potential to transfer to an online application. The concept of Leblond's model carried out in this thesis was transferred to an industrial context at the Salzgitter Mannesmann Forschung [Pet11] as well.

Another important point in modelling the influence of the temperature on the ferrite transformation kinetics as the $g_{Temp}(T)$ function is that the function should never be defined at the lower limit of the ferrite transformation temperature range as zero as performed preliminary in [Suw10]. This is because the ferrite transformation region expands when it is promoted with large deformation. Under a severe deformation, the

ferrite transformation can be possible even slightly under the B_s temperature. A minute value at the lower and upper and upper limits of the $g_{Temp}(T)$ function is recommended to avoid any numerical problem.

7.3 Comments on the phase field modelling

It is interesting to employ this class of model to investigate the microstructure especially when there is a strong deviation in the microstructure. For instance, the phase field modelling in this work demonstrates the local carbon partitioning and rationalises the evolution of the retained austenite in large austenite islands in the Mn-Mo DP steel and can compare directly to the case of smaller austenite islands in the same microstructure. It also yields the ferrite grain size distribution, not only the single value of average ferrite grain size.

The phase field modelling concept defines interfaces between grains. As the thickness of 1 μm is assigned due to numerical reasons, the interfaces occupy some area in the microstructure. It is therefore important to note that the equilibrium ferrite fraction in the phase field simulation will not be reached as up to 5% of the microstructure is occupied by the interface.

So far the interface velocity between the austenite and ferrite is taken to be a fitting parameter, which shows to control the ferrite transformation kinetics most significantly. This gives no physical meaning but it seems to be common in the scientists' community of the austenite to ferrite transformation [Lee98, Mec05, Hua06]. This is because investigating the interface mobility itself requires a much deeper analysis. Additionally, if the diffusion-controlled transformation is assumed in the simulation, it is mandatory to calibrate the interface mobility such that the transformation is solely controlled by the diffusion process in a calculation domain with tiny grid size, i.e. 0.01 μm [Böt11]. This is not affordable in a large calculation domain. Then the calibrated mobility can be transferred to the larger domain with coarse grid size.

The nucleation process is a separate sub-model coupled in the MICRESS code. It is not related to the phase field algorithm. It is the second most important factor in controlling the transformation kinetics. Although the best effort was put to extract the nucleation information from the transformed microstructure, no exact information on the nucleation can be easily given as it required an advanced in-situ investigation. The interface mobility

and the nucleation model work mutually and it is extremely difficult to achieve a single explicit set of parameters which give the best matching to the experiment.

It is reported [Mil06] that some discrepancy between the experiment and simulation is contributed from the difference in the dimensions. In other words, the actual phase transformation takes place in three dimensions and the grains grow in spherical shape. On the other hand, the ferrite grains grow in two dimensions in cylindrical fashion. This also contributes to some deviation in the grain shape.

The ferrite fraction in the Mn-Mo steel does not increase in the samples with longer transformation time, while that in the simulation does a little. One can argue that a phenomenon such as solute drag can be the reason of this. Such the phenomenon is however beyond the scope of this thesis.

7.4 Comments on the thermodynamic modelling

This class of modelling does not relate to time nor distance scale and need only the chemical composition as the input. It is sound in the theory but as soon as the process is far from equilibrium, the results must be utilised with a great care. For example, although the A_{e3} and A_{e3d} temperatures can be calculated explicitly, the process window should be also guided by the empirical A_{r3} temperatures.

The calculated critical temperatures as well as the A_{c3d} , W_s and B_s under the diffusional control approach, i.e. common tangent and parallel tangent methods, show to be reasonable. The questionable results are in the case of B_s and M_s temperatures calculated under the diffusionless approach as well as the W_s temperature from the diffusion-controlled's common tangent method.

An argument for the B_s temperature is that bainite transformation lies in between the displacive and the reconstructive mechanism or diffusionless and diffusion-controlled and it is still controversial. There are also a number of followers for both the diffusion-controlled and nucleation-controlled kinetics. Following Bhadeshia's nucleation controlled approach [Bha82, Ree92, Ree92b], the B_s and W_s temperatures were achieved under 2 calculation steps, i.e., diffusion-controlled nucleation for both Widmanstätten ferrite and bainite followed by the diffusional growth with the common tangent method for the Widmanstätten ferrite and the diffusionless growth for bainite. Following the simpler

approach by Lee [Lee92], the B_s and W_s temperatures are derived by only a single step, i.e. the diffusion-controlled nucleation.

8 CONCLUSIONS

This thesis work profits from carrying out different classes of modelling and can analyse the austenite to ferrite transformation in the hot rolling of DP steels very efficiently in different aspects. Referring to the modelling classes and the predictivity criterion from the literature review, each modelling class from this work can be located between the axes of computational cost/time and predictivity in a diagram as shown in Fig. 112. The JMAK rate form model gives lowest predictiveness with lowest computational time. The CALPHAD approach yields in highest predictiveness with relatively low computational time. The phase field model, coupled with a nucleation model, provides less predictiveness due to its large number of unknown fitting parameters. It consumes also the most computational time. However, one can observe the effect of many controlling factors in details both in thermodynamics and kinetics aspect and it is therefore still very beneficial.

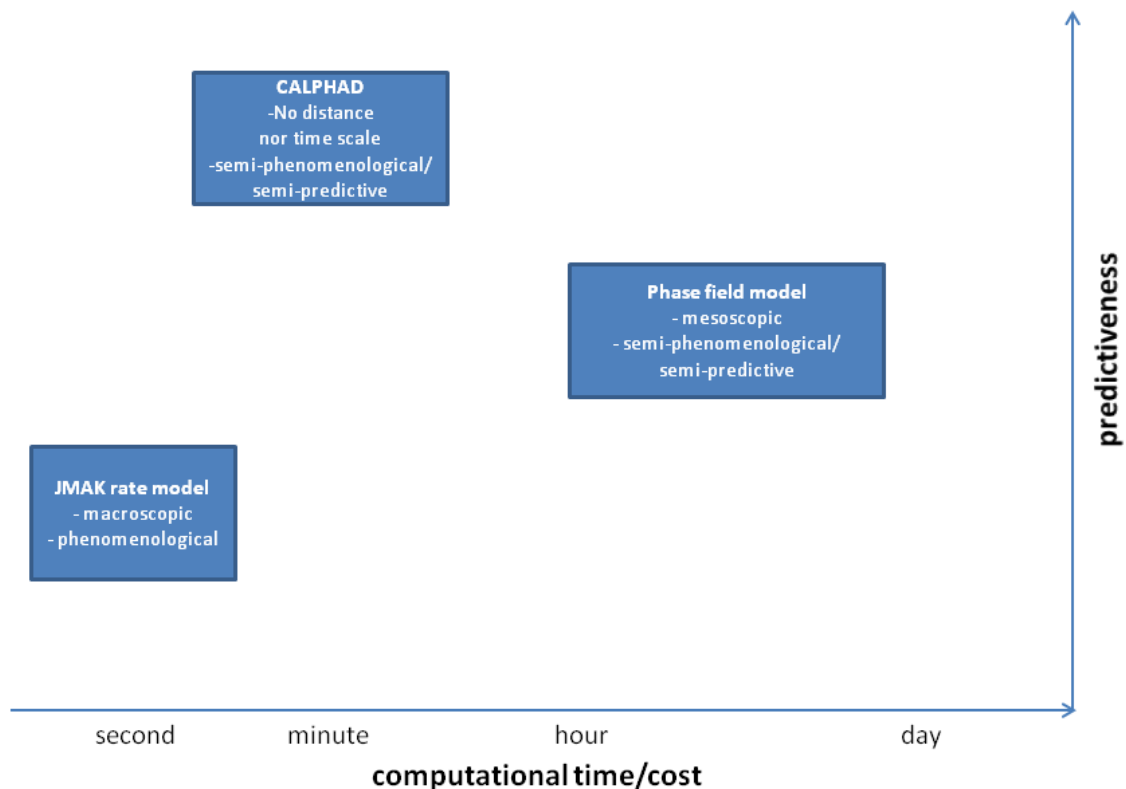


Fig. 112 The allocation of each modelling group on the coordination between computational cost/time and predictiveness.

The phenomenological macroscopic kinetics model is simple and employs fast algorithm. It enables an effective computer-based process design and can point out the process window as a function of the temperature on ROT and austenite conditioning. It is the only class for

the online usage in industrial application. The thermodynamic calculation is useful as a guideline for the related critical temperatures and also shows the effect of the alloy's chemical composition. The mesoscopic phase field model can demonstrate the effect of nucleation and growth of ferrite on the ferrite grain size and distribution as well as the carbon partitioning. It is suitable for process and product development.

The access of the modelling input parameter depends also on the steels' chemical composition. The Mn-Mo DP steel has a stronger dependency on both the transformation temperature and austenite conditioning than the Mn-Si DP steel. Its transformation kinetics is generally also dramatically slower and it is easier to make numerical modelling, as the microstructure development can be easier '*frozen*' by the stepwise quenching. Additionally, the acceleration of the ferrite transformation kinetics by the austenite conditioning can be demonstrated more apparently in a material with slower transformation kinetics. Its model will therefore have higher sensitivity on the austenite conditioning.

A secondary finding is that hot-rolled DP steel can be produced from the alloying concept for cold-rolled DP steel. Nevertheless, this makes the development of the DP structure much more difficult as the industrial process window is rather narrow.

This work also confirms the finding from the literature that the austenite grain size in the industrial rolling lies between 20-50 μm . It does not depend strongly on the starting grain size, which is in order of a few millimetres after reheating. This is because many repeated recrystallisations between the rolling passes make the final austenite grain size approaching to the above mentioned range. To focus on the rolling case, it is recommended to keep the austenite grain size in this range before the phase transformation.

The novelty of this work comes from the '*modified CCT diagram*' and the investigation of the carbon partitioning which results in a significant amount of retained austenite. This is rarely reported in the literature. The combination of investigating the carbon profile with the high resolution FEG EPMA and simulating it with the phase field model provides the best proof of the carbon gradient in the remaining austenite islands.

9 Bibliography

- [1] Ahm98 N.A. Ahmad, A.A. Wheeler, W.J. Boettinger and G.B. McFadden: Solute Trapping and Solute Drag in a Phase-Field Model of Rapid Solidification, Phys. Rev. E, 58 (1998), pp. 3436-3450.
- [2] Ali90 A. Ali and H.K.D.H. Bhadeshia: Nucleation of Widmanstätten ferrite, Mat. Sci. Tech., 6 (1990), pp. 781-784.
- [3] Akb95 G.H. Akbari, C.M. Sellars and J.A. Whiteman: Austenite and Ferrite Grain Sizes in Interstitial Free Steel, Mat. Sci. Tech., 11 (1995), pp. 1261-1265.
- [4] Ana92 G. Anan, S. Nakajima, M. Miyahara, S. Nanba, M. Umemoto, A. Hiramatsu, A. Moriya and T. Watanabe: A Model for Recovery and Recrystallisation of Hot Deformed Austenite Considering Structural Heterogeneity, ISIJ Int., 32 (1992), pp. 261-266.
- [5] And02 J.O. Andersson, T. Helander, L. Höglund, P. Shi and B. Sundman: Thermo-Calc & DICTRA, Computational Tools for Materials Science, Calphad, 26 (2002), pp. 273–312.
- [6] And65 K.W. Andrews: Empirical Formulae for the Calculation of Some Transformation Temperatures, JISI, 203 (1965), pp. 721-727.
- [7] And83 H.L. Andrade, M.G. Akben, and J.J. Jonas: Effect of Molybdenum, Niobium and Vanadium on Static Recovery and Recrystallization and on Solute Strengthening in Microalloyed Steels, Met. Mat. Trans., 14A (1983), pp. 1967-1977.
- [8] Ane86 E. Anelli, M. Ghersi, A. Mascanzoni, M. Paolicchi, A. Aprile, F. Granato, G. Liquori and G. Rizzo: Plate Rolling of HSLA Steel with Control of Microstructure, Boll. tec. Finsider, 1986, No. 407, pp. 84-87.
- [9] Ane92 E. Anelli: Application of Mathematical Modelling to Hot Rolling and Controlled Cooling of Wire Rods and Bars, ISIJ Int., 32 (1992), pp.440-449.
- [10] Ang06 J. Angeli, E. Füreder, M. Panholzer and A.C. Kneissl: Eching Techniques for Characterizing the Phases of Low-Alloy Dual Phase and TRIP Steels, Prakt. Metallogr., 43 (2006), pp. 489-504.
- [11] Arc1 Dual Phase Steels, Product Sheet, http://www.arcelormittal.com/automotive/saturnus/sheets/A1_EN.pdf,
- [12] Aar70 H. Aaronson, C. Laird and K.R. Kinsman: Mechanisms of Diffusional Growth of Precipitate Crystals. In: *Phase Transformations*, ASM, 1970.
- [13] Avr39 M. Avrami: Kinetics of Phase Change. I, General Theory, J. of Chem. Phys., 7 (1939), pp.1103–1112
- [14] Avr40 M Avrami: Kinetics of Phase Change. II, Transformation-Time Relations for Random Distribution of Nuclei, J. of Chem. Phys., 8 (1940), pp. 212–224.

- [15] Avr41 M. Avrami: Kinetics of phase change. III, Granulation Phase Change and Microstructures, J. of Chem. Phys., 9 (1941), pp. 177–184.
- [16] Azu05 M. Azuma, N. Fujita, M. Takahashi, T. Senuma, D. Quidort and T. Lung: Modelling upper and low Bainite Transformation in Steels, ISIJ Int., 45 (2005), pp. 221-228.
- [17] Bar82 J. Barralis, G. Maeder: Métallurgie Tome I, Métallurgie Physique, Collection Scientifique ENSAM, 1982, p.270.
- [18] Böt11 B. Böttger: Personal communication, 2011.
- [19] Bey05 J. H. Beynon and C. M. Sellar: Models for Predicting Microstructural Evolution In S.L. Semiatin (ed.): *ASM Handbook Vol. 14A on 'Metalworking: Bulk Forming'*, ASM, 2005.
- [20] Bey92 J. H. Beynon and C. M. Sellar: Modelling Microstructure and its Effects during Multipass Hot Rolling, ISIJ Int., 32 (1992), pp. 359-367.
- [21] Bha01 H.K.D.H. Bhadeshia: Bainite in Steels – Transformations, Microstructure and Properties, 2nd ed., London, IOM, 2001.
- [22] Bha82 H.K.D.H. Bhadeshia: Bainite, J. Phys., 43 (1982), pp. 437-441.
- [23] Bha85 H.K.D.H. Bhadeshia: Diffusional Formation of Ferrite in Iron and its Alloys, Prog. Mat. Sci. 29 (1985), pp. 321-386.
- [24] Blã89 J.G. Blãs et al.: Influência da Composição Química e da Velocidade de Resfriamento sobre o Ponto A_{r3} em Aços de Baixo C Microligados ao Nb. In: *Congresso Anual da Associação Brasileira de Metais*, ABM, São Paulo, Out, 1 (1989), pp. 11-29.
- [25] Ble02 W. Bleck: Using the TRIP effect – the dawn of a promising group of cold formable steels, Proc. Int. Conf. on TRIP-Aided High Strength Ferrous Alloys, Ghent, June 2002.
- [26] Ble04 W. Bleck, S. Papaefthymiou and A.Frehn: Microstructure and Tensile Properties in Dual Phase and TRIP Steels, Steel Res. Int., 75 (2004), pp. 704-710.
- [27] Ble10 W. Bleck (Ed.): Material Science of Steel, 2nd ed., Aachen, Mainz, 2010, pp. 176–177.
- [28] Ble10a W. Bleck und D. Hömberg: Fortsetzungsantrag auf Gewährung einer Sachbeihilfe zum Forschungsvorhaben "Simulation, Optimierung und Regelung von Gefügebildung und mechanischen Eigenschaften beim Warmwalzen von Mehrphasenstählen", 2010.
- [29] Bok98 A. Bokota and S. Iskierka: Numerical Analysis of Phase Transformations and Residual Stresses in Steel Cone-Shaped Elements Hardened by Induction and Flame Methods, Int. J. Mech. Sci., 40 (1998), pp. 617–629.

- [30] Bor88 F. Boratto, S. Yue, J.J. Jonas and T.H. Lawrence: Design of Schedules for the Production of High Strength Microalloyed Steel Strip in a Hot Stickle Mill, Proc. Thermec'88, ISIJ, 1 (1988), pp. 383-390.
- [31] Bra75 H. Brandis: Rechnerische Bestimmung der Umwandlungstemperaturen von niedriglegierten Stählen, TEW Techn. Berichte, 1 (1975), pp. 8-10.
- [32] Bra81 J.R. Bradley and H.I. Aaranson: Growth Kinetics of Grain Boundary Ferrite Allotriomorphs in Fe-C-X Alloys, Metall. Trans., 12A (1981), pp. 1729-1741.
- [33] Bro96 M. Brokate and J. Spreckels: Hysteresis and phase transitions. In: Applied Mathematical Science Vol. 121, Springer, 1996, p.310.
- [34] Cah56 J.W. Cahn: Transformation Kinetics during Continuous Cooling, Acta Metal., 4 (1956), pp.572-575.
- [35] Cah56a J.W. Cahn: The Kinetics of Grain Boundary Nucleation Reactions, Acta Metal., 4 (1956), pp.449-459.
- [36] Car44 L.A. Carapella: Computing A'' or M_s (Transformation Temperature on Quenching) from Analysis, Metal. Progress, 46 (1944), pp. 108-118.
- [37] Cho84 P. Choquet, P. Fabregue, J. Giusti and B. Chamont: Proc. Int. Conf. on High Strength Low Alloy Steels. Australia, 1984, p.28.
- [38] Cho85 P. Choquet, A. LeBon and C. Perdix: Mathematical Model for Predictions of Austenite and Ferrite Microstructures in Hot Rolling Processes, IRSID Report, St. Germain-en-Laye, 7 (1985), pp. 1025-1030.
- [39] Cho90 P. Choquet, P. Fabregue, J. Giusti, B. Chamont, J.N. Pezant and F. Blanchet: Modelling of Forces, Structure and Final Properties during the Hot Rolling Process on the Hot Strip Mill. In: S. Yue ed., *Mathematical Modelling of Hot Rolling of Steel*, Montreal, CM, 1990, pp. 34-43.
- [40] Chr75 J. W. Christian: The Theory of Transformations in Metals and Alloys, Part 1, Oxford, Pergamon Press, (1975).
- [41] Cle55 P.J. Clemm and J.C. Fisher: Nucleation of Secondary Phases, Acta Metall., 3 (1955), pp. 70-73.
- [42] Den92 S. Denis, D. Farias, and A. Simon: Mathematical Model Coupling Phase Transformations and Temperature Evolutions in Steels, ISIJ Int., 32 (1992), pp. 316–325.
- [43] Die88 G. Dieter: Mechanical Metallurgy, Singapore, McGraw-Hill, 1988, p. 524.
- [44] Dig <http://www.digimizer.com/>
- [45] Don96 B. Donnay, J. C. Herman, V. Leroy, U. Lotter, R. Grossterlinder and H. Pircher: Microstructure Evolution of C-Mn Steels in the Hot-Deformation Process, Proc. of 2nd Int. Conf. on Modelling of Metal Rolling Processes, ed. by J. H. Beynon, P. Ingham, H. Teichert and K. Waterson, The Institute of Materials, London (UK), (1996), pp. 23-35.

- [46] Eno92 M. Enomoto: Prediction of TTT-Diagram of Proeutectoid Ferrite Reaction in Iron Alloys from Diffusion Growth Theory, ISIJ Int., 32 (1992), pp. 297-305.
- [47] Fac05 V.D. Fachinotti, A. Cardona and A.A. Anca: Solid-state Microstructure Evolution in Steels, Proc. Congress on Computational Mechanics VIII - MECOM 2005, AMCA, Buenos Aires, Argentina, November 2005.
- [48] Fan98 M. Fanfoni and M. Tomellini: The Johnson-Mehl-Avrami-Kolmogorov model: A brief review, Il Nuovo Cimento D, 20 (1998), pp. 1171–1182
- [49] Far06 J. Farjas and P. Roura: Modification of the Kolmogorov–Johnson–Mehl–Avrami rate equation for non-isothermal experiments and its analytical solution, Acta Mater., 54 (2006), pp. 5573–5579.
- [50] Faz05 F. Fazeli: Modeling the Austenite Decomposition into Ferrite and Bainite, The University of British Columbia, Doctoral Thesis, 2005.
- [51] Fin96 H. Finkler and M. Schirra: Transformation Behaviour of High Temperature Martensitic Steels with 8-14% Chromium, Steel Res., 67 (1996), pp. 328-342.
- [52] Gau06 D. Gaude-Fugarolas and P.J. Jacques: A New Physical Model for the Kinetics of the Bainite Transformation, ISIJ Int., 46 (2006), pp. 712-717.
- [53] Gla97 T. Gladman ed.: The Physical Metallurgy of Microalloyed Steels, London: Institute of Materials, 615 (1997), pp. 148, 234,
- [54] Gra46 R. A. Grange, H.M. Stewart: The Temperature Range of Martensite Formation, Trans. AIME, 167 (1946), p. 467.
- [55] Gro08 R. Großterlinden, J. Aldazabbal, O. Gracia, H.H. Dickert, P. Suwanpinij, E. Dimakarakou, E. Kamoutsis, A.I. Katsamas, Hebesberger, K. Satzinger: Design of bainite in steels from homogeneous and inhomogeneous microstructures using physical approaches, RFCS Technical Report No. 3, 01/07/08 – 31/12/08.
- [56] Gué79 G. Guénin, Polytechnic Institute Lyon, Ph.D. thesis, 1979.
- [57] Gup93 S.P. Gupta: Kinetics of Ferrite Transformation in an HSLA Steel Containing Nb, Steel Res. Int., 64 (1993), pp. 623-629.
- [58] Hac08 K. Hack (ed.): The SGTE casebook-Thermodynamics at Work, 2nd ed, Cambridge, Woodhead Publishing Limited, 2008.
- [59] Han01 H. N. Han and S.H. Park: Model for Cooling and Phase Transformation Behaviour of Transformation induced Plasticity Steel on Runout Table in Hot Strip Mill, Mat. Sci. Tech., 17 (2001), pp. 721-726.
- [60] Haw83 E.B. Hawbolt, B. Chau, and J.K. Brimacombe: Kinetics of Austenite-Pearlite Transformation in Eutectoid Carbon Steel, Metall. Trans., 14A (1983), pp. 1803-1815.
- [61] Haw85 E. B. Hawbolt, B. Chau and J. K. Brimacombe: Kinetics of Austenite-Ferrite and Austenite-Pearlite Transformation in a 1025 Carbon Steel, Metall.

- Trans., 16A (1985), pp. 565-578.
- [62] Hay <http://www.hayes-lemmerz.com/>
- [63] Hil04 M. Hillert and J. Ågren: On the Definitions of Paraequilibrium and Orthoequilibrium, *Scrip. Mater.*, 50 (2004), pp. 697–699.
- [64] Hil75 M. Hillert: Diffusion and Surface Control of Reactions in Alloys, *Metall. Trans.* 6A (1975), pp. 5-19.
- [65] Hil99 M. Hillert: *Phase Equilibria Phase Diagrams and Phase Transformations*, Cambridge University Press, Cambridge, 1999.
- [66] Hod91 P. D. Hodgson, R. E. Gloss and G. L. Dunlop: Microstructure Evolution during Rod and Bar Rolling, 32nd Mechanical Working and Steelmaking Conference, ISS-AIME, Cincinnati, 1991, pp. 527-538.
- [67] Hod92 P.D. Hodgson and R.K Gibbs: A Mathematical Model to Predict the Mechanical Properties of Hot Rolled C-Mn and Microalloyed Steels, *ISIJ Int.*, 32 (1992), p. 1329-1338.
- [68] Hod93 P.D. Hodgson: Mathematical Modelling of Recrystallisation Processes During the Hot Rolling of Steel, University of Queensland, Doctoral thesis, 1993, p. 3.
- [69] Hod95 P.D. Hodgson, L.O. Hazeldon. D.L. Matthews and R.E. Gloss: Microalloying '95, eds. M. Korchynsky et al., ISS of AIME, Warrendale, PA USA, 1995, pp. 341-353.
- [70] Hof10 O. Hoffman: Downstream Activities in Example from the Perspective of ThyssenKrupp's Automotive Customers, Proc. of 10th Int. Conf. Steel Rolling, China, Beijing, 2010, pp.74-80.
- [71] Höm11 D. Hömberg: Personal communication, December 2011.
- [72] Höm97 D. Hoemberg: Irreversible Phase Transitions in Steel, *Math. Methods in App. Sci.*, 20(1997), pp. 59–77.
- [73] Hou78 H.P. Hougardy: Die Darstellung des Umwandlungsverhaltens von Stählen in den ZTU-Schaubildern, *Härtereitechn. Mitt.* 33(1978), p.63-70.
- [74] Hua06 C.J. Huang and D. Brown: Phase-Field Model Prediction of Nucleation and Coarsening during Austenite/Ferrite Transformation in Steels, *Met. Mat. Trans.*, 37A (2006), pp. 589-598.
- [75] Hum04 F.J. Humphreys and M. Hatherly: Recrystallisation and Related Annealing Phenomena, 2nd ed., Oxford, Elsevier, 2004, p. 415.
- [76] IMJ <http://rsbweb.nih.gov/ij/>
- [77] Jac02 P.J. Jacques, P. Harlet, F. Delannay: Critical assessment of the phase transformations occurring during the heat treatment of TRIP-assisted multiphase steels, Proc. Int. Conf. TRIP-Aided High Strength Ferrous Alloys, Ghent, June 2002, pp.129-134.

- [78] Jan84 B. Jansson, Royal Institute of Technology, Doctoral thesis, 1984.
- [79] Jan07 K.G.F. Janssens, D. Raabe, E. Kozeschnik, M.A. Miodownik and B. Nestler: Computational Materials Engineering - An Introduction to Microstructure Evolution, Elsevier, 2007.
- [80] Joh39 W. A. Johnson and R. F. Mehl: Reaction Kinetics in Processes of Nucleation and Growth, Trans. of Ame. Inst. Mining and Met. Eng, 135 (1939), pp. 416–458.
- [81] Kat08 A.I. Katsamas and G. N. Haidemenopoulos: A Semi-Empirical Model for the Evolution of retained Austenite via Bainitic Transformation in Multiphase TRIP Steels, Steel Res. int., 79 (2008), pp. 875-884.
- [82] Ker92 A. Kern, J. Degenkolbe, B. Müsgen and U. Schriefer: Computer Modelling for the Prediction of Microstructure Development and Mechanical Properties of HSLA Steel Plates, ISIJ Int., 32 (1992), pp. 387-394.
- [83] Kir83 J.S. Kirkaldy and D. Venugopalan.: Prediction of Microstructure and Hardenability in Low Alloy Steels. In: A.R. Marder and J.I. Goldstein (ed.) *Phase Transformations in Ferrous Alloys*, AIME, Warrendale, 1983, pp. 125-148.
- [84] Koi59 D.P. Koistinen and R.E. Marburger: A General Equation Prescribing the Extent of the Austenite-martensite Transformation in Pure Iron-carbon and Plain Carbon Steels, Acta Met. 7 (1959), pp. 59–60.
- [85] Kol37 A.N. Kolmogorov: Statistical theory of crystallization of metals, Izvestia Akademia Nauk SSSR Ser. Mathematica, 1 (1937), pp. 355–359.
- [86] Kop00 T.A. Kop, Y. van Leeuwen, J. Sietsma and S. van der Zwaag: Modelling the Austenite to Ferrite Phase Transformation in Low Carbon Steels in Terms of the Interface Mobility, ISIJ Int. 40 (2000), pp.713-718.
- [87] Kop01 T.A. Kop, G.W. Remijn, V. Svetchnikov, J. Sietsma and S. Zwaag: Some Observations on the Effect of Austenitisation Conditions on the Transformation Kinetics in an HSLA Steel and Related C-Mn steels, J. Mat. Sci., 36 (2001), pp. 1863-1871.
- [88] Koz11 Ernst Kozeschnik: Modeling the Material Steel – Basics, Limits, Trends, seminar, 02.12.2011, Aachen.
- [89] Kri97 G.P. Krielaart, J. Sietsma and S. van der Zwaag: Ferrite Formation in Fe-C Alloys during Austenite Decomposition under Non-equilibrium Interface Conditions, Mat. Sci. Eng., 237 A (1997), pp. 216-223.
- [90] Kri98 G.P. Krielaart and S. van der Zwaag: Kinetics of Gamma-Alpha Phase Transformation in Fe-Mn Alloys Containing low Manganese, Mater. Sci. Technol., 14 (1998), pp. 10-18.
- [91] Kul80 A. Kulmburg: Beitrag zur Vorausberechnung von ZTU-Schaubildern,

- Härtereitechnische Mitteilungen-HTM 35 (1980), pp. 52-58.
- [92] Kun98 T. Kunitake and Y. Okada: The Estimation of Bainite Transformation Temperatures in steels by empirical formulas, JISI, 84 (1998), pp. 137-141.
- [93] Kva98 T. Kvačakaj and I. Mamuzic: A Quantitative Characterization of Austenite Microstructure after Deformation in Nonrecrystallization Region and its Influence on Ferrite Microstructure after Transformation, ISIJ Int., 38 (1998), pp. 1270-1276.
- [94] Kwo88 O. Kwon, K. Kang, K. Lee, J. Lee, K. Lee and R. Chang: The Structural/Property Prediction and Control Model for Plain Carbon Steels, RIST, Pohang, 1988.
- [95] Kwo92 O. Kwon: A Technology for the Prediction and Control of Microstructural Changes and Mechanical Properties in Steel, ISIJ Int. 32(1992), pp.350-358.
- [96] Lac03 S. Lacroix, Y. Bréchet, M. Véron, D. Quidort, M. Kandel and T. Lung: Influence of Deformation on Austenite to Ferrite Transformation in low Carbon Steels. In: *Experimental Approach and Modelling*, Proc. MS&T, Chicago, November 2003, CD.
- [97] Leb84 J. Leblond and J. Devaux: A New Kinetic Model for Anisothermal Metallurgical Transformation in Steels including Effect of Austenite Grain Size, Acta Metal., 32 (1984), pp. 137-146.
- [98] Leb85 J. B. Leblond, G. Mottet, J. Devaux and J.C. Devaux: Mathematical Models of Anisothermal Phase Transformations in Steels and Predicted Plastic Behaviour, Mat. Sci. Tech., 1 (1985), pp. 815-822.
- [99] Led80 L.A. Leduc: Doctoral thesis, University of Sheffield, 1980.
- [100] Lee01 Y. van Leeuwen, M. Onink, J. Sietsma and S. van der Zwaag: The Gamma-Alpha Transformation Kinetics of low Carbon Steels under Ultra-fast Cooling Conditions, ISIJ Int., 41 (2001), pp. 1037-1046.
- [101] Lee02 Y.K. Lee: Empirical Formula of Isothermal Bainite Start Temperature of Steels, J. Mat. Sci. Let., 21 (2002), pp. 1253-1255.
- [102] Lee07 S. H. Lee and K. J. Lee: The Effect of Si on the Nucleation Kinetics of Ferrite in Dual Phase Steels, J. Korean Inst. Metals and Materials, 45 (2007), pp. 389-396.
- [103] Lee92 K. J. Lee, J. K. Lee, K. B. Kang and O. Kwon: Mathematical Modelling of Transformation in Nb Microalloyed Steels, ISIJ Int., 32 (1992), pp. 326-334.
- [104] Lee98 Y. van Leeuwen, S. Vooijs, J. Sietsma and S. van der Zwaag: The Effect of Geometrical Assumptions in Modelling Solid-State Transformation Kinetics, Met. Mat. Trans. 29A (1998), pp. 2925-2931
- [105] Lee99 J.K. Lee et al.: Prediction of Tensile Deformation Behaviour of Formable Hot Rolled Steels, Posco Technical Research Laboratories

- Report, Pohang, 1999.
- [106] Li98 M.V. Li, D. V. Niebuhr, L. L. Meekisho and D. G. Atteridge: A Computational Model for the Prediction of Steel Hardenability, Metall. Mat. Tran., 29B (1998), pp 661-672.
- [107] Liu07 D. Liu, F. Fateh and M. Matthias: Modelling of Microstructure Evolution during Hot Strip Rolling of Dual Phase Steels, ISIJ Int., 47 (2007), pp. 1789–1798.
- [108] Liu07a D. Liu, F. Fateh, M. Matthias and W.J. Poole: A Microstructure Evolution Model for Hot Rolling of a Mo-TRIP Steel, Met. Mat. Trans. 38A (2007), pp. 894-909.
- [109] Log03 I. Loginova, J. Odqvist, G. Amberg and J. Ågren: The Phase-Field Approach and Solute Drag Modelling of the Transition to Massive $\gamma \rightarrow \alpha$ Transformation in Binary Fe-C Alloys, Acta Mater. 51 (2003), pp. 1327-1339.
- [110] Log04 I. Loginova, J. Ågren and G. Amberg: On the Formation of Widmanstaetten Ferrite in Binary Fe-C-Phase-field Approach, Acta Mat., 52 (2004), pp.4055-4063.
- [111] Lor03 U. Lorenz and J-J. Esser: Homogeneity of Deformation, Materialprüfung, 45(2003), pp.449-454.
- [112] Lor04 U. Lorenz: Anwendung von Werkstoffmodellen auf die Phasenumwandlung und die Austenitkonditionierung von Stählen, RWTH Aachen University, Dissertation, 2004.
- [113] Lus03 M.T. Lusk, W. Wang, X. Sun and Y.K. Lee: On the Role of Kinematics in Constructing Predictive Models of Austenite Decomposition. In: E.B. Damm and M.J. Merwin (eds.), *Austenite Formation and Decomposition*, Proc. MS&T, Warrendale, October 2003.
- [114] Lus97 M.T. Lusk and H.J. Jou: On the rule of additivity in phase transformation kinetics, Met. Mat. Trans., 28A (1997), pp.287-291.
- [115] Mat02 H. Matsuda, F. Kitano, K. Hasegawa, T. Urabe, Y. Hosoya: Metallurgy of continuously annealed high strength TRIP steel sheet, Proc. Int. Conf. TRIP-Aided High Strength Ferrous Alloys, Ghent, June 2004, pp. 113-119
- [116] Mat04 H. Matsuda and H.K.D.H. Bhadeshia, Proc. Royal Soc. A, 460 (2004), pp. 1707-1722.
- [117] Mav88 L.T. Mavropoulos, J.J. Jonas: Effect of the Combined Addition of Niobium and Boron on Static Recrystallization in Hot Worked Austenite, Canadian Met. Quarterly, 27(1988), pp.235-246.
- [118] Mec05 M. G. Mecozzi, J. Sietsma, S. Van der Zwaag, M. Apel, P. Schaffnit and I. Steinbach: Analysis of the Gamma- \rightarrow Alpha Transformation in a C-Mn Steel by Phase-field Modelling, Met. Mat. Trans., 36A (2005), pp. 2327-2340.

- [119] Mil04 M. Militzer and W. J. Poole: A Critical Comparison of Microstructure Evolution in Hot Rolled and Cold Rolled Dual Phase Steels, Pro. of Int. Conf. on Advanced High Strength Sheet Steels for Automotive Applications, AIST, Warrendale, PA, U.S.A., June, 2004, pp. 219-229.
- [120] Mil06 M. Militzer, M.G. Mecozzi, J. Sietsma and S. van der Zwaag: Three-Dimensional Phase Field Modelling of the Austenite-to-ferrite Transformation, Acta Mat., 54 (2006), pp. 3961-3972.
- [121] Mil08 M. Militzer: Microstructure Models for Hot-Rolling of Advanced High Strength Steels, Proc. TMP2008, Padua, September 2008, paper 118, CD.
- [122] Moe08 N. Meolans, B. Blanpain and P. Wollants: An introduction to phase-field modeling of microstructure evolution, Computer Coupling of Phase Diagrams and Thermochemistry, 32 (2008), pp. 268-294.
- [123] Moh10 H. Mohrbacher: Principal Effects of Mo in HSLA Steels and Cross Effects with Microalloying Elements, Int. Seminar in Applications of Mo in Steels, China, Beijing, June 2010, pp. 75-96.
- [124] Muk09 K. Mukherjee: Grain Refinement in Dual Phase Steels, The University of British Columbia, Doctoral Thesis, 2009.
- [125] Mur06 A. Murugaiyan, A. S. Podder, A. Pandit, S. Chandra, D. Bhattacharjee and R. K. Ray: Phase Transformations in two C-Mn-Si-Cr Dual Phase Steels, ISIJ Int., 46 (2006), pp. 1489–1494.
- [126] Mur75 L.E. Murr: Interfacial phenomena in metals and alloys, Reading, MA, Addison-Wesley, 1975.
- [127] Nad08 M. Naderi, A. Saeed-Akbari and W. Bleck: The Effects of Non-isothermal Deformation on Martensitic Transformation in 22MnB5 Steel, Mat. Sci. Eng. 487A (2008), pp. 445–455.
- [128] Nan90 S. Nanba, M. Katsumata, T. Inoue, S. Nakajima, G. Anan, A. Hiramatsu, A. Moriya, T. Watanabe and M. Umemoto: Computer program of thermodynamical factors for phase transformation in low alloy steels of 10 elements. (Simulation of phase transformation to predict the mechanical properties of steels--I), CAMP-ISIJ, 1990, 3, p.871
- [129] Neh46 A. E. Nehrenberg: The Temperature Range of Martensite Formation, Trans. AIME, 167(1946), p. 494-498.
- [130] Ouc79 C. Ouchi, et al.: The Effect of Hot Rolling Condition and Chemical Composition on the Onset Temperature of Gamma-Alpha Transformation After Hot Rolling, Trans. ISIJ, 22 (1982), pp. 214-222.
- [131] Pay44 P. Payson, C.H. Savage: Martensite Reactions in Alloy Steels, Trans. ASM, 33 (1944), pp. 261-275.
- [132] Pet11 T. Petermann: Numerische Modellierung der Gefügezusammensetzung von

- warmgewalzten Dualphasenstählen in Abhängigkeit der chemischen Zusammensetzung und der Prozessparameter des Warmwalzens unter Verwendung statistischer sowie werkstoffkundlich-physikalischer Modellansätze als Grundlage für die Prognose mechanisch technologischer Eigenschaften, Bachelorarbeit, SZMF and IEHK, July 2011.
- [133] Pet70 E.R. Petty: Martensite – Fundamental and Technology, Bristol, Longman, 1970, p.2
- [134] Pic78 F. Pickering: Physical Metallurgy and the Design of Steels, London, Applied Science Publishers, 1978, p. 63.
- [135] Pic86 F.B. Pickering: Steels: Physical Metallurgy Principles. In: *Encyclopedia of Materials Science and Engineering*, Cambridge, The MIT Press, Vol. 6, 1986.
- [136] Pin12 P. Pinard, A. Schwedt, A. Ramazani, P. Suwanpinij, H. Quade, U. Prahl and S. Richter: Bainite identification by combined EBSD and EPMA measurements, EBSD Conference, 26th – 28th March 2012, National Physical Laboratory (NPL), Teddington, UK.
- [137] Por92 D.A. Porter and K.E. Easterling: Phase Transformations in Metals and Alloys, 2nd ed., pp.289-290.
- [138] Qui01 D. Quidort and Y.J.M. Brechet: Isothermal Growth Kinetics of Bainite in 0.5% C Steel, *Acta Mater.*, 49 (2001), pp. 4161-4170.
- [139] Qui02 D. Quidort and Y. Brechet: The Role of Carbom on the Kinetics of Bainite Transformation in Steels, *Scripta Mater.*, 47 (2002), pp. 151-156.
- [140] Qui02b D. Quidort and Y.J.M. Brechet: A Model of Isothermal and Non Isothermal Transformation Kinetics of Bainite in 0.5% C Steels, *ISIJ Int.*, 42 (2002), pp. 1010-1017.
- [141] Raj05 J. Rajek: Computer Simulation of Precipitation Kinetics in Solid Metals and Application to the Complex Power Plant Steel CB8, Graz University of Technology, Doctoral Thesis, 2005.
- [142] Rap04 M. Rappaz: Phase Field Formalism, Doctoral School, Material Sciences and Engineering, École polytechnique fédérale de Lausanne (EPFL), June 2004.
- [143] Ree92 G.I. Rees and H.K.D.H. Bhadeshia: Bainite Transformation Kinetics Part 2. Modified Model, *Mat. Sci. Tech.*, 8 (1992), pp. 985-993.
- [144] Ree92b G.I. Rees and H.K.D.H. Bhadeshia: Bainite Transformation Kinetics Part 2. Non-uniform Distribution of Carbon, *Mat. Sci. Tech.*, 8 (1992), p. 994-996.
- [145] Rét99 T. Réti and I. Felde: A Non-linear Extension of the Additively Rule, *Comp. Mat. Sci.*, 15 (1999), pp. 466-482.
- [146] Rob83 W. Roberts, A. Sandberg, T. Siwecki and T. Werlefors: Prediction of Microstructure Development during Recrystallization Hot Rolling of Ti-V Steels, *Int. Conf. Tech., Applications of HSLA Steels*, Philadelphia, 1983, pp.

- 67-84.
- [147] Row46 E.S. Rowland and S.R. Lyle: The Application of M_s Points to Case Dpth Measurement, Trans. ASM, 37 (1946), pp. 27-47.
- [148] Rud11 J. Rudnizki, B. Böttger, U. Prah, and W. Bleck: Phase-Field Modelling of Austenite Formation from a Ferrite plus Pearlite Microstructure during Annealing of Cold-Rolled Dual-Phase Steel, Met. Mat. Trans., 42A (2011), pp. 2516-2525.
- [149] Rus70 K.C. Russell: Nucleation in Solids. In: H.I. Aaronson (ed.), *Phase Transformations*, 1970, p.217-268.
- [150] Rus80 K.C. Russell: Nucleation in Solids: The Induction and Steady State Effects, Adv. in Colloid Interface Sci., 13 (1980), pp. 205-318.
- [151] Sau04 N. Saunders Z. Guo, X. Li, A.P. Miodownik and J.P. Schillé: The Calculation of TTT and CCT Diagrams for General Steels, Internal report, Sente Software Ltd., 2004.
- [152] Sch35 E. Scheil: Anlaufzeit der Austenitumwandlung, Archiv für das Eisenhüttenwesen, 8 (1935), pp. 565-567.
- [153] Sel90 C. M. Sellars: Modelling—an interdisciplinary activity. In: S. Yue (ed.), *Intl. Symp. on Mathematical Modelling of Hot Rolling of Steel*, Hamilton, Ontario, pp. 1-18.
- [154] Sel90a C.M. Sellars: Modelling microstructural Development during Hot Rolling, Mat. Sei. Tech., 6 (1990), pp. 1072-1081.
- [155] Sel90b C.M. Sellars: The Physical Metallurgy of Hot Working. In: C.M. Sellars and G. Davies (eds.), *Hot Working and Forming Processes*, , The Metals Soc., London, 1980, p. 3-15.
- [156] Sel95 C. M. Sellars: Basics of Modelling for Control of Microstructure in Thermomechanical Controlled Processing, Ironmaking and Steelmaking, 22 (1995), pp. 459-464.
- [157] Sen84 T. Senuma, H. Yada, Y. Matsumura and T. Futamura: Structure of Austenite of Carbon Steels in High Speed Hot Working Processes, Tetsu-to-Hagané, 70 (1984), pp. 2112-2119.
- [158] Sen86 T. Senuma and H. Yada: Microstructural Evolution of Plain Carbon steels in multiple hot working, Proc. 7th Riso Int. Symp. Metallurgy and Materials Sci., Roshilde, 1986, pp. 547–552.
- [159] Ser04 S. Serajzadeh: Modelling of Temperature History and Phase Transformations during Cooling of Steel, J. Mat. Proc. Tech. 146 (2004), pp.311-317.
- [160] Shi81 C. Shiga, et al.: Development of Large Diameter High Strength Line Pipes for Low Temperature Use, Kawasaki

- Steel Technical Report, Dec. 1981, pp. 97-109.
- [161] Sic20 F. Siciliano, Jr. and J. J. Jonas: *Met. Mat. Trans.*, 31A(2000), pp. 511-530.
- [162] Sic99 SICILIANO JR., F.: *Mathematical Modeling of the Hot Strip Rolling of Nb Microalloyed Steels*. Doctoral thesis, McGill University, February 1999, 165 p.19.
- [163] Sin98 S.B. Singh and H.K.D.H. Bhadeshia: *Topology of grain deformation*, *Mat Sci Tech*, 14 (1998), pp. 832-834.
- [164] Ste03 G. Steinbeck: *Ergebnisse des Workshops Automobil-/Stahlindustrie*, October 2003, Linz, Austria. – Discussion Result of VDEh committee
- [165] Ste56 W. Steven, A.G. HAYNES: *The Temperature of Formation of Martensite and Bainite in Low Alloy Steels*, *Journal of the Iron and Steel Institute*, 183(1956), pp. 349-359.
- [166] Stei96 I. Steinbach, F. Pezzolla, B. Nestler, M. Seeßelber, R. Prieler, G.J. Schmitz, J.L.L. Rezende: *A phase field concept for multiphase systems*, *Physica. D* 94 (1996) pp. 135–147.
- [167] Stei99 I. Steinbach, F. Pezzolla: *A generalized field method for multiphase transformations using interface fields*, *Physica. D* 134 (1999) pp. 385–393.
- [168] Str05 H. Strandlund: *Simulation of Diffusional Processes in Alloys*, KTH Royal Institute of Technology, Doctoral Thesis, 2005.
- [169] Stu54 W. Stuhlmann: *Die Aussage der ZTU-Schaubilder*, *Härterei-Technische Mitteilungen-HTM* 6 (1954), p.31-48.
- [170] Sue87 M. Suehiro, T. Senuma, H. Yada, Y. Matsumura and T. Arivoshi: *Kinetic Model for Phase Transformation of Low C Steel during Continuous Cooling*, *Tetsu-to-Hagané*, 73 (1987), pp. 1026-1033.
- [171] Sun05 X. Sun, Q. Liu, and H. Dong: *Deformation Induced Ferrite Transformation and Grain Refinement in Low Carbon Steel*, *Proc. of 1st Int. Conf. Proc. Super-High Strength Steels*, Rom, November 2005, paper 35.
- [172] Sun98 W.P. Sun, M. Militzer, E.B. Hawbolt and T.R. Meadowcroft: *Analysis and Modelling of Austenite Grain Refinement and Growth during Hot Rolling*, *Trans. ISS*, 25 (1998), pp.85-94.
- [173] Suw09 P. Suwanpinij, J. Rudnizki, U. Prah, and W. Bleck: *Investigation of the Effect of Deformation on γ - α Phase Transformation Kinetics in Hot-Rolled Dual Phase Steel by Phase Field Approach*, *Steel Res. Int.*, 80 (2009), pp 616-622.
- [174] Suw10 P. Suwanpinij, K. Mukherjee, M. Graf, U. Prah, W. Bleck and R. Kawalla: *Towards Modelling of Phase Transformation and Mechanical Properties in Hot Rolled Dual Phase Steel*, *Proc. of TMS Annual Meeting*, 14-18 February 2010, Seattle, USA, CD.
- [175] Suw10a P. Suwanpinij, N. Togobytska, U. Prah, W. Weiss, D. Hömberg, and W.

- Bleck: Numerical Cooling Strategy Design for Hot Rolled Dual Phase Steel, Steel Res. Int., 81 (2010), pp.1001-1009.
- [176] Sve97 A.V. Sverdlin and A.R. Ness: The Effects of Alloying Elements on the Heat Treatment of Steel, Steel Heat Treatment Handbook, ed., Marcel Dekker, New York, 1997, pp. 45-91.
- [177] Tak91 M. Takahashi and H.K.D.H. Bhadeshia: A Model for Microstructure of some Advanced Bainitic Steels, Mater. Trans., JIM, 32 (1991), pp. 689-696.
- [178] Tam88 I. Tamura, H. Sekine, T. Tanaka and C. Ouchi: Thermomechanical Processing of High-strength Low-alloy Steels, London: Butterworths, 1988, pp. 20-21, 31-32, 129, 210.
- [179] TCC TCC™ Thermo-Calc® Software User's meeting Version S, p.8-25.
- [180] Thi06 R.G. Thiessen, Physically-Based Modelling of Material Response to Welding Delft University of Technology, Doctoral Thesis, 2006, p.130.
- [181] Ume83 M. Umemoto, H. Ohtsuka and I. Tamura: Transformation to Pearlite from Work-hardened Austenite, Trans. Iron Steel Inst. Jpn., 23 (1983), pp. 775-784.
- [182] Ven01 M. Venkatraman, O. N. Mohanty and R. N. Ghosh: Modelling of Transformation Kinetics in HSLA 100 Steel during Continuous Cooling, Scandi. Jour. of Metall., 30 (2001), pp. 8-13.
- [183] Wei97 M. C. Weinberg, D. P. Birnie III and V. A. Shneidman: Crystallization Kinetics and the JMAK Equation, J. Non-Crystalline Solids, 219 (1997), pp. 89-99.
- [184] Wil87 M. Wildau and H. Hougardy: Influence of the M5-Temperature on Stresses and Changes in Dimension, HTM, 42 (1987), pp. 261-268.
- [185] Wol01 P. van der Wolk: Modelling CCT Diagrams of Engineering Steels Using Neural Network, Technische Universiteit Delft, Doctoral Thesis, 2001.
- [186] Wol07 M. Wolff, S. Boettcher and M. Böhm: Phase Transformations in Steel in the Multi-phase Case — General Modelling and Parameter Identification, report 02-07, July 2007, Zentrum für Technomathematik, Universität Bremen.
- [187] Yad88 H. Yada: Prediction of Microstructural Changes and Mechanical Properties in Hot Strip Rolling, Proc. Int. Symp. on Accelerated Cooling of Rolled Steel, ed. G.E. Ruddle and A.F. Crawley, Pergamon, 1988, p. 105.-120
- [188] Ye04 J.S. Ye, H.B. Chang and T.Y. Hsu: Kinetics Model of Isothermal Ferrite and Pearlite Transformations under Applied Stress, ISIJ International, 44 (2004), pp. 1079-1085.
- [189] Yos92 A. Yoshie, M. Fujioka, Y. Watanabe, K. Nishioka and H. Morikawa: Modelling of Microstructural Evolution and Mechanical Properties of Steel Plates Produced by Thermo-mechanical Control Process, EISIJ Int. 32 (1992), pp. 395-404.

- [190] Zen49 C. Zener: Theory of Growth of Spherical Precipitates from Solid Solutions, J. App. Phys., 20 (1949), pp. 950-953.
- [191] Zha92 J. Zhao: Continuous Cooling Transformation in Steels, Mat. Sci. Tech., 8 (1992), pp. 997-1003.
- [192] Zhu97 Y.T. Zhu, T.C. Lowe and R.J. Asaro: Assessment of the theoretical basis of the Rule of Additivity for the nucleation incubation time during continuous cooling, J. Appl. Phys. 82 (1997), pp. 1129-1137.

10 Curriculum vitae

Selected International Publications

- 2012 P. Suwanpinij, P. Pinard, S. Richter, W. Bleck: **Simulation of Microstructure Development and Carbon Partitioning in Hot Rolled Dual Phase Steels by Phase Field Method**, TMP2012, 10.-12.09.2012, Sheffield, UK.
- 2012 P. Suwanpinij, U. Prah, W. Bleck, R. Kawalla: **Fast algorithms for phase transformations in dual phase steels on the hot strip mill Run Out Table (ROT)**, Archives of Civil and Mechanical Engineering 12 (2012), pp.305–311
- 2012 P. Suwanpinij, D. Yan, U. Prah, W. Bleck: **Phase Transformation Modelling for Different Hot Rolled Dualphase Steels**, Steel Research Int. 83 (2012) Special Ed., Proc. 14th Int. Conf. Metal Forming, pp.903-906.2010
- 2010 P. Suwanpinij, N. Togobytska, U. Prah, W. Weiss, D. Hömberg, and W. Bleck: **Numerical Cooling Strategy Design for Hot Rolled Dual Phase Steel**, Steel Research Int. 81 (2010) no.11, pp.1001-1009
- 2010 P. Suwanpinij, K. Mukherjee, M. Graf, U. Prah, W. Bleck, R. Kawalla: **Towards Modelling of Phase Transformation and Mechanical Properties in Hot Rolled Dual Phase Steel**, Proc. TMS Annual Meeting, 14-18 February 2010, Seattle, USA, CD.
- 2009 P. Suwanpinij, J. Rudnizki, U. Prah and W. Bleck: **Investigation of Effect of Deformation on γ - α Phase Transformation kinetics in Hot-Rolled Dual Phase Steel by Phase Field Approach**, Steel Research Int. 80 (2009) no.9, p.616-622
- 2004 M. Krzyzanowski, P. Suwanpinij, and J.H. Beynon: **Analysis of Crack Development, Both Crack and Closure, in Steel Oxide Scale Under Hot Compression**, Proc. 8th Int. Conf. on Numerical Methods in Industrial Forming Processes (NUMIFORM2004), 13-17 June 2004, Ohio, USA.
- 2003 P. Suwanpinij: **Improvement of Product Surface Finish During Hot Rolling**, Dissertation, Department of Engineering Materials, University of Sheffield, UK.
- 2003 P. Suwanpinij, U. Kitkamthorn, I. Diewwanit and T. Umeda: **Solidification Characteristics of 356, 380 and 390-type Aluminum Alloys and Influence from Copper and Iron**, Materials Transactions 44 (2003), no.5, p.845-852.

Work Experience

Dec 2003-Apr 2006 **Metallurgical Engineer Level 4 and 5**, Department of Primary Industry and Mines, Ministry of Industry, Thailand

Educational Background

From Oct 2006 **PhD Candidate** in Department of Ferrous Metallurgy (IEHK), RWTH Aachen University, Germany, on '*Deformation Induced Phase Transformation in Hot Rolled DP Steels*' (Supported by Royal Thai Government Scholarship, under the Cooperation between DAAD and CHE)

2002-2003 Master of Metallurgy (**MMet**) with **Distinction**, Department of Engineering Materials University of Sheffield, UK (Supported by Royal Thai Government Scholarship)

1997-2001 **B.Eng.** (Bachelor of Engineering) with **GPA 3.83/4.00, First Class Honour, Gold Medal**, Department of Metallurgical Engineering, Chulalongkorn University, Bangkok, Thailand

1986-1997 Chulalongkorn University Demonstration School (Satit Chula School), Bangkok, Thailand